Verwerking en karakterisering van polymere materialen tot sferische poeders
als mogelijke bouwmaterialen voor fusiegebaseerde additieve productietechnieken

Processing and Characterization of Polymeric Materials to Spherical Powders
as Candidate Build Material for Fusion Based Additive Manufacturing

Nicolas Mys

UNIVERSITEIT
GENT

PROMOTORS

prof. dr. ing. L. Cardon
Ghent University
Faculty of Engineering and Architecture
Department of Materials, Textiles and Chemical Engineering

prof. dr. ir. A. Verberckmoes
Ghent University
Faculty of Engineering and Architecture
Department of Materials, Textiles and Chemical Engineering

EXAMINATION COMMITTEE

Prof P. De Baets	(Chair)	Ghent University, Belgium
Prof. L. Cardon	(Promotor)	Ghent University, Belgium
Prof A. Verberckmoes	(Promotor)	Ghent University, Belgium
Prof. D. D'hooge	(Dean)	Ghent University, Belgium
Dr. F. De Ruyck		University College Ghent, Belgium
Prof. C. Martins		University of Minho, Portugal
Prof. K. Ragaert		Ghent University, Belgium
Prof. M. Vanhaelst		Ghent University, Belgium

RESEARCH INSTITUTE

Ghent University
Department of Materials, Textiles and Chemical Engineering
Tech Lane Ghent Science Park/Campus A
Technologiepark Zwijnaarde 915
B-9052 Gent
Nicolas.mys@ugent.be

EXPRESSION OF GRATITUDE

*Before all I would like to dedicate this dissertation to my godchild Flo, to whom
I will surely read countless times from this book as a riveting bedtime story.*

Writing a PhD is a lot like going on an expedition and this doctoral expedition was one of the longest and hardest trips I have ever made in the academic mountain range. I have been gone for over 4 years. I was weary, but resting fast, tired, but sleeping deep, hungry for more, and devouring everything on my path. For four years I have explored the depths and the heights of my topic, walking along its powdery slopes trying to assess the dangers and pitfalls on my path while gazing at my end goal. Were I not roped in with my two promotors and walking alongside a good party of academic climbers, I would have surely fallen. Nevertheless, gradually, layer by layer, my PhD took form…

In this regard I feel I should thank my two promotors prof. dr. ing. Ludwig Cardon and prof. dr. ir. An Verberckmoes for catching my every fall, hauling me up and sending me back out on route. Their continuous support and patience has helped me through some tough obstacles. Frank De Ruyck also deserves a special thanks for helping me clear a path through the mist of the statistical designs and prof. dr. Isabel Van Driessche for providing the spray drying tools to do it with.

A good alpinist never ventures into the unknown by himself, therefore I must also thank my other rope parties, better known as my fellow colleagues from CPMT, for creating a pleasant and inspiring work atmosphere. Dahang, Els, Kurt, Lingyan, Maja, Nicolas, Ruben, Sara, Sisi, Veerle, and Willem: thank you! I would like to thank especially Tom Wieme, Karen Van Kets and Laurens Delva for doing a last partner check before I made my final climb. Yet I can only climb as well as my gear can carry me, for this I would also like to thank Mustafa Erkoç and Marcel Moerman for continuously repairing what I have broken and creating what I still have yet to break. Also prof. Kim Ragaert, though she sometimes loomed over me like a dark cloud, she let through a few rays of sunshine now and then to help me on my way.

I would also like to thank the members of the jury, the other climbing members of the Polyforce team and those who contributed to the project. Bart Goderis, Brecht Van Hooreweder, Jean-Pierre Kruth, Paula Moldenaers, Peter Van Puyvelde, Philippe Brasseur, Tom Craegs, Toon Roels and Vito Leo and; thank you for the fruitfull discussions and the supplying of samples. I would like to thank also the fellow Polyforce'rs for their contribution to my research over the years: Dieter, Leander, Michael, Olivier, Sasan; thank you for climbing this mountain with me!

Furthermore, the importance of a good basecamp cannot be underestimated in a venture like this. Sometimes a good home cooked meal, a few beers and above all

good company to whom I could vent or just simply take my mind off of things with is all the adventurer needs to get grounded again and restart with reinvigorated enthusiasm. For this I have to thank my family who supported me all through my academic path and always left me free to make my own choices and directions. It was easier knowing they were behind me and therefor this is also their merit. Similarly I would like to thank my friends from high school. As one should never do on traitorous terrain, we never split up and therefor still have many adventures to go on! On the same note, my friends from chemistry deserve a big thanks for reminding me when and where I had classes, when I was astray again. But most of all for all the after class activities and later on the PhD guidance they provided. A special thanks to Wannes for reading a chapter of mine and giving me advice on the subject. It served me well, thank you.

Finally I would like to thank my girlfriend Marijke who has known me throughout most of my chemical lifetime. She taught me to plan better and work harder and kept supporting and loving me unconditionally, leaving me my occasional outbursts when I felt the call of the mountains. Life with you is an adventure on its own.

ABSTRACT

Selective Laser Sintering (SLS) is a powder-based Additive Manufacturing (AM) technique to produce complex 3D parts layer by layer. The development of new powder materials suitable for SLS constitutes one of the main research topics of today. As the marked share mostly consists of polyamide (PA) materials, the application window for SLS remains rather small. Therefore, the introduction of new polymeric materials could broaden this application field. As most production methods do not allow for immediate production of suitable powders for SLS, new processing methods have to be investigated that can process the candidate materials into polymer powders usable for laser sintering. This PhD research has focused on expanding the material palette for SLS through the processing of 3 candidate engineering polymers with distinctly different properties compared to polyamide. The polymers in question are syndiotactic polystyrene (sPS), polysulfone (PSU) and polyphenylsulfone (PPSU). A wide array of processing techniques has been considered of which the physicochemical spray drying technique and the mechanical rotor milling technique were chosen as most suitable. The produced powders were afterwards characterized on size and shape in order to see if the powders meet the requirements needed for processing through SLS. Ideally, powders should be spherical of nature, exhibiting smooth surfaces and a mean diameter in the range of 45 – 90 µm. Next, the powders were investigated in order to see if there was any influence of the processing technique on the intrinsic and extrinsic properties that could affect processing through SLS. In a second part of the PhD as an alternative way of expanding the material palette, the creation of a polymer composite to improve the properties of the matrix was performed. This was done by mixing functionalized montmorillonite (MMT) into a polysulfone matrix by twin-screw extrusion. The extruded films were examined on any change in mechanical properties to examine the effect of the MMT in the PSU matrix.

As there exists a vast variety of polymers available for traditional processing techniques like injection molding or extrusion, it is interesting from a commercial and a research point of view to process the pellets in which these grades are readily available as a starting point for processing. In all three case studies the polymers could be processed in spherical powders using the rotor milling technique. Powders were found to have a spherical nature with good powder flowability assessed by the Hausner ratio. Particle size distributions (PSD) all lie within the desired range and were easily obtained using a three step refinement process in which the pellets were milled sequentially from pellet form to powder form of decreasing size with each step. PSD of all three case studies presented a mean diameter around 50 µm with a standard deviation of 15 µm. A final sieving step ensured the removal of inconsistencies and ensured good powder flow behavior.

ABSTRACT

Though the spray drying process shows great promise, further research still has to be done on this subject. From the three case studies polysulfone presented the most promise displaying smooth morphology and particle size of 26,1 µm. A response surface model (RSM) was elaborated exposing the most critical factors influencing particle size and particle morphology in the spray drying process. A careful balance has to be found in order to obtain spherical particles with a more optimized particle size. An augmented design could be a valuable addition in further improving the processing parameters. Additionally, FIB-SEM measurements provided clarity about the density of the particles confirming hollow spheres to be formed instead of fully dens particles.

GPC measurements revealed no significant degradation for both processing methods, contrary to the samples investigated which were processed by the more industrial cryogenic milling methods. Investigation of the thermal properties of the powder samples revealed a minor thermal history imparted on the materials which should be kept into account when sintering. Again, the cryogenically milled samples revealed aberrant behavior displaying a strong decrease in glass transition and in the case of sPS a decrease in crystallinity.

Functionalization of the nanoclays was performed by grafting a silane derivate called APTES onto the clay surface's free hydroxyl groups. The amine moiety present on the APTES was thereafter used to covalently bind 4-sulfophthalic acid via amidation onto the clay surface. This addition of an aryl sulfide is expected to increase compatibility of the hydrophilic nanoclays and the more hydrophobic polysulfone.

CHNS measurements revealed successful silanation on the nanoclays yet indicated no significant sulfonation to have occurred. XRD measurements of the samples indicated by a shift in diffraction peaks that the grafting process also occurred inside the clay galleries, which is needed for good intercalation with the polymer chains.

The blending of the composites occurred using twin screw extrusion with polysulfone as a matrix and the organically modified nanoclays by silylation. The high processing temperatures of polysulfone proved to be an impediment in the blending process as they provided the onset of degradation for the organic linkers. This caused the formation of air bubbles made by volatile degradation products which caused bad compatibilization of the nanoclays with the matrix and did not result in a significant increase in properties.

This dissertation has contributed to the material palette for SLS by identifying two processing routes to transform polymer pellets into spherical powders and adding three virgin engineering polymers to the gamma. It exposed critical problems regarding the processing of said polymers in regards to spray drying and twin-screw extrusion and offers possible solutions as interesting research topics.

SAMENVATTING

Selectief Laser Sinteren (SLS) is een poeder gebaseerde additieve productietechniek (AM, Additive Manufacturing) waarbij een complex 3D object laaggewijs wordt opgebouwd. De ontwikkeling van nieuwe poedermaterialen die kunnen gebruikt worden voor het SLS proces vormt vandaag een van de belangrijkste onderzoeksonderwerpen. Doordat de polyamides (PA) het overgrote deel van de beschikbare materialen uitmaken, blijven de mogelijke applicaties vrij beperkt tot de eigenschappen van deze klasse. De introductie van nieuwe polymeermaterialen tot dit gamma zou een enorme verbreding van dit toepassingsveld betekenen. Echter, polymeren worden niet standaard in poedervorm geproduceerd dat voldoet aan de vereisten voor verwerking via SLS. Dit wil zeggen dat er onderzoek gedaan moet worden naar verwerkingstechnieken die deze materialen kunnen omzetten in een geschikte vorm. Deze dissertatie heeft zich gericht op het uitbreiden van het materiaalpalet voor SLS door het introduceren van drie kandidaat materialen voor het laser sinteren. Hierbij werd er onderzoek verricht naar verscheidene verwerkingstechnieken waarbij er gefocust werd op de fysicochemische techniek genaamd sproeidrogen en de mechanische techniek genaamd rotor millen. De materiaalkeuze werd gebaseerd op *engineering polymers* welke zich onderscheiden in mechanische, chemische en thermische eigenschappen van de al beschikbare polyamides. De betrokken polymeren zijn syndiotactisch polystyreen (sPS), polysulfon (PSU) en polyfenylsulfon (PPSU). De geproduceerde poeders werden vervolgens gekarakteriseerd op hun grootte en vorm om te zien of deze zich kwalificeren als bouwmateriaal voor het sinterproces. Poederpartikels dienen sferisch te zijn met een glad oppervlak en een gemiddelde diameter in het bereik van 45 - 90 µm. Vervolgens werden de poeders onderzocht op enige veranderingen in intrinsieke en extrinsieke eigenschappen door de verwerkingstechniek zelf die het sinterproces zouden kunnen beinvloeden. In het tweede deel van het doctoraat werd er op een alternatieve manier bijgedragen aan het materiaalpalet voor SLS via het creëren van een composietmateriaal. Hiertoe werd montmorilloniet nanoklei (MMT) chemisch gefunctionaliseerd om beter in te mengen in een polysulfon matrix. Het blenden werd uitgevoerd op een dubbelschoef extruder waarbij dunne films geëxtrudeerd werden. Deze werden onderzocht in veranderingen in de mechanische eigenschappen om het effect van de MMT in de PSU matrix te bepalen.

Aangezien er een grote verscheidenheid aan polymeren beschikbaar is voor traditionele verwerkingstechnieken zoals spuitgieten of extrusie, is het interessant vanuit een commercieel en onderzoeksoogpunt de pellets te verwerken waarin deze conventioneel voorkomen. In alle drie de casestudies kunnen de polymeren in sferische poeders worden verwerkt met behulp van de rotor milling techniek. Poeders zijn van sferische aard en hebben een goede poedervloei, bepaald door de Hausner-Ration (HR). De deeltjesgrootteverdelingen (PSD) liggen allemaal binnen het

gewenste bereik en werden gemakkelijk verkregen met behulp van een driestaps proces waarbij de pellets vermaald worden van pellets tot poeders en verder verfijnd worden tot poeders van kleinere diameter. PSD van alle drie casestudies toont een gemiddelde diameter van ongeveer 50 μm met een standaardafwijking van 15 μm. Een laatste ingevoerde zeefstap zorgde voor het verwijderen van inconsistenties en zorgde voor een goed vloeigedrag van de poeders.

Hoewel het sproeidroogproces veelbelovend is, moet nog verder onderzoek gedaan worden over dit onderwerp. Uit de drie casestudies presenteerde polysulfon de beste waarden met een gladde morfologie en gemiddelde deeltjesgrootte rond 26,1 μm. Een statistisch model werd uitgewerkt om de meest kritische factoren die de deeltjesgrootte en deeltjesmorfologie beïnvloeden in het sproeidrogingsproces bloot te stellen. Het instellen van de processparameters houdt een voorzichtige balans in om sferische deeltjes te verkrijgen met een meer geoptimaliseerde deeltjesgrootte. Een vervolgmodel in het statistisch ontwerp kan een waardevolle aanvulling zijn om de verwerkingsparameters verder te verbeteren. Bovendien leverden FIB-SEM metingen bewijs dat holle sferen geproduceerd werden via deze instellingen.

GPC-metingen duiden geen significante degradatie voor beide vewerkingsmethoden aan, in tegenstelling tot de onderzochte monsters verkregen door de materialen cryogeen te vermalen. Onderzoek naar de thermische eigenschappen van de poeders onthulde een kleine thermische geschiedenis op de materialen die in acht moet genomen worden tijdens het sinteren. Opnieuw bleken de cryogeen vermalen poeders afwijkend gedrag te vertonen in een sterke afname in glastransitietemperatuur en kristalliniteit (in het geval van sPS).

Functionalisatie van de nanoclays werd uitgevoerd door het condenseren van een silaanderivaat genaamd APTES op de vrije hydroxylgroepen van de kleimineralen. De aminengroep aanwezig op de APTES werd daarna gebruikt om een covalente binding aan te gaan met 4-sulfoftaalzuur via amidatie. Door deze toevoeging van een arylsulfide wordt verwacht dat de compatibiliteit van de hydrofiele nanoclays en het meer hydrofobe polysulfon verbetert.

CHNS-metingen toonden een succesvolle silanering op de nanoclays aan, echter bleek er geen significante sulfonering plaats te vinden. XRD-metingen van de monsters toonden een verschuiving in diffractiepieken welke aangeven dat het entproces ook plaatsvond tussen de kleiplaatjes. Dit is nodig voor goede intercalatie met de polymeerketens.

De inmenging van nanoklei werd uitgevoerd door middel van dubbelschroef extrusie met polysulfon als een matrix en de organisch gemodificeerde nanoclays door silylering. De hoge verwerkingstemperaturen van polysulfon blijken hierbij een belemmering te zijn in het mengproces. Door de hoge verwerkingstemperatuur

beginnen de organische linkers te degraderen. Dit heeft de vorming van luchtbellentot gevolg, welke vluchtige afbraakproducten veroorzaakt. Dit zorgt op zijn beurt voor slechte compatibilisatie van de nanoclays met de matrix wat niet resulteerde in een significante toename van de beoogde eigenschappen.

Dit doctoraat heeft bijgedragen aan het materiaalpalet voor SLS door twee verwerkingsroutes te identificeren om polymeerpellets in sferische poeders te transformeren en drie *engineering* polymeren aan het gamma toe te voegen. Het stelde kritische problemen bloot in de verwerking van de genoemde polymeren met betrekking tot sproeidrogen en dubbelschroef extrusie en biedt mogelijke oplossingen als interessante onderzoeksonderwerpen.

SAMENVATTING

TABLE OF CONTENTS

TABLE OF CONTENTS

LIST OF SYMBOLS & ABBREVIATIONS

SYMBOLS

δ	Hildebrand Solubility Parameter [MPa$^{1/2}$]
ε	Strain [%]
η	Viscosity [Pa.s]
η_0	Zero shear rate viscosity [Pa.s]
θ	Angle between the incident beam and the scattering planes [°]
λ	wavelength [m]
μm	Micrometer (=10^{-6} m) [m]
ρ	Density [kg/m³]
σ	Stress (MPa)
ΔH^0_f	Enthalpy of fusion of a 100% crystalline polymer [J/kg]
ΔH_c	Enthalpy of crystallization [J/kg]
$\Delta H_{c, cold}$	Enthalpy of cold crystallization [J/kg]
ΔH_f	Enthalpy of fusion [J/kg]
M_n	Number average molecular weight [kg/mol]
M_w	Weight average molecular weight [kg/mol]
P	Polydispersity
T_c	Crystallization temperature [°C]
T_g	Glass transition temperature [°C]
T_{in}	Inlet temperature in spray drying process [°C]
T_m	Melting temperature [°C]
wt.%	Weight percentage [%]
X_c	Crystallinity [%]
$NaMMT_x$	Pristine montmorillonite, the subscript denoting the wt.% added to the PSU matrix
$SiMMT_x$	Silylated montmorillonite, the subscript denoting the wt.% added to the PSU matrix
$SMMT_x$	Sulfonated montmorillonite, the subscript denoting the wt.% added to the PSU matrix
$CMMT_x$	Commercial montmorillonite with organic spacer, the subscript denoting the wt.% added to the PSU matrix

ABBREVIATIONS

AM	Additive Manufacturing
aPS	Atactic Polystyrene
APTES	(3-aminopropyl)triethoxysilane
BM	Ball Milling/Ball Miller

SYMBOLS & ABBREVIATIONS

DMF	N,N-Dimethylformamide
DSC	Differential Scanning Calorimetry
EAB	Elongation At Break
EDC	1-Ethyl-3-(3-dimethylaminopropyl)carbodiimide
FFR	Feed Flow Rate
FIB-SEM	Focussed Ion Beam Scanning Electron Microscopy
FTIR	Fourier Transform Infrared Spectroscopy
GFR	Gas Flow Rate
GPC	Gel Permease Chromatography
HDT	Heat Deflection Temperature
HR	Hausner Ratio
KB	Kneading Block
MES	2-(N-morpholino)ethanesulfonic acid
MFI	Melt Flow Index
MMT	Montmorillonite
NHS	N-hydroxysuccinimide
P14	Pulverisette 14
PA	Polyamide
PAEK	Polyaryletherketone
PEEK	Polyether ether ketone
PP	Polypropylene
PP	Polypropylene
PPSU	Polyphenylsulfone
PSD	Particle Size Distribution
PSU	Polysulfone
R5000	Radel polyphenylsulfone viscous grade
R5600	Radel polyphenylsulfone low viscous grade
RM	Rotor Milling/Rotor Miller
RSM	Response Surface Model
RT	Room Temperature
SD	Spray Drying/Spray Dryer
SEM	Scanning Electron Microscopy
SLS	Selective Laser Sintering
SPA	4-Sulfophthalic acid
sPS	Syndiotactic polystyrene
STA	Simultaneous Thermal Analysis
TGA	ThermoGravimetric Analysis
TPU	Thermoplastic Polyurethane
UTS	Ultimate Tensile Strength
WSC	1-Ethyl-3-(3-dimethylaminopropyl)carbodiimide (a.k.a. EDC)
XRD	X-Ray Diffraction

Chapter 1

INTRODUCTION

This chapter gives a concise background outline of the research questions on which this doctorate rests. Selective laser sintering, its operating principle and the material shortage problematic are discussed. Finally, an overview of the manuscript is offered.

Additive Manufacturing (AM) refers to a set of 3D printing techniques which produce end-use 3D parts. In AM parts are produced directly from a digital model otherwise known as a Computer Aided Design (CAD) file [1], [2]. The model is sliced in discrete layers and then built layer-by-layer by the AM machine. Different forms of AM techniques are available nowadays of which Fused Deposition Modeling (FDM) is the most accessible form of 3D printing for the common man. Selective Laser Sintering (SLS) is another AM technique in which three dimensional objects are sintered out of polymeric powder material by the use of a CO_2-laser beam.

The part production process is schematically represented in Figure 1-1, on the next page. The production process starts with a 3D CAD (Computer Aided Design) file made by the designer which is sliced in discrete layers. Each layer represents a cross-section of the model which is used for the layerwise building process. In the sinterstation a thin layer of powder (typically 100 µm) is spread evenly by a roller or knife from the powder supply to the build platform. The layer is heated and parts of it are subsequently sintered using a CO_2-laser and scanning mirrors according to the CAD file cross-section. In doing so the polymer particles are fused together and the surrounding powder that was not molten, supports the melt. The process then repeats itself by spreading a new thin layer of powder over the previous one until all layers of the build are sintered and the part is formed. Upon completion of the build the part is left to cool as a whole and is removed from the surrounding power or 'part cake' [1]. This powder can then be recycled for further sintering of other models.

Brought to life in 1987 by the hands of Carl Deckard at the University of Texas, the technique was used mainly for rapid prototyping purposes [3]. It gained interest because of its capability to print more complex geometric structures than possible with other AM techniques without the need for support structures or tooling. Thanks to the specific processing technique in which the surrounding powder of the powder bed acts as support, complex tailor made objects are possible in low volumes with practically no extra cost [4].
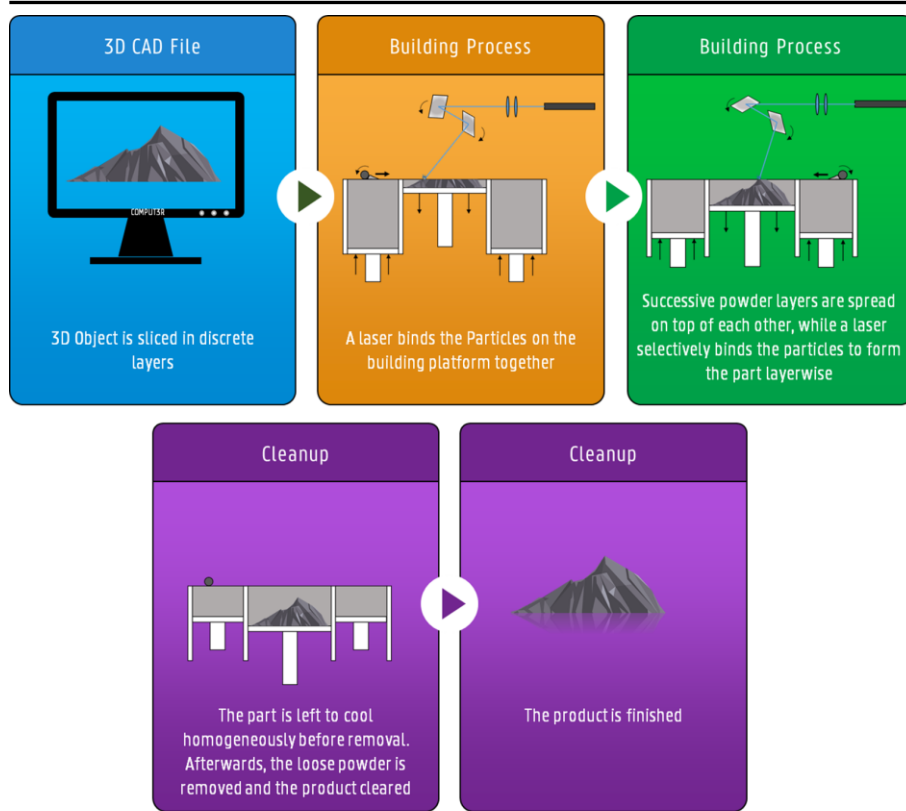
Figure 1-1: SLS process schematically represented

Though this technique found its origin in Rapid Prototyping (RP), one began to understand its true potential by trying to produce functional prototypes and actual end-use parts. Especially because of its potential to produce technical parts, AM has gained considerable interest over the last decades [4]–[7]. This shift from modelling products to actual end-use parts also caused a shift in interest towards the properties of the material itself. Emphasis on the mechanical, thermal and chemical properties is now more prominent depending on the application at hand. Since many materials show limited processability, the applications remain restricted to the properties of the available materials for SLS. Despite of the commercial interest in SLS, the variety of polymers available for processing remains rather scarce. According to Goodridge et al. [1] there are currently tens of thousands material grades available for injection molding whereas for laser sintering there are approximately 30. This amount is sure to have increased by now with the introduction of the polyarylketones (PEEK, PEKK, PAEK) [8], [9], polystyrene (PS) [10], polycarbonate (PC) and thermoplastic elastomers as TPU [11]. However, most of the published work still focusses on polyamides, either as a single material or as blend or composite [12]–[14]. Very little work has been published on the investigation of distinctly new polymers. To this day, polyamides make up the vast majority of available materials on the market [6]. With the growing number and variety of applications that require components that can

withstand high mechanical loads, have high density, be chemically resistant to solvents, caustic or acidic solutions or be thermally resistant for high temperature applications, the current materials available are no longer sufficient to meet the demands posed on the 3D models. There is a pressing need to expand the material range in order to account for these demands. This research project focusses on two main ways of doing so.

The first viable way of adding to the range of materials available for SLS is by making use of the large amount of material grades available for the traditional manufacturing processes like injection molding. Investigating which of these materials are also applicable for the sintering process should be the first step in this research for supplementary materials. Polymers should exhibit properties that distinguish them from the already available materials while still allowing sintering within the processing confines of the laser sintering apparatus. The polymer must particularly resist thermal degradation as the powders are often heated for prolonged times in order to decrease thermal shrinkage and shrinkage due to crystallization [7]. This will be discussed more at length in the section *Thermal properties* in Chapter 2.

In addition adding new virgin material one can also contribute to expanding the application window for SLS by improving the mechanical or physical properties of polymeric materials by reinforcing them with micron- to nanoscale sized inorganic filers. Polymer nanocomposites are particularly interesting for SLS as only a small volume of fillers is necessary in order to have a significant effect on the properties of the composite [1]. In this regard nanoclays have been widely incorporated in a large variety of materials like polypropylene and polyamide materials like PA6 [15]–[17]. In this research, the nanoclay Montmorillonite is incorporated in a polysulfone matrix in order to create a nanocomposite with unique properties. In order to achieve this goal, the nanoclays were organically modified to improve compatibility with the matrix. It is in this respect that this research area will be investigated in the last chapter of this dissertation.

Next, as most of these materials only exist in the form of pellets, these materials should be processed into powder form suitable for laser sintering. Strict requirements are imposed on the powder build materials. The powder should be able to spread evenly and without any inconsistencies over the build platform of the sinter station in order to print objects with upmost accuracy. For the same reason, the powder particles should be small enough to print high resolution parts and yet remain large enough to avoid severe electrostatic loading and volatilization upon sintering. To ease the powder flow the powders should be as spherical as possible, exhibiting smooth surfaces and avoid angular or sharp edges [18]. Characterization of the produced powders thus makes up an important part of this thesis in order to see if the produced samples fit with the ideal powder characteristics further explained in the *Material characterization methods* section in Chapter 2.

In addition to this, there does not exist a general production method to produce the polymer material in the right size and morphology that can be readily processed using SLS. Hence, as most commercially available materials are not produced directly in powder form, a suitable processing method has to be found in order to convert these materials to the powder form of correct size and morphology. Next to the precipitation process [1], [19], [20], cryogenic milling is often used in industry [18], [21], these techniques are often very energy consuming and furthermore do not attain the coveted morphology. In order to find the best powderization method as a better alternative to these processes, both physicochemical and mechanical powderization techniques should be explored.

Finally, the produced powders should not change dramatically in their intrinsic properties as these determine the application of the end product. The influence of the processing technique on the thermal properties of the material as well as phenomena like degradation due to processing should be kept to a minimum. In this regard the produced powders should undergo a series of characterization methods determining the change in intrinsic and extrinsic properties due to the processing methods in question.

In conclusion, it is the aim of this research to expand the application window by increasing the gamma of materials available for SLS using the vast amount of resources of injection molding grades. An answer is being sought to the research question as to whether there are better processing options than the current mechanical processing techniques. Through the use of case studies different powderization methods are investigated and optimized in their processing parameters. These new polymer candidates are investigated in collaboration with the University of Leuven and industrial partners. The powders are be thoroughly tested and characterized in order to see if they fit the SLS powder criteria at the University of Ghent while their processability in regards to sintering is investigated at the University of Leuven. The powders are inspected for any change in their extrinsic and intrinsic properties which may be imparted by the processing technique. The next chapter explains the used methodology applied in these case studies shortly while the following three chapters are devoted to each of the materials individually, investigating them methodically. The question of the possibility of upscaling the optimized methods is raised in a separate chapter. While in the final chapter an alternative answer to the research question of how to increase the application window for SLS is examined by the formation of polymer composites. The fillers are examined and improved for their compatibility with the polymer matrix after which the properties of the composites are characterized. After successful implementation these composites can then be processed in powder form using the optimized techniques.

REFERENCES

[1]   R. D. Goodridge, C. J. Tuck, and R. J. M. Hague, "Laser sintering of polyamides and other polymers," *Prog. Mater. Sci.*, vol. 57, no. 2, pp. 229–267, 2012.

[2]   N. Hopkinson, R. Hague, and P. Dickens, *Rapid manufacturing: an industrial revolution for the digital age*. John Wiley & Sons, 2006.

[3]   S. K. Tiwari, S. Pande, S. Agrawal, and S. M. Bobade, "Selection of selective laser sintering materials for different applications," *Rapid Prototyp. J.*, vol. 21, no. 6, pp. 630–648, 2015.

[4]   G. M. Vasquez, C. E. Majewski, B. Haworth, and N. Hopkinson, "A targeted material selection process for polymers in laser sintering," *Addit. Manuf.*, vol. 1, no. 4, pp. 127–138, 2014.

[5]   D. S. Thomas and S. W. Gilbert, "Costs and cost effectiveness of additive manufacturing," *NIST Spec. Publ.*, vol. 1176, p. 12, 2014.

[6]   Wohlers associates, "Wohlers Reports," 2009. [Online]. Available: http://www.wohlersassociates.com/books-reports.html. [Accessed: 25-Jun-2015].

[7]   D. Drummer, D. Rietzel, and F. Kühnlein, "Development of a characterization approach for the sintering behavior of new thermoplastics for selective laser sintering," *Phys. Procedia*, vol. 5, pp. 533–542, 2010.

[8]   M. Schmidt, D. Pohle, and T. Rechtenwald, "Selective laser sintering of PEEK," *CIRP Ann. Technol.*, vol. 56, no. 1, pp. 205–208, 2007.

[9]   D. Drummer, D. Rietzel, and F. Kühnlein, "Development of a characterization approach for the sintering behavior of new thermoplastics for selective laser sintering," *Phys. Procedia*, vol. 5, pp. 533–542, 2010.

[10]   D. Strobbe, S. Dadbakhsh, L. Verbelen, and P. Van Puyvelde, "Selective laser sintering of polystyrene : a single layer approach," no. 1, pp. 2–7.

[11]   S. Ziegelmeier, P. Christou, F. Wöllecke, C. Tuck, R. Goodridge, R. Hague, E. Krampe, and E. Wintermantel, "An experimental study into the effects of bulk and flow behaviour of laser sintering polymer powders on resulting part properties," *J. Mater. Process. Technol.*, vol. 215, pp. 239–250, Jan. 2015.

[12]   K. K. B. Hon and T. J. Gill, "Selective laser sintering of SiC/polyamide composites," *CIRP Ann. Technol.*, vol. 52, no. 1, pp. 173–176, 2003.

[13]   R. D. Goodridge, M. L. Shofner, R. J. M. Hague, M. McClelland, M. R. Schlea, R. B. Johnson, and C. J. Tuck, "Processing of a polyamide-12/carbon nanofibre composite by laser sintering," *Polym. Test.*, vol. 30, no. 1, pp. 94–100, 2011.

[14]   J. Bai, R. D. Goodridge, R. J. Hague, and M. Song, "Carbon nanotube reinforced Polyamide 12 nanocomposites for laser sintering," *Proceeding Solid Free. Fabr. Symp.*, vol. 7, pp. 98–107, 2012.

[15]   L. Delva, T. Van De Keere, R. Alves, K. Ragaert, A. Gaspar-Cunha, L. Cardon, and J. Degrieck, "Extrusion and characterization of nanoclay filled polypropylene," *Adv. Prod. Eng. Manag.*, vol. 8, no. 2, p. 88, 2013.

[16]   A. Olad, "Polymer/clay nanocomposites," in *Advances in diverse industrial applications of nanocomposites*, InTech, 2011.

[17]   S. S. Ray and M. Okamoto, "Polymer/layered silicate nanocomposites: a review from preparation to processing," *Prog. Polym. Sci.*, vol. 28, no. 11, pp. 1539–1641, 2003.

[18]   S. Ziegelmeier, F. Wöllecke, C. Tuck, R. Goodridge, and R. Hague,

"Characterizing the Bulk & Flow Behaviour of LS Polymer Powders."

[19]   M. Schmid, A. Amado, and K. Wegener, "Materials perspective of polymers for additive manufacturing with selective laser sintering," *J. Mater. Res.*, vol. 29, no. 17, pp. 1824–1832, 2014.

[20]   J. Kruth, G. Levy, R. Schindel, T. Craeghs, and E. Yasa, "Consolidation of Polymer Powders by Selective Laser Sintering," *Int. Conf. Polym. Mould. Innov.*, pp. 15–30, 2008.

[21]   R. D. Goodridge, C. J. Tuck, and R. J. M. Hague, "Progress in Materials Science Laser sintering of polyamides and other polymers," *Prog. Mater. Sci.*, vol. 57, no. 2, pp. 229–267, 2012.

Chapter 2

MATERIALS AND METHODS

The first section of this chapter is devoted to the first step in expanding the gamma of materials; the material selection. It summarizes all material properties which distinguish the candidate material from the commercially used polyamide polymers. In the next section the main processing techniques are discussed together with their communition method. Lastly, the particle size and morphology assessment methods are described.

2. 1. MATERIAL SELECTION

2. 1. 1. Introduction

Polymers are a class of long organic molecules or macromolecules that are build up out of many repeating subunits or monomers. Thanks to their broad range of properties they are used in an enormous range of products in everyday life. Generally, they can be subdivided into two main groups: thermosets and thermoplastics. The former is composed of long polymer chains that are chemically crosslinked, creating a large molecular network in which the polymer chains have restricted mobility, rendering it insoluble and unable to be molten. In the latter case however, the polymer chains interact physically through intermolecular forces making it possible to undergo phase transitions.

Depending on their molecular structure, thermoplastics can adopt either a randomly oriented conformation or a partly oriented conformation in which parts of their chains are aligned in a crystalline structure. These so-called semi-crystalline materials remain solid until enough thermal energy is absorbed to break down these crystalline formations after which the material experiences a sudden viscosity drop. On the other hand, the randomly oriented thermoplastics cannot melt and experience only a gradually decreasing viscosity with temperature increase. Thereby forming the amorphous class of polymers.

Another classification can be made based on the material properties; this leads to the distinction between commodity, engineering and high performance materials. This classification along with its characteristic properties for each class is depicted in Figure 2-1.
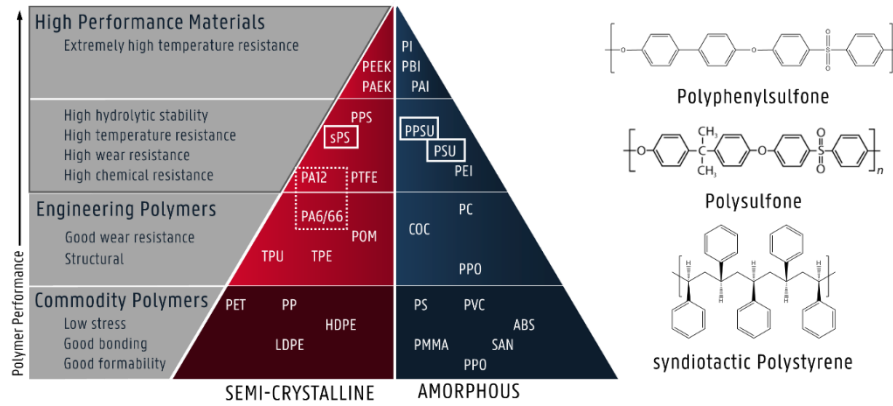
Figure 2-1: Classification pyramid situating the polymers of interest in comparison to Polyamide: Polysulfone (PSU), Polyphenylsulfone (PPSU) and syndiotactic Polystyrene (sPS) in full squares and Polyamide (PA) in a dotted square

Currently, the vast majority of the processable polymer materials are polyamides (PA6, PA11 and PA12 mainly), in pure, blended or reinforced form [1]–[6]. Next to this, in more recent years, other materials have been introduced for processing through laser sintering such as polyaryletherketones (PAEK, PEEK, PEKK) [7]–[9], polystyrene (PS) [10], polycarbonate (PC), polypropylene (PP) and thermoplastic elastomers as TPU [11]. From the variety in requirements of polymer consumer products it is clear that this material palette needs to be expanded in order to widen the application window for laser sintering. Figure 2-2 scales the distribution of the materials for the SLS market according to Wohlers report [12]; a clear overabundance of PA materials is visible here.
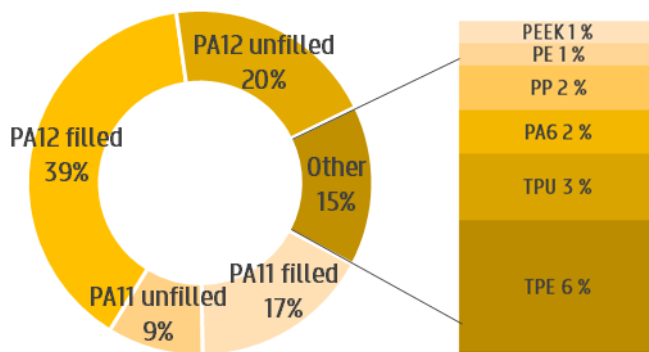

Figure 2-2: Material distribution for the SLS market [12]

Theoretically, any polymeric material from a classification pyramid like in Figure 2-1 can be processed via laser sintering. In reality, this is not the case. The production of a reliable 3D object with good mechanical properties is not straightforward. A large

variety of parameters have to be optimized and certain criteria have to be met. Gibson et al. [13] has grouped these SLS process parameters into four categories, depicted in Figure 2-3, which need to be optimized in order to obtain a high quality 3D model. The optimization of these four categories is part of the overall research project called PolyForce, of which this PhD is part of. The project is a collaboration of the University Leuven and University Ghent in collaboration with industrial partners such as Materialise and Solvay. Of these four categories described, this doctoral thesis will focus on the powder based properties.

In order to expand the material palette the candidate polymer material has to display considerably different properties than the currently available polymers for laser sintering in order to make new applications possible for the laser sintering technique. In this work the engineering polymers were chosen as, next to better mechanical properties, they provide higher thermal and better chemical resistance than the polyamide materials available [14]-[23]. Next, as most commercially available materials are not produced directly in powder form a suitable processing method has to be found in order to convert these materials to the powder form of correct size and
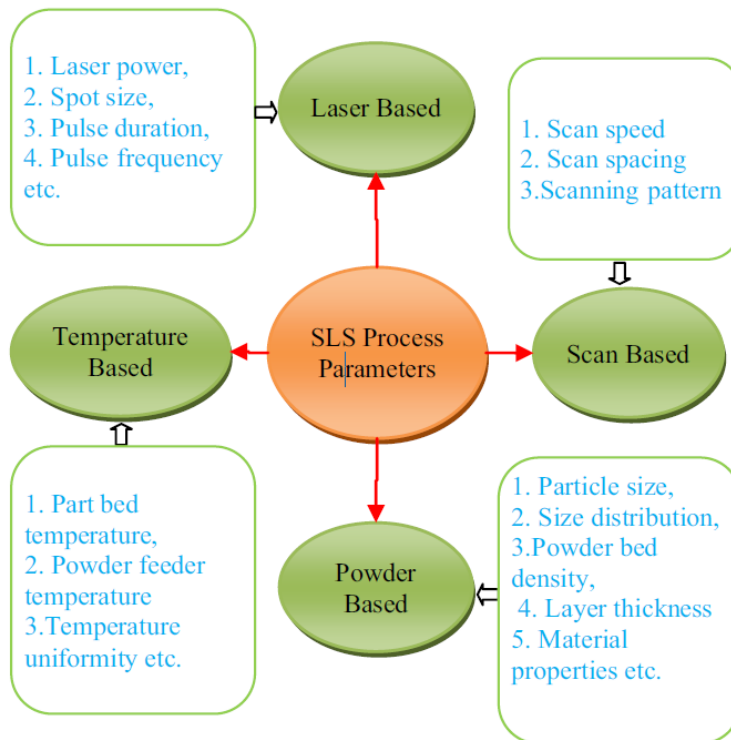

Figure 2-3: SLS processing parameters according to Gibson et al. [13], [21]

morphology. As the deposition of a smooth thin powder layer without inconsistencies is essential for sintering, powders have to be spherical without rough surfaces or sharp edges [22]. The particles must furthermore have a size distribution in the range of 45-90 µm [22]. Diameters smaller than this lower limit risk too much static build up while bigger diameters increase the porosity of the final part. Obtaining the correct size and morphology of the particles is essential as these properties have an impact on both the processing via laser sintering as on the properties of the final part (porosity, mechanical properties, etc…). Finally, the produced powders have to be investigated on any change in intrinsic properties that have occurred due to the processing method. Afterwards, in collaboration with the University of Leuven (KUL) and Materialise, these powders are tested in actual sinter experiments[1].

The processing and characterization of the materials chosen will be discussed in the following chapters.

2. 1. 2. Polyamides

As mentioned above a limited variety of applicable polymers exist for SLS processing. This is in stark contrast with the vast variety of basic polymers available for traditional processing techniques like injection molding or extrusion. Moreover, of the polymers available, the market is dominated by polyamides, in particular by PA12 and PA11 (Figure 2-2). Polyamides are semi-crystalline polymers classified as engineering to high performance engineering polymers (see Figure 2-1). They generally consist of aliphatic chains connected by an amide bond represented as RC(O)NHR (see Figure 2-4).
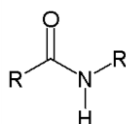
Figure 2-4: General structure of polyamide

In general semi-crystalline materials are preferred over amorphous polymers because of their sharp viscosity drop when heated above the melting temperature (further explained in section 2. 3. 4.). This causes a better coalescence upon sintering and higher density of the formed object. A common problem of semi-crystalline polymers is their tendency to shrink when they crystallize. In order to overcome this the polymer in question should exhibit a large processing window [22], i.e. the thermal region in-between the melting temperature and onset of crystallization temperature. Semi-crystalline polymers are heated and kept in this processing window during the build process in order to postpone crystallization and prevent shrinkage of the underlying

---

[1] University Leuven, Additive Manufacturing Research Group led by prof. dr. ir. Jean Pierre Kruth and prof. dr. ir. Brecht Van Hooreweder

layers. In doing so, warpage is prevented. Afterwards the part is cooled slowly in its whole to allow for homogeneous crystallization (further explained in section 2. 3. 4.).

Polyamides have a glass transition temperature of 40-45 °C [16] (Figure 2-6, T_g) and generally show a good processing window with a melting temperature of 170 -184 °C (T_m) and a crystallization temperature of 144-150 °C (T_c). They are usually found in their γ (hexagonal) phase but can also be formed in an α and β phase by adjusted temperature treatments [23]. Polyamides are also noted for their relatively high tensile strength (40 – 59 MPa, Figure 2-6, UTS), good creep resistance as well as excellent abrasion and heat resistance (57-95°C, Figure 2-6, HDT). They are excellent for use in aqueous systems and acceptable for use in organic solvents and weak alkalis yet are not to be used in any kind of acid system of aromatic or halogenated solvents. The materials properties are summarized in Figure 2-6 and Table 2-1 for a full listing of their properties.

The popularity of the polyamide materials in the field of additive manufacturing is in part due to their history in the field of rapid manufacturing as well as their ease in processing and relatively low cost [24]. The tensile strength and elastic modulus can nowadays be fine-tuned using the right processing conditions, in such a way that they become comparable to their injection molded counterparts [22]. Three commercial PA12 types in particular are part of the most commonly used materials: DuraForm® PA from 3D systems, PA 2200 from EOS and Orgasol® Invent smooth from Arkema. Schmid and Wegener [25], [26] investigated the differences in processing behavior that make these polymers so suited for processing in laser sintering by looking at their thermal behavior. They observed that there were man made differences in the thermal profile of the PA12-SLS polymers in order to make a better fit for the SLS conditions. More specifically, the melting point (T_m) and melting enthalpy (ΔH_m) was adjusted to higher values as well as the lowering of the crystallization point (T_c) in order to increase the 'processing window' of the polymers. In this regard they postulate that a heat treatment is performed during powder production of the polymers to increase the enthalpy of melting and change the crystal structure. They go on by suggesting that, in order to lower the onset of crystallization, a molecular structure change is implemented. Most likely this is done by co-condensing a small amount of a second monomer (e.g. monomer of PA6 in the case of PA12). Another phenomena that is inherent to polyamides is that they are prone to post condensation. Though this is usually unwanted in polymers as this implies a change in molecular weight and thus a change in the intrinsic properties of the material. In the case of SLS however this effect is double. In the case of post-condensation occurring in and through the interlayers this can lead to parts with increased interlayer bonding and hence better mechanical properties. The loose powder surrounding the part however also will degrade making it more difficult for reuse. It should be noted that this effect is just possible when the premature crystallization of the individual layers is suppressed and

the material is left for a significant amount of time at the elevated temperatures for processing conditions (dry atmosphere etc…). [26]

The polyamide materials find their applications in various fields either in their pure form or as blends or composites. Their lightweight, rigidity, durability and toughness making them ideal in direct manufacturing applications like Boeing's air ducting systems for F18 fighting jets [27]. Also in the medical world the PA materials find lots of applications: in hearing aid industry PA12 SLS powders have been used to make hearing aid shells custom made for the end-user's ears. For the same reason they are often used for the production of tailor-made prostheses and eye glass frames & lenses. On the other hand they are also used in kitchenware & housing applications as well as architectural & art uses for their chemical resistance, insulation properties, smooth look and good feature details [21]. Next to this the PA materials are still frequently used for design verification models and limited functional prototypes [27].

Though the polyamide family is still the main polymer when it comes to the selective laser sintering process, its possible applications remain limited to the mechanical, thermal and chemical properties of the polymer itself. There is a need for increasing the number and diversity of polymers that can be processed by SLS in order to widen this application window. Materials displaying good chemical resistance and high thermal properties would be a welcome addition to the material palette expanding possible applications for SLS considerably. In the next sections, three possible polymer candidates will be suggested for processing into feed material for SLS. The materials in question will be defended on the basis of their good thermal, chemical resistance and mechanical properties and compared in this regard to the polyamide family with its properties described above.

2. 1. 3. Polyphenylsulfone

Polyphenylsulfone is an amorphous thermoplastic which is classified as a high performance engineering polymer (see Figure 2-1). This amorphous polymer belongs to the class of sulfone polymers giving it its transparent amber shine. The chemical structure of the polyphenylsulfone is given next to the classification pyramid in Figure 2-1.

Along with a sulfone moiety ($-SO_2-$) and ether linkage (-O-) the para substituted aryl groups contribute to the repeat unit of the material. The high thermal stability is attributed by the conjugated system of the diphenyl sulfone group and the strong bond strength of the aromatic structures. This conjugated system also provides a good resistance against oxidation and imparts the high strength, high resistance and excellent flame retardancy into the material yet renders it rigid. Flexibility in the polymer backbone is provided by the inclusion of flexible 'hinge' bonds such as the ether linkage and the sulfonyl moiety.

Polysulfones are highly resistant to aqueous mineral acids, bases, oxidizing agents and fairly resistant to apolar solvents (see Table 2-1). The former makes the material ideal for medical applications as it is easily sterilized using steam or by autoclave [28]. The latter offers the material good chemical resistivity which is beneficial for transportation purposes of chemical solvents or heated fluids. PPSU is suitable as membrane for Solvent Resistent NanoFiltration (SRNF, [29]); a method to separate solvents and catalysts from processing streams. The mechanical and thermal properties of the PPSU polymers are compared to the properties of the DuraForm PA powder for SLS and the conventional PA12 polymer class in Figure 2-6. In line of its high Heat Deflection Temperature (207 °C, [30], [31], HDT) PPSU offers high mechanical stability at elevated temperatures giving good prospects for parts production in selective laser sintering. PPSU shows greater elongation at break than commercial PA materials (60-120 %, Figure 2-6, EAB) and a higher modulus, indicating a stronger, tougher material. Additionally, PPSU exhibits better impact resistance than the PA12 grades. Sulfone polymers are very resistant to crack formation or propagation resulting in a good impact resistant material.

PPSU, being amorphous, does not possess a melting or crystallization temperature. The stereochemistry of the sulfone group hinders the tendency for the polymers to melt crystallize. As a result the polymer does not present a sharp viscosity drop over temperature like polyamides and remains more viscous. Conversely, they do not exhibit a sudden change in specific volume which is often accompanied with this crystallization or melting step upon consolidation or heating respectively. This is beneficial in the production of multilayer parts as the layers are less prone to material shrinkage or warpage.

Amorphous polymers tend to be less attractive for SLS due to their higher viscosities causing poorer coalescence upon sintering leaving a higher porous structure as sintered part. However, due to the crystallinity of commonly used SLS polymers it is difficult to obtain transparent parts with SLS. Because of its transparency together with the better mechanical and thermal properties of the material described above, this material was selected as a viable candidate for selective laser sintering.

Two grades of PPSU; R5000 and R5600 were chosen to investigate for processing, their viscosities reflected in their MFI values: 14-20 g/10 min (R5000, 365 °C, 5 kg [30]), 34-40 g/10 min (R5600, 365 °C, 5 kg [31]).

2. 1. 4. Polysulfone

Polysulfone (PSU) is another amorphous thermoplastic which is classified as a high performance engineering polymer (see Figure 2-1). This amorphous polymer also belongs to the class of sulfone polymers giving it a comparable transparent amber shine as the polyphenylsulfones. The chemical structure of the polyphenylsulfone is given next to the classification pyramid in Figure 2-1.

Polysulphone differs from polyphenylsulfone in the sense that is has an extra functional group in between the benzene rings, the so-called isopropylidene moiety (see Figure 2-1). Along with a sulfone moiety ($-SO_2-$) and ether linkage (-O-) the para substituted aryl groups contribute to the repeat unit of the material.

Polysulphone, like polyphenylsulfone, exhibits high thermal stability which is attributed by the conjugated system of the diphenyl sulfone group and the strong bond strength of the aromatic structures. This conjugated system also provides a good resistance against oxidation and imparts the high strength, high resistance and excellent flame retardancy into the material yet makes the material rigid. Flexible 'hinge' bonds such as the ether linkage, the isopropylidene and the sulfonyl moiety are responsible for the flexibility in the polymer backbone. This added flexibility due to the extra presence of the isopropylidene group results in a lower T_g and a lower melt viscosity than that of the polyphenylsulfones, as depicted in Figure 2-5. The latter being an important factor for selective laser sintering as lower melt viscosities result in denser parts. Furthermore, the aliphatic group causes slightly less moisture absorption and is an electron-pusher, enriching the electron density of the neighboring benzene groups.
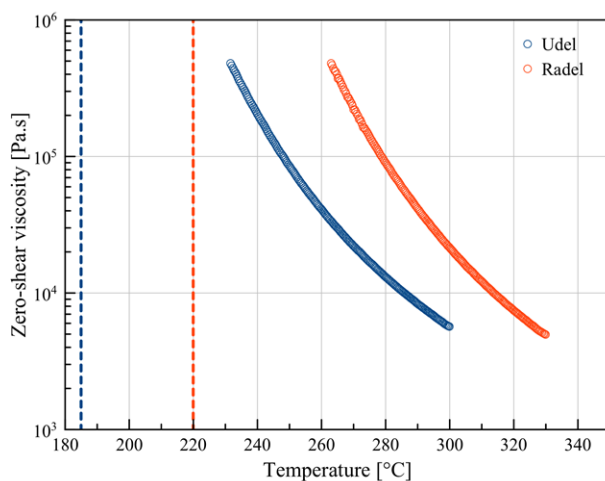

Figure 2-5: Zero-shear viscosity versus temperature rheology curves of the PSU Udel P 1700 and PPSU Radel R5000 grade. Dotted lines represent the glass transition temperature of the grades. Curve thanks to [32]

Polysulfone is not only characterized by a high tensile strength and modulus, it also is known to have a better elongation at break compared to PA (Figure 2-6). Compared to the conventional PA, PSU is more resistant against caustic and acidic solvents yet does not do well on aromatic and halogenated solvents. These are known to cause stress cracking [17]. The good chemical resistance makes PSU ideal in applications where heated solvents have to be transported and dimensional stability is required like water distribution manifolds. PSU has also been used as industrial battery container as the material is very resistant against bases and acids [17]. Additionally their ability to be sulfonated (to PSU-SO$_3$H) makes them ideal for ion exchange membranes applications and normal filtration applications in corrosive fluids or systems under pressure because of their good chemical resistance and mechanical properties [33]– [35].

As PSU is also an amorphous polymer it does not present a crystallization or melt temperature, the bulky backbone hinders the polymers to pack and form crystal structures. It is therefore less prone to material shrinking as conventional semi-crystalline polymers and exhibits high thermal stability. The latter is reflected in the high HDT (Figure 2-6) and the unusually high degradation temperature (475 °C). Additionally, PSU brings an added benefit of transparency due to its amorphous nature.

2. 1. 5. Syndiotactic Polystyrene

Syndiotactic polystyrene (sPS) is a semi-crystalline thermoplastic which is classified as a high performance engineering polymer (see Figure 2-1). The polymer has a high degree of stereoregularity in which the phenyl side groups have an alternating configuration along the hydrocarbon backbone. The chemical structure of sPS is given next to the classification pyramid in Figure 2-1.

sPS retains its glass transition temperature at 100°C for its amorphous phase but because of its interchain packing into a semi crystalline structure it also has a relatively high melting point (T_m at ~274 °C, Figure 2-6). Upon cooling the polymer has a high crystallization rate displaying a crystallization peak around 244 °C [20]. The bulky phenyl groups of sPS furthermore prevent close interchain packing of the molecules in the crystal making the density of the crystalline phase near equal to that of the amorphous phase at ambient temperature [19], [20]. This is beneficial upon consolidation of the sintered part.

Contrary to its fully amorphous atactic form, sPS is extremely difficult to solubilize at room temperature. The amorphous regions of sPS can be swollen with good solvents like aromatics or chlorinated aromatics and will dissolve at temperatures above glass transition temperature [20]. This chemical resistance makes the polymer ideal for applications involving harsh environments like acids, bases, oils, water and steam. Table 2-1 displays a relative comparison between the chemical resistivity of

PA and sPS. Both sPS and PA are susceptible to aromatic and chlorinated aromatic compounds. Nonetheless, sPS displays a better resistance against acids, bases and heated aqueous solvents.

The mechanical and thermal properties of PA (both injection grade and DuraForm; a PA sintering powder) and sPS are also compared in Figure 2-6. sPS offers in general higher thermal properties with a significantly higher melting temperature at (274 °C) and good Heat Deflection Temperature (95 °C, HDT). Neat sPS is a fairly stiffer material than PA, this is reflected in the modulus of sPS that is double of that of the PA (3900 MPa, Modulus). The polymer is strong but brittle expressing a low elongation at break value. (1,3 %, EAB). The stiffness of the material is primarily related to the interactions involving bond bending and stretching [20]. Neat sPS is therefor often reinforced using glass fibers up to 30 and 40 wt.% creating a unique material with improved properties like impact resistance. Malanga et al. [20] have made an extensive review on the subject gathering data about the intrinsic properties of neat as well as several forms of reinforced sPS. For the purpose of this doctoral research, neat sPS will be examined on processability into microspheres and the impact the processing method may infer upon the material.

Next to this, syndiotactic polystyrene also has good electrical properties as insulating material because of its low dielectric constant and low dissipation factor [20]. It is a highly hydrophobic material leading to low moisture absorption which is beneficial upon processing minimizing effects like fuming or porosities due to water vapor. Amorphous atactic polystyrene is already available in powder form for SLS (CastForm/3D Systems, PrimeCast/EOS DSM) yet to our knowledge no attempts on sPS processing through SLS have been made. Because of this and the aforementioned property differences with PA, the polymer proves itself to be a viable candidate as testing material for SLS.
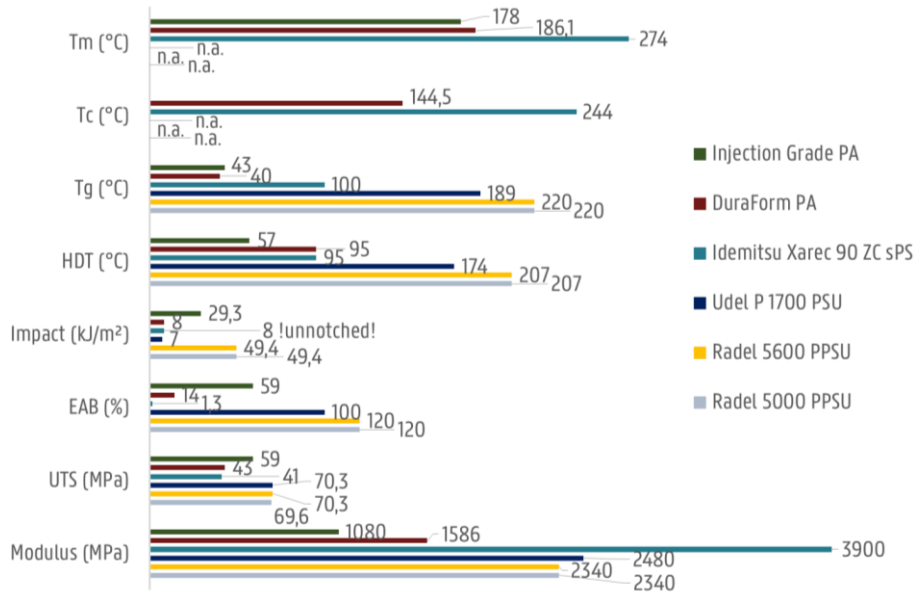
Figure 2-6: Comparison of the three polymer candidates' (Radel R5000 & R5600 PPSU, Udel P1700 PSU and XAREC 90ZC sPS) properties to injection molding grade PA12 and commercial SLS material DuraForm PA. The DuraForm PA data was taken from the material data sheet (XY direction). Left: Mechanical and thermal properties displaying the melting temperature (T_m), crystallization temperature (T_c), glass transition temperature (T_g), heat deflection temperature at 1,8 MPa (HDT), Izod notched Impact at 23 °C, elongation at break (EAB) and modulus. Data from [14]–[20], [30], [31], [36]

Table 2-1: Right: the chemical resistivity of the three polymer candidates (Radel R5000 & R5600 PPSU, Udel P1700 PSU and XAREC 90ZC sPS) compared to the polyamide polymer class: HAS: Heated Aqueous Solvents, AS: aromatic solvents, XHC: halogenated hydrocarbons. Data from [14]–[20], [30], [31], [36]

	PA	PSU	PPSU	sPS
Acids	Poor	Good	Good	Good
Bases	Fair	Good	Good	Good
Organic Solvents	Good	Good	Good	Good
Aromatic solvents	Poor	Poor	Poor	Poor
Halogenated hydrocarbons	Poor	Poor	Poor	Poor
oxygenated solvents	Good	Poor	Poor	Good
heated aqueous solvents	Fair	Good	Good	Good

2. 2. MATERIAL PROCESSING METHODS

As stated before, one of the stumbling blocks in the progression of laser sintering is the limited range of materials available. There is a pressing need for processing methods to convert the commercially available pellets into spherical powders that can be used as build material for laser sintering.

In industry, conventional ball milling -either cryogenically or at ambient temperature- is used. This technique often leads to particles with a too wide size distribution and undesired morphology [37], [38] (Figure 2-7). Furthermore, these methods often take a lot of time and tend to leave a large amount of waste material that was not fully fractionated. Despite this fact, this technique is still the most used in the industry albeit mostly at cryogenic temperatures to speed up the pulverization process. Several studies have already been performed on the influence of ball milling on the mechanical properties of the polymer in question [39], the intrinsic properties such as molecular weight [40], the thermal properties of the polymer [41], and its structural changes regarding amorphization [42] by mechanical treatment.

Rotor milling is a relatively new mechanical processing technique that can prove to be a valuable alternative to the conventional techniques. This semi-continuous technique allows shorter residence time of the material, which shortens processing time and minimizes the possibility of material degradation. Furthermore, materials can be milled to a predefined range of particle sizes by using inset sieves. To that end, rotor milling is studied as one of the polymer powderization methods and it is compared to ball milling as benchmarking technique.

Other processing methods concern more physicochemical methods like thermal-induced phase separation (TIPS) [43]–[45], diffusion-induced phase separation (DIPS) [44] and evaporation phase separation (EPS) [46]. These methods are said to achieve more spherical particles yet require vast amounts of non-solvents to induce the phase separation. In addition to this, particle size is often too small and agglomerations of the particles above a certain weight percentage can form a hurdle limiting the yield of the process severely [47]. In this regard, the author of this work proposes Spray drying (SD) for the physicochemical production of microspheres as build material for SLS. The technique virtually eliminates this agglomeration phenomenon by individually drying the atomized droplets. Because of this, one can increase the maximum weight percentage of the polymer solution to be processed in comparison to other dissolution methods, thus increasing the yield. Using an inert loop, the evaporating solvents can be readily recovered, making this an interesting technique as more exotic solvents are often used to dissolve the desired polymers.

Figure 2-7 displays the different morphologies one can obtain using the different powder generation processes. Particles with smooth surface and spherical or toroidal morphology are usually obtained for spray drying processes of polymers. Using the

rotor milling sequence spherical shapes can also be obtained with slightly rougher surface. Particles obtained via ambient or cryogenic milling tend to be angular and inadequate in most cases which is unfavourable for SLS processing. While cryogenic and ambient milling are discussed in this dissertation, the main focus of this research will be on the mechanical rotor milling and physicochemical spray drying technique.
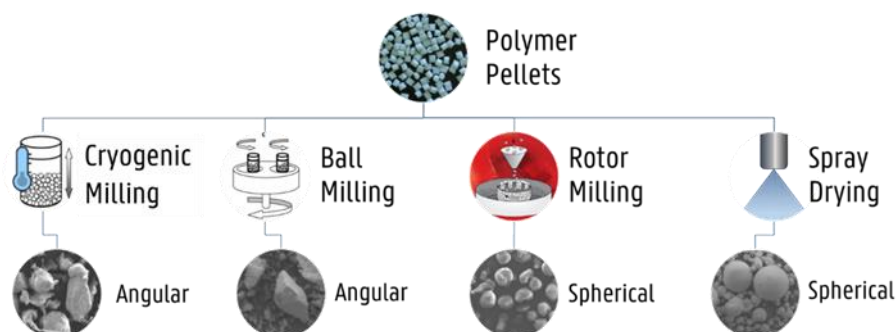

Figure 2-7: Different morphologies of powders due to the different processing techniques the material has undergone

2. 2. 1. Rotor Milling

Rotor milling is used as the principle mechanical processing technique to transform the polymer pellets into spherical powders. The rotor milling setup is depicted in the left panel of Figure 2-8, the right panel in this figure depicts a scheme of the inside of the rotor miller and is used to explain the process.

In this process, pellets are fed into the rotor mill through a hopper (1) and due to the centrifugal force, impact against the high speed rotating rotor blade (3). Particles deform under impact at the contact area, experiencing a high strain rate which ultimately leads to breakage. The kinetic energy of the rotor blade is transferred partly onto the pellets upon impact. As elastic stress reaches a critical level, locally incipient cracks are formed which aid in the fragmentation process. After the initial fragmentation the particles are driven outwards under influence of the centrifugal force and experience shear forces between the rotor and inset sieve ring used (4), causing further fragmentation and the rounding of the particles by the rotating motion of the blade. Once fragmented to the required size the particles can pass the mesh of the inset sieves and are collected in the collection chamber (2) or filtered off using a cyclone system.

The total residence time of the powders is kept short in order to ensure no degradation occurs and avoid the material to become plasticized to the rotor blade and mesh. The use of the cyclone system with aspirator also ensures a constant flow of air at ambient temperature over the sieve ring, cooling the latter and reducing the risk of heat buildup.
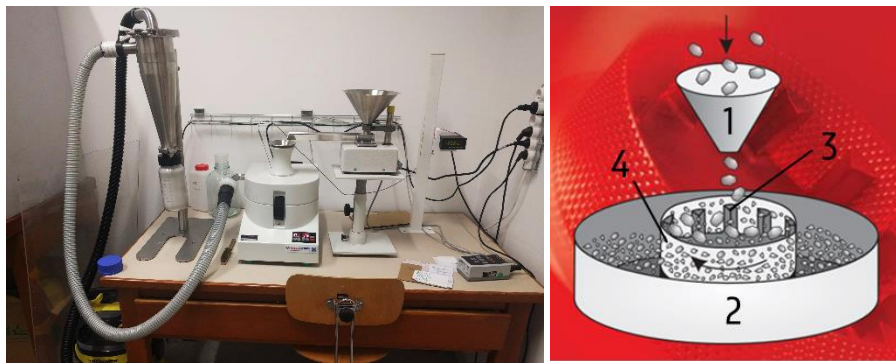
Figure 2-8: The rotor milling setup from left to right: cyclone system, the Pulverisette 14 and the automatic feeder. The right panel represents a schematic representation of the rotor milling process with (1) the hopper, (2) the collection ring, (3) the 12-fingered rotor blade and (4) the inset sieve [48]
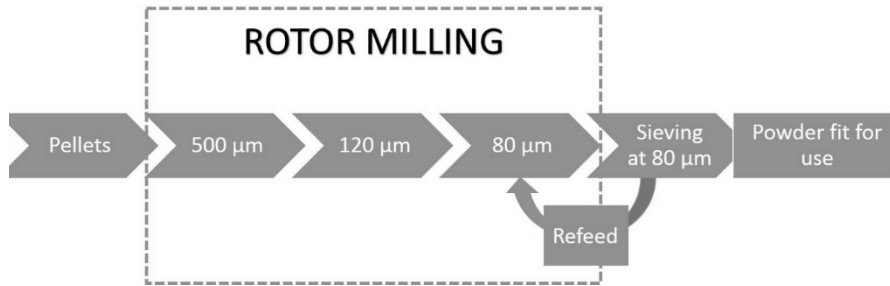
Figure 2-9: Schematics of the rotor milling process with the three step refinement. After milling, the powders are sieved and the redundant powder can be re-fed to the rotor miller for further refinement.
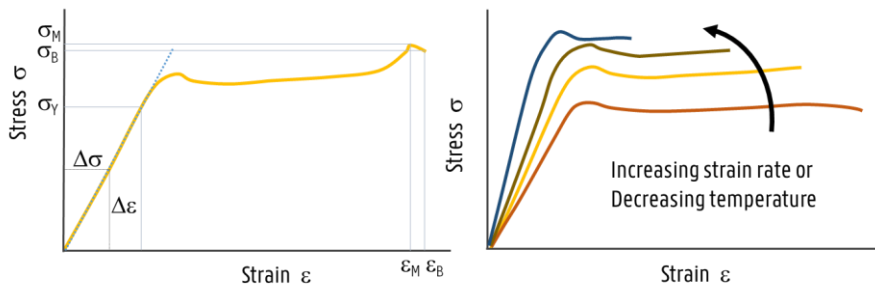
Figure 2-10: Left: Stress-strain curves for polymeric materials with σ_B denoting the stress at break, σ_M the maximum stress, σ_Y stress at yield, ε_B denoting the elongation at break, ε_M elongation at the maximum stress and ε_Y elongation at yield. Right: Effect of decreasing temperature or increasing strain rate on the modulus of polymeric materials

The polymer pellets were processed by a three-step communition process on a Fritsch Pulverisette 14 rotor mill, followed by a sieving step in order to obtain the right particles in size and morphology. In the first step the pellets were pulverized to a coarse powder using an inset sieve with mesh size 500 μm. Then, a second and third refinement step further pulverize the powder to a fine powder using an inset sieve of 120 and 80 μm subsequently. A 12-ribbed rotor blade was used to this end which rotates at 15000 RPM to achieve pulverization. This was augmented to 18000 RPM for the final milling step. The resulting powder was sieved and isolated using a cyclone system. During the milling process the rotor mill was cooled by air at room temperature using an aspirator connected to the cyclone system. The process is schematically depicted in Figure 2-9 and allows a refeeding of the particles who are left behind on the sieves. For analysis purposes only the powders which underwent 1 cycle without refeed were used.

In order for fragmentation to occur the required energy input in the form of mechanical work must be high enough for breakage to occur. The energy required for fragmentation can be correlated to the energy of break in the stress strain curve for very high strain rates. For a normal polymeric material the stress strain curve is typically displayed as in Figure 2-10, left. With the energy of break given as the surface area under the stress strain curve:

$$E_B = \int_0^{\varepsilon_B} \sigma(\varepsilon) d\varepsilon$$

Equation 2-1

As strain rate increases, the polymer material behaves more like a brittle material as the polymer chains do not have sufficient time to adapt to the deformation to which they are subjected (Figure 2-10, right [49]). The modulus for brittle materials is fairly large with almost no deformation occurring prior to breakage. The material behaves as a strong material but the breaking work per unit volume remains small. Hence, only a low energy of break needs to be overcome by mechanical work of the Pulverisette in order for communition to occur. In the case of tougher materials deformations can occur at high stresses. This means that the energy at break will as a result be higher and communition is more arduous. In order to decrease the energy of break in this case one can decrease the temperature of the material, decreasing the polymer chain mobility and by extend making the material more brittle (Figure 2-10, right). For this reason, during milling of the selected materials, a cyclone system is coupled to the P14 which allows a flow of air at ambient temperature at all times over the rotor blade and sieving unit allowing it to cool down.

When the energy input provided by the high speed rotating rotor blade is not sufficient enough to exceed the energy of break, elastic (reversible) deformation followed by plastic (irreversible) deformation will occur. If the particle in question escapes the mechanical deformation in time by passing through the inset sieve elastic unloading will occur with permanent deformations in the particle at hand. For bigger particles

dissipation of energy can occur more easily leading to more deformation which does not always result in fragmentation. Smaller particles exhibit a smaller surface area, less dissipation of energy can occur and fragmentation is supposed to be more dominant in this case.

Fragmentation of the particles is further promoted by incipient cracks in the material. Cracks or cavities may develop caused by frequent mechanical deformations. Heterogeneities in the material give regions of stress concentration which are potential sites for the formation of cavities that can be transformed under certain conditions into cracks [50]. These are said to aid the fragmentation process by propagating if enough energy is supplied. Fragmentation at incipient cracks demands less energy as the stress concentration at the crack tips is higher.

The milling process itself is known to generate some heat by the stretching and deformation of the polymer itself because of its entropic penalty [51]. It is important that this heat is dissipated as quickly and efficiently as possible in order to hamper the material from becoming too soft and deform even more, generating even more heat. By ensuring the rotor blade has sufficient kinetic energy in order to easily overcome the energy at break and efficiently cooling both sieve and material through creation of an airflow in the miller one reduces the retention time of the material and can avoid detrimental heat build-up which can result in plasticization of the material.

2. 2. 2. Ball Milling

Ball milling was performed on a Fritsch Pulverisette 500 planetary ball mill with three ceramic cups containing ceramic balls of 25 mm. The three cups are arranged on a rotating support disk fitted with a mechanism that allows the ceramic containers to rotate around their own axes as well. Figure 2-11 depicts the ball mill setup with a schematic representation of the working principle of the planetary ball mill by Hiroshi Mio et al [52]. The ceramic cups are loaded with a measured amount of polymer pellets. The ball mill works at a set value of 1400 RPM and samples are taken at constant intervals (15 minutes) to be examined on size and morphology. The minimum communition time to achieve particles with desired size is estimated in this manner. Heat build-up during communition is minimized by letting the powders condition to room temperature after each sampling run.
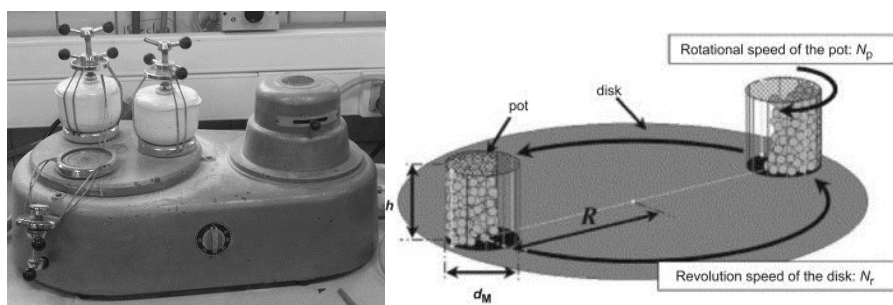
Figure 2-11: The ball mill setup with a schematic diagram of the working principle of the planetary ball mill [52]
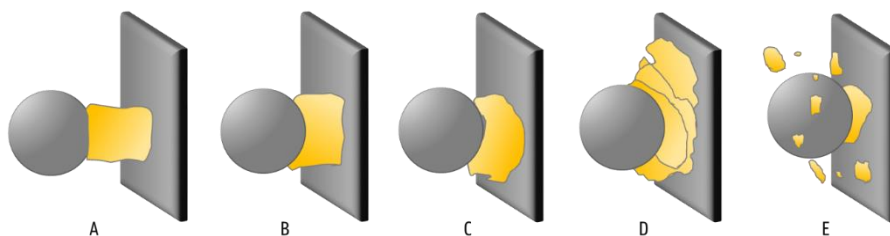

Figure 2-12: Schematics of fragmentation process by ball milling: (A) impact of charge material on grinding material, (B) elastic deformation (reversible), (C) plastic deformation (irreversible), caused by high shearing stress making the material flatten and elongate, (D) cold welding of flattened particles and (E) Fragmentation of the flattened particles by fatigue failure [53]

Both the centrifugal force produced by the containers rotation as the force produced by the revolution of the cups on the support disk act on the vial contents. The overlapping of the centrifugal forces causes the sample material and ceramic balls to bounce off the inner walls and collide with each other under high impact. In said way the kinetic energy is transferred from the charge medium by impact and friction. Generally, the bigger the space available in the crucible, the longer the travelling distance of the charge material becomes to travel to the other side of the container and thus the higher kinetic energy the charge material can achieve.

The grinding material undergoes a large assortment of stresses: compression, attrition, shear and impact. Giuliana Gorrassi and Andrea Sorrentino [53] described in their critical review the fragmentation process and the mechano-chemistry of polymers being processed by mechanical milling. They explained that particles, when subjected to mechanical stress, firstly become flattened or elongated going through elastic and plastic deformation. This process goes together with a progressive reduction in thickness. As the particles are continuously exposed to these deformations they are subjected to fatigue failure and fragmentation. The continuous elongation and fragmentation produces heat and is slowed down by a cold welding phenomenon between the layers. Figure 2-12 summarizes the fragmentation phenomenon inside the

ball mill. Ductile polymers are expected to display more elongated structures while more rigid, brittle polymers are expected to simply fragment and reduce in size. Furthermore, in industry, cryogenic temperatures are often uphold in the process in order to make the material more brittle and fragment more easily due to its reduction in energy of break (see Figure 2-10, right) [54]. Bai et al. [37] state that mechanical milling can sever polymer molecules, creating free radicals which may react to other molecules producing crosslinks or grafts. This degradation of the polymer is promoted by the local temperatures and the high energy collisions between the milling balls. Milling at lower temperatures is expected to reduce degradation by the elimination of these local temperatures otherwise encountered at ambient temperature milling [55]. Though the activation energy required to break the molecular bonds of the polymer is largely supplied by the external stress, the thermal vibrations of the atoms that make up the polymer chains augment this stress. Therefore lower temperatures should decrease the degradation phenomena. Particles are said to break into angular structures displaying sharp edges and rough surface which is not ideal for laser sintering [11], [22], [37], stressing the importance of finding a more suitable processing technique.

Giuliana Gorrassi and Andrea Sorrentino [53] further concluded that a number of irreversible processes go together with the milling process and can be identified as activation, cracking and condensation. The determining step being cracking, representing the first step for mechanical degradation. They state that, irrespective of the stage in the milling process, free radicals are formed which can initiate chemical reactions like grafting and crosslinking.

This technique has been incorporated as a benchmarking technique in order to compare both ambimilling and cryogenic milling to rotor milling and spray drying as a processing technique.

2. 2. 3. Spray Drying

Spray drying is used as physicochemical processing technique to transform the polymer pellets into spherical powders. Figure 2-13 depicts the laboratory set up next to a technical drawing of its design. The scheme is used to explain the process as follows: in this processing technique a polymer is first dissolved into a suitable solvent. The polymer solution (B) is then pumped at a certain feed rate to an atomizer (3) which sprays the solution through the use of an atomizing gas (A) into a heated chamber (4). The droplets move through the heated chamber upon which the jetted droplets get oversaturated due to evaporation of the solvent and eventually precipitation of the polymer in the droplets takes place leaving polymer powders. These are then taken away by the heating gas to a cyclone system (6) where the particles are separated into a collection funnel (8) and the gas is taken away (7) to a condenser or outlet system.
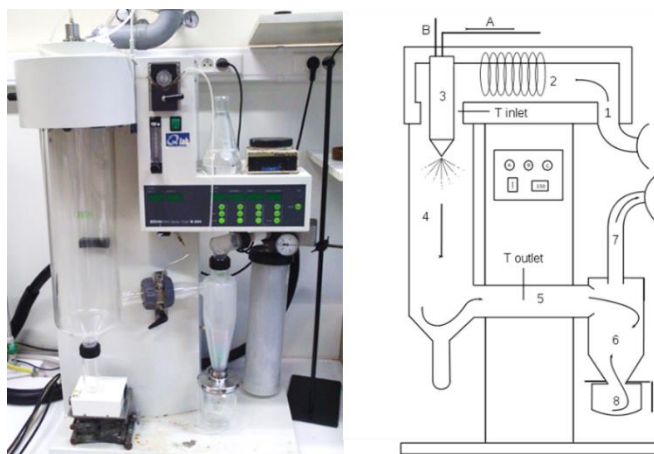
Figure 2-13: The laboratory spray dryer Buchi Mini B 290 and a technical drawing of its design. (A) polymer solution; (B) atomizing gas (pressurized air or N2); (1) inlet of gas (2) heating element; (3) atomizing unit; (4) drying chamber; (5) connection to cyclone system with thermocouple; (6) cyclone system; (7) gas outlet and (8) collection vessel [56]

A good understanding of polymer dissolution plays a vital role for the selection of a suitable solvent that can dissolve the polymer and can easily be atomized. To this end, a parameter based approach was used in the selection process of a good solvent which will be elaborated in the next section. Afterwards the polymer solution is characterized using viscosimetry and atomized.

2. 2. 3. a. Hansen solubility parameters

Like for all of the mixing processes, for mutual solubility of the polymer material and solvent, the Gibbs free energy of mixing, ΔG_{mix}, should be negative. The Gibbs free energy of mixing can be defined as

$$\Delta G_{mix} = \Delta H_{mix} - T\Delta S_{mix}$$ *Equation 2-2*

With ΔH_{mix} the enthalpy change on mixing, T the absolute temperature and ΔS_{mix} the entropy change upon mixing. As the dissolution of high molecular weight polymers is associated with a small positive entropy change, the sign of the free energy change will be dependent on the enthalpy change.

Hildebrand and Schott [57], with contributions of Scatchard [58], introduced the concept of cohesive energy density and stipulated that the enthalpy of mixing can be written as:

$$\Delta H_{mix} = V_{tot}\left[(\Delta E_1^V/V_1)^{1/2} - (\Delta E_2^V/V_2)^{1/2}\right]^2 \Phi_1\Phi_2$$ *Equation 2-3*

With V_{tot} the total volume of the mixture, ΔE_i^V the energy of vaporization of the species i, V_i the molar volume of i, Φ_i the volume fraction of i of the mixture and the subscripts 1 and 2 respectively denoting the polymer material and the solvent.

The fraction $\Delta E_1^V / V_1$ can also be termed as the cohesive energy density (CED); the energy required to break all intermolecular interactions per unit volume of a material.

The CED equation is written as:

$$CED = E/V = (\Delta H_{vap} - RT)/V \qquad\qquad \textit{Equation 2-4}$$

Here, ΔH_{vap} is the enthalpy of vaporization.
The Hildebrand solubility parameter is defined as the square root of the CED and is depicted as the symbol δ

$$\delta = CED^{1/2} = (E/V)^{1/2} \qquad\qquad \textit{Equation 2-5}$$

Using Equation 2-4 and Equation 2-5, Equation 2-3 can be rewritten as:

$$\Delta H_{mix}/V = (\delta_1 - \delta_2)^2 \, \Phi_1 \Phi_2 \qquad\qquad \textit{Equation 2-6}$$

Looking at the Gibbs free energy equation (Equation 2-2) dissolution ($\Delta G_{mix} \leq 0$) can take place when the difference in solubility parameters ($\delta_1 - \delta_2$) is small.
Though the use of the cohesive energy density to predict the miscibility of a material in a solvent is valid, the predictions made with the Hildebrand solubility parameter do not account for specific interactions like hydrogen bonding, morphology or crosslinking [59]. The total energy of vaporization consists of several individual parts arising from atomic dispersion forces, molecular dipole-dipole forces and molecular hydrogen bonding [60]. Hansen accounted for these interactions by splitting the cohesive energy into three segments: the non-polar dispersive interactions E_D. These affect all molecules and are made up by the electromagnetic field created by the movement of electrons orbiting around a nucleus. This force attracts all atoms to one another. The polar cohesive forces are represented by E_P, this interaction is produced by the permanent dipole-dipole interactions between molecules. The third interaction represents hydrogen bonding; E_H. These interactions are weaker than covalent bonds but much stronger than the dipole-dipole interactions.

$$E = E_D + E_P + E_H \qquad\qquad \textit{Equation 2-7}$$

Hansen thus rewrote the Hildebrand solubility parameter as

$$\delta_{tot}^2 = \delta_D^2 + \delta_P^2 + \delta_H^2 \qquad\qquad \textit{Equation 2-8}$$

When selecting a good solvent to dissolve the polymer material, the solvent must have similar solubility parameters in order to minimize the difference in solubility parameters and by extension minimize the enthalpic term of the Gibbs free energy equation for miscibility.

2. 2. 3. b. Ubbelohde Viscosimetry

Next, as there exists a viscosity limit on the atomization performance of the Buchi B 290 mini spray dryer of 300 MPa.s [61], a viscometric study should be performed on the created solutions in function of their weight percentage using Ubbelohde viscosimetry (Schott-Geräte Gmbh). Tests are performed at 25 °C using the chosen solvent to dissolve the polymer in practice. All measurements were performed in accordance with ISO 3105. The kinematic viscosities ν (unit mm/s) are obtained by measuring the effluent time t (unit sec) through a capillary with defined capillary constant K and correcting for non-laminar flow behavior with a predefined correction value y. The calculation is described in Equation 2-9:

$$\nu = K(t - y)$$

<div align="right">*Equation 2-9*</div>

Subsequently these values were converted to their dynamic viscosity η_{dyn} (unit MPa.s) through multiplication with the solution density ρ (Equation 2-10). Solution density was determined gravimetrically measuring fixed volumes of the respective solution.

$$\eta_{dyn} = \rho\nu$$

<div align="right">*Equation 2-10*</div>

2. 2. 3. c. Spray drying process

Spray drying was performed on a Buchi B290 equipped with a two-fluid nebulizer connected to pressurized air. The nozzle orifice size was 2,0 mm and was water cooled. The aspirator ran at a maximum air velocity of 40 m³/h. The heater inlet temperature, temperature of solution, solution feeding rate, feed concentration and gas flow rate are the main processing parameters of the spray drying process. Using the lab scale spray dryer, a maximum particle size of 25 µm can be obtained [62]. It is the goal of this research to optimize the spray drying parameters for the candidate polymers after which the process can be scaled up to a pilot system achieving larger particles. As optimization directly on a pilot system is not economically feasible, this approach was deemed best. The optimization of the size and morphology of the particles encompasses the variation of the above-mentioned parameters in a systematic approach which is specific for each polymer solution individually. Details of the optimization process of the spray drying parameters will hence be reported in the chapters concerning each polymer material. The resulting powder was sieved off using a cyclone system and investigated by the characterization methods described below.

2. 3. MATERIAL CHARACTERIZATION METHODS

Strict requirements are imposed on powder build material for selective laser sintering. In order for the novel polymer powders to have an even and uniform spread over the building platform the created powders must have a good flowability. Furthermore, a thin homogeneous layer of powder with high packing density needs to be deposited in order to sinter parts without too much porosity. Ideally, powders should have a high sphericity with smooth surface and rounded edges in order to facilitate flow. Additionally, to optimize packing density particles should have a particle size distribution in the range of 45-90 µm [22], [63].

Flow behavior of particles is affected by a variety of parameters such as moisture, cohesive forces between particles, temperature and the aforementioned particle shape and size. Powder flow can be measured using Hausner Ratio measurements which expresses the ratio of the bulk over tapped density of the powders as an indication for powder flow. Though these measurements give a good indication of the flow behavior of the particles it is advised to take the dynamic flow properties of the powders into account to get a more realistic description of the behavior. Zieglmeier et al. [63] combined the HR with FT-4 powder rheometer measurements to take the cohesive forces between the powder particles into account and used a revolution powder analyzer for flowability testing. Schmid et al. [64] summarized the main techniques used for measuring the powder flow explaining the Hausner ratio at length. In order to minimize other factors like the moisture uptake of the powders, powders are always advised to dry a significant amount of time before processing.

In this work, powder flow is assessed by morphology measurements, particle size distribution as well as the Hausner ratio of the obtained powders. These will be further elucidated in the next sections.

2. 3. 1. Particle size assessment

The obtained powder samples were processed using SEM microscopy on a JEOL JSM-7600F at low voltage (2kV) and working distance of 8mm after being sputtered with gold using a BAL-TEC SCD 005 Sputter Coater at 25mA. The samples were subsequently analyzed for particle distribution and morphology using the imaging software Image J.

Particle size of powder particles can be described using different values: for perfectly spherical particles a single value is used (i.e. the diameter). Non-spherical particles can be described using multiple width and length measures (Figure 2-14, [65]). Each measurement technique measures size based on its own physical principle. Using image analysis particles can be described by their maximal or minimal diameters, perimeter, projected area or equivalent spherical diameter. The particles in this work were characterized using their maximum diameter (case C in Figure 2-14).
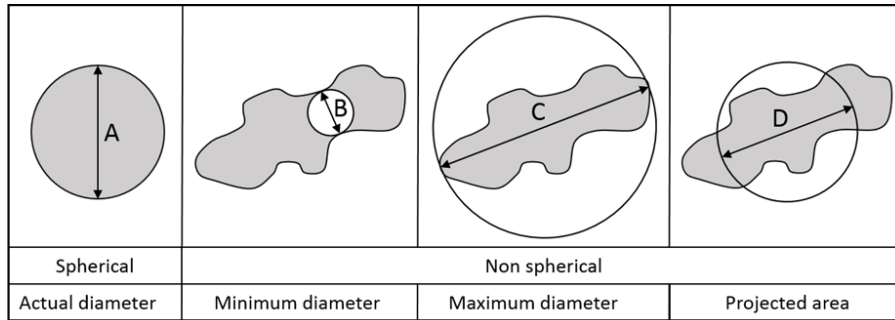
Figure 2-14: Shape factor of particles. Non-spherical particles can be measured using minimal and maximal diameters, projected area or equivalent diameter. In this work the maximum diameter was used consistently.

2. 3. 2. Morphology assessment

The morphology of the particles was assessed based on their shape (sphericity) as well as their roundness. Both have been found to impact flow characteristics of powder bulk material substantially [66]. Ziegelmeier et al. [11] did an extensive experimental and literature study into the bulk and flow behavior of polymer powders for laser sintering concluding that angular and irregularly shaped particles have a natural tendency to interlock with each other, increase adhesive bonds and resist free flowing. For this reason only well rounded and particles with high sphericity were considered suitable for sintering. Because of the variety of particle shapes, detailed classification is very difficult. Sphericity is often a quantitative parameter, which can be expressed as the degree of similarity of a given particle to a sphere. Roundness is both a measure of smoothness of the surface as well as the rounding of the edges. Visual patterns are most commonly used to determine the degree of roundness and sphericity [67]. The Powers' pattern (Table 2-2, [68]) is one of the most popular patterns which connect roundness and sphericity. The chart offers a quick and easy way to process and classify the samples and gives an idea of the suitability of the samples for laser sintering.

Table 2-2: The Powers particle sphericity and roundness scale [68]. The classification of each particle will be used as a measure in which particles are suitable for sintering or not. Particles inside the black line are considered well rounded and spherical enough for sintering purposes

2. 3. 3. Hausner Ratio assessment

The behavior of the produced powders is largely dependent on the morphology of the powders [69], [70] and can affect processability and the quality of produced parts by SLS significantly. Almost free flowing behavior is expected of the SLS powders in order to achieve a good even spread of a thin layer of powder over the building platform. To investigate the flow properties of the created powder, the bulk and tapped density were determined for each fraction and are represented together with their respective Hausner Ratio. The Hausner ratio (HR) describes the ratio of the tapped and bulk density of a powder and classifies the powders flowability [63], [64], [71]. It can be subdivided into three main regions:

- HR < 1,25: powder is easily fluidized
- 1,25 < HR < 1,4: decreasing fluidization behavior
- HR > 1,4: fluidization problems

The HR test was performed by gravimetrically measuring the densities of the powder at ambient conditions using a graduated cylinder and powder funnel. After measuring the bulk density, the powder was subjected to a sequence of taps by placing the cylinder on the baseplate of a Retsch Vibratory Sieve Shaker AS 200 digit (Benelux Scientific BVBA, Eke, Belgium) for 60 s at 60% of its maximal amplitude.

Afterwards, the volume was measured again to determine the tapped density. To increase its statistical outcome, each powder sample was measured over 10 times (using fresh powder every time). As the flow behavior is influenced by temperature and humidity the powders were dried in an oven and left to cool to room temperature prior to characterization. The Hausner ratio was calculated as follows:

$$HR = \frac{\rho_{tapped}}{\rho_{bulk}}$$ *Equation 2-11*

where ρ_{bulk} and ρ_{tapped} are the freely settled bulk density of the powder and the tapped density of the powder in which the powder is tapped until no further changes occur.

2. 3. 4. Thermal properties

In the sinterstation the polymers are subjected to changing temperatures. On the one hand, the powders are being preheated in order to reduce laser power and minimize shrinkage during the building process. On the other hand the polymers are heated to high temperatures in order to selectively fuse particles together. In the case of semi-crystalline polymers this is done just above the melting temperature while in the case of amorphous polymers just above the glass transition temperature.

During this heating, polymers undergo a transition from solid or glassy material to softer material to a viscous flowing melt which often involves a change in specific volume [72]. This change is illustrated in Figure 2-15 by a theoretical volume-temperature curve for amorphous and semi-crystalline polymers. During heating, the polymer chains absorb thermal energy relating to a higher mobility of the polymer chains. This is reflected in the volume-temperature curve as a gradually increasing slope. Before the glass transition temperature the chain segments of the polymer are 'frozen' in a glassy state with very limited mobility giving rise to only a slight expansion of the volume with temperature. Once passed this temperature the chain segments have absorbed enough thermal energy for the segments to move more freely giving rise to a higher increase in specific energy over temperature. As semi-crystalline polymers have highly ordered regions with usually higher density, they experience a sudden increase in specific volume upon heating above the melting temperature. Here the crystalline regions of the polymer are broken down expanding the material. Amorphous polymers do not experience this sudden increase however and are as a result less prone to severe shrinkage upon cooling. Despite this, they typically have higher melt viscosities than the semi-crystalline polymers which increases the risk of higher part porosities when sintering [22]. Figure 2-16 illustrates how the melting of the crystalline regions is accompanied by a sudden viscosity drop whereas the amorphous polymers only experience a gradually decreasing viscosity over temperature. As a result denser parts can be build when using semi-crystalline polymers and heating above the T_m than generally achieved using amorphous polymers.
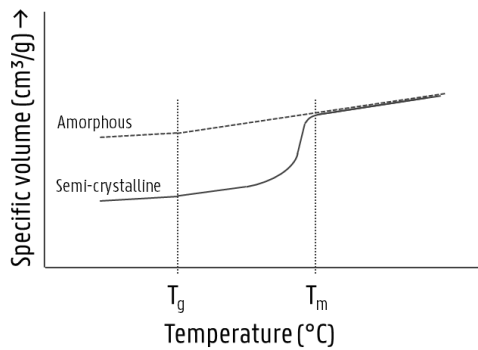
Figure 2-15: The theoretical variation of specific volume with temperature for amorphous and semi-crystalline polymers
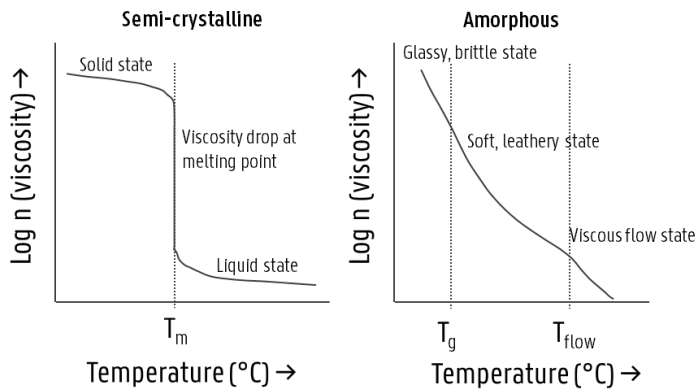
Figure 2-16: Theoretical viscosity-temperature relation in semi-crystalline and amorphous polymers. Semi-crystalline polymers experience a sudden viscosity drop when melting whereas amorphous polymers only show a gradual decrease in viscosity over temperature [73]

Next to changes in specific volume due to phase transitions also thermal shrinkage during building must be minimized in order to minimize warpage.

A primary measure to overcome this shrinking behavior lies in the selection of materials: polymers exhibiting low material shrinkage will be more advantageous in this regard. Next to this, the powder bed is being heated during the build process in order to postpone crystallization and reduce thermal gradients between laser heat and powder bed temperature. For semi-crystalline polymers the sintered parts are kept just below the melt temperature during the whole sinter process. Afterwards, the material is allowed to cool and crystalize homogeneously as to prevent inhomogeneous shrinkage. For the amorphous polymers the powder bed is generally kept below T_g. Figure 2-17 displays the theoretical processing window and sinter window for a polymer candidate. The processing window referring to the temperature in which the powder bed is kept and the sinter window to the temperature which the laser has to achieve for a short amount of time in order to selectively fuse particles together [22].
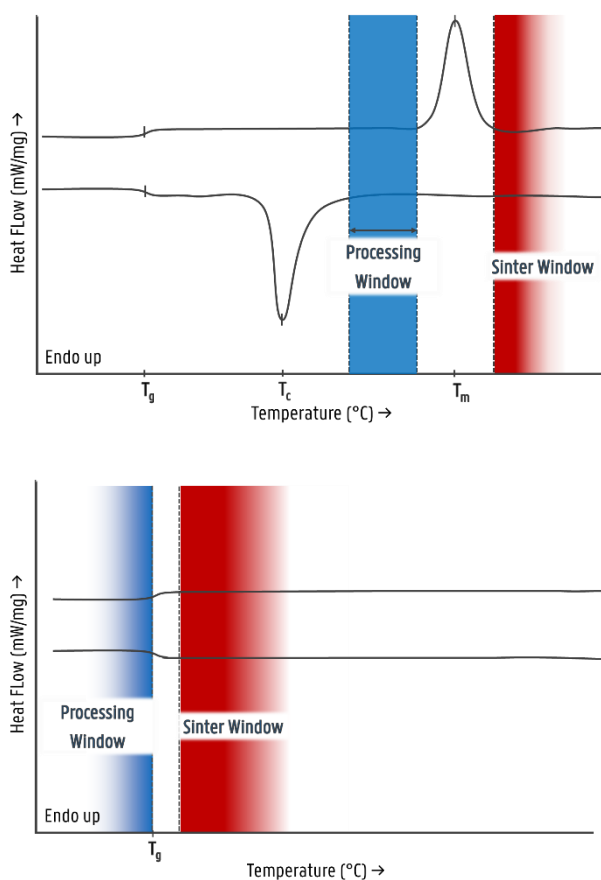
Figure 2-17: Hypothetical processing and sinter windows of semi-crystalline (up) and amorphous (down) polymers

As can be derived from the above mentioned explanation the feed material for SLS is exposed to high temperatures for long periods of time as well as temperature spikes during heating. It is therefore important to consider the thermal properties of the selected candidates and investigate for their thermal stability as well as any changes that might be imposed on to their thermal behavior due to the processing method. This thermal history is important in the case of optimization of the sinter parameters. In this study Thermogravimetric Analysis (TGA) is performed in order to investigate the thermal degradation temperature of the newly selected materials. Differential Scanning Calorimetry (DSC) is also performed to have an insight on any change in intrinsic properties like degradation due to the processing method or thermal history imparted by the processing method. Additionally, the TGA measurements were used to investigate the influence of Montmorillonite (MMT) fillers on the thermal properties and determine the filler content. Gel Permeation Chromatography (GPC) measurements were performed on the produced samples to get a quantitative description of the possible degradation occurring due to processing.

2. 4. CONCLUSIONS

The optimization of laser sintering parameters encompasses a large set of factors of which this study focusses on the powder based properties. Investigation of the laser and scan based properties is being performed by colleagues of the University Leuven at the Additive Manufacturing Research Group [10] and the temperature properties at the Soft Matter Rheology and Technology department of the University of Leuven [74], [75].

This chapter gave a quick overview of the polymers that are currently being used for Selective Laser Sintering in particular the class of polyamides. The literature study shows that by extending the gamma of materials the application window for laser sintering may be greatly expanded. To this regard novel polymer candidates were examined by comparing the candidates' mechanical, chemical and thermal properties to that of the most commonly used PA as a validation of possible alternative materials. Next to this, the processing methods are elucidated with their main communition principles. The research objective being the processing of commercially available polymers via novel processing techniques into spherical powders in the range of 45-95 μm exhibiting free flowing behavior. The morphology and particle size being the key goals in achieving free flowing powders. This behavior is characterized using Hausner ratio measurements and further investigated at KU Leuven. The thermal behavior of the produced powders is not to be neglected in this case and should be investigated using DSC and TGA measurements for any change in intrinsic properties as this may affect the optimization of the sintering parameters. Any degradation due to processing is to be avoided during the powderization process and is monitored using GPC measurements.

The discussed methods will be applied in the next chapters on the selected polymer materials and discussed at length.

2. 5. REFERENCES

[1]   W. Zhou, X. Wang, J. Hu, and X. Zhu, "Melting process and mechanics on laser sintering of single layer polyamide 6 powder," *Int. J. Adv. Manuf. Technol.*, vol. 69, no. 1–4, pp. 901–908, 2013.

[2]   R. D. Goodridge, R. J. M. Hague, and C. J. Tuck, "Effect of long-term ageing on the tensile properties of a polyamide 12 laser sintering material," *Polym. Test.*, vol. 29, no. 4, pp. 483–493, 2010.

[3]   A. Wegner, R. Harder, G. Witt, and D. Drummer, "Determination of Optimal Processing Conditions for the Production of Polyamide 11 Parts using the Laser Sintering Process," *Int. J. Recent Contrib. from Eng. Sci. IT*, vol. 3, no. 1, pp. 5–12, 2015.

[4]   J. Bai, R. D. Goodridge, R. J. Hague, and M. Song, "Carbon nanotube reinforced Polyamide 12 nanocomposites for laser sintering," *Proceeding Solid Free. Fabr. Symp.*, vol. 7, pp. 98–107, 2012.

[5]   D. Drummer, K. Wudy, M. Drexler, and S. C. Jana, "Modelling of the aging behavior of polyamide 12 powder during laser melting process," in *AIP Conference Proceedings*, 2015, vol. 1664, no. 1, p. 160007.

[6]   S. R. Athreya, K. Kalaitzidou, and S. Das, "Processing and characterization of a carbon black-filled electrically conductive Nylon-12 nanocomposite produced by selective laser sintering," *Mater. Sci. Eng. A*, vol. 527, no. 10, pp. 2637–2642, 2010.

[7]   M. Schmidt, D. Pohle, and T. Rechtenwald, "Selective laser sintering of PEEK," *CIRP Ann. Technol.*, vol. 56, no. 1, pp. 205–208, 2007.

[8]   D. Drummer, D. Rietzel, and F. Kühnlein, "Development of a characterization approach for the sintering behavior of new thermoplastics for selective laser sintering," *Phys. Procedia*, vol. 5, pp. 533–542, 2010.

[9]   D. Pohle, S. Ponader, T. Rechtenwald, M. Schmidt, K. A. Schlegel, H. Münstedt, F. W. Neukam, E. Nkenke, and C. von Wilmowsky, "Processing of Three-Dimensional Laser Sintered Polyetheretherketone Composites and Testing of Osteoblast Proliferation in vitro," in *Macromolecular Symposia*, 2007, vol. 253, no. 1, pp. 65–70.

[10]   D. Strobbe, S. Dadbakhsh, L. Verbelen, and P. Van Puyvelde, "Selective laser sintering of polystyrene : a single layer approach," no. 1, pp. 2–7.

[11]   S. Ziegelmeier, P. Christou, F. Wöllecke, C. Tuck, R. Goodridge, R. Hague, E. Krampe, and E. Wintermantel, "An experimental study into the effects of bulk and flow behaviour of laser sintering polymer powders on resulting part properties," *J. Mater. Process. Technol.*, vol. 215, pp. 239–250, Jan. 2015.

[12]   T. Wohlers, *Additive Manufacturing and 3D Printing State of the Industry - Annual Worldwide Progress Report*. 2014.

[13]   I. Gibson, D. W. Rosen, and B. Stucker, "Additive Manufacturing Technologies Rapid Prototyping to Direct Digital Manufacturing. 2010." Springer.

[14]   3D Systems, "DuraForm ® PA Plastic DataSheet," 2010. [Online]. Available: http://www.rpc.msoe.edu/datasheets/sls/Duraform_PA.pdf.

[15]   H. Zarringhalam and N. Hopkinson, "Post-Processing of Duraform™ Parts for Rapid Manufacture," in *14th SFF Symposium, Austin*, 2003.

[16]   GRANTA MI, "CES Edupack - Polymer Database." 2016.

[17]   Solvay, *Udel Polysulfone Design Guide*. Solvay.

[18]   L. Idemitsu Kosan Co., "XAREC® 90ZC - Crystalline Polymers - Neat SPS Homo Polymer," *Product Information*, 2011. [Online]. Available: http://plasticker.de/recybase/docs/2332_1380533306.pdf.

[19]   J. Schellenberg and H. Leder, "Syndiotactic polystyrene: Process and applications," *Adv. Polym. Technol.*, vol. 25, no. 3, pp. 141–151, 2006.

[20]   M. Malanga and T. H. Newman, "Syndiotactic Polystyrene," in *Encyclopedia of Polymer Science and Technology*, John Wiley & Sons, Inc., 2002.

[21]   S. K. Tiwari, S. Pande, S. Agrawal, and S. M. Bobade, "Selection of selective laser sintering materials for different applications," *Rapid Prototyp. J.*, vol. 21, no. 6, pp. 630–648, 2015.

[22]   R. D. Goodridge, C. J. Tuck, and R. J. M. Hague, "Laser sintering of polyamides and other polymers," *Prog. Mater. Sci.*, vol. 57, no. 2, pp. 229–267, 2012.

[23]   D. L. Bourell, T. J. Watt, D. K. Leigh, and B. Fulcher, "Performance limitations in polymer laser sintering," in *Physics Procedia*, 2014, vol. 56, no. C.

[24]   J.-P. Kruth, X. Wang, T. Laoui, and L. Froyen, "Lasers and materials in selective laser sintering," *Assem. Autom.*, vol. 23, no. 4, pp. 357–371, 2003.

[25]   M. Schmid and K. Wegener, "Thermal and molecular properties of polymer powders for Selective Laser Sintering (SLS)," in *AIP Conference Proceedings*, 2016, vol. 1779, no. 1, p. 100003.

[26]   M. Schmid, A. Amado, and K. Wegener, "Materials perspective of polymers for additive manufacturing with selective laser sintering," *J. Mater. Res.*, vol. 29, no. 17, pp. 1824–1832, 2014.

[27]   S. C. Lao, W. Yong, K. Nguyen, T. J. Moon, J. H. Koo, L. Pilato, and G. Wissler, "Flame-retardant Polyamide 11 and 12 Nanocomposites: Processing, Morphology, and Mechanical Properties," *J. Compos. Mater.*, vol. 44, no. 25, pp. 2933–2951, 2010.

[28]   WESTLAKE PLASTICS COMPANY, "Products for Medical Applications," 2017. [Online]. Available: http://www.mcnealplasticmachining.com/pubs/WestlakeMPMGuide.pdf.

[29]   S. Darvishmanesh, J. C. Jansen, F. Tasselli, E. Tocci, P. Luis, J. Degrève, E. Drioli, and B. Van der Bruggen, "Novel polyphenylsulfone membrane for potential use in solvent nanofiltration," *J. Memb. Sci.*, vol. 379, no. 1–2, pp. 60–68, Sep. 2011.

[30]   Solvay, "Radel ® R-5000," *Technical Data Sheet*, 2014. [Online]. Available: http://catalog.ides.com/Datasheet.aspx?I=92041&FMT=PDF&E=1445. [Accessed: 28-Mar-2017].

[31]   Solvay, "Radel ® R-5600," *Technical Data sheet*, 2014. [Online]. Available: http://catalog.ides.com/Datasheet.aspx?I=92041&FMT=PDF&E=137208. [Accessed: 28-Mar-2017].

[32]   J.-P. Kruth and B. Van Hooreweder, "University Leuven - Additive Manufacturing Research Group." [Online]. Available: http://set.kuleuven.be/am/.

[33]   E. Klein, "Affinity membranes: a 10-year review," *J. Memb. Sci.*, vol. 179, no. 1, pp. 1–27, 2000.

[34]   R. Naim, a. F. Ismail, H. Saidi, and E. Saion, "Development of sulfonated polysulfone membranes as a material for Proton Exchange Membrane (PEM)," *Proc. Reg. Symp. Membr. Sci. Technol. 2004*, 2004.

[35]   T. Sata, M. Tsujimoto, T. Yamaguchi, and K. Matsusaki, "Change of anion exchange membranes in an aqueous sodium hydroxide solution at high temperature," *J. Memb. Sci.*, vol. 112, no. 2, pp. 161–170, Apr. 1996.

[36]   Solvay Specialty Polymers, "Radel® PPSU, Veradel® PESU & Acudel® modified PPSU -Design Guide." [Online]. Available: www.solvay.com/en/binaries/Radel-PPSU-Veradel-PESU-Acudel-PPSU-

Design-Guide_EN-227541.pdf.

[37]   C. Bai, R. J. Spontak, C. C. Koch, C. K. Saw, and C. M. Balik, "Structural changes in poly (ethylene terephthalate) induced by mechanical milling," vol. 41, pp. 7147–7157, 2000.

[38]   S. Jonna and J. Lyons, "Processing and properties of cryogenically milled post-consumer mixed plastic waste," *Polym. Test.*, vol. 24, no. 4, pp. 428–434, Jun. 2005.

[39]   J. Pan and W. J. D. Shaw, "Properties of a mechanically processed polymeric material," *J. Appl. Polym. Sci.*, vol. 52, no. 4, pp. 507–514, Apr. 1994.

[40]   H. L. Castricum, H. Yang, H. Bakker, and J. H. Van Deursen, "A Study of Milling of Pure Polymers and A Structural Transformation of Polyethylene," in *Materials Science Forum*, 1996, vol. 235–238, pp. 211–216.

[41]   J. Font and J. Muntasell, "Effect of ball milling on semicrystalline bisphenol A polycarbonate," *Mater. Res. Bull.*, no. 35.5, pp. 681–687, 2000.

[42]   T. Ishida, "Mechanical alloying of polytetrafluoroethylene with polyethylene," *J. Mater. Sci. Lett.*, vol. 13, no. 9, pp. 623–628, 1994.

[43]   H. Matsuyama, "Formation of polypropylene particles via thermally induced phase separation," *Polymer (Guildf).*, vol. 41, no. 24, pp. 8673–8679, Nov. 2000.

[44]   P. van de Witte, P. J. Dijkstra, J. W. A. van den Berg, and J. Feijen, "Phase separation processes in polymer solutions in relation to membrane formation," *J. Memb. Sci.*, vol. 117, no. 1–2, pp. 1–31, Aug. 1996.

[45]   S.-W. Song and J. M. Torkelson, "Coarsening effects on the formation of microporous membranes produced via thermally induced phase separation of polystyrene-cyclohexanol solutions," *J. Memb. Sci.*, vol. 98, no. 3, pp. 209–222, Jan. 1995.

[46]   R. K. Arya, "Drying induced phase separation in multicomponent polymeric coatings—simulation study," *Int. J. Sci. Technol. Res*, vol. 1, pp. 48–52, 2012.

[47]   N. Mys, T. Haverans, A. Verberckmoes, and L. Cardon, "Production of syndiotactic polystyrene powder for part manufacturing through SLS," in *Polymer and Moulds Inovations*, 2014.

[48]   Fritsch, "Variable Speed Rotor Mill and Cross Beater Mill," *Class. line Prod. Leafl.*

[49]   M. A. Meyers and K. K. Chawla, *Mechanical behavior of materials*, vol. 2. Cambridge University Press Cambridge, 2009.

[50]   T. L. Smith, "Rupture processes in polymers," *Pure Appl. Chem.*, vol. 23, no. 2–3, pp. 235–254, 1970.

[51]   B. Z. Shakhashiri, *Chemical demonstrations: A handbook for teachers of chemistry*, vol. 2. Univ of Wisconsin Press, 1985.

[52]   H. Mio, J. Kano, and F. Saito, "Scale-up method of planetary ball mill," *Chem. Eng. Sci.*, vol. 59, no. 24, pp. 5909–5916, Dec. 2004.

[53]   G. Gorrasi and A. Sorrentino, "Mechanical milling as a technology to produce structural and functional bio-nanocomposites," *Green Chem.*, vol. 17, no. 5, pp. 2610–2625, 2015.

[54]   S. Wennerstrum, T. Kendrick, J. Tomaka, and J. Cain, "Size reduction solutions for hard-to-reduce materials," *Powder bulk Eng.*, vol. 16, no. 1, pp. 43–49, 2002.

[55]   A. P. Smith, J. S. Shay, R. J. Spontak, C. M. Balik, H. Ade, S. D. Smith, and C. C. Koch, "High-energy mechanical milling of poly (methyl methacrylate), polyisoprene and poly (ethylene- alt -propylene)," vol. 41, pp. 6271–6283, 2000.

[56]   A. Newman, "Making Amorphous API," in *Pharmaceutical Powder X-ray*

Diffraction Symposium, 2012.

[57]   R. L. Scott and R. L. Hildebrand, "The solubility of nonelectrolytes," *New York, Reinhold Publ. Corp*, vol. 374, 1950.

[58]   G. Scatchard, "Equilibrium in non-electrolyte mixtures.," *Chem. Rev.*, vol. 44, no. 1, pp. 7–35, 1949.

[59]   B. A. Miller-Chou and J. L. Koenig, "A review of polymer dissolution," *Prog. Polym. Sci.*, vol. 28, no. 8, pp. 1223–1270, 2003.

[60]   C. M. Hansen, *Hansen Solubiliy Parameters: a user's handbook*, Second Edi. London: CRC Press, 2012.

[61]   C. Arpagaus, N. Schafroth, and M. Meuri, "Laboratory Scale Spray Drying Of Inhalable Drugs: A Review," *Best@Buchi*, no. 59, 2010.

[62]   Buchi and GEA Niro, "Scale-up from the Buchi Mini Spray Dryer B-290 to the Niro Mobil Minor," *Information Bulletin*, 2008. [Online]. Available: http://static1.buchi.com/sites/default/files/downloads/B-290_Scale-up_B-290_Niro_MOBILE_MINOR_en_01.pdf.

[63]   S. Ziegelmeier, F. Wöllecke, C. Tuck, R. Goodridge, and R. Hague, "Characterizing the Bulk & Flow Behaviour of LS Polymer Powders."

[64]   M. Schmid, F. Amado, G. Levy, and K. Wegener, "Flowability of Powders for Selective Laser Sintering (SLS) investigated by Round Robin Test," in *High Value Manufacturing: Advanced Research in Virtual and Rapid Prototyping: Proceedings of the 6th International Conference on Advanced Research in Virtual and Rapid Prototyping, Leiria, Portugal, 1-5 October, 2013*, 2013, p. 95.

[65]   H. Scientific, "A guidebook to particle size analysis," *Horiba Instruments, Inc*, pp. 1–29, 2012.

[66]   A. Bodhmage, "Correlation between physical properties and flowability indicators for fine powders." University of Saskatchewan Saskatoon, 2006.

[67]   W. Grabowski and J. Wilanowicz, "The structure of mineral fillers and their stiffening properties in filler-bitumen mastics," *Mater. Struct.*, vol. 41, no. 4, pp. 793–804, 2008.

[68]   M. C. Powers, "Comparison chart for estimating roundness and sphericity," *AGI data sheet*, vol. 18, no. 1, 1982.

[69]   M. Schmid, A. Amado, and K. Wegener, "Polymer powders for selective laser sintering (SLS)," in *AIP Conference Proceedings*, 2015, vol. 1664, p. 160009.

[70]   A. Amado, M. Schmid, G. Levy, and K. Wegener, "ADVANCES IN SLS POWDER CHARACTERIZATION," vol. 12.

[71]   G. V Barbosa-Cánovas, E. Ortega-Rivas, P. Juliano, and H. Yan, "Bulk properties," *Food Powders Phys. Prop. Process. Funct.*, pp. 55–90, 2005.

[72]   I. Gibson and D. Shi, "Material properties and fabrication parameters in selective laser sintering processnull," *Rapid Prototyp. J.*, vol. 3, no. 4, pp. 129–136, Dec. 1997.

[73]   K. G. Budinski, *Engineering Materials: Properties and Selection*, 8th editio. New Jersey: Pearson Prentice Hall, 2005.

[74]   L. Verbelen, "Towards scientifically based screening criteria for polymer laser sintering," KU Leuven, 2016.

[75]   S. Dadbakhsh, L. Verbelen, O. Verkinderen, D. Strobbe, P. Van Puyvelde, and J.-P. Kruth, "Effect of PA12 powder reuse on coalescence behaviour and microstructure of SLS parts," *Eur. Polym. J.*, vol. 92, pp. 250–262, 2017.

Chapter 3

CASE STUDY: PROCESSING OF POLYPHENYLSULFONE

This chapter encompasses the processing of polyphenylsulfone as a case study in which the techniques discussed in Chapter 2 are applied in order to create spherical PPSU powders. The virgin material is processed and the powders characterized on their extrinsic and intrinsic properties.

3. 1. SPRAY DRYING

3. 1. 1. Polymer solubility

In order to process the polymer via this physicochemical processing technique one must find a suitable solvent in order to dissolve said polymer. To this end a parameter based approach was selected based on the Hansen Solubility Parameter (HSP) model [1]. Sulfone polymers are soluble in polar aprotic solvents, Table 3-1 displays a selection of most commonly used solvents for polymer precipitation along with the Hansen solubility parameters. Water has a significantly different HSP and therefore acts as a non-solvent. During solution experiments and further processing using spray drying dry materials and glassware are as a result indispensable. DMF is a solvent commonly used in processing Radel PPSU for various applications like membrane synthesis [2], [3]. Furthermore, it has a boiling point which lies well within the processing parameters for the Buchi Mini Spray Dryer B-290 [4] allowing sufficient freedom for optimization of these parameters. For these reasons this solvent was selected for further processing of PPSU.

Table 3-1: Hansen Solubility Parameters of PPSU and from possible solvents and anti-solvents for PPSU. Data from [1], [3]

	δ_{tot} (MPa$^{1/2}$)	δ_d (MPa$^{1/2}$)	δ_p (MPa$^{1/2}$)	δ_h (MPa$^{1/2}$)
Radel 5000	20,7	18,7	5,0	7,4
Radel 5600	20,7	18,7	5,0	7,4
N-methyl pyrrolidine (NMP)	18,6	17,0	2,8	6,9
Tetrahydrofuran (THF)	19,5	16,8	5,7	8,0
N,N-Dimethyl formamide (DMF)	24,9	17,4	13,7	11,3
Diphenyl sulfone	25,8	21,1	14,4	3,4
Sulfolane	29,4	20,3	18,2	10,9
Water (H_2O)	30,1	18,1	17,1	16,9

After selecting DMF as a suitable solvent for PPSU, the maximum solubility of PPSU in DMF was determined. This was done gravimetrically as the minimum solvent weight necessary to completely dissolve a weighted sample of PPSU. The solubility was expressed in weight percentage polymer (wt.%). Practically, a weighted sample of PPSU was refluxed at 153 °C, measured amounts of solvent were added until the material was completely dissolved. Afterwards the solution was left to cool at room temperature before further processing. The experiments were repeated three times to minimize experimental errors. Table 3-2 gives the solubility of both Radel grades in DMF both in wt.% as in g/mL.

Table 3-2: Solubility values of R5000 and R5600 in DMF

	Solubility (g/mL)	Solubility (wt.%)
Radel 5000	0.074	7.300 ± 0.006
Radel 5600	0.078	7.640 ± 0.008

Next, as there exists a viscosity limit on the atomization performance of the Buchi B 290 mini spray dryer of 300 MPa.s [5], a viscometic study was performed on the created solutions in function of their weight percentage PPSU using Ubbelohde viscosimetry (Schott-Geräte Gmbh). Tests were performed at 25°C using DMF as solvent. All measurements were performed in accordance with ISO 3105. Figure 3-1 displays the solution viscosities for both grades of PPSU. It is clear that R5600 is a lower viscous grade than R5000 and both grades do not exceed the viscosity limit for atomization with the Mini spray dryer.
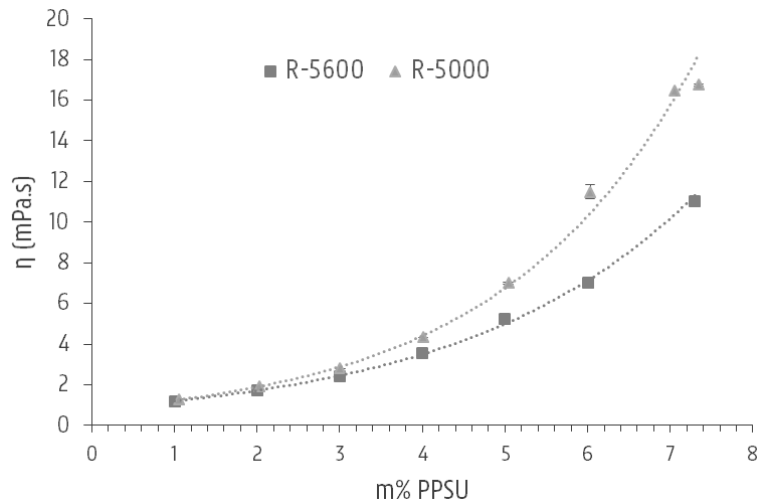
Figure 3-1: Solution viscosity of R5000 and R5600 in function of their weight percentage using Ubbelohde viscosimetry. R5600 is clearly a lower viscous grade

3. 1. 2. Design of Experiments: Screening Experiments and Response Surface Model

As mentioned before; spray drying entails a physicochemical form of processing polymer pellets into spherical powders based on solution-precipitation phenomena. This process offers several advantages; firstly, due to the tendency to minimize surface tension, the droplets have a natural tendency to dry out in spherical particles. Particle morphology is better controlled by the setting of crucial processing parameters and the technique offers good reproducibility. As a result, no post processing is necessary contrary to other processing methods.

Conventionally, spray drying is used in the pharmaceutical industry [6] for the processing of low molecular weight compounds which exhibit a low Peclet number (i.e. the ratio between droplet evaporation rate and diffusional motion of the solutes [7]). Processing novel polymers like PPSU, a high molecular weight polymer which exhibits a high Peclet number (the diffusional motion of the solutes is slower than the velocity of the receding droplet surface), is not at all similar in behavior and requires a thorough investigation of the influence of the processing parameters on the size and morphology of the obtained particles. The development and optimization of a spray drying methodology is often empirical and experimentally driven. Traditional methods frequently use an iterative Design of Experiments (DOE) [8] to optimize the process parameters and achieve particles with the defined properties. This is often a time-intensive exercise and does not always result in a robust understanding of the process. The purpose of this work was to investigate the most critical process parameters that influence particle size and morphology, understand their influence and optimize said parameters in order to achieve micron size spherical particles that can be used as feeding material for selective laser sintering purposes. To this end the theoretical principles of the particle formation process were related to the process variables specified by a Response Surface Model (RSM) [9]. In experimental design a RSM is used when the critical factors influencing the response are determined by foregoing screening experiments. The main goal of the methodology is to create a predictive model that allows to determine the relationship between the factors and the response. This model can thereafter be used to optimize the settings of the process. The structure and size of particles formed by spray drying have been examined and described extensively in literature [10]–[13] exposing the crucial factors regarding particle formation. These factors were confirmed by preliminary experiments and incorporated in the response surface model in order to optimize size and morphology of the spray dried PPSU particles.

3. 1. 2. a. Factor selection

Due to the high possible number of influential processing parameters on size and morphology of the spray dried particles, preliminary experiments were performed combined with a literature survey.

Cal and Sollohub [14] reported the crucial parameters that have a direct influence on the particles to be the inlet temperature of the drying air, the drying gas flow rate, the solution feed rate and feed concentration. They represented a table with mutual interrelationships among the spray drying parameters yet concluded these relationships to be more of a guideline compelling the operator to follow an approach of trial and errors. R. Vehring [6] and Nadiyanto and Okuyama [13] pointed out the importance of the diffusional motion of the solutes and the ratio of said physical quantity to the evaporation rate of the solvent as a critical parameter for particle formation. Both authors performed an in depth study on particle formation mechanisms and elucidate a scheme which connect the aforementioned parameters to these particle morphologies.

From this study five crucial factors were retained which are defined in Table 3-3: feed concentration (wt.%, x_1), inlet temperature (T_{in}, °C, x_2), gas flow rate (GFR, mL/s, x_3), feed flow rate (FFR, mL/min, x_4) and MFI of the material (g/10min, x_5).

Two grades of polyphenylsulfone were provided by Solvay and were tested: Radel R5000 and R5600, a high and low viscous grade exhibiting MFI values (x_5) of 17 and 37 g/10min (365 °C / 5,0 kg) respectively. This factor plays an important role in further processing through SLS as low melt viscosities are preferable for the sinter process. For each continuous factor 3 levels were entered into the model (minimum, center and maximum) to detect and identify any factor causing a nonlinear effect. For modeling the effect of the discrete factor MFI (x_5) the two levels mentioned are specified; the high viscous level by the Radel R5000 grade and a low viscous level by the R5600 grade. The grades were dissolved in N,N-Dimethylformamide (DMF, purity +99,5%, CARL ROTH) by reflux at different levels of concentration (x_1), i.e. 4; 5,5 and 7 wt.% corresponding to the low, center and high value of the concentration range (see further on). The solution viscosity of the grades was determined via Ubbelohde viscosimetry and their respective curves depicted in Figure 3-1. Each level correlates with viscosities of 4,4; 8,3 and 15,8 mPa.s for the R5000 grade and 3,5; 6,0 and 10,2 mPa.s for the R5600 grade. Both grades clearly differ in solution viscosities which may reflect in different spray dried particles as well. The solutions were subsequently heated to 150 °C and fed to the nozzle at defined solution feed rate (x_4); at 7,4; 12,05 and 16,7 mL/min respectively. The heated solution was then atomized in the two-fluid nozzle at gas flow rates (x_3) of 122; 175 and 228 mL/s into the drying chamber where the droplets were dried out by a heating gas at a temperature (x_2) of 180; 200 or 220 °C respectively. After collection, the samples were dried in a vacuum

chamber at 300 mmHg and elevated temperature of 50 °C for two days prior to characterization.

Using JMP 13 software a 20 run five factor experimental design is generated. The relationship of two responses of interest Y, i.e. mean particle size (Y_1) and particle morphology, i.e. the percentage particles with adequate sphericity and roundness (Y_2), in relation to the processing parameters x_1 to x_5 are investigated and used to find the ideal set of parameters which optimizes the response values.

Table 3-3: Five factor experimental design Particle Size and Morphology study

Factor	x_1	x_2	x_3	x_4	x_5
Experiment	Feed Concentration (wt.%)	Inlet Temperature (°C)	Gas Flow Rate (mL/s)	Feed Flow Rate (mL/min)	MFI (g/10 min, 365 °C, 5,0 kg)
RSM1	7	180	122	16,7	17
RSM2	7	180	228	7,4	17
RSM3	5,5	220	175	12,05	37
RSM4	5,5	200	228	12,05	17
RSM5	4	220	122	16,7	17
RSM6	7	200	175	12,05	37
RSM7	7	220	122	16,7	37
RSM8	5,5	200	175	7,4	17
RSM9	7	220	175	16,7	17
RSM10	7	220	122	7,4	17
RSM11	4	200	122	7,4	37
RSM12	5,5	180	122	7,4	37
RSM13	4	180	228	7,4	37
RSM14	4	220	228	7,4	17
RSM15	4	180	228	16,7	17
RSM16	4	180	122	12,05	17
RSM17	7	180	228	16,7	37
RSM18	4	220	228	16,7	37
RSM19	4	180	122	16,7	37
RSM20	7	220	228	7,4	37

Due to the expected nonlinear relationship between the response value and the processing parameters the following linear polynomic model is proposed [15]:

$$Y_k = \beta_{k,0} + \sum \beta_{k,i} x_i + \sum \beta_{k,ij} x_i x_j + \sum \beta_{k,ii} x_i^2 + \epsilon_k$$

Equation 3-1

where Y_k is the response value (either particle size or morphology), x_i are the respective factors, β is a vector of unknown constant coefficients referred to as parameters and ϵ_k is the experimental error corresponding to observation Y_k. The considered model (1) allows the user to establish an approximate relationship between the response value and the processing parameters x_i, which can then be used to predict response values for a given setting of control variables. More importantly, it determines the optimum settings of variables that result in the maximum response. Furthermore, the significance of the factors can be determined based on the H_0 hypothesis which assumes that a given parameter is not significant. Assessment of effect significance is based on the p-value which states that an effect is considered to be significant when $p < 0,05$.

3. 1. 2. b. Response factors Particle size and Particle morphology

The obtained powder samples corresponding to each set of processing parameters listed above were processed using SEM microscopy on a JEOL JSM-7600F at low voltage (2kV) and working distance of 8 mm. The samples were sputtered with gold using a BAL-TEC SCD 005 Sputter Coater at 25mA prior to inspection. Subsequently, particle distribution and morphology was assessed using the imaging software Image J.

The morphology of the particles was assessed based on their shape (sphericity) as well as their roundness according to the described method (see Chapter 2). For statistical analysis these percentages were subjected to a logit transformation, which is:

$$logit\ Y_2 = log\left(\frac{Y_2}{100 - Y_2}\right)$$

Equation 3-2

where p is the percentage particles with desired roundness and sphericity in the sample. This transformation treats very small and very large values symmetrically, pulling out the tails and pulling in the middle around 0.5 or 50%.

Table 3-4 shows the response obtained after analysis of the RSM samples. Mean particle size ranged from 5,34 µm to 14,52 µm while the morphology of the particles displayed a larger range going from absolutely no suitable to 22,3% apt particles.

Table 3-4: Response values on particle size and particle morphology of the RSM experiments

Response value	Y_1	Y_2
Experiment	Mean particle size (µm)	Particle morphology (%)
RSM1	13,23	6,9
RSM2	10,06	2,9
RSM3	10,16	3,3
RSM4	8,54	2,9
RSM5	11,21	1,9
RSM6	10,32	13,6
RSM7	14,52	22,3
RSM8	9,54	2,5
RSM9	9,21	11,9
RSM10	11,07	26
RSM11	11,18	0
RSM12	9,95	2,3
RSM13	7,32	0,5
RSM14	6,9	0,6
RSM15	7,92	0
RSM16	12,39	0,2
RSM17	6,02	6,3
RSM18	8,24	1
RSM19	12,39	1,1
RSM20	5,34	14,2

3. 1. 2. c. Response Surface Model Evaluation: Particle Size

The model for the mean particle size (Y_1) has an R^2 of 0,82, its corresponding residual diagram is shown in Figure 3-2. The Y_1 models´ significant effects are portrayed in scaled format in Table 3-5 and show a distinct negative effect of the GFR (x_3) on particle size and a significant interaction of inlet temperature and MFI (x_2*x_5). Though MFI (x_5) and T_{in} (x_2) are not considered significant effects on their own, they were kept in the model because of the significant interaction they portray with each other. The interaction is displayed in Figure 3-3.

Table 3-5: Scaled estimates on mean particle size

Estimates of the effects on particle size	Estimate		Prob>|t|
GFR (mL/s) (x_3)	-0,043814		<,0001*
MFI (g/10min) (x_5)	-0,2315		0,3833
T_{in} (°C) (x_2)	-0,008219		0,5768
T_{in} (°C) *MFI (g/10min) (x_2*x_5)	0,0388571		0,0173*
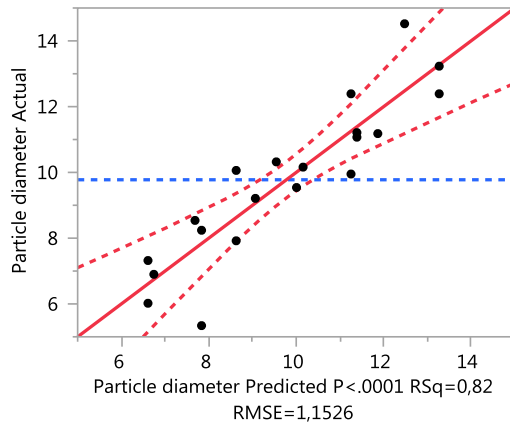
Figure 3-2: Predicted versus experimentally measured particle diameter (Y₁)
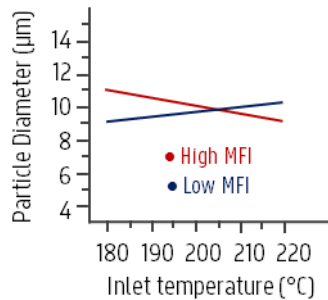
Figure 3-3: Interaction plot of Inlet temperature and material grade on particle size

Atomization of the polymer solution occurs through the creation of high frictional forces over the liquid that is fed through the spray drying nozzle. The frictional force causes liquid disintegration into a spray of droplets and is greatly influenced by the carrier gas properties [14]. Increasing GFR has a negative effect on particle size by an increase in friction and therefore leads to more severe liquid disintegration into finer droplets, reducing particle size.

When looking at the interaction plot of inlet temperature (T_{in}) and MFI (Figure 3-3) one can see that for low T_{in}, the low viscosity grade (high MFI) is preferred. With increasing T_{in} a shift to the higher viscosity grade (low MFI) is favorable for higher mean particle size. The T_{in} has an important effect on the solvent evaporation from the droplet [14]. Increasing the T_{in} will stimulate early enrichment of solutes at the droplet surface by faster evaporation of the solvent. A concentration gradient will occur which will cause a diffusional motion of the solutes inwards against the concentration gradient. At the high level of T_{in} the evaporation rate will be much faster than the diffusional motion of the polymer chains causing early enrichment of solutes and subsequent precipitation with the formation of a shell at the droplet surface. Due to the high evaporation, a thick skin or shell is created which is mechanically strong enough to support itself in the case of the viscous grade, resulting in more particles

with a higher sphericity and better particle size [13]. While this is also the case for the low viscosity grade, thinner shells are formed due to better diffusional flow, which are less mechanically stable. During solvent evaporation of the particles in the drying chamber the droplet surface will tend to recede pulling the thinner shells inwards causing wrinkled or dimpled structures [6], [11], [13]. Vehring et al. [7] explained these effects for polymer solutions at length using both a numerical and analytical model. As polymer solutions are generally very viscous they are commonly defined by a large Peclet number which is related to a low diffusion rate. Low diffusion rates can result in skim or shell formation depending on the parameters used. This evaporation model is illustrated in Figure 3-4 and elucidated by practical example through the micrographs of the respective experimental runs in Figure 3-5.

Low molecular weight solutions benefit a large diffusion rate that allows the solutes to migrate relatively easily inside the droplet. When the solvent evaporates at the surface of the droplet, a concentration gradient is created that diminishes to the inside of said droplet. As more solvent evaporates the surface of the droplet recedes and saturation occurs leading to homogeneous precipitation throughout the droplet. This leads to a dense particle (Figure 3-4, A). However, when dealing with large molecular weight materials, the diffusion rate is slow compared to the speed of the receding surface and a shell is formed. If the drying rate is slow, a thin shell is formed, not mechanically stable enough to sustain itself (Figure 3-4, B). As the solvent evaporates on the shell will collapse forming toroid-like or wrinkled structures. On the other hand, if thedrying rate is high, the shell will attain a critical thickness stable enough to sustain itself (Figure 3-4, C). In this case the evaporation continues by migration of the solvent molecules through capillary flow and precipitation occurs resulting in a density of the particle that decreases inwards.
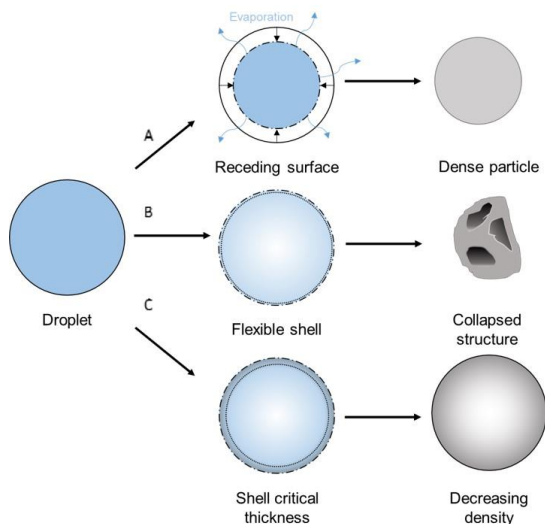
Figure 3-4: Particle formation process during drying of the polymer solution droplets. (A) low viscosity material with large diffusional rate, (B) high viscosity solution with formation of thin shell and (C) high viscosity solution with formation of mechanically stable shell
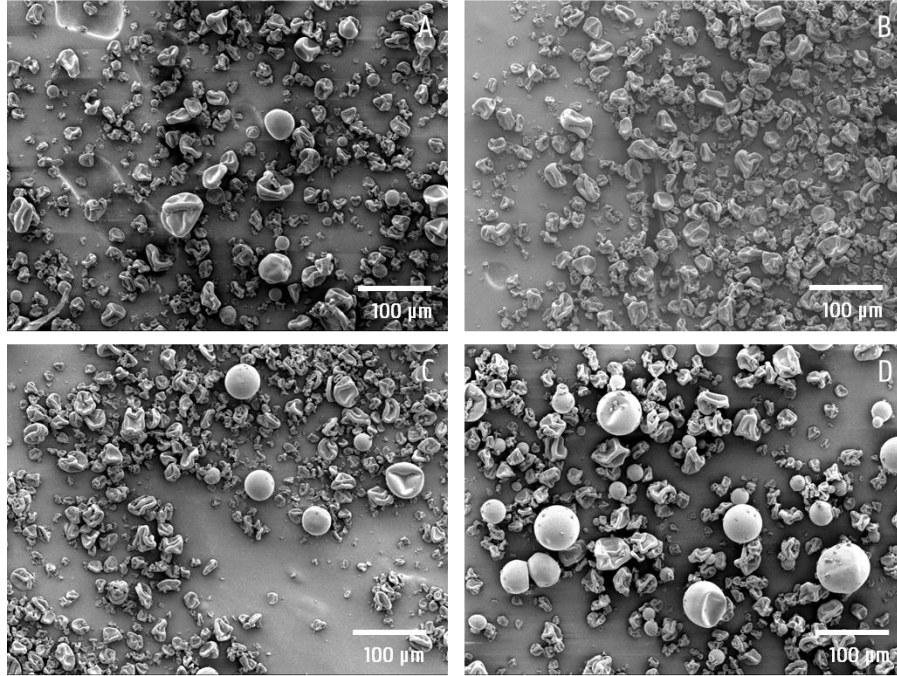
Figure 3-5: Micrographs illustrating the x_2*x_5 interaction. (A) low T_{in}, high MFI; (B) low T_{in}, low MFI; (C) high T_{in}, high MFI and (D) high T_{in}, low MFI. Note the inflated particles which are more common with higher inlet temperatures.

3. 1. 2. d. Response Surface Model Evaluation: Particle Morphology

The model for particle morphology (Y_2) has an R^2 of 0,86 and its respective residual diagram is shown in Figure 3-6. Particle morphology is affected by the solute material and by the drying conditions (GFR, FFR and T_{in} primarily). This is reflected in the model by a significant positive effect for feed concentration (x_1) as well as significant positive interactions for gas flow rate and MFI (x_3*x_5), FFR with MFI (x_4*x_5) and negative interactions for GFR with FFR (x_3*x_4), the T_{in} with MFI (x_2*x_5) and a negative quadratic effect for feed concentration (x_1*x_1). The scaled effects are displayed in Table 3-6 and the interactions are graphically depicted in Figure 3-7.

Feed concentration is known to have a large effect on the mobility of the solids as increasing the concentration entails an increase of the solution viscosity restricting mobility severely [11]. This is reflected in the quadratic effect of concentration on the morphology of the particles. This nonlinear effect entails an optimal value that can be found to achieve the highest amount of spherical particles. The optimal settings are displayed in Figure 3-9. As can be seen from the prediction profiler, the optimum for the feed concentration is found close to the saturation limit of polyphenylsulfone (7,1 wt.%), this can also be seen as a minimum concentration needed to mechanically
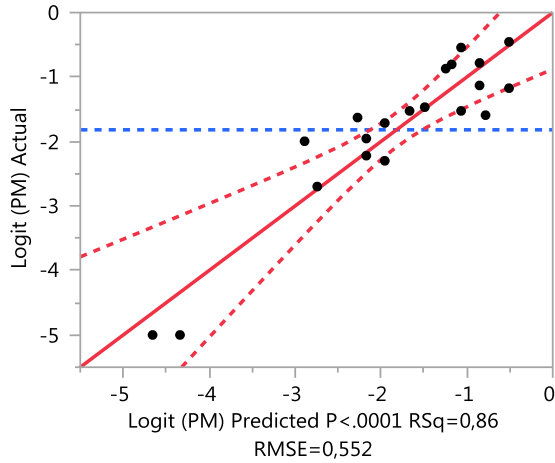
Figure 3-6: Predicted versus experimentally measured particle morphology (Y₂)

Table 3-6: Scaled estimates on particle morphology

Scaled estimates on morphology	Scaled Estimate		Prob>|t|
Concentration (m%) (x₁)	0,8708727		<,0001*
Concentration (m%) (quadratic term) (x₁*x₁)	-0,876686		0,0198*
GFR (mL/s) * FFR (mL/min) (x₃*x₄)	-0,536218		0,0039*
Tᵢₙ (°C) * MFI (x₂*x₅)	-0,319237		0,0394*
GFR (mL/s) * MFI (x₃*x₅)	0,4961471		0,0050*
FFR (mL/min) * MFI (x₄*x₅)	0,3886169		0,0162*
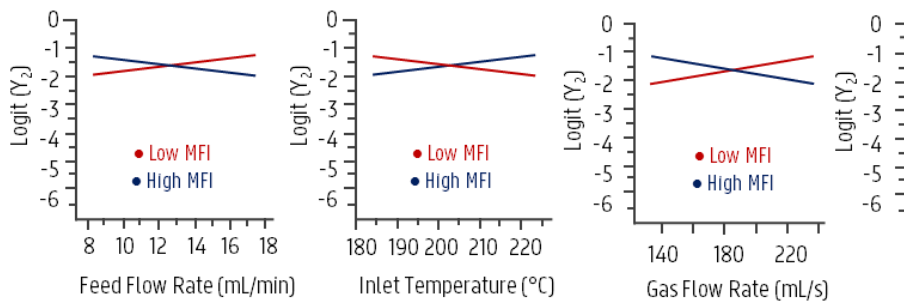
*Figure 3-7: Interaction plots of the Feed Flow Rate versus MFI (x₄*x₅), Inlet Temperature versus MFI (x₂*x₅), Gas Flow Rate versus MFI (x₃*x₅) and Feed Flow Rate versus Gas Flow Rate (x₃*x₄). High and low values depicted are the high and low levels used in the response surface model in Table 3-3*

stabilize the particle during drying as postulated by J. Vicente et. al. [11] and Elversson and Fureby [16]. Upon higher concentrations, the diffusional flux of the solutes is hindered more severely leading to early skin formation creating a shell that is more stable with smooth surface. In combination with high evaporation rates (high x_2), spherical particles are expected to form [11]. Very diluted feed concentrations lead to thin shell or skins to be formed which are more flexible upon drying and have the tendency to move inwards with the receding droplet surface. Occurrences like shriveling, inflation or particle breakage are more prone to happen resulting in the low morphology value in the prediction profiler. When selecting the high viscous grade of PPSU, high gas flow rates are beneficial in order to have better jetting of the liquid stream into droplets. Reducing gas flow rate would result in incomplete or bad jetting giving rise to bad particle morphologies like stringing [11]. Furthermore, high gas flow rates result in jetting of smaller droplets into the drying chamber which dry out faster. These smaller droplets reach their critical shell thickness more quickly resulting in more spherical particles.

One would expect the same trend regarding to polymer grade and inlet temperature and yet, according to the model, this is not the case. Higher inlet temperatures tend to work better on low viscous grades. Though this is contrary to what one may find in literature [7], [11], a possible explanation could lie in the fact that at these low viscous grades particle inflation is more prone to happen resulting in bigger particles with still a smooth shell yet smaller in thickness. Vicente et. al. [11] has encountered this phenomenon and ascribes this to the increased vapor pressure that is created inside the particle. During drying, the temperature of the particle approaches that of its surrounding temperature which is controlled by the inlet temperature. As this temperature is chosen above the boiling point of the solvent, the pressure inside the particle may exceed external pressure and the particle may expand as a result of this. This phenomenon tends to occur more easily at particles containing more flexible shells which are promoted to be formed in the lower viscous grades. Particle inflation is difficult to assess and not always easy to differentiate from normal particles. Figure 3-8 displays an inflated particle in RSM 10.

Lower feed rates may result in incomplete atomization. Due to the higher viscosity of the viscous polyphenylsulfone grade it is advisable to use higher feed rates to prevent stringing phenomena and other incomplete jetting behavior [17].

Gas flow rate and solution feed rate interact contrariwise in regard to particle morphology in the sense that the jetting of the solution is largely dependent on these two parameters. A careful balance must be found between these two parameters. The drying gas flow rate has an influence on the retention time of the droplets inside the drying chamber. The higher the gas flow rate, the shorter the retention time of the particles inside the drying chamber [14]. High solution feed rates would in this case result in incomplete drying of the particles and cause a thin shell to form resulting in

50

insufficiently dried particles with undesirable morphology. In case of low gas flow rates, high solution feed rates are advisable in this case as the particles spend more time in the drying chamber allowing them to dry out more completely. This must be nuanced however as the gas flow rate must still be high enough in order to atomize the liquid stream and the drying chamber volume must be sufficient to completely dry out the droplets.

Figure 3-9 displays the optimal settings in order to achieve particles with the highest amount of sphericity. In this case 50,5% spherical particles are theoretically feasible to obtain. It depicts a high concentration above the limit to form a critical shell. Furthermore high gas flow rate and low feed flow rate are advised to promote firm atomization of the liquid feed into fine droplets that can dry out fast. In order to promote the formation of the critical shell the high viscous grade is chosen. Inlet temperature is kept at 180°C, this will decrease risk of inflated particles with consequential shriveling after evaporation of the solvent.
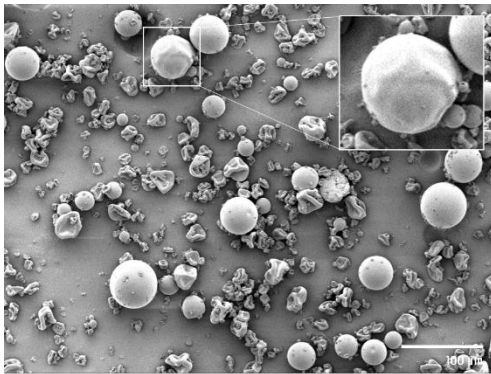

Figure 3-8: RSM 10 depicted with inflated particle noticeable by the deflation by the loss in pressure during cooling
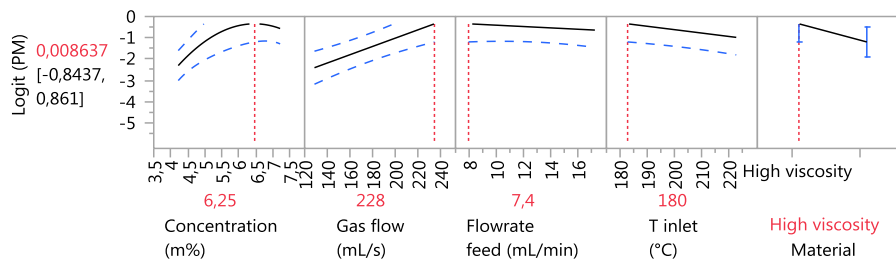
Figure 3-9: Prediction profiler of particle morphology indicating the optimal settings to achieve the most spherical particles

3. 1. 2. e. Optimization of spray drying process using the Response Surface Model

After identification of the significant effects on morphology and particle size, the response surface model is used to perform an optimization of the spray drying process. Optimal processing conditions for spherical particles with maximum particle size are acquired from the model and are depicted in Figure 3-10. The model predicts particles with a mean particle size of 13,27 µm that can be obtained, of which 19,0% are of adequate sphericity and roundness. In order to achieve these particles a minimum concentration of 6,25 wt.% is required. At this concentration, in combination with the following process parameters, particles are most likely to achieve a critical thickness of the polymeric shell which is mechanically stable enough to support itself. Gas flow rate remains as low as possible in order to maximize retention time inside the drying chamber and maximize the size of the atomized droplets, for this reason feed flow rate is at its highest level. Inlet temperature remains at its lowest value, this decreases risk at inflated particles and consequential shriveling after evaporation of the solvent out of the sphere. The low viscous grade (high MFI) of PPSU is preferred for this process which is favorable for further processing later on through SLS.

When using the high viscous grade material, optimal processing conditions have shifted to higher temperatures (220 °C, Figure 3-11) and only a best particle size of 12,48 µm with 12,5 % spherical particles can be achieved. The higher temperature is said to promote solvent evaporation and stimulate the rigid shell yet at increased risk of particle inflation and collapse of shriveled structures, hence the lower value of particle morphology.

The current optimal parameter settings allow for the best particle size/morphology ratio yet particle morphology can be drastically improved according to the model by making a small concession on particle size. By increasing the inlet temperature to the highest setting faster solvent evaporation is promoted with the formation of a critical thick shell stable enough to support itself. Particle diameter is reduced in this way to 11,39 µm yet the amount of favorable particles is increased to 50,5% (Figure 3-12). These parameter settings are in accordance with the best experimental run (RSM 7) in which a particle size of 14,52 µm was attained with 22,3 % of the particles of adequate morphology.

As the best results could be obtained with the Radel 5600 low viscous grade, it is advisable to perform an augmented design in order to refine the current response surface model and remove any remaining ambiguities. In this case additional runs should be constructed focusing on the R5600 High MFI grade.

Figure 3-10: Prediction profiler of particle size response and particle sphericity response in order to find the optimal processing conditions to achieve particles with both high sphericity and particle size.

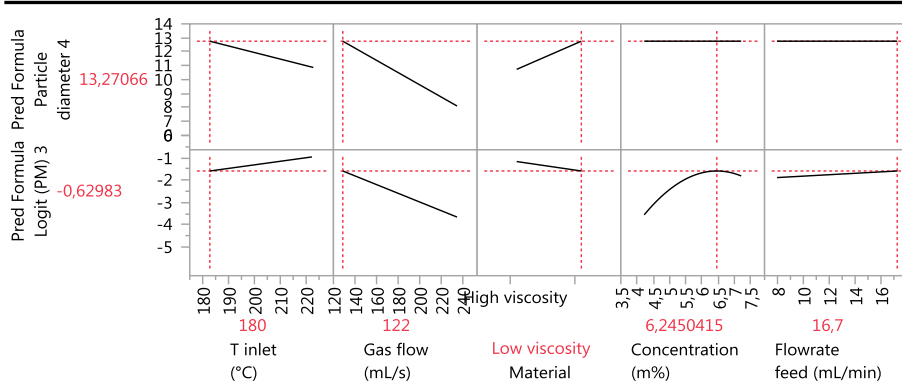*Figure 3-11: Prediction profiler of particle size response and particle sphericity response in order to find the optimal processing conditions to achieve particles with both high sphericity and particle size for the high viscous grade material.*
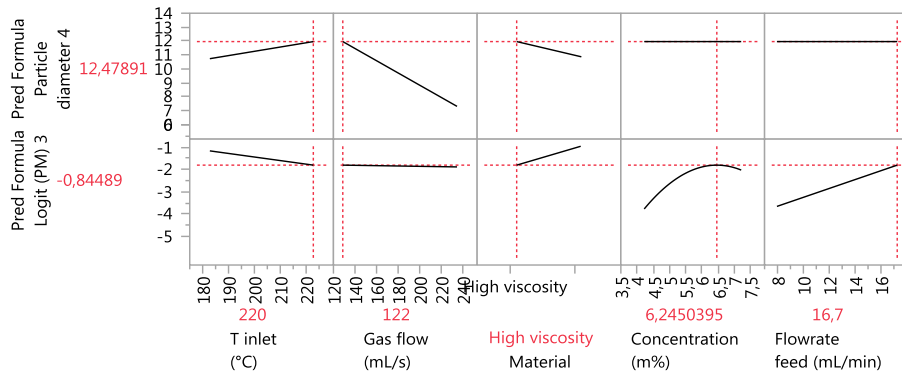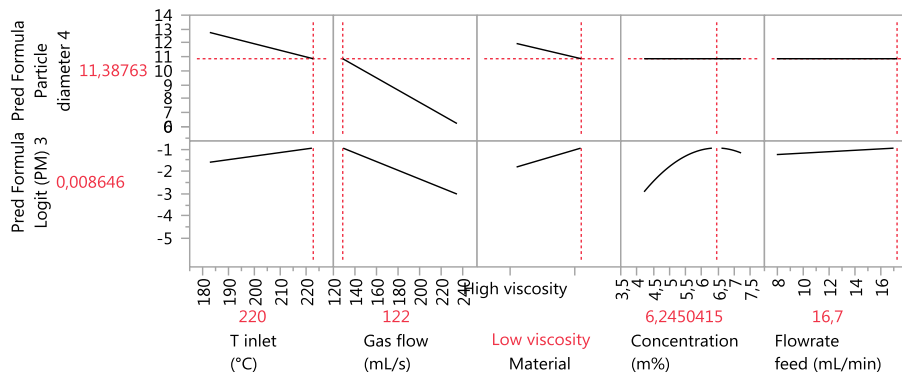

Figure 3-12: Deviated approach to the optimal settings reducing particle size by a small amount yet increasing particle roundness and sphericity by a fair amount.

3. 1. 2. f. Conclusions regarding the Response Surface Model

The important processing parameters for microsphere production of polyphenylsulfone have been identified and used for optimization of the spray drying process using a Response Surface Model. Two responses were evaluated to this end, i.e. particle diameter and particle morphology, and optimized using the JMP prediction profiler. From the investigated parameters the gas flow rate was identified to have a crucial effect on particle size and a less pronounced positive interaction of the MFI and the inlet temperature was found. The model was largely dependent on the efficiency of atomizing the polymer solution and provided new insights in the processing of polyphenylsulfone into microspheres through spray drying.

These two models were combined in order to find the optimal conditions to create particles with large diameter and good morphology. The prediction profiler portrayed an optimal particle size of 13,27 µm with 19 % of the particles displaying good sphericity and roundness according to the Power scale. To achieve these values a minimum concentration of 6,25 m% is needed. Gas flow rates remains at its lowest level (122 mL/s) and feed rate at its highest (16,7 mL/min) in order to atomize as large droplets as possible. The inlet temperature remains at its lowest value (180 °C) and the low viscous Radel 5600 grade is preferred. An alternate approach was put forward in which the inlet temperature was increased to its highest setting (220°C), drastically improving particle morphology while making a small concession on particle diameter (11,39 µm). These parameter settings were in accordance with the best experimental run (RSM 7) in which a particle size of 14,52 µm was attained with 22,3 % of the particles of adequate morphology. At these conditions however a higher risk of particle inflation exist leaving particles with a thin shell.

Spray drying has the advantage of creating spherical particles with a smooth surface which is ideal for powder flow in the laser sintering process. Using the current lab scale set up it was not possible to increase the particle size into the ideal range for SLS. Scale up to a pilot scale spray dryer could possibly provide a solution to this problem. Additional experimental runs in the form of an augmented design can further refine the response surface model focusing on the low viscous grade which has been proven to be the best material to produce microspheres. Though particle diameter needs to be augmented to form a better fit as feed material for SLS, the microspheres could already be usable in other applications such as micromolding and rotor moulding and lab-scale sinter tests as is. Thin shell spherical particles produced by the spray drying technique also presents unique properties to the material like decreased density, better thermal insulation and optical scattering and may be interesting in applications using microcapsules, pigments, opacifyers, damping materials, etc… [18]

3. 2. CRYOGENIC MILLING

A sample of PPSU R5600 was cryogenically milled by Dakota Coatings NV. The sample was investigated as a means for comparison to the industrial standard of milling.

3. 2. 1. Particle morphology

Size reduction of the raw material with the help of liquid nitrogen and different grinding tools was performed at the site at Dakota Coatings NV. When inspecting morphology of the particles no sphericity was found (see Figure 3-13). Particles were angular in shape ranging from 12 to 276 µm. Due to the milling at cryogenic temperature the particles are pulverized through brittle fractures causing sharp edges and a variety of shapes. Table 3-7 summarizes the particle morphology determined via the described method in the Chapter 2.
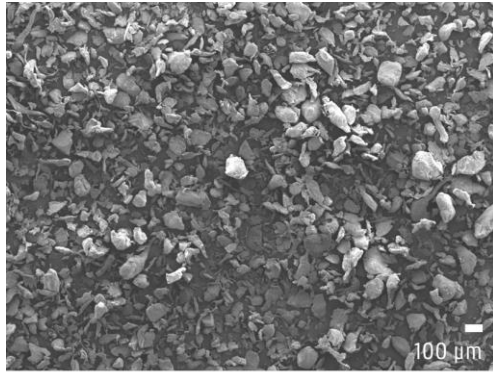
Figure 3-13: Micrograph from cryogenically milled R5600 sample

Table 3-7: Particle size distribution of the cryogenically milled PPSU R5600 material together with the percentage spherical particles obtained

	Y_1		Y_2
Sample	Mean particle size (µm)	Standard Deviation (µm)	Particle morphology (%)
Cryogenically milled R5600	75,62	40,26	0

3. 2. 2. Particle size

The cryogenically milled PPSU was investigated for particle size distribution (PSD) and found to have a mean particle size of 75,62 µm with a standard deviation of 40,26 µm with the distribution slightly positively skewed. The PSD of the powder is depicted in Figure 3-14 and summarized in Table 3-7. Though particles are within the desired range for SLS, the angular shape and low sphericity are undesirable for good powder flow.
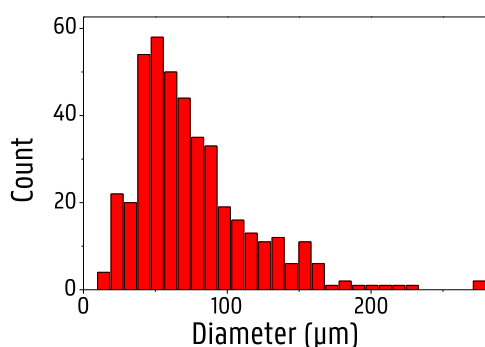
Figure 3-14:Particle size distribution of cryogenically milled R5600 PPSU

3. 3. ROTOR MILLING

The PPSU pellets were processed by the three-step communition process described in Chapter 2 on a Fritsch Pulverisette 14 rotor mill, followed by a sieving step in order to obtain the right particles in size and morphology. The 12-ribbed rotor blade was used at 15000 RPM to achieve pulverization which was augmented to 18000 RPM for the final milling step. During the milling process the rotor mill was cooled by air at room temperature using an aspirator connected to the cyclone system. For analysis purposes only the powders which underwent 1 cycle without refeed were used.

3. 3. 1. Particle morphology

Via the three-step communition process the PPSU R5600 pellets are processed to powder form after which the powder is sieved again in order to remove remaining inconsistencies. Figure 3-15 displays micrographs of samples taken from each step of the powderization process. The respective particle size distributions and corresponding percentage of particles exhibiting the ideal morphology according to the Powers' scale is represented in Figure 3-16 and Table 3-8. In the first processing step the PPSU pellets are pulverized in the rotor mill using a sieve of 500 µm to form a coarse powder of very irregular structures of varying size with often little to no sphericity (Figure 3-15, A). Structures were found to have a particle size ranging from 39 µm to 913 µm demonstrating elongated rough irregular structures. This processing step was introduced to prevent the pellets from plasticizing against the high speed rotating mill when pulverizing the material to even smaller particle size.

In rotor milling breakage occurs by a rotating 12 ribbed cutting blade which impacts at high speed against the particles. Upon impact the kinetic energy of the impact tool gives rise to fragmentation and deformation in the contact area. As with ball milling, breakage will occur when the force on the particle reaches a critical level. Fractionation is mediated by the occurrence of incipient cracks as a result of high local stresses. When the energy input provided by the high speed rotating rotor blade is not sufficient enough to exceed the energy of break, elastic (reversible) deformation followed by plastic (irreversible) deformation will occur. If the particle in question

56

escapes the mechanical deformation in time by passing through the inset sieve elastic unloading will occur with permanent deformations in the particle at hand. This can be seen by the rough angular structures in the coarse powders and the first refinement step. For bigger particles dissipation of energy can occur more easily leading to more deformation which does not always result in fragmentation. Hence the large diversity in structures apparent in the respective micrographs. Smaller particles exhibit a smaller surface area, less dissipation of energy can occur and fragmentation is supposed to be more dominant in this case.

The milling process itself is said to generate some heat by the stretching and deformation of the polymer because of its entropic penalty [19]. It is important that this heat is dissipated as quickly and efficiently as possible in order to hamper the material from becoming too soft and deform even more, generating more heat. By ensuring the rotor blade has sufficient kinetic energy in order to easily overcome the energy at break and efficiently cooling both sieve and material by creating an airflow in the miller one reduces the retention time of the material and can avoid detrimental heat build-up which can result in plasticization of the material.

During the subsequent refinement steps particle morphology visibly increased which is reflected in Table 3-8 by the percentage of spherical particles with apt roundness and sphericity. The fractions endure an extra deformation by the rotating motion of the rotating blades causing the particles to round off with every refinement step. The first refinement step increases the amount of suitable particles to 14,5 % while the final fraction contains 60% of particles with adequate roundness and sphericity according to Power's scale. After an extra sieving step at 80 µm this is further increased to 62,82 % by the removal of bigger inconsistencies.

Table 3-8: Particle size distribution of the PPSU R5000 material in each of the individual processing steps together with the percentage spherical particles obtained in each step.

	Y$_1$		Y$_2$
Sample	Mean particle size (µm)	Standard Deviation (µm)	Particle morphology (%)
RM500	245,08	200,69	0
RM120	122,57	97,01	14,5
RM80	73,80	39,71	60
Sieved	51,00	14,31	62,82
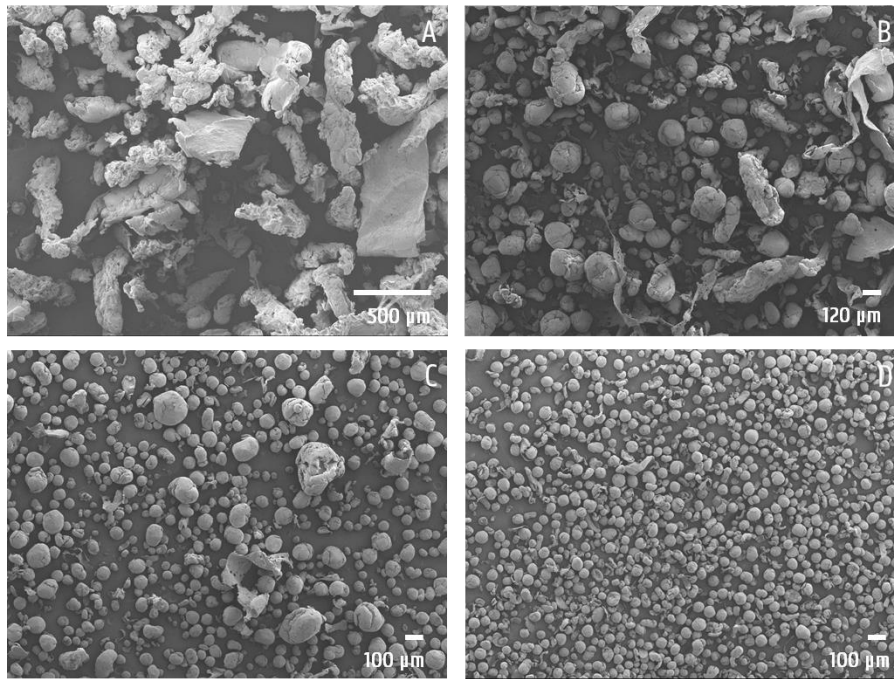
Figure 3-15: PPSU R5600 powder undergoing the three step pulverization process with additional sieving step: (A) Milling of PPSU pellets into a coarse powder at 500 µm, (B) first refinement step by milling the coarse powder at 120 µm, (C) second refinement step by further pulverization of the refined powder at 80 µm and (D) the final powder after additional sieving at 80 µm removing any leftover inconsistencies.

3. 3. 2. Particle size

The three step communition process by the rotor miller decreases particle size sequentially while improving morphology. Figure 3-16 displays the PSDs of the micrographs in Figure 3-15 which are representative for the milling process. In the first step, pellets are processed to a rough powder with a wide spread on particle size. Particles ranged from 39 µm to 913 µm demonstrating elongated rough irregular structures. During refinement steps by processing to 120 and 80 µm respectively particle size as well as standard deviation on particle size decreased substantially. Refining the coarse powder by processing at 120 µm decreased mean particle size to 120,57 µm with a standard deviation of 97,01 µm. A large part of the elongated irregular structures are fragmented and partly rounded already in this step. Further processing to 80 µm allows reduction of particles to a mean size of 73,8 µm with 39,71 µm standard deviation. The most part of the remaining inconsistencies are now fragmented and further rounding of the particles takes place. The extra sieving step is subsequently introduced in order to filter out any remaining irregularities resulting in a further decrease in particle size with smaller deviation on particle size. The final result being a product displaying 62,82 % particles of adequate morphology and sphericity having a mean particle size of 51 µm.
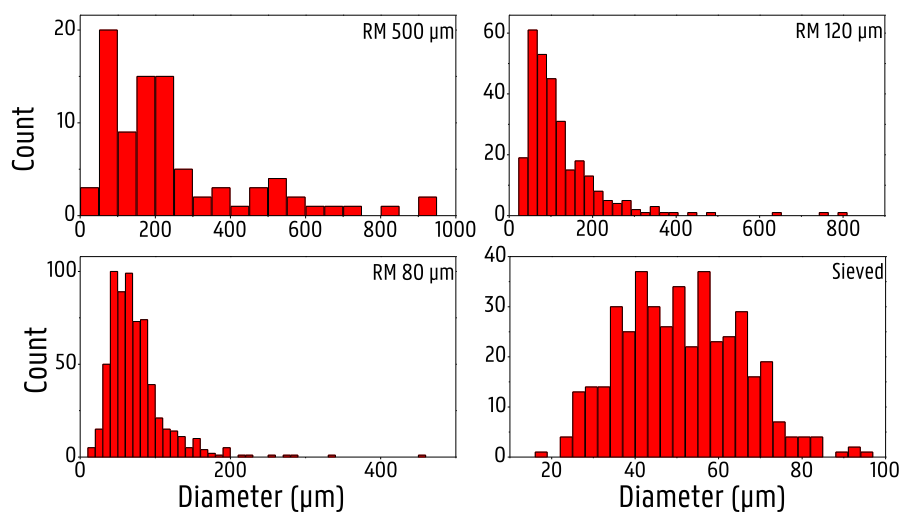
Figure 3-16: Particle Size Distributions of the PPSU R5600 material subjected to the three step milling process and additional sieving. The micrographs in Figure 3-15 are representative for the PSD displayed.

3. 4. MATERIAL CHARACTERIZATION

3. 4. 1. GPC measurements

GPC was used as a direct way to measure degradation by calculating the molecular weight of the virgin and processed samples. GPC measurements were performed on a Waters Instrument, with RI detector (2414 Waters), equipped with three Polymer Standards Services GPC serial columns (1 X GRAM Analytical 30 Å, 10 μm and 2 x GRAM Analytical 1000 Å, 10 μm). PMMA standards (690 g.mol^{-1} to 1944000 g.mol^{-1}) were used for calibration and DMA containing LiBr (0.42 g.mL^{-1}) was used as a solvent at a flow rate of 1 mL.min^{-1}. Molecular weight and dispersities were determined using Empower software. Samples were injected with a PL-AS RT autosampler. Infrared measurements were carried out with an ATR Perkin Elmer FT-IR spectrum 1000 in a range of 4000 cm^{-1} to 600 cm^{-1}. Each sample was measured in triplicate and analysed using SPSS. The GPC measurements performed on the rotor milled sample subjected to the three step communion process, the spray dried sample and virgin grade PPSU R5600 are depicted in Figure 3-17 with their respective values of molecular weight and polydispersity displayed in Table 3-9. Both number average molecular weight (M_n) and weight average molecular weight (M_w) of the samples were compared statistically to that of the virgin sample to see if any change in molecular weight could be ascribed to the processing method. In this regard the cryogenically milled PPSU sample was also investigated yet could not be dissolved for analysis through GPC. Conceivably, severe crosslinking through degradation by the processing technique has resulted in bad dissolution in the elution solvent for GPC

measurements. In the case of the other samples, t-test analysis revealed no significant change in number (M_n) nor weight average molecular weight (M_w) leading to believe that an insignificant amount of degradation due to processing has occurred..

Table 3-9: GPC measurements of virgin and processed PPSU samples

GPC Measurements			
Sample	$M_w{}^1$ (g/mol)	$M_n{}^2$ (g/mol)	Polydispersity[3]
Unprocessed PPSU R5600	36106 ± 608	11269 ± 182	3,204 ± 0,057
Rotor Milling	35884 ± 95	11213 ± 151	3,201 ± 0,051
Spray Drying	35339 ± 412	11974 ± 1358	2,972 ± 0,372
Cryogenic Milling	n.a.	n.a.	n.a.

[1] Weight average molecular weight; weighted molecular weight according to weight fractions
[2] Number average molecular weight; total weight of the sample divided by the number of molecules in sample
[3] Polydispersity; ratio of M_w/M_n as a measure of heterogeneity of sizes of molecules in the sample
[4] n.a. = not applicable
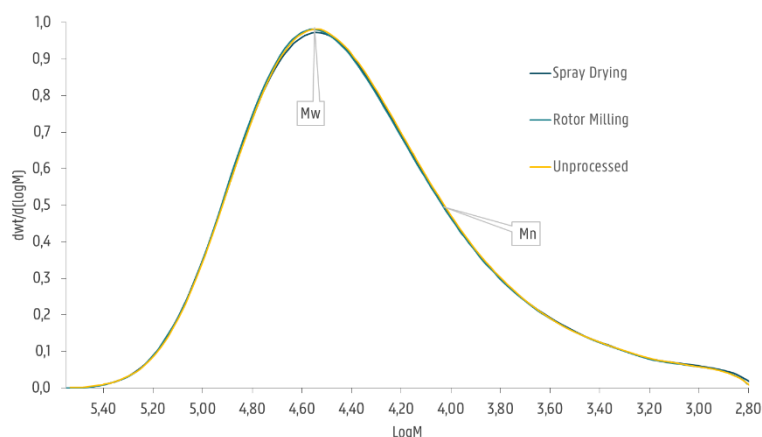
Figure 3-17: Molecular weight distribution derived from elution profile of virgin R5600, rotor milled and spray dried PPSU. The cryogenically milled PPSU was unable to dissolve in the GPC eluent for analysis. The M_w and M_n values are displayed in Table 3-9

3. 4. 2. TGA measurements

TGA measurements were performed on the PPSU material under nitrogen atmosphere with a heating rate of 10 °C/min to a maximum temperature of 900 °C. The measurement is shown in Figure 3-18 and reveals a 1 % degradation temperature of 503,8 °C. The degradation occurs in two steps: first by cleavage of the heteroatomic bonds (C-S, C-O) followed by C-C bond cleavage relating to the release of small volatiles like SO_2, CO, CO_2, benzene and phenol followed by the degradation of the thermally more stable aromatic compounds like biphenyl, diphenyl ether and dibenzofuran molecules follow to a lesser extent [20]. The subsequent degradation step represents the slow decomposition of char formed by oxidation [21]. The measurements reveal the high thermal stability of the material and suggest not to

exceed 500 °C when processing the material in order to prevent degradation. After 900 °C a large residual mass is still present of 44,71 % suggesting the presence of a large amount of residual char which decomposes further at higher temperatures. The derived degradation temperature was used later on in DSC measurements. The data can be valuable for the processing of PSU in later sintering experiments in regards to the setting of the laser parameters.
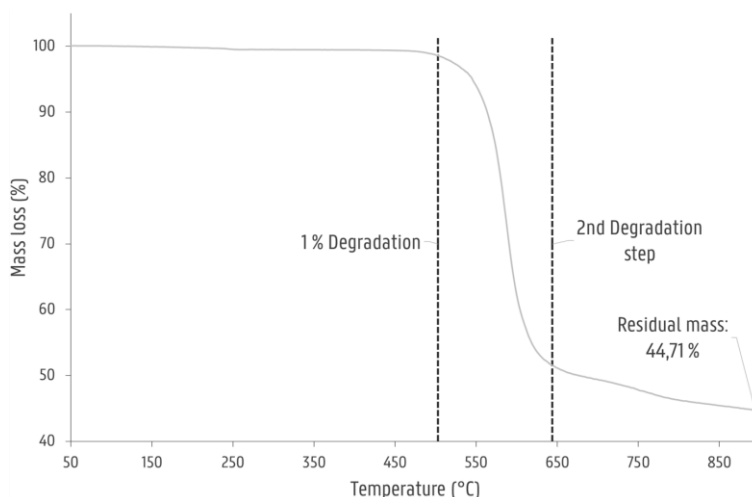
Figure 3-18: TGA measurement of PPSU R5600 virgin material at 15 °C/min heating rate

3. 4. 3. DSC measurements

The thermal properties of the produced powders were analyzed using a Netzsch DSC 204F1 under nitrogen atmosphere. Samples were contained in an open Aluminum pan and referenced against an empty open Aluminum pan. A heating rate of 10 °C/min was used to heat the DSC to 450 °C to determine the effects of degradation and thermal history imparted during processing. A second heating run under the same conditions was performed to determine if any change in thermal properties had occurred. A baseline subtraction was done to correct for any slope or variation in heat transfer effects. The samples never deviated more than 3 % in weight of the virgin sample (22,31 mg) which was used for comparison. Figure 3-19 & Figure 3-21 depict the first and second heating runs of processed R5600 samples using rotor milling and spray drying. In the case of rotor milling, the final product as can be seen in Figure 3-15,D was characterized while in the case of spray drying the sample with highest spherical morphology was used. This corresponds with sample RSM 10.
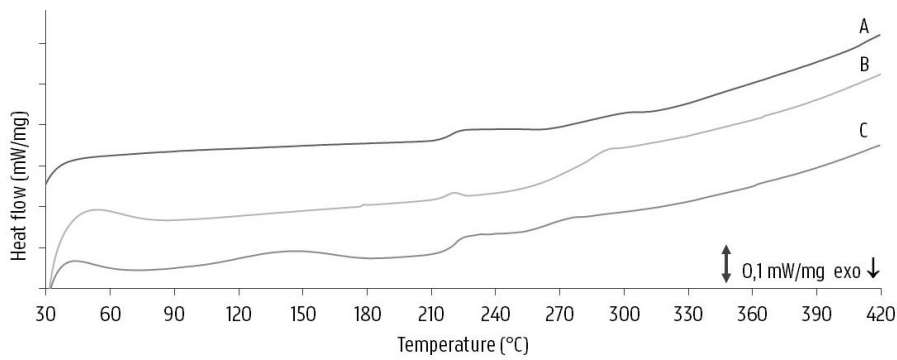
Figure 3-19: DSC measurement of the first heating run of (A) Virgin R5600, (B) Rotor milled R5600 to 80 µm and (C) Spray dried R5600 with parameter settings of RSM10
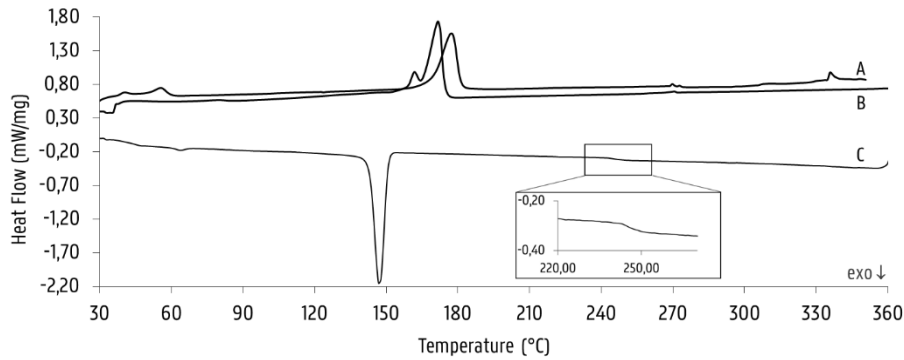
Figure 3-20: DSC run of cryogenically ball milled PPSU displaying (A) the first thermal run with an endothermic peak at 177,7 °C, (B) the second thermal run with a dual endotherm at 162,7 and 171,8 °C and (C) the cooling run with an exothermic peak at 142,7 °C and a glass transition temperature at 243,1 °C
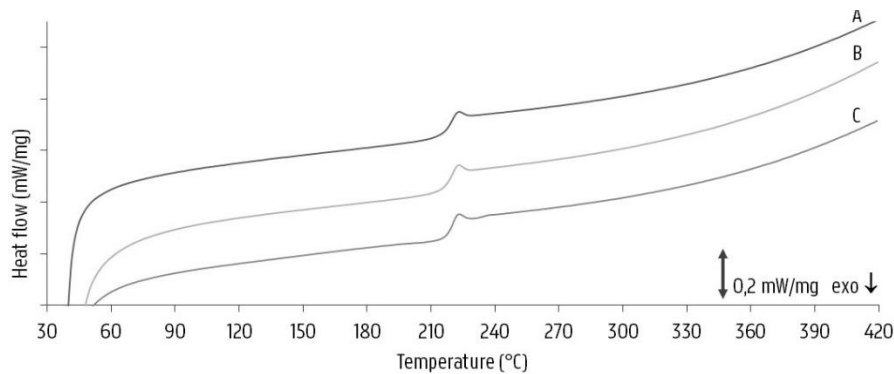
Figure 3-21: DSC measurement of the second heating run of (A) Virgin R5600, (B) Rotor milled R5600 to 80 µm and (C) Spray dried R5600 with parameter settings of RSM10

As PPSU is an amorphous polymer, we would expect the corresponding curves to be quite flat with only the glass transition temperature as a change in baseline. The glass transition temperature represents the reversible transition in the amorphous regions within fully amorphous or semi crystalline materials from a hard and relatively brittle "glassy" state into a molten or rubber-like state, as a critical temperature is reached. The thermograms of the first heating run show in that the different processing techniques have varying effects on the thermal behavior of PPSU.

The thermogram of the virgin PPSU in Figure 3-19,A exhibits a glass transition temperature of 219,2 °C. In the case of rotor milling in Figure 3-19,B a small endothermic peak is visible ranging from 271,6 °C to 323,1 °C having an area of 4,508 J/g. The peak disappears upon heating above the endotherm's offset and is no longer visible in the second heating run in Figure 3-21,B. The appearance of the endothermic peak suggests an influence imposed by the processing method on the polymer chains. Upon each milling step the material impacts on the rotor blades which fragments the material by stretching and shearing it apart. Furthermore, the particles experience an extra shearing by the inset sieve behind the rotor blade. This causes some orientation into the polymer chains which goes along with heat release and a lower entropy. As the polymer is heated up in the DSC the molecules regain enough thermal energy to return to their more entangled state through the entropic force in an endothermic process. This principle of frozen in entropic stress has previously been described by in literature [22], [23]. The samples produced by spray drying have undergone two thermal processes: first dissolution by reflux, then atomization and subsequent drying in the drying chamber at elevated temperature. Samples were dried in a vacuum oven at 50 °C for one day before analysis. Still, a remaining solvent peak can be seen at around 153 °C (boiling point of DMF) in Figure 3-19,C. Longer drying under vacuum is advised to remove remaining solvent. The T_g at 221,5 °C is also followed by a small endothermic peak ranging from 249,1 °C to 305 °C with an area of 1,479 J/g. This peak also disappears upon heating above its offset temperature and is no longer visible in the second heating run in Figure 3-21,C. It suggest also a form of orientation is imposed on to the polymer chains by the processing method.

The biggest deviation from the unprocessed PPSU is represented by the thermogram of the cryogenically milled polyphenylsulfone and is depicted separately in Figure 3-20. Here, from an irregular baseline an endothermic peak is seen at 177,7 °C with an area of 43,04 J/g in the first heating run (Figure 3-20,A). The glass transition is undiscernible in this first heating run or in the second. Determination of the T_g at 243,1 °C in the cooling curve depicted in the inset in Figure 3-20,C reveals a substantial increase in T_g suggesting severe degradation. Upon inspecting the second heating run the endothermic peak remains present displaying a dual endotherm peaking at 171,8 °C with an area of 50,58 J/g. The justification for these peaks remains unclear. As PPSU is an amorphous polymer it seems unlikely for the oligomeric

degradation products to form a crystalline fraction. Contamination by the industrial supplier seems more likely.

The second heating runs in Figure 3-21 show that, with the exception of the cryogenically milled powders (depicted in Figure 3-20), all thermal history imparted by the processing technique can be removed by heating implying no permanent influence of the processing technique on the thermal behavior of the material. Furthermore, the glass transition temperatures of all samples never deviates for more than 0,7 °C from the glass transition of the virgin material of 220,6 °C.

3. 4. 4. Powder flow

In this study, the HR of only the rotor-milled and cryogenically milled samples could be calculated, as the spray-drying and ball milling experiments were conducted on lab scale and did not produce enough quantity to allow HR to be determined. Furthermore, as particle size of the spray dried sample was fairly low, the electrostatic charging of the powders hampered measurements severely. Both grades of PPSU were processed via the described process stated above to ensure the material grade does not play a role in the communion process. Figure 3-22 depicts tapped and bulk density as well as the Hausner ratio determined for each fraction. The Hausner ratios are further summarized in Table 3-10.

Throughout the milling steps the Hausner ratio decreases for both grades ending up for the sieved fraction below the upper limit of good powder flowability. With every successful milling step the powder density increases as particle size decreases. Generally, for particles above 100 μm the weight of the particles tends to overcome the interparticle forces [24], [25]. This means that the bad powder density and resulting bad HR is mainly caused by the unfavorable morphology which hampers the particles when sliding over each other by mechanisms like mechanical interlocking. Furthermore, the irregular shapes and forms can cause larger pore volumes due to bad packing decreasing density even more. As the coarse powder is refined to 120 μm a large portion of the inconsistencies disappears resulting better packing and a strong decrease in HR. This can also be derived from the PSD measurements on R5600 summarized in Table 3-8: as the spread on particle size decreases as well, the resulting effect is better packing. Further milling to 80 μm and subsequent clean up by an extra sieving step further reduces the inconsistencies. Here, the interparticle forces such as Van de Waals and electrostatic forces are said to become dominant. Particle size is further decreased along with a finer spread on mean size. Packing of fine particles can be hindered by the formation of aggregates or agglomerates because of the relatively strong cohesive forces which increase the spread on the HR slightly. The cryogenically milled powder displays a different behavior. Exhibiting a powder density situated between that of the 500 to 120 μm milled powders of the R5000 and R5600 grades, a relatively high HR is measured of 1,44 ± 0,03. Previous PSD measurements revealed the mean diameter of the materials to be 75,62 ± 40,26 μm in

size. Particles approaching spherical shape and smoother surface tend pack in denser form [26]. Angular and edge shaped particles such as can be seen in Figure 3-13 for the cryogenically milled sample show more random packing resulting in a bulk structure with interparticle bridges and larger internal friction forces because of their rough surface [27]. As a result of their larger divergence from spherical morphology and smooth surface these effects play a detrimental role on the powder flow resulting in a larger Hausner ratio.
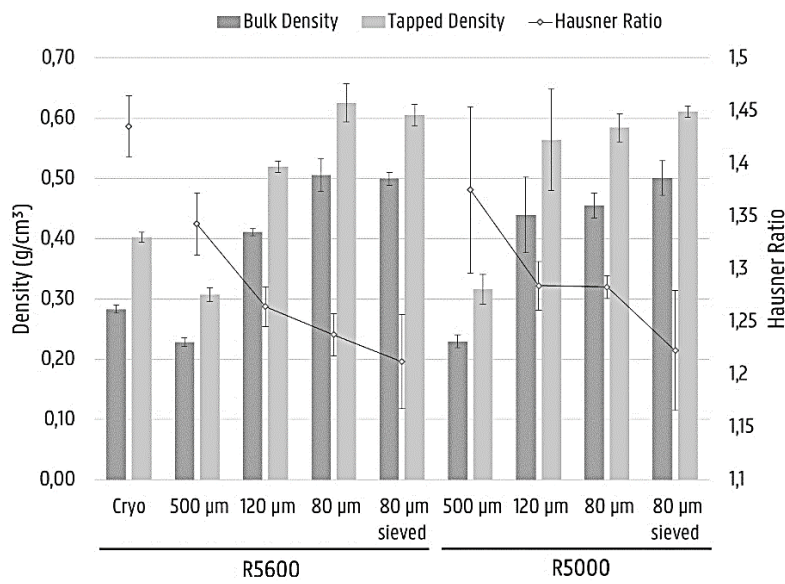
Figure 3-22: Tapped and bulk density with the respective Hausner Ratio of each fraction of the rotor milling process. Hausner Ratios are measured from the R5000 and R5600 grade as wel as the cryogenically milled R5600

Table 3-10: Hausner ratio measurements of the R5000, R5600 and cryogenically milled PPSU samples

Hausner Ratio Measurements	
Fraction	Hausner Ratio
R5000	
500 μm	$1,37 \pm 0,08$
120 μm	$1,28 \pm 0,02$
80 μm	$1,28 \pm 0,01$
80 μm sieved	$1,22 \pm 0,06$
R5600	
500 μm	$1,35 \pm 0,03$
120 μm	$1,26 \pm 0,02$
80 μm	$1,23 \pm 0,02$
80 μm sieved	$1,22 \pm 0,04$
Cryogenically milled R5600	
Cryogenic fraction	$1,44 \pm 0,03$

3. 5. CONCLUSIONS

This chapter was dedicated to the processing and characterization of PPSU pellets into powder form suitable for processing through SLS. By the use of spray drying PPSU pellets could be processed to powder form of which 22,3 % of the particles displayed apt morphology in terms of sphericity and roundness according to Power's scale. Particle size for this set of parameters came to 14,52 µm with a standard deviation of 11,47 µm. Though a Response Surface Model gas flow rate was found to be the crucial factor on particle size and to lesser extend the positive interaction of the material grade and the inlet temperature. Morphology was found to be greatly influenced by concentration. Gas flow rate and feed flow rate, inlet temperature and material grade were found to have negative interactions on morphology while gas flow rate and material grade, feed flow rate with material grade were found to have positive interactions on morphology. At the optimal processing conditions according to the model a mean particle size of 13,5 µm can be obtained of which 12,5% are of adequate sphericity and roundness. Further optimization of morphology could be done by changing gas flow rate and solution feed rate settings to an intermediate value of 162 mL/s and lowering the feed flow rate to its lowest value of 7,4 mL/min allowing a more harsh atomization condition. The inlet temperature remains unchanged at 220 °C in order to encourage the fast evaporation yet the lower viscosity grade is chosen to improve solute mobility during drying. Though this approach diminishes particle size by a small amount (particle size of 10 µm instead of 13,5 µm) it increases particle morphology by a fair amount (36,7 % particles with adequate sphericity and roundness instead of 12,5 %).

Through the use of a three step communition process using the Pulverisette 14 rotor miller the PPSU pellets were processed to a coarse powder which was refined in two sequential milling steps. The resulting powder was further refined by sieving at 80 µm resulting in a powder of which 62,82 % of the particles were of adequate morphology and sphericity having a mean particle size of 51 µm with a standard deviation of 14,31 µm.

The powders created were investigated on any change in thermal properties due to the processing method via DSC. Though spray drying and rotor milling both displayed some relaxation imparted by the processing method which manifested itself as a small endothermic peak. These influences were completely swept away after heating above the offset of these peaks. The cryogenically milled powder however displayed a prominent endotherm around 177 °C which manifested itself as a dual melting peak in the second heating run. The presence of these endotherms together with a sharp crystallization peak in the cooling run suggest the presence of a semi-crystalline component of other nature than the PPSU polymer.

Powder flow in the rotor milled samples improved with every processing step ending in good flowability after the final sieving step. The final powder displaying a HR of

1,22 ± 0,02 and 1,22 ± 0,06 respectively for the R5600 and R5000 grade. Again the cryogenically milled sample displayed different flow behaviour with a HR of 1,44 ± 0,03. The absence of spherical structures in this case causines a significantly higher HR.

3. 6. REFERENCES

[1]   C. M. Hansen, *Hansen Solubiliy Parameters: a user's handbook*, Second Edi. London: CRC Press, 2012.

[2]   Solvay Specialty Polymers, "Radel® PPSU, Veradel® PESU & Acudel® modified PPSU -Design Guide." [Online]. Available: www.solvay.com/en/binaries/Radel-PPSU-Veradel-PESU-Acudel-PPSU-Design-Guide_EN-227541.pdf.

[3]   Y. Liu, X. Yue, S. Zhang, J. Ren, L. Yang, Q. Wang, and G. Wang, "Synthesis of sulfonated polyphenylsulfone as candidates for antifouling ultrafiltration membrane," *Sep. Purif. Technol.*, vol. 98, pp. 298–307, 2012.

[4]   BÜCHI Labortechnik, "Operation Manual Mini Spray Dryer B-290."

[5]   C. Arpagaus, N. Schafroth, and M. Meuri, "Laboratory Scale Spray Drying Of Inhalable Drugs: A Review," *Best@Buchi*, no. 59, 2010.

[6]   R. Vehring, "Pharmaceutical particle engineering via spray drying," *Pharm. Res.*, vol. 25, no. 5, pp. 999–1022, 2008.

[7]   R. Vehring, W. R. Foss, and D. Lechuga-Ballesteros, "Particle formation in spray drying," *J. Aerosol Sci.*, vol. 38, no. 7, pp. 728–746, 2007.

[8]   M. J. Maltesen, S. Bjerregaard, L. Hovgaard, S. Havelund, and M. van de Weert, "Quality by design – Spray drying of insulin intended for inhalation," *Eur. J. Pharm. Biopharm.*, vol. 70, no. 3, pp. 828–838, Nov. 2008.

[9]   S. A. S. Institute, *JMP10: Design of Experiments Guide*. Cary, NC, USA: Sas Inst, 2012.

[10]   P. Walzel, "Influence of the spray method on product quality and morphology in spray drying," *Chem. Eng. Technol.*, vol. 34, no. 7, pp. 1039–1048, 2011.

[11]   J. Vicente, J. Pinto, J. Menezes, and F. Gaspar, "Fundamental analysis of particle formation in spray drying," *Powder Technol.*, vol. 247, pp. 1–7, 2013.

[12]   J. Elversson and A. Millqvist-Fureby, "Particle size and density in spray drying-effects of carbohydrate properties.," *J. Pharm. Sci.*, vol. 94, no. 9, pp. 2049–2060, 2005.

[13]   A. B. D. Nandiyanto and K. Okuyama, "Progress in developing spray-drying methods for the production of controlled morphology particles: From the nanometer to submicrometer size ranges," *Adv. Powder Technol.*, vol. 22, no. 1, pp. 1–19, 2011.

[14]   K. Cal and K. Sollohub, "Spray drying technique. I: Hardware and process parameters," *J. Pharm. Sci.*, vol. 99, no. 2, pp. 575–586, 2010.

[15]   A. I. Khuri and S. Mukhopadhyay, "Response surface methodology," *Wiley Interdiscip. Rev. Comput. Stat.*, vol. 2, no. 2, pp. 128–149, 2010.

[16]   J. Elversson and A. Millqvist-Fureby, "Particle size and density in spray drying—effects of carbohydrate properties," *J. Pharm. Sci.*, vol. 94, no. 9, pp. 2049–2060, 2005.

[17]   D. E. Walton, "The morphology of spray-dried particles a qualitative view," *Dry. Technol.*, vol. 18, no. 9, pp. 1943–1986, 2000.

[18]   B. Wei, S. Wang, H. Song, H. Liu, J. Li, and N. Liu, "A review of recent progress in preparation of hollow polymer microspheres," *Pet. Sci.*, vol. 6, no. 3, pp. 306–312, 2009.

[19]   B. Z. Shakhashiri, *Chemical demonstrations: A handbook for teachers of chemistry*, vol. 2. Univ of Wisconsin Press, 1985.

[20]   A. M. Díez-Pascual and A. L. Díez-Vicente, "Effect of TiO 2 nanoparticles on the performance of polyphenylsulfone biomaterial for orthopaedic

implants," *J. Mater. Chem. B*, vol. 2, no. 43, pp. 7502–7514, 2014.

[21]   U. Braun, U. Knoll, B. Schartel, T. Hoffmann, D. Pospiech, J. Artner, M. Ciesielski, M. Döring, R. Perez-Graterol, J. K. W. Sandler, and V. Altstädt, "Novel Phosphorus-Containing Poly(ether sulfone)s and Their Blends with an Epoxy Resin: Thermal Decomposition and Fire Retardancy," *Macromol. Chem. Phys.*, vol. 207, no. 16, pp. 1501–1514, Aug. 2006.

[22]   L. C. E. Struik, "Orientation effects and cooling stresses in amorphous polymers," *Polym. Eng. Sci.*, vol. 18, no. 10, pp. 799–811, Aug. 1978.

[23]   C. Bai, R. J. Spontak, C. C. Koch, C. K. Saw, and C. M. Balik, "Structural changes in poly (ethylene terephthalate) induced by mechanical milling," vol. 41, pp. 7147–7157, 2000.

[24]   A. B. Yu, J. Bridgwater, and A. Burbidge, "On the modelling of the packing of fine particles," *Powder Technol.*, vol. 92, no. 3, pp. 185–194, 1997.

[25]   R. Y. Yang, R. P. Zou, and A. B. Yu, "Computer simulation of the packing of fine particles," *Phys. Rev. E*, vol. 62, no. 3, pp. 3900–3908, Sep. 2000.

[26]   R. P. Zou and A. B. Yu, "Evaluation of the packing characteristics of mono-sized non-spherical particles," *Powder Technol.*, vol. 88, no. 1, pp. 71–79, 1996.

[27]   S. Ziegelmeier, P. Christou, F. Wöllecke, C. Tuck, R. Goodridge, R. Hague, E. Krampe, and E. Wintermantel, "An experimental study into the effects of bulk and flow behaviour of laser sintering polymer powders on resulting part properties," *J. Mater. Process. Technol.*, vol. 215, pp. 239–250, Jan. 2015.

Chapter 4

CASE STUDY: PROCESSING OF POLYSULFONE

This chapter encompasses the processing of polysulfone as a case study in which the techniques discussed in Chapter 2 are applied in order to create spherical PSU powders. The virgin material is processed and the powders characterized on their extrinsic and intrinsic properties.

4. 1. SPRAY DRYING

4. 1. 1. Polymer solubility

The Hansen Solubility Parameter (HSP) [1] for polysulfone and possible solvents are represented in Table 4-1. As apparent from the chemical resistivity represented in Table 2-1 (Chapter 2), PSU is soluble in aromatic, oxygenated and chlorinated hydrocarbons. Dissolution in oxygenated solvents can occur as spontaneously as by stirring at room temperature. Furthermore, the boiling point of the solvent must be taken into account in order to allow sufficient freedom for optimization of the processing parameters on the Buchi Mini Spray dryer B-290 [2]. For this reason DMF was chosen as suitable solvent for further experiments.

Table 4-1: Hansen Solubility Parameters of PSU and from possible solvents and anti-solvents for PSU. Data from [1]

	δ_{tot} (MPa$^{\frac{1}{2}}$)	δ_d (MPa$^{\frac{1}{2}}$)	δ_p (MPa$^{\frac{1}{2}}$)	δ_h (MPa$^{\frac{1}{2}}$)
Udel P1700 PSU	*23,6*	*19,8*	*11,2*	*6,2*
(N,N)-Dimethylformamide (DMF)	24,9	17,4	13,7	11,3
(N,N)-Dimethylacetamide (DMAc)	22,8	16,8	11,5	10,2
Dimethylsulfoxide (DMSO)	26,7	18,4	16,4	10,2
Phenol	24,1	18,0	5,9	14,9
Toluene	18,2	18,0	1,4	2,0
Chloroform	19,0	17,8	3,1	5,7

The maximum solubility of PSU was tested by gravimetric experiments as the minimum solvent weight necessary to dissolve a weighted sample of PSU. Dissolution occurred by stirring the PSU pellets at room temperature until completely dissolved. Gravimetrical experiments were replicated three times to minimize experimental errors. The maximum solubility of PSU in DMF was found at 18,18 wt.% or 0,21 g/mL. The deviation of the obtained solubility values was too small to measure.

Next, the solution viscosity was tested using a Thermo Scientific HAAKE viscotester 550 rotational viscosimeter according to ISO 3219 to see if the viscosity limit on the Buchi B290 mini spray dryer [3] is exceeded. Samples were conditioned at constant

temperature of 25 °C by a HAAKE K15 thermostatic bath and measured at 10 RPM using the MVI spindle. Each sample was measured at least three times. The results for the viscosity were then averaged. The concentration-viscosity plot is represented in Figure 4-1. From this curve it was clear that no solutions over 15 wt.% should be sprayed in order to maintain good jetting. In reality however, no solutions over 14 wt.% were sprayed due to the formation of threadlike structures in the drying chamber above this threshold. The critical parameters for spray drying were optimized a systematic one-factor-at-a-time (OFAT) approach. Best values were obtained using 12 wt.% solutions, which will be discussed in this work.

A PSU solution of 12 wt.% in DMF was heated to 150 °C and fed to the two-fluid nozzle with a nozzle orifice diameter of 2,0 mm. The feed flow rate was 7,4 mL/min. The prepared solution was heated to decrease the solution viscosity and hence increase the diffusion rate of the solutes during drying. The heated solution was then atomized by the two-fluid nozzle into the drying chamber where the droplets were dried by the use of dry air at 210 °C.
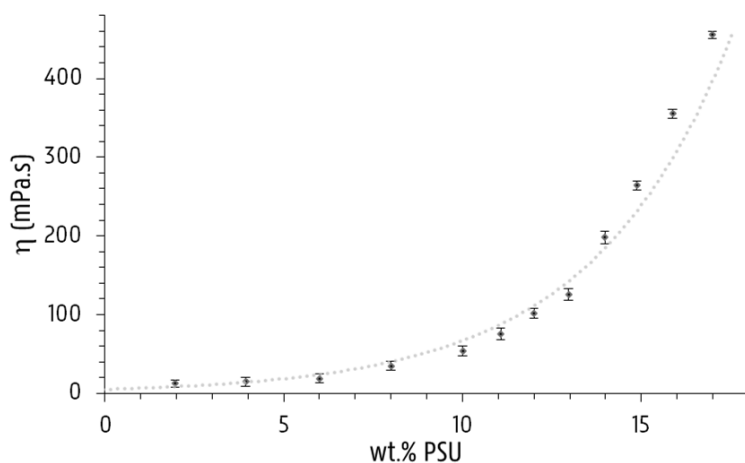
Figure 4-1: Viscosity measurements using a HAAKE Viscotester 550 to obtain a concentration-viscosity curve. Solutions higher than 15 wt.% exceed the viscosity limit for the spray drying apparatus and are therefore to be avoided.

4. 1. 2. Particle morphology

Upon processing the SEM micrographs of the spray dried sample (see Figure 4-2 and Table 4-2) it is clear that the lion's share of the particles produced by spray drying consist of microspheres. A small part of the particles exhibits either a collapsed or a string-like structure (see insets Figure 4-2). The latter can be caused by too high viscosity of the solution causing bad jetting behavior (see lower inset Figure 4-2) while the former has more to do with the drying phenomenon of high molecular weight compounds (see upper inset Figure 4-2). Polymer solutions generally exhibit a large Peclet number which is related to a low diffusion rate. Low diffusion rate of

the solute can result in skim or shell formation which in turn can collapse depending on the parameters used. Table 4-2 summarizes the mean particle size with standard deviation and particle morphology obtained via the optimal processing conditions dictated above.
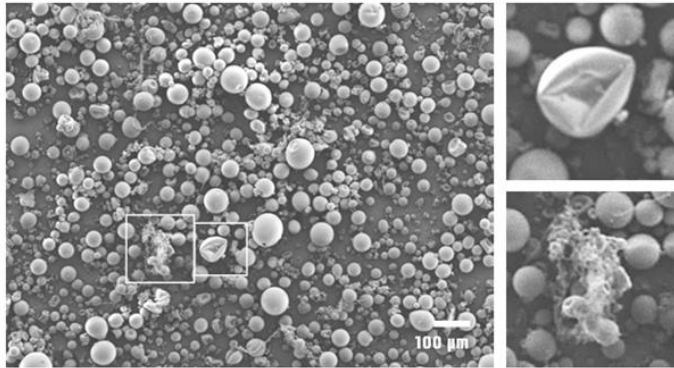
Figure 4-2: Micrograph depicting the sample obtained from the spray drying experiment using the two-fluid nozzle as atomizer

Table 4-2: Particle size distribution of the PSU powder obtained by spray drying together with the percentage spherical particles in the sample.

	Y_1		Y_2
Sample	Mean particle size (µm)	Standard Deviation (µm)	Particle morphology (%)
Spray Drying	26,10	12,80	71,01

4. 1. 3. Particle size

The corresponding PSD analysis on the micrograph in Figure 4-2 is presented in Figure 4-3. Though spray dried particles are predominantly spherical the mean particle size is only 26,1 µm with a standard deviation of 12,8 µm. The particle size curve is slightly skewed to the higher diameter range. The higher concentration that is possible to achieve with PSU in DMF in comparison to PPSU does lead to bigger microspheres yet their dimensions still fall below the favorable range of 45-90 µm. Further increase of the particle size is possible by increasing nozzle size and drying chamber which implies upscaling from the Buchi B290 to a larger model as larger droplet size is required to obtain bigger particles [4]. This is not possible with the current setup, yet ample amount of pilot scale models exist that could meet this demand.
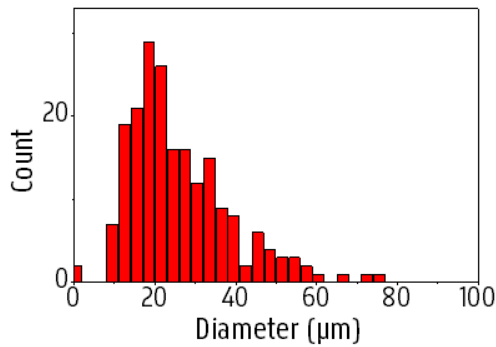
Figure 4-3: The particle size distribution of the spray dried PSU using the optimal processing parameters

4. 2. BALL MILLING

4. 2. 1. Particle morphology

When investigating the morphology of the powders obtained by the ball milling method in Figure 4-4, one can see that it does not meet the dimensional requirements which one looks for in SLS powders. After 10 minutes of ball milling (Figure 4-4, A) the PSU pellets had already been fractionated partly into a very fine powder. SEM investigation of this fine powder revealed that it is neither spherical nor of the required size (see Table 4-3). Instead angular structures were apparent, which was to be expected with this technique as the material is more prone to brittle fractions. Unlike with sPS (see Chapter 5), no flattening of the particles or agglomeration occurs. Particles readily fractionate into a fine powder. Further milling only increases the amount of fine powder while diminishing the size of the larger pellets. After one hour, a large diversity in particle sizes still exists, showing almost unfractionated pellets next to very fine powders (Figure 4-4, B).
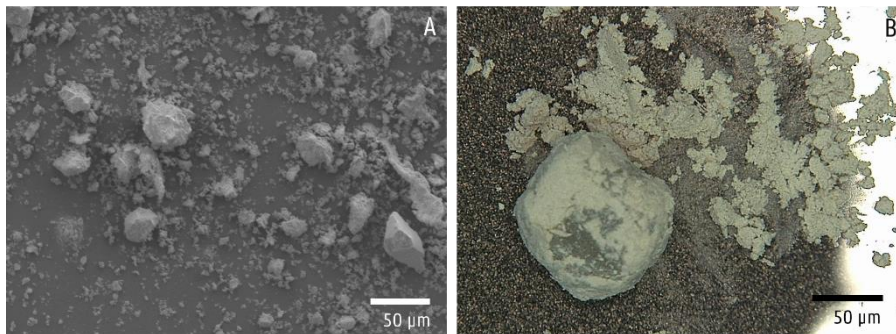
Figure 4-4: (A) micrograph of the fine powders reveals too small particles even after only 10 minutes of milling and (B) Microscopic image of The PSU powder after 1 hour of milling.

4. 2. 2. Particle size

After 1 hour of ball milling the PSU pellets, two general groups of powder fractions are formed: a large group consisting of nearly unfractionated pellets and a group of finely pulverized material (Figure 4-4, B). Particle size analysis of the fine fraction after one hour is displayed in Figure 4-5 (right) and summarized in Table 4-3. It reveals the particles to be already too small for the use of SLS with a mean particle size of 0,87 µm and standard deviation of 1,30 µm. Therefore, new milling runs were performed and samples were taken at shorter time intervals (10 minutes). However, inspection of these samples (Figure 4-5, left) reveal that even after 10 minutes pellets pulverize partially into fine powders of unfitting morphology with mean particle sizes of 1,72 ± 1,49 µm. Possibly the high mechanical stress the material is subjected to in the ball mill causes the polysulfone to pulverize with brittle fractures into fine powders. Further milling (sampling after every 10 minutes for 4 hours) caused the remaining unfractionated material to pulverize with the same result. Additionally the powder started to discolor with time as seen by the frequent sampling suggesting degradation. It is widely known that ball milling is prone to induce degradation in polymeric material [5], [6]. This will be further discussed in section regarding the DSC and GPC results.
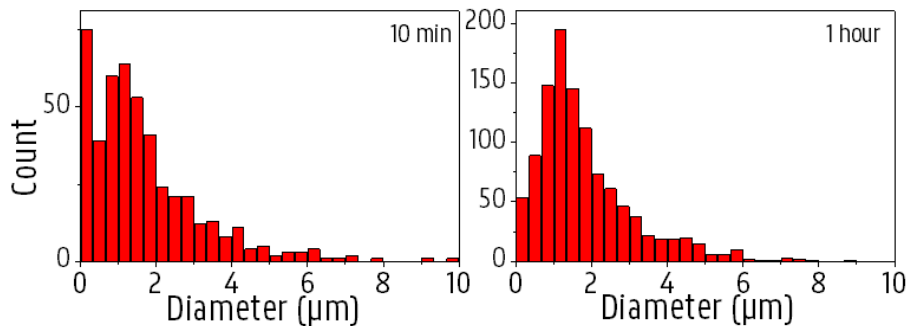
Figure 4-5: Particle Size Distributions of the ball milled samples. Left: fine powders investigated after 10 minutes of milling. Right: PSD taken of the sample after 1 hour of milling

Table 4-3: Particle size distribution of the PSU powder obtained by ball milling for 1 hour and 10 minutes respectively. The fine powder fractions are always investigated on PSD. These are denoted by BM1hour[a] together with BM10min[b].

	Y_1		Y_2
Sample	Mean particle size (µm)	Standard Deviation (µm)	Particle morphology (%)
BM1hour[a]	0,87	1,30	0
BM10min[b]	1,72	1,49	0

4. 3. ROTOR MILLING

4. 3. 1. Particle morphology

Like previous materials, the PSU pellets are subjected to the three-step milling process. Micrographs of the samples undergoing each of the steps are depicted in Figure 4-6.

Subjecting PSU pellets to this three-step refinement process resulted a steady increase in spherical morphology (see Table 4-4). Where the coarse powder practically does not display any sphericity, spherical structures can be found already in the first refinement step at 120 µm. Further refinement causes extra fractionation of the material imposing finer spherical particles and less inconsistencies with 26,52 % particles of good morphology. Finally, the extra sieving step removes the lion share of the inconsistencies leaving a good end product of 38,99 % good spherical particles. The particle size of these powders leaning more to the aspired range of 45-90 µm. Particle size distributions are noted in Table 4-4. Moreover, when observing the rotor milled sample no discoloration was noticed with every of the subsequent processing steps. The adjusted cooling procedure may play a role in this regard.

The increase in sphericity by each refinement step and the rough structures of the coarse powders can be explained by the same reasoning as elaborated in Chapter 3 for the rotor milling of PPSU.

When the energy input provided by the high speed rotating rotor blade is not sufficient enough to exceed the energy of break, elastic (reversible) deformation followed by plastic (irreversible) deformation will occur. If the particle in question escapes the mechanical deformation in time by passing through the inset sieve elastic unloading will occur with permanent deformations in the particle at hand. This can be seen by the rough angular structures in the coarse powders and the first refinement step. For bigger particles dissipation of energy can occur more easily leading to more deformation which does not always result in fragmentation, hence the large diversity in structures apparent in the respective micrographs. Smaller particles exhibit a smaller surface area, less dissipation of energy can occur and fragmentation is supposed to be more dominant in this case. Contrary to ball milling an additional shearing force is present in rotor milling between the rotating blade and sieve ring. Particles endure an extra deformation by the rotating motion of the rotating blades causing the particles to round off. As PSU is of the same family of polymers as PPSU yet has a lower T_g than PPSU ($T_g = 189$ °C for PSU vs. 220 °C for PPSU) one could suggest that PSU is more sensitive to deformation by the milling process resulting in a higher sphericity than PPSU.

Table 4-4: Particle size and particle morphology of the material going through each of the steps of the rotor milling sequence

	Y$_1$		Y$_2$
Sample	Mean particle size (µm)	Standard Deviation (µm)	Particle morphology (%)
RM500	302,82	226,97	0
RM120	100,32	56,20	17,00
RM80	58,80	37,46	26,52
Sieved	51,80	15,20	38,99
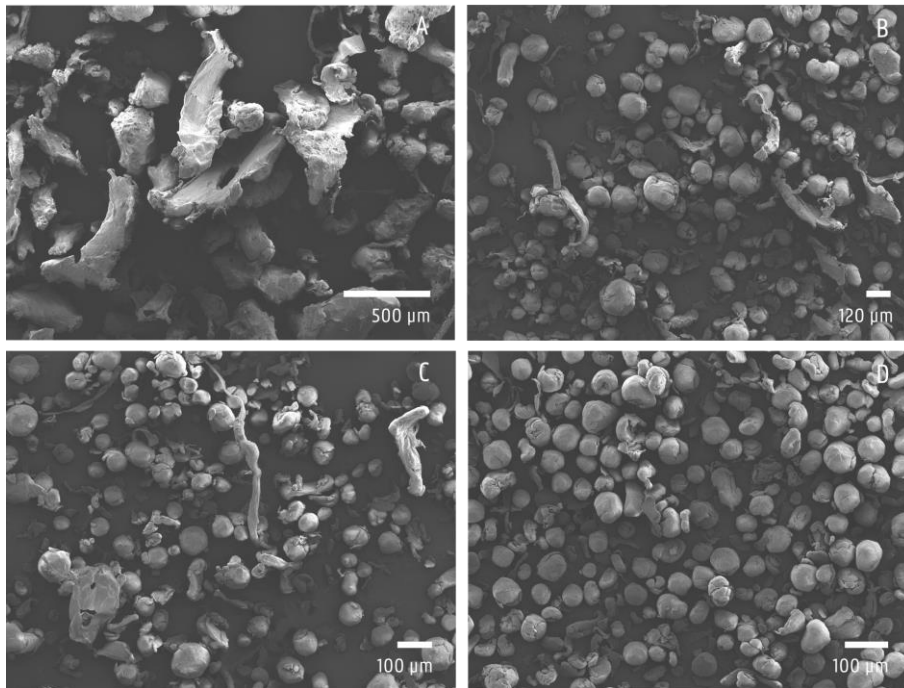
Figure 4-6: PSU powder undergoing the three step pulverization process with additional sieving step: (A) Milling of PSU pellets into a coarse powder at 500 µm, (B) first refinement step by milling the coarse powder at 120 µm, (C) second refinement step by further pulverization of the refined powder at 80 µm and (D) the final powder after additional sieving at 80 µm removing any leftover inconsistencies.

4. 3. 2. Particle size

PSD performed on the powder of the first refinement step revealed a mean size of 302,82 µm with a standard deviation of 226,97 µm. The large variation is understandable as this first milling step only transforms the pellets into a coarse powder of various sizes. Further refinement reduced the size of the particles while preserving the spherical form. Milling at 120 µm reduced the size of the powders to 100,32 µm with a smaller standard deviation of 56,20 µm. The last milling step further decreases particle size to 58,80 ± 37,46 µm. Though this value is already within desirable range, the larger standard deviation is caused by the long inconsistencies visible in Figure 4-6 and by the tail of the PSD in Figure 4-7. For this reason a sieving step is introduced to eliminate these inconsistencies by isolating them from the bulk powder. Particle size investigation of the final powder revealed a mean size of 51,8 µm with a standard deviation of 15,2 µm, which is ideal for sintering experiments. PSD values are summarized in Table 4-4 and depicted in Figure 4-7. Upon sieving one can clearly see that the tail present in the 80 µm fraction is no longer visible and the PSD is more normally distributed around 51,8 µm.
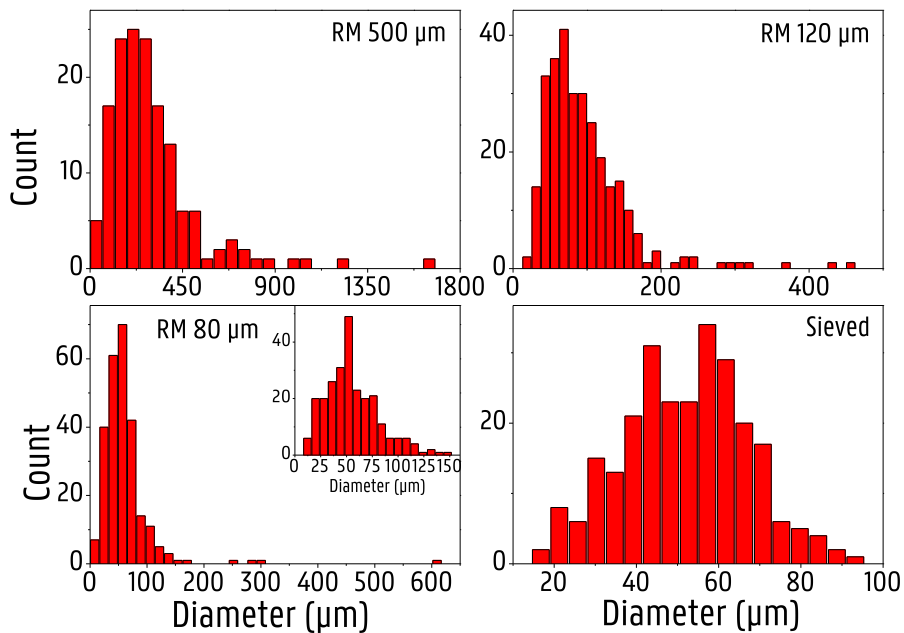
Figure 4-7: Particle Size Distribution of the rotor milled PSU going through the three step refinement process with additional sieving. The inset in the 80 µm fraction displays the PSD of the 80 µm fraction without the tail which is present because of the inconsistencies.

4. 4. MATERIAL CHARACTERIZATION

4. 4. 1. GPC measurements

Samples investigated on change in molecular weight concerned the ball milled sample which was left to mill for 10 minutes, the rotor milled sample going through the three-step communition process, the spray dried sample at best parameter settings (described above) and the unprocessed PSU as a reference sample. The weight average molecular weight, number average molecular weight and polydispersity were statistically compared against the unprocessed PSU for significant differences. These are described in Table 4-5. No significant differences in weight or number average molecular weight for the rotor milled and spray dried samples were found when compared to the unprocessed polysulfone suggesting no significant degradation phenomena due to the processing methods. The slight change in M_n and M_w for the spray drying method could indicate that spray drying is more prone to degradation as it shows the largest change in molecular weight compared to the unprocessed polymer. This was to be expected as the PSU undergoes two thermal treatments in order to be processed to powder form. Firstly by dissolving by reflux and secondly by the spray drying process. Although this is a very small change (approx. 2% and 3% for weight and number average molecular weight respectively) this could be suggesting a small amount of crosslinking due to degradation that has occurred. As for the ball milled sample; dissolving the sample material for analysis through GPC seemed not possible, pointing towards severe crosslinking through degradation upon ball milling.

The degradation process of polysulfone materials has been extensively studied since their discovery. Polysulfones tend to degrade by heteroatom bridge cleavage causing the material to further degrade by random chain scission, crosslinking and possibly the β-scission of the isopropylidene moiety [7]–[12]. Possible degradation paths of polysulfone are given in Figure 4-9. In the case of the ball milled sample this premise is justified by the fact that the polymer was unable to dissolve in the eluent for GPC measurements, the discoloration seen while ball milling and by DSC measurements discussed in section 4. 4. 3.

Table 4-5: GPC measurements of unprocessed PSU compared to the processed samples using rotor milling, spray drying and ball milling

GPC Measurements			
Sample	M_w^1 (g/mol)	M_n^2 (g/mol)	Polydispersity[3]
Unprocessed PSU P1700	60318 ± 283	29805 ± 146	$2,02 \pm 0,40 \times 10^{-2}$
Rotor Milling	60293 ± 217	30298 ± 1272	$1,99 \pm 0,11$
Spray Drying	61662 ± 110	30804 ± 1769	$2,01 \pm 0,09$
Cryogenic Milling	n.a.	n.a.	n.a.

[1] Weight average molecular weight; weighted molecular weight according to weight fractions

[2]   Number average molecular weight; total weight of the sample divided by the number of molecules in sample

[3] Polydispersity; ratio of M_w/M_n as a measure of heterogeneity of sizes of molecules in the sample

[4] n.a. = not applicable
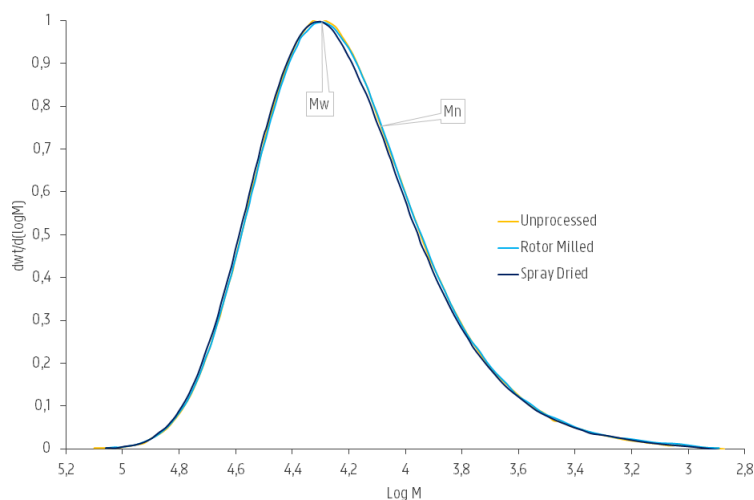
Figure 4-8: Molecular weight distribution derived from the elution profile of unprocessed PSU, rotor milled and spray dried PSU. The ball milled PSU was unable to dissolve in the eluent for analysis. The M_w and M_n values are displayed in Table 4-5.
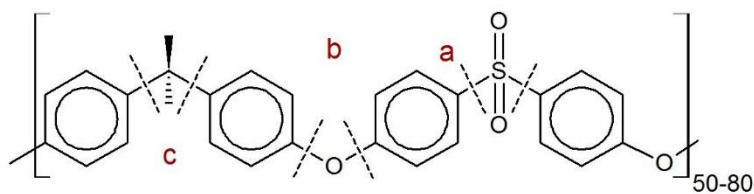
Figure 4-9:Possible degradation mechanisms of polysulfone represented by dotted lines: (a) crosslinking by phenylation of phenyl radical formed by cleavage of the C-S bond, (b) intramolecular phenylation by hydrogen abstraction by the phenylradical, (c) β-scission of isopropylidene radical following H-abstraction [7], [9], [11]

4. 4. 2. TGA measurements

The thermal stability of the polysulfone polymer was investigated using TGA measurements. These were performed under nitrogen atmosphere with a heating rate of 10 °C/min to a maximum temperature of 850 °C. From the measurement shown in Figure 4-10 one can derive the PSU to be thermally stable up to 475 °C. After this degradation occurs; first by cleavage of the heteroatomic bonds (C-S, C-O) followed by C-C bond cleavage. Then, a slow second decay can be seen noting the slow decomposition of char produced in the first decay step. Hence, it is advised for further analysis not to exceed 475 °C. A residual mass of 31,06 % is visible after the thermal run indicating a fair amount charring to occur due to the oxygen and aromatic containing backbone [12], [13]. The decomposition of this char occurs slowly over a wide range of higher temperatures. The derived degradation temperature was used later on in DSC measurements. The data furthermore can be valuable for the processing of PSU in later sintering experiments in regards to the setting of the laser parameters.
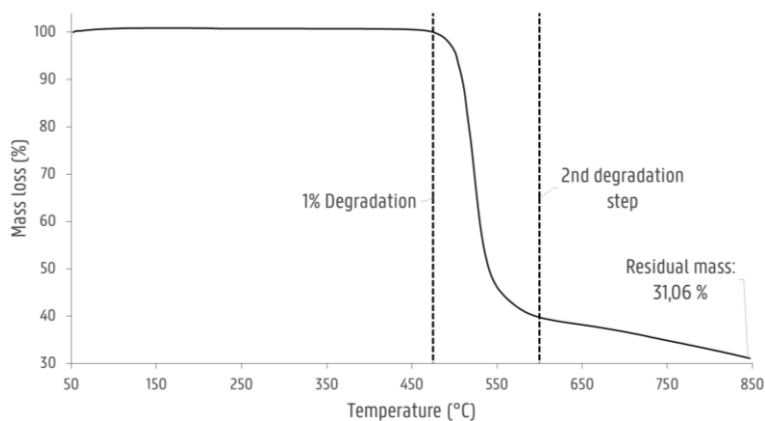
Figure 4-10: TGA curve of unprocessed PSU in order to determine the point of 1% degradation which should not be crossed to avoid degradation. Degradation occurs in two steps, leaving behind a marge amount of residual mass

4. 4. 3. DSC measurements

The thermal properties of the produced powders were analyzed using the same thermal run as performed on PPSU. Samples were subjected to a heating rate of 10°C/min and heated from room temperature to 450 °C under nitrogen atmosphere. Both first and second heating run were analyzed in order to examine the influence of the processing method on the thermal properties of the material. The investigated samples never deviated more than 1,2 % in weight compared to the virgin materials' weight (25,8 mg). The thermograms of the first and second heating run on all samples are depicted in Figure 4-11 and Figure 4-12, respectively.

Like PPSU, PSU is an amorphous polymer leading to expect no change in the baseline of the thermogram except for the glass transition temperature. However, as is visible in the first heating run, the processing methods impart their influence on the thermal behavior of the polymer material. With the exception of ball milling, these changes are reversible as the normal thermal profile of PSU is regained in the second run. Virgin PSU (Figure 4-11,C) exhibits a glass transition temperature at 189 °C followed by enthalpic relaxation. In the case of high-energy ball milling (Figure 4-11,D) the glass transition temperature is almost indistinguishable, appearing at 196 °C. The inset of Figure 4-11 depicts this by the change in the second derivative of the baseline curve. Upon reheating, this glass transition remains sternly diminished and is almost indiscernible. This stern diminishment of the T_g is indicative of severe of degradation occurring during processing of PSU. Mechanical milling could conceivably cause chain scission in the polymer molecules with the creation of free radicals, which may then react with other polymer strains causing crosslinking. Though chain scission should cause a decrease in T_g, the grafting or crosslinking process should increase its value. Together with the fact that the milled powder was unable to be dissolved for GPC measurements and the discoloration noticed during each sampling step, degradation by crosslinking seems a logical explanation. Furthermore, a broad endothermic peak is observed which exhibits a maximum at 359 °C. The appearance of this endothermic peak in the thermogram has not yet been fully explained. Bai et. al. [14] describe a biaxial stretching and orientation of the polymer chains that occurs due to the compressive and shearing deformation of the collisions with the balls and crucible of the ball mill. This causes some orientation into the polymer chains which goes along with heat release and a lower entropy. As explained in the previous chapter the polymer is heated up in the DSC the molecules regain enough thermal energy to return to their more entangled state through the entropic force in an endothermic process. This ordering of the polymer chains can be seen as the phenomenon of frozen in entropic stress [15] and could be an explanation for the high temperature endotherm. The disappearance of the endothermic peak in the second heating run further confirms this hypothesis of the frozen in orientation of the chains which relaxes upon heating and becomes fully amorphous again with adequate thermal energy.
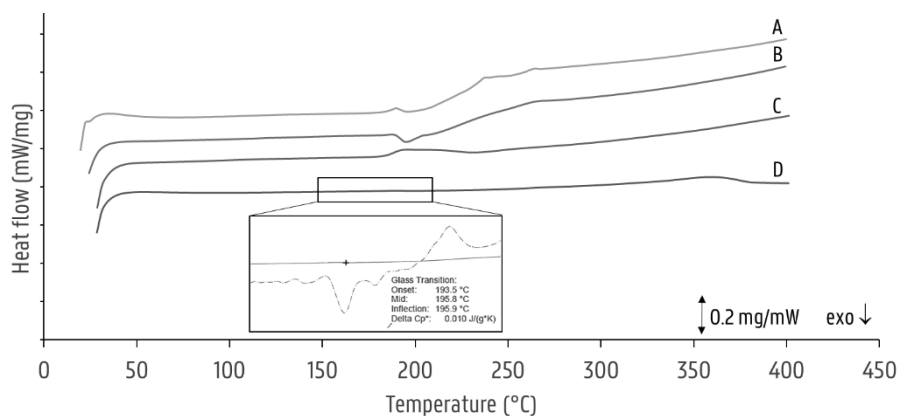
Figure 4-11: Thermograms representing the first heating run of the processed samples: (A) Spray dried, (B) rotor milled going through all processing steps, (C) Unprocessed and (D)ball milled for 10 minutes
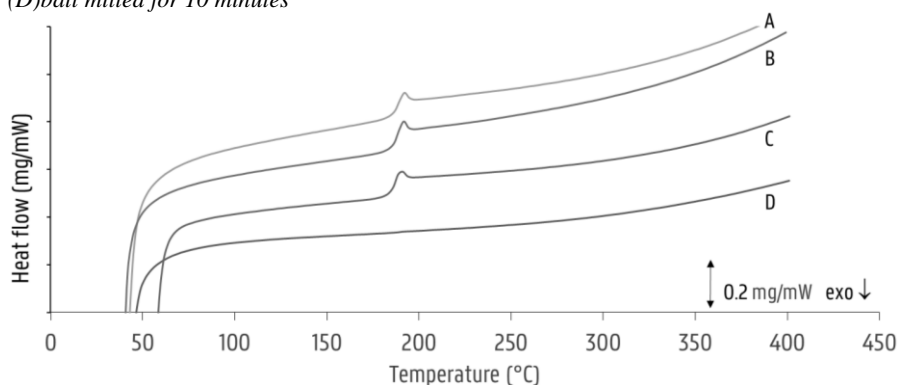
Figure 4-12: Thermograms representing the second heating run of the processed samples: (A) Spray dried, (B) rotor milled going through all processing steps, (C) Unprocessed and (D)ball milled for 10 minutes

A different trend is found when looking at the rotor milled PSU (Figure 4-11,B). A clear T_g at approx. 189 °C is visible followed by a slight endothermic peak going from 210 °C to 236 °C. The peak, as was the case with ball milling, disappears upon heating above the endotherm and reanalyzing in the second heating run (Figure 4-12,B) and suggests orientation imposed by the processing method on to the polymer chains. During processing the polymer chains of the material stretch out when the pellets of powder impact on the rotor blades and get further sheared apart between the blades and the sieving ring. Upon the first heating run an endothermic peak is then visible ascribed to the relaxation of the chains. Upon the second run the T_g remains visible and stable indicating no severe degradation occurring in the process.

With spray drying the PSU was first dissolved, then atomized and dried to form spherical particles. Samples were consequently dried for two days in a vacuum oven

at 50 °C in order to remove any residual solvent. A clear T_g is visible at 188 °C with two small endothermic peaks at 237 °C and 262 °C in the first heating run (Figure 4-11,A). These peaks disappear upon heating above their offset temperature and also suggest a form of orientation imposed on to the polymer chains by the processing method through the high shearing rates the polymers experience while jetting into the drying chamber. The second heating curve shows a clear T_g again at 189 °C in accordance with the unprocessed PSU (Figure 4-12,A).

4. 4. 4. Powder flow

A HR test was performed on the produced powders by gravimetrically measuring the densities of the powders at ambient conditions using a graduated cylinder and powder funnel. After measuring the bulk density, the tapped density was determined by subjecting the powder to a sequence of taps on the baseplate of a Retsch Vibratory Sieve Shaker AS 200 digit for 60 seconds at 60% of its maximal amplitude. The powder samples were measured over 10 times after which the values are statistically evaluated and outliers removed. The HR of the rotor milled samples could only be calculated as the spray drying and ball milling experiments were conducted on lab scale and did not produce enough quantity to allow HR to be determined. Furthermore, the particle size of the samples available was too small enabling electrostatic buildup hampering the measuring and dispensing of the powders into the funnel.

Figure 4-13 depicts the Hausner ratio's measured of each of the rotor milled fractions. With each milling step, the density increases while the HR decreases reaching a final HR value of 1,21 (see Table 4-6) for the sieved fraction. This indicated that bot the packing of the powder and powder flowability is more favorable with each processing step. Though the final sieving step did not affect powder flowability substantially it is done to improve powder size and dispersion and the powder density.
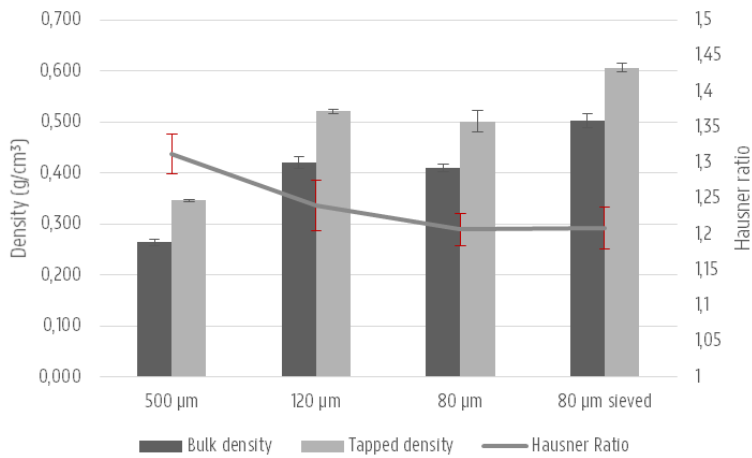
Figure 4-13: Hausner ratio of the rotor milled powder through each processing step. HR is calculated from the ratio of the tapped and bulk density depicted in graph

Table 4-6: Hausner Ratios calculated from the density measurements of each rotor milling processing step

	Powder flow			
	500 µm	120 µm	80 µm	80 µm Sieved
Hausner Ratio	1,31 ± 0,03	1,24 ± 0,04	1,21 ± 0,02	1,21 ± 0,03

4. 4. 5. Particle density

In addition to the bulk density of the produced powders, the true density of particle density was determined qualitatively through FIB-SEM measurements. Next to morphology and size, true density is a particle property which is crucial for the SLS process as dense particles would result in less porosity of the produced parts. FIB-SEM was performed on a FEI Nova 600 Nanolab Dual Beam FIB-SEM on both spray dried as rotor milled samples to investigate particle density by selectively ion milling material of the particle away. To this end particles were first sputter-coated with Au for SEM imaging after which the area of interest was sputtered with Pt to protect the top surface of the area of interest from damage and unwanted milling during preparation.

Due to the low diffusional flow of these high molecular weight polymers, the materials are prone to dry out in the spray drying process with the formation of a shell at the droplet surface. Depending on the evaporation rate, the shell achieves either a critical thickness to support itself or remains too thin and flexible causing it either to move with the receding droplet surface and collapse or to inflate due to pressure buildup by evaporation [16]–[19]. Knowledge of the thickness of the shells achieved in the spray drying process is therefore very valuable and should be obtained before proceeding to upscale-experiments.

The micrographs portrayed in Figure 4-14 clearly display the rotor milling process (micrographs A & B) delivering dense particles whereas the spray drying process unfortunately delivers thin shelled particles (micrographs C &D). Though these spherical particles are said to have achieved a critical thickness stable enough to sustain itself the vast majority of the particle remains hollow. Further investigation of the micrographs reveals the shell thickness not to exceed 1 µm. This hollow interior in turn imparts a low bulk density of the powder, which is unfavorable in laser sintering as it introduces defects into the layers. These unique properties however might be applicable in other fields requiring lightweight materials for thermal insulation or in the research field of microencapsulation, pigmentation, opacifyers, damping materials etc… [20]
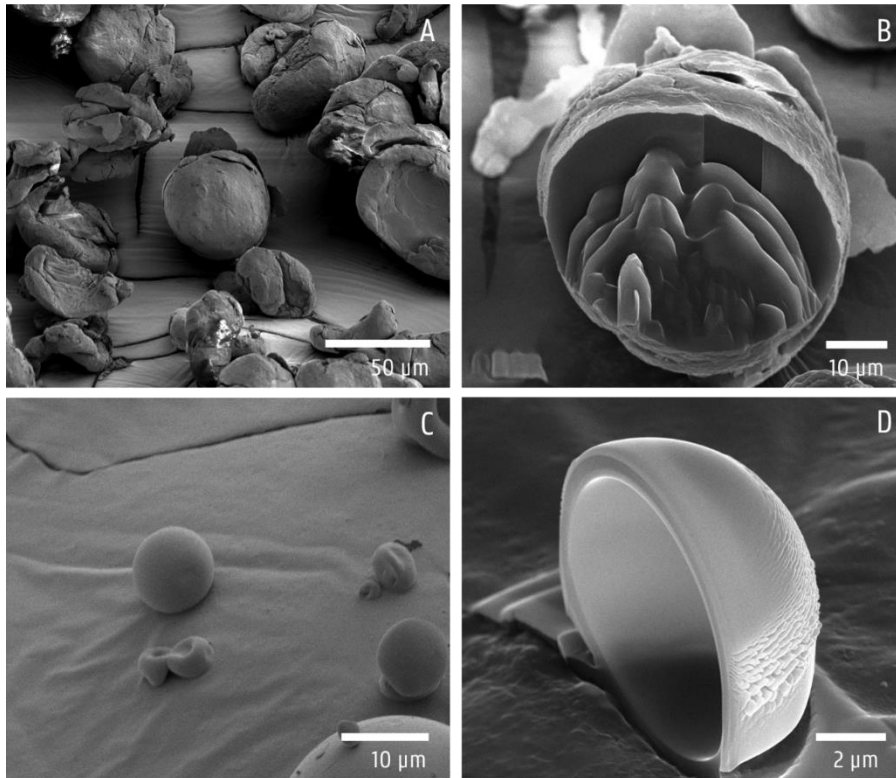
Figure 4-14: FIB-SEM micrographs of a rotor milled particle (A) and its crosssection (B) and a spray dried particle (C) and its crosssection (D)

4. 5. SINTER TESTS AT KU LEUVEN

The investigated powders were further tested at the University of Leuven for the powder flow quality by use of a lab-scale powder spreader device [21], material shrinkage and sinter quality. For a more detailed discussion of this part I would gladly refer to the work of the Additive Manufacturing Research Group and Soft Matter Rheology and Technology department at the KU Leuven[1,2] as this is their niche and core task in the PolyForce project. As PSU is amorphous no shrinkage step is present (except for thermal shrinkage) contrary to the case for the semi-crystalline polymers. Figure 4-15 depicts the change in specific volume for PSU as described in the datasheets versus the measured values of PA 2200 and PA Orgasol at KU Leuven. PSU clearly experiences a gentler decrease in specific volume upon cooling than is the case for the PA polymers. The material remains however viscous upon heating necessitating a higher laser energy to overcome the viscosity of the material. Figure 4-16 illustrates the large temperature gap that has to be overcome between the glass transition temperature (dotted line) and the zero shear viscosity below 10000 Pa.s.
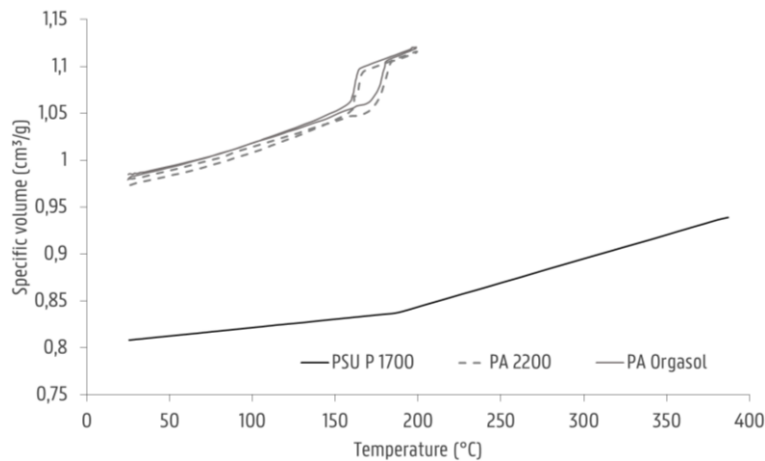
Figure 4-15: Specific volume measurements of PA Orgasol and PA 2200 [22] *versus PSU P 1700* [23]

---

[1] University Leuven, Additive Manufacturing Research Group led by prof. dr. ir. Jean Pierre Kruth and prof. dr. ir. Brecht Van Hooreweder

[2] University Leuven, Soft Matter Rheology and Technology (SMaRT) led by prof. Peter Van Puyvelde and prof. Paula Moldenaers
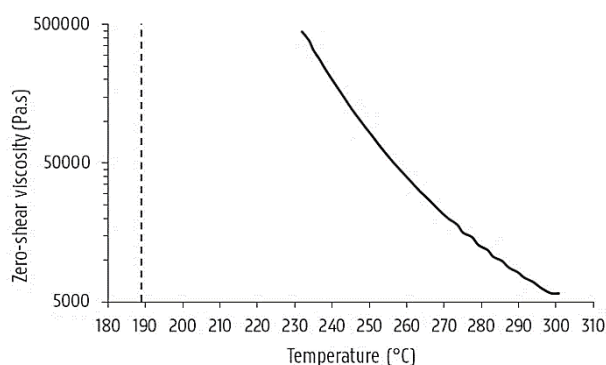
Figure 4-16: Zero-shear viscosity according of PSU P1700 (full line) in function of temperature. The dotted line represents the glass transition temperature of PSU. Curve courtesy of KU Leuven.

As the glass transition of the polymer is quite high (T_g of 189 °C, see section 4. 4. 3. DSC measurements), the bed temperature is set at its maximum stable temperature of 195 °C and the laser beam's energy density is changed systematically to determine the settings for optimal coalescence.

During initial tests, single layer experiments were performed on a DTM Sinterstation 2000 equipped with a CO_2-laser (Gaussian profile with diameter 450 µm). The process happens under N_2-atmosphere with up to 5.5 % O_2. These revealed limited warpage, the extent of which increasing when insufficiently preheating. Burning and sacking remained to a minimum as well only showing some discoloration at the edges. These findings allowed for the production of multilayer parts. However, preliminary experiments on multilayered structures revealed limited coalescence and poor consolidation resulting in a sponge like structure. While by increasing energy density a decrease in pore volume was observed; external voids remained considerably present (see Figure 4-17). As a result, mechanical properties derived from tensile tests on these tensile bars sintered from the PSU powder remain far under their potential. The tensile properties of the single layer structure are represented in Figure 4-17 next to the SEM micrograph of a single layer. These explain the lower values obtained during initial testing. The multilayer tensile bars are represented in Figure 4-18. Nevertheless, the obtained sintered material might be suitable for other types of applications, e.g. in the domain of membrane separation were porosities as such are a must.

	Single layer specimen	
	UTS (MPa)	EAB (%)
PSU	14,94 ± 0,51	0,04 ± 0,01
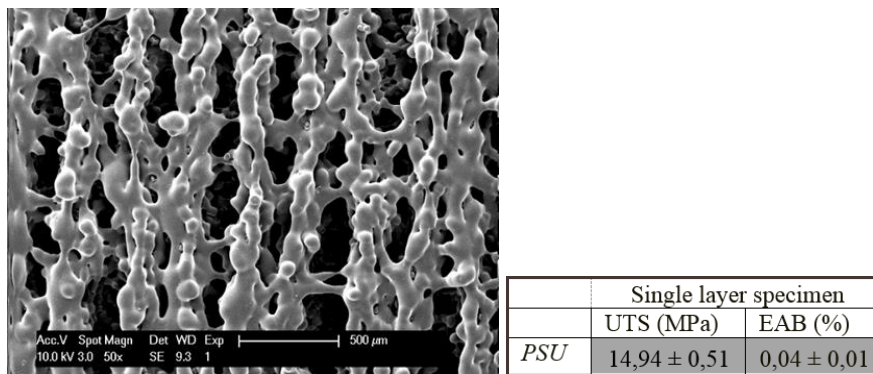
Figure 4-17: Micrograph of single layer part from PSU provided by KU Leuven revealing the sponge like structuretogether with the mechanical properties characterized at KU Leuven

Figure 4-18: Sintered parts from PSU powder provided by KU Leuven.

4. 6. CONCLUSIONS

Polysulphone pellets were processed into powder form for the use in Selective Laser Sintering. Of the processing methods tested, rotor milling and spray drying displayed the best results.

Rotor milling could successfully be used in a three step refinement process to produce particles of desired size (51,8 ± 15,2 μm), morphology and density. The relatively spherical particles exhibited good powder flow behavior reflected in a Hausner Ratio of 1,21.

In the case of spray drying particles were prominently spherical yet particle size deemed slightly lacking (26,1 μm ± 12,8 μm). Moreover, the technique resulted in spraying smooth spherical particles consisting of thin shells of not more than 1 μm thickness. Further increase of particle diameter was hindered by the dimensions of the laboratory spray dryer and extra optimization in this regard is necessary. This problem can be solved by the use of a pilot scale spray dryer with larger drying chamber and bigger nozzle diameter (see Chapter 6). Further research regarding increasing the shell thickness of the spheres could prove very valuable and could be done through the adaptation of the response surface model used in Chapter 3 by adding the shell thickness as a response value that needs to be optimized.

Ball milling proved not to be a suitable method of processing the PSU as severe degradation occurred. Additionally particles were angular in shape and well below the aspired size range (1,7 ± 1,5 μm).

GPC measurements revealed no significant degradation to occur in both spray drying and rotor milling processes. All processing methods imparted some orientation in the polymer chains causing extensive enthalpic relaxation visible in the DSC measurements. These endothermic peaks should be taken into account when setting the sintering parameters as the powder bed will most likely not exceed these temperatures but remain below the glass transition temperature of 189 °C. In the case of ball milling a clear shift in glass transition temperature was observed and an endothermic peak in the high temperature region. As this peak disappears in the second heating run it suggests a form of reversible orientation imparted by the communition method.

Actual sinter tests on the rotor milled powder were performed at the KU Leuven confirming the suitability of the produced powders for laser sintering applications through single layer tests. Absence of extensive warpage allows multilayer tests to be performed in the form of tensile bars for mechanical characterization. However due to extensive porosities in the parts, the mechanical properties of the parts so far remain below their potential and further optimization in sintering parameters remains

necessary in this regard to achieve mechanical properties closer to that of the virgin material.

4. 7. REFERENCES

[1]   C. M. Hansen, *Hansen Solubiliy Parameters: a user's handbook*, Second Edi. London: CRC Press, 2012.

[2]   BÜCHI Labortechnik, "Operation Manual Mini Spray Dryer B-290."

[3]   C. Arpagaus, N. Schafroth, and M. Meuri, "Laboratory Scale Spray Drying Of Inhalable Drugs: A Review," *Best@Buchi*, no. 59, 2010.

[4]   Buchi and GEA Niro, "Scale-up from the Buchi Mini Spray Dryer B-290 to the Niro Mobil Minor," *Information Bulletin*, 2008. [Online]. Available: http://static1.buchi.com/sites/default/files/downloads/B-290_Scale-up_B-290_Niro_MOBILE_MINOR_en_01.pdf.

[5]   J. Font and J. Muntasell, "Effect of ball milling on semicrystalline bisphenol A polycarbonate," *Mater. Res. Bull.*, no. 35.5, pp. 681–687, 2000.

[6]   A. P. Smith, J. S. Shay, R. J. Spontak, C. M. Balik, H. Ade, S. D. Smith, and C. C. Koch, "High-energy mechanical milling of poly (methyl methacrylate), polyisoprene and poly (ethylene- alt -propylene)," vol. 41, pp. 6271–6283, 2000.

[7]   S. Kuroda, K. Terauchi, K. Nogami, and I. Mita, "Degradation of aromatic polymers—I. Rates of crosslinking and chain scission during thermal degradation of several soluble aromatic polymers," *Eur. Polym. J.*, vol. 25, no. 1, pp. 1–7, Jan. 1989.

[8]   G. Molnár, A. Botvay, L. Pöppl, K. Torkos, J. Borossay, Á. Máthé, and T. Török, "Thermal degradation of chemically modified polysulfones," *Polym. Degrad. Stab.*, vol. 89, no. 3, pp. 410–417, Sep. 2005.

[9]   S. Kuroda, A. Nagura, K. Horie, and I. Mita, "Degradation of aromatic polymers—III. Crosslinking and chain scission during photodegradation of polysulphones," *Eur. Polym. J.*, vol. 25, no. 6, pp. 621–627, Jan. 1989.

[10]   C. L. Beyler and M. M. Hirschler, "Thermal decomposition of polymers," *SFPE Handb. fire Prot. Eng.*, vol. 2, 2002.

[11]   Y.-L. Zhao, W. H. Jones, F. Monnat, F. Wudl, and K. N. Houk, "Mechanisms of thermal decompositions of polysulfones: A DFT and CBS-QB3 study," *Macromolecules*, vol. 38, no. 24, pp. 10279–10285, 2005.

[12]   H. Zhang, *Fire-safe polymers and polymer composites*. Office of Aviation Research, Federal Aviation Administration, 2004.

[13]   T. Ranganathan, M. Beaulieu, J. Zilberman, K. D. Smith, P. R. Westmoreland, R. J. Farris, E. B. Coughlin, and T. Emrick, "Thermal degradation of deoxybenzoin polymers studied by pyrolysis-gas chromatography/mass spectrometry," *Polym. Degrad. Stab.*, vol. 93, no. 6, pp. 1059–1066, 2008.

[14]   C. Bai, R. J. Spontak, C. C. Koch, C. K. Saw, and C. M. Balik, "Structural changes in poly (ethylene terephthalate) induced by mechanical milling," vol. 41, pp. 7147–7157, 2000.

[15]   L. C. E. Struik, "Orientation effects and cooling stresses in amorphous polymers," *Polym. Eng. Sci.*, vol. 18, no. 10, pp. 799–811, Aug. 1978.

[16]   R. Vehring, "Pharmaceutical particle engineering via spray drying," *Pharm. Res.*, vol. 25, no. 5, pp. 999–1022, 2008.

[17]   J. Vicente, J. Pinto, J. Menezes, and F. Gaspar, "Fundamental analysis of particle formation in spray drying," *Powder Technol.*, vol. 247, pp. 1–7, 2013.

[18]   A. B. D. Nandiyanto and K. Okuyama, "Progress in developing spray-drying methods for the production of controlled morphology particles: From the nanometer to submicrometer size ranges," *Adv. Powder Technol.*, vol. 22, no.

1, pp. 1–19, 2011.

[19]   J. Elversson and A. Millqvist-Fureby, "Particle size and density in spray drying-effects of carbohydrate properties.," *J. Pharm. Sci.*, vol. 94, no. 9, pp. 2049–2060, 2005.

[20]   B. Wei, S. Wang, H. Song, H. Liu, J. Li, and N. Liu, "A review of recent progress in preparation of hollow polymer microspheres," *Pet. Sci.*, vol. 6, no. 3, pp. 306–312, 2009.

[21]   M. Van den Eynde, L. Verbelen, and P. Van Puyvelde, "Assessing polymer powder flow for the application of laser sintering," *Powder Technol.*, vol. 286, pp. 151–155, Dec. 2015.

[22]   L. Verbelen, "Towards scientifically based screening criteria for polymer laser sintering," KU Leuven, 2016.

[23]   Solvay, *Udel Polysulfone Design Guide*. Solvay.

Chapter 5

CASE STUDY: PROCESSING OF SYNDIOTACTIC POLYSTYRENE

This chapter encompasses the processing of syndiotactic polystyrene as a case study in which the techniques discussed in Chapter 2 are applied in order to create spherical sPS powders. The virgin material is processed and the powders characterized on their extrinsic and intrinsic properties.

5. 1. SPRAY DRYING

5. 1. 1. Polymer solubility

Analogous to the previous two case studies a parameter based approach was selected based on the Hansen Solubility Parameter (HSP) model [1]. sPS is soluble in aromatic solvents and chlorinated aromatic solvents above their glass transition temperature. Several solvents were screened of which a selection is displayed in Table 5-1. Of these solvents, m-xylene proved to be the most suitable experimentally exhibiting the best solubility.

Table 5-1: Hansen Solubility Parameters of sPS and from possible solvents and anti-solvents for sPS. Data from [1], [2]

	δ_{tot} (MPa$^{1/2}$)	δ_d (MPa$^{1/2}$)	δ_p (MPa$^{1/2}$)	δ_h (MPa$^{1/2}$)
Xarec 90ZC sPS	*19,3*	*18,5*	*4,5*	*2,9*
m-xylene	18,0	17,8	0,8	2,7
Benzene	18,5	18,4	0,0	2,0
Chloroform	19,0	17,8	3,1	5,7
Phenol	24,1	18,0	5,9	14,9
Toluene	18,2	18,0	1,4	2,0

The maximum solubility of sPS was thereafter tested by gravimetric experiments as the minimum solvent weight necessary to dissolve a weighted sample of sPS. Dissolution occurred by refluxing sPS at 139 °C (boiling point of m-xylene) until dissolved and left to cool at ambient temperature before further processing. Gravimetrical experiments were replicated three times to minimize experimental errors. The maximum solubility of sPS in m-xylene was found at $4,1 \pm 0,1$ wt.% or $36,3 \pm 0,9$ mg/mL.

Due to the viscosity limit on the Buchi B290 mini spray dryer [3] solution viscosity was tested using Ubbelohde viscosimetry (Schott-Geräte Gmbh) and later on, on a HAAKE Viscotester 550 rotational viscosimeter yet both measurements could not be performed due to the high tendency of sPS to crystallize at room temperature. As syndiotactic polystyrene is highly crystalline and tends to crystallize from solution

[4], the latter was heated to avoid gelation and clogging of the nozzle in further experiments. Furthermore, no concentrations above 3,4 wt.% were used and as a measure to further prevent this gelation/crystallization phenomenon the tubes were preheated by spraying warm solvent prior to spray drying the polymer solution. The critical parameters were optimized using a systematic one-factor-at-a-time (OFAT) approach.

In the case of the two-fluid nozzle, nozzle orifice size measured 2,0 mm and was water cooled. A solution of 2,5 wt.% was heated to 150 °C and fed to the nozzle using fluoroelastomer tubes at a feed rate of 20 mL/min. The heated solution was thereafter atomized using the two-fluid atomizer into the drying chamber using a gas flow rate of 439 L/h. Particles were subsequently dried by a heating gas (pressurized air) which was heated at 200 °C. The resulting powder was sieved off using a cyclone system and investigated. Described parameters were used to achieve the powder samples on which the characterizations listed below were performed.

5. 1. 2. Particle morphology

Inspection of the micrograph for the spray dried sample revealed spherical particles albeit at too small diameter (see Figure 5-1). A small portion of the microparticles displays a dimpled morphology. One would expect all spherical particles, as the maximal structural stability of a solution is in its spherical form. However, much like in the discussed case of polysulfone and polyphenylsulfone a concentration gradient will occur due to the low diffusion rate inherent by the large molecular weight of the polymer. The droplet will become saturated as the maximum solubility for sPS in solution is easily attained by the evaporation of a small amount of solvent from the system. sPS has a high crystallization rate and is able to readily crystallize from solution in its γ- and δ-form [4], [5]. Through this solvent induced crystallization a thick shell can be formed saturated with solvent. As the particle moves down the drying chamber the solvent further evaporates and the shell tends to shrink by a small amount displaying the dimpled like structures. Woo et. al. [4] performed a conformational study on the crystal structure of sPS with toluene and concluded that by evaporation of the toluene solvent a change in lattice parameters could be observed, corresponding with a change in dimensions.

Due to the low concentration of polymer in solution, further increasing particle diameter without compromising morphology remains difficult. Because of the crystallization behavior of sPS in solution, the spraying of higher concentrations is virtually impossible without extended heat or pressure systems to increase solubility. In this case, the maximum solubility is only 4,1% which means only very diluted solutions can be sprayed. As a result, the creation of bigger droplets by increasing nozzle diameter or feed rate would result in a thinner skin formation and ultimately in more shriveled particles [6], [7].

Figure 5-1: Micrograph depicting the sample obtained from the spray drying experiment using the two-fluid nozzle and optimized processing parameters

5. 1. 3. Particle size

The spray dried particles obtained via the above mentioned method were predominantly spherical. Particle size distribution assessment revealed a mean particle size of 6,6 μm with a standard deviation of 6,9 μm with the distribution slightly positively skewed (Figure 5-2). Though some particles reached a diameter within the desired range of 45-90 μm for SLS, the major portion remained well below this. A possible explanation could lie in the fact that for these experiments the concentration of polymer remains pretty low. Because sPS is highly crystalline and tends to crystallize from solution by formation of a gel, it is very difficult to spray higher concentrations. Furthermore the maximum solubility is only 4,1 wt.% which means that only very diluted solutions can be sprayed. Table 5-2 summarizes the mean particle size with standard deviation and particle morphology obtained via the optimal processing conditions dictated above.
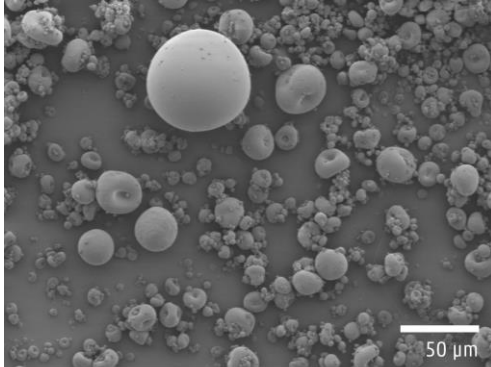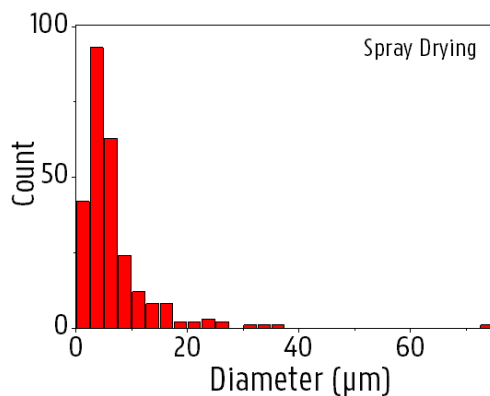

Figure 5-2: Micrograph depicting the sample obtained from the spray drying experiment using the two-fluid nozzle as atomizer. the particle size distribution is displayed next to the micrograph

Table 5-2: Particle size distribution of the sPS powder obtained by spray drying together with the percentage spherical particles in the sample.

	Y_1		Y_2
Processing method	Mean particle size (µm)	Standard Deviation (µm)	Particle morphology (%)
Spray Drying	6,6	6,9	56,7

5. 2. BALL MILLING

Conventional ball milling was used as a means of comparison to the alternative processing methods used in this paper. Though this technique is typically performed at cryogenic temperatures in order to speed up the communition process the current setup did not allow for these conditions. Therefor all milling experiments were executed at ambient temperature. A planetary ball mill (Fritsch 105 Pulverisette type 500) with 3 ceramic crucibles and ceramic balls of 25 mm diameter were loaded with $10,1 \pm 0,1$ g of sPS pellets. Milling was performed at 1400 RPM with samples taken at different intervals.

5. 2. 1. Particle morphology

During ball milling the sample undergoes various morphological changes. In Figure 5-3, particle size and morphology were plotted versus milling time which depicts this change clearly. After 15 minutes already a significant portion of the sPS pellets has fractionated in large rough angular structures and a fraction of very fine particles which were later on investigated for PSD (see Figure 5-4). All particles are of non-spherical nature. After 45 minutes the as ground powder begins to flatten by the impact of the balls into flakes and get partially cold welded together upon continuous milling (the low diffusivity of the polymer molecules is expected to hinder this process considerably). This flattening of the particles is noticed in the PSD as well by the small increase in particle size and is visible in the insets in Figure 5-3. During the milling process this fractionation of the larger pellets and the flattening of the flakes continues with no apparent improvement of morphology for the use of SLS.
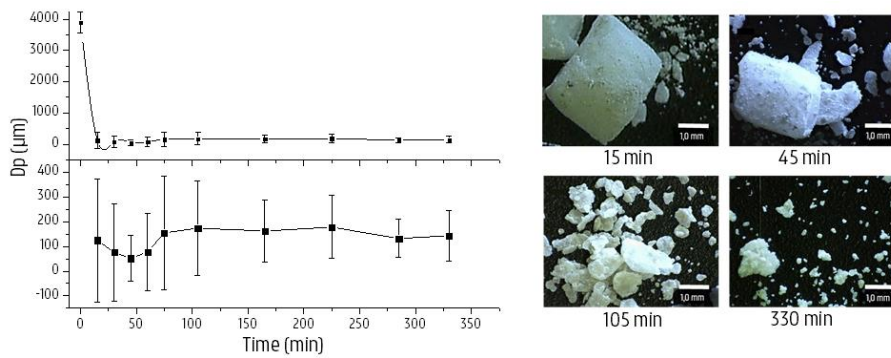
Figure 5-3: Evolution of average particle size and morphology of ball milled sPS as a function of time. The above panel displays the sudden decay in particle size due to immediate fractionation of the brittle sPS. The lower panel focusses on the fractionation itself. The particle size distribution of the ground material is very broad with angular structures that get flattened over time.

5. 2. 2. Particle size

When looking at the graph in Figure 5-3 for the ball milled sample an immediate decrease in particle size is visible. Within 15 minutes the pellets fractionate already partly resulting in a part of small and rough angular structures of about $10{,}6 \pm 9{,}2$ μm (see Figure 5-4) and a part of bigger, slightly fractionated or yet unfractionated pellets, several orders of magnitude larger. The particle size distribution on the fractionated pellets after 15 minutes (marked by the red square in Figure 5-4) is given in Figure 5-4. Particles are already well below the desired range and show little to no sphericity. After 45 minutes a minimum in mean particle size is reached, hereafter the particle size increases again and levels off. The end result is a fine powder with a PSD ranging around 142 μm with a few particles still as 228 large as 987 μm. During the whole process particle size distribution is very broad for the as-ground powder due to the remaining large fractions but becomes considerably narrower with milling time.
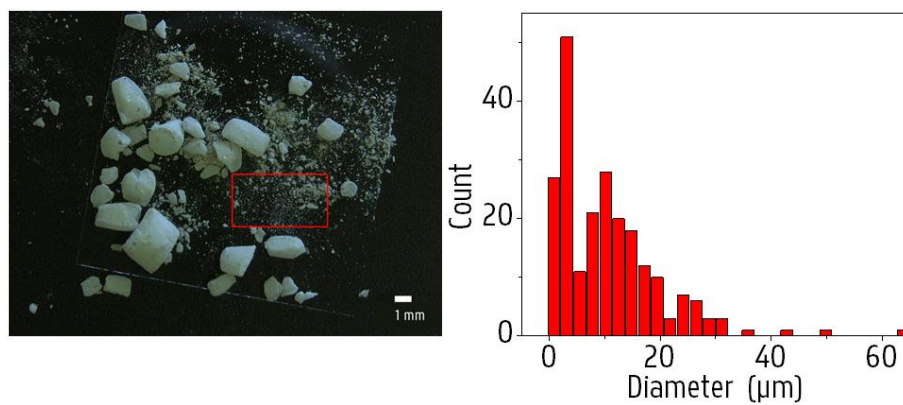
Figure 5-4: Particle size distribution of the fractionated sPS powder after 15 minutes of ball milling. The powder marked in the red square (right) was analyzed for PSD (left).

Table 5-3: Particle size distribution of the sPS powder obtained by ball milling for 15 minutes. The small fraction (red square in Figure 5-4) is displayed by BM15[a] together with the PSD of the whole fraction (whole of Figure 5-4) by BM15[b].

	Y_1		Y_2
Sample	Mean particle size (µm)	Standard Deviation (µm)	Particle morphology (%)
BM15min[a]	10,69	9,24	0
BM15min[b]	174,94	513,71	0

[a] PSD of the fine powder represented in the red square in Figure 5-4
[b] PSD of the whole sample represented by microscopic image in Figure 5-4

5. 3. ROTOR MILLING

The sPS pellets were processed by a three-step communition process on a Fritsch Pulverisette 14 rotor mill, followed by a sieving step in order to obtain the right particles in size and morphology. In the first step the pellets were pulverized to a coarse powder using a sieve with mesh size 500 µm. In a second and third refinement step the coarse powder was further pulverized to a fine powder and sieved at 120 and 80 µm, subsequently. A 12-ribbed rotor blade was used at 15000 RPM to achieve pulverization which was augmented to 16000 RPM for the final milling step. The resulting powder was sieved and isolated using a cyclone system. During the milling process the rotor mill was cooled by air at room temperature using an aspirator connected to the cyclone system. For analysis purposes only the powders who underwent 1 cycle without refeed were used.

5. 3. 1. Particle morphology

Micrographs of the material in each of the milling steps is depicted in Figure 5-5 and corresponding values of morphology and particle size are summarized in Table 5-4. A noticeable increase in sphericity is reported with each refinement step. The coarse powder displays little to no spherical structures and is mostly composed of elongated stretched structures. In the second stage sphericity is already noticeable though a large part of the powder remains string-like or as large elongated forms. Therefore, a third is introduced to further decrease particle size and increase morphology to the desired form. To remove any unwanted structures the powder is sieved using a vibratory sieve at 80 µm. The results are fairly spherical particles of which 26,83 % fulfill the requirements according to the Powers' scale with a small amount of inconsistencies. When compared to the milling of amorphous material like Polysulfone (see Chapter 4) one can see that the crystallinity of the material and the consequent brittleness inherent to the neat material hampers the rounding effect the rotor mill may impose on the material. This is reflected in the incompletely rounded particles that are partly fractionated in the sample and the lower value of percentage spherical particles. No indication of cold welded structures is apparent as previously seen in the case of ball milling.
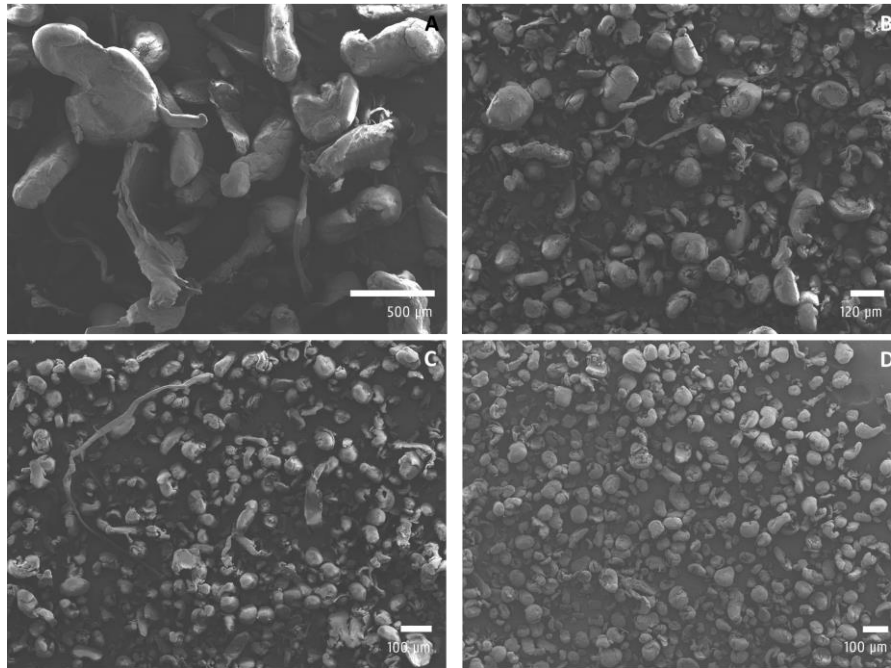
Figure 5-5: sPS powder undergoing the three step pulverization process with additional sieving step: (A) Milling of sPS pellets into a coarse powder at 500 µm, (B) first refinement step by milling the coarse powder at 120 µm, (C) second refinement step by further pulverization of the refined powder at 80 µm and (D) the final powder after additional sieving at 80 µm removing any leftover inconsistencies.

Table 5-4: Particle size and particle morphology of the material going through each of the steps of the rotor milling sequence

	Y_1		Y_2
Sample	Mean particle size (μm)	Standard Deviation (μm)	Particle morphology (%)
RM500	672,94	244,51	0
RM120	72,78	41,56	14,85
RM80	46,02	21,93	24,62
Sieved	49,22	15,61	26,83

5. 3. 2. Particle size

The three step communition process by the rotor miller decreases particle size sequentially while improving morphology. Table 5-4 displays the decrease in particle size with every milling step while Figure 5-6 gives the particle size distribution of the final product. In the first stage the pellets are converted to a rough powder with a mean size of 672,94 μm and a large standard deviation of 244,51 μm. In the second stage the particle size is further diminished to a mean size of approximately 72,78 μm and a standard deviation of 41,56 μm. In the last processing step the powders are reduced to a mean particle size of 46,02 μm with a standard deviation of 21,93 μm. After the final sieving step using the vibratory sieve at 80 micron a powder is obtained displaying a particle size of 49,22 μm with a standard deviation of 15,61 μm. The particle size distribution is slightly positively skewed to the larger diameters and falls within the favorable range of particle diameters required for SLS processes.
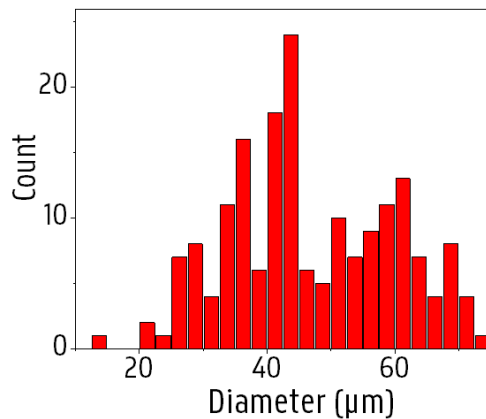
Figure 5-6:Particle Size Distribution of the rotor milled sPS going through the three step refinement process with additional sieving

5. 4. MATERIAL CHARACTERIZATION

5. 4. 1. GPC measurements

As sPS is highly crystalline and has a high chemical resistance, investigation of degradation is difficult as GPC measurements are not easily feasible. Samples were unable to be dissolved in the solvents used for conventional GPC measurements forcing another method to determine a change in intrinsic properties. High temperature GPC is a valuable option yet not very common making the analysis very expensive. Instead, the change in glass transition temperature and crystallinity was correlated to investigate for a trend in degradation (see further on).

5. 4. 2. TGA measurements

In order to investigate the thermal stability of the sPS, TGA measurements were performed. The measurements provide valuable information that can be used for further analysis and provide additional info in regards to the further processing of sPS through sintering. Measurements were performed under nitrogen atmosphere with a heating rate of 10 °C/min to a maximum temperature of 450 °C. The thermogram of the respective run is depicted in Figure 5-7 and clearly displays the sPS to be stable up to temperatures of 300 °C. After this the sPS begins to degrade slowly displaying a 1wt.% degradation at 306,3 °C. Hence, it is advised for further analysis not to exceed this temperature.
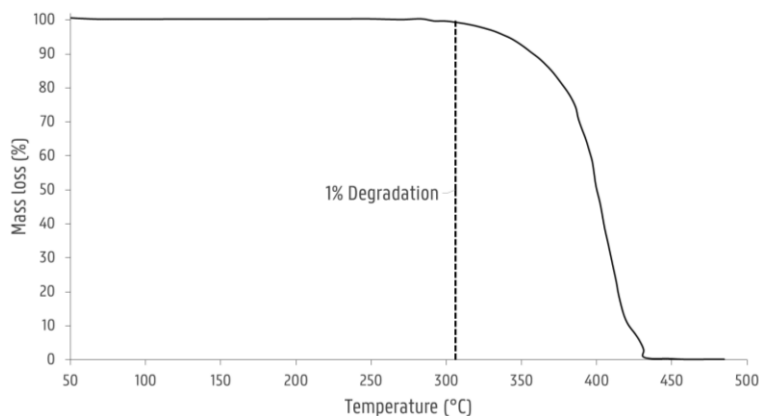
Figure 5-7: TGA curve of unprocessed sPS in order to determine the point of 1% degradation which should not be crossed to avoid degradation

5. 4. 3. DSC measurements

The thermal history imparted on the powders by each of the processing methods was investigated using the first heating curve. This heating run could be especially helpful in setting the parameters for laser sintering for which these powders are intended. To explore the reversibility of the structural changes imparted by the processing techniques a second heating run is explored. A heating rate of 10 °C/min was used to heat the samples to 300 °C. This maximum temperature was determined by TGA measurements. An isotherm of 5 minutes was upheld at this temperature in order to ensure all crystalline regions were fully molten so no remaining crystallites could induce heterogeneous nucleation to form a specific crystal structure. Samples were thereafter cooled at specific rate (10 °C/min) in order to induce the pure α"-form crystallization which is characterized as a dual melting peak in the thermogram [4]. The crystallinity of each processed sample was determined using the heat of fusion of the pure α"-form and compared to the unprocessed sample as a measure to determine degradation. As degradation of syndiotactic polystyrene is believed to occur via random chain scission this initial decrease in molecular weight could impact crystallinity [8]–[10]. Crystallinity was determined using the following formula:

$$X_c = \frac{\Delta H_f - \Delta H_{c,cold}}{\Delta H_f^0} \times 100 \qquad\qquad\qquad \textit{Equation 5-1}$$

where ΔH_f is the heat of fusion, $\Delta H_{c,\ cold}$ is the enthalpy of cold crystallization and ΔH_f^0 is the theoretical heat of fusion of sPS displaying 100% crystallinity, being 53,2 J/g [11]. Multiple measurements were performed to determine any significant change in crystallinity in this regard. All samples were investigated under nitrogen atmosphere. Table 5-5 displays the calculated values of crystallinity using the abovementioned formula and the data derived from the thermograms depicted in Figure 5-8 and Figure 5-9.

Syndiotactic polystyrene is a polymorphic semi-crystalline polymer. Four crystal types (α, β, δ and γ) with sub-modifications for both the α- and β-form exist depending on if the material is thermal (α- and β-form) or solvent (δ and γ-form) treated. E. M. Woo et al. [4] did an extensive review on the complex polymorphism of syndiotactic polystyrene explaining the thermal profiles of the more common α- and β-forms with their trans-planar conformation and helical conformation associated with the δ- and γ-forms. The polymorph behavior of sPS described in this paper is reflected in the first heating run of the unprocessed material by a broad endothermic peak at 277 °C. An isotherm at 300 °C was uphold for 5 minutes in order to completely melt all remaining crystallites. Next, following the same heating rates as described by Woo et al. [4] the polymer was cooled down in order to stimulate pure α"-crystal formation. A sharp crystallization peak was found in this cooling run starting at 250 °C and peaking at 244 °C. The type of crystallinity is expressed in the second heating run by the dual melting peak at 265 °C and 272 °C, identified as P-II and P-

IV, and a minor endothermic peak at 246 °C, labeled as $P_{a,\alpha}$ attributed to the annealing effect of the cooling rate on the α''-type crystal. The crystallinity of the sPS was calculated at 59 %.

Upon processing of the sPS significant changes in thermal behavior occur. In the case of spray drying a relatively large cold crystallization peak becomes apparent at 139 °C. This can be explained when looking at the spray drying process: a large temperature gradient exists between the drying chamber at high temperature and the collection vessel in which the microspheres are collected at practically ambient temperature. Partial quenching is believed to occur which is reflected by cold crystallization upon the first thermal run. The glass transition is found at 92 °C but increases back to 98,9 °C in the second thermal run suggesting no severe degradation to have occurred during processing. The broad melting peak at 275 °C also deviates a little from the polymorphic profile as seen with untreated sPS by the appearance of a small shoulder: a partial preferred crystallization from solvent due to the thermal treatments upon processing is said to occur. Crystallinity of the processed sPS was reduced to 32,3 % but increases back to 61,1 % in the second heating run. Upon the second thermal run the thermal history of the processing technique is swept away and a clear α''-structure is recovered evidenced by the dual melting peaks at 263 °C and 273 °C. The initial decrease in crystallinity can hence be explained by the fast cooling of the particles upon consolidating in the drying chamber and subsequent cooling in the collecting chamber resulting in a more amorphous sPS than the virgin material. The final percentage of crystallinity calculated in the second heating run in Figure 5-9 expresses an increase of 3,2 % relative to the unprocessed form. This slight increase once more suggests possible but no significant degradation.

When looking at the mechanical processing techniques a similar trend of amorphization can be seen. In the case of rotor milling an exothermic peak is detected at 132 °C upon heating. Here, the cold crystallization peak at 132 °C can be attributed to amorphization due to the mechanical treatment. This strain-induced amorphization of the crystalline regions is also known as decrystallization or disaggregation and is explained by D. Raabe et al. [12] as sheared crystalline lamellae that break apart into sets of crystalline blocks with severe lattice defects, also called mechanical melting. The crystallinity of the as ground powder is lower than its untreated form and shows a crystallinity of 45,3 %. A second DSC run reveals a return of the dual melting peaks though a larger incision is visible between the two characteristic peaks. Crystallinity was calculated at 64,6 % displaying an increase of 6,2 %. Once more this could suggest some mechanical degradation though not to a significant extent. Though the milling process only takes up a fraction of seconds, the powders are subjected to multiple treatments to further reduce the particle size which could have a cumulative effect on degradation behavior. Finally, the glass transition temperature was measured at 95,7 °C, in close agreement to the unprocessed sample.

In the case of ball milling a more drastic change in thermal behavior occurs. A more complex exothermic peak is found after the glass transition as a result of amorphization due to the mechanical treatment. The exothermic peak is not as expressed as is the case with the other processing techniques. Bai et al. [13] clarified that this could be explained by an oriented morphology induced by the biaxial stresses that are inherent in ball milling. The relaxation of the chains during the heating run could compensate for the exothermic crystallization. One might remark that, in the second heating run, the glass transition temperature is slightly lower than usual measuring at 98,1 °C suggesting some degradation that occurred during milling. Degradation of the polymer is likely to occur via chain scission produced by the high-energy collisions between polymer and ceramic balls. These chain scissions can create free radicals which may then react with other molecules in the system to produce crosslinks or grafts. The crystallinity values of the sample ball milled for 15 minutes support this premise; a crystallinity of 23,7 % and 32,6 % is found in the first and second DSC run respectively accounting for a significant reduction in crystallinity of 44,8 %.

In order to statistically determine if there is a significant change in crystallinity due to the processing method multiple DSC measurements were performed. The values are depicted in Table 5-5. Despite the noteworthy exothermic peaks seen for all processed samples, differences in melting temperatures between treated and untreated sPS remain quite small. All samples have a polymorphic melting peak around 272 °C in the first heating run and clearly regain the dual melting peaks representative of the α"-structure in the second heating run. Furthermore, when comparing the heat of fusion of these characteristic melting peaks through t-test analysis, no significant change was found when comparing the unprocessed sPS to the rotor milled samples (p = 0,192) or the spray dried samples (p = 0,341). In the case of the ball milled sample, a one-sample t-test was performed with the unprocessed heat of fusion as a population and the heat of fusion of the ball milled sample as a single value as no extra runs could be performed on this sample. As the DSC is supposed to give accurate measurements its value was considered to be a constant by approximation. Results on the one sample t-test revealed the heat of fusion to be significantly different from the population with a p-value of 0,001, rejecting the null hypothesis that no difference exist between the true mean of the heat of fusion of the unprocessed samples and the constant value which is the heat of fusion of the ball milled sample.

Crystallinity percentage calculation determined on these α"-structure melting peaks (see Table 5-5) indicates both spray drying and rotor milling increase the crystallinity of the sPS while the ball milling sample is severely reduced in crystallinity, however the spray dried and rotor milled powders have a crystallinity close to that of the unprocessed sPS. Ball milling exhibited a significant deviation. This sample is considered to be subject the most to degradation.

Table 5-5: Enthalpy values calculated from thermograms in Figure 5-8 and Figure 5-9 with
the resultant percentages of crystallinity calculated according to Equation 5-1

	First heating run			
	Unprocessed	Spray dried	Rotor milled	Ball milled
$\Delta H_{c,\,cold}$ (J/g)	n.a.	$15{,}37 \pm 0{,}22$	$11{,}35 \pm 0{,}35$	1,96
ΔH_f (J/g)	$26{,}60 \pm 2{,}06$	$32{,}57 \pm 0{,}80$	$35{,}40 \pm 0{,}70$	14,57
Crystallinity (%)	$50{,}00 \pm 3{,}90$	$32{,}30 \pm 1{,}30$	$45{,}30 \pm 1{,}30$	23,70
	Second heating run			
$\Delta H_{c,\,cold}$ (J/g)	n.a.	n.a.	n.a.	n.a.
ΔH_f (J/g)	$31{,}38 \pm 0{,}80$	$32{,}53 \pm 1{,}72$	$34{,}37 \pm 3{,}29$	17,33
Crystallinity (%)	$59{,}00 \pm 1{,}50$	$61{,}10 \pm 3{,}20$	$64{,}60 \pm 6{,}20$	32,60

Figure 5-8: Thermograms representing the first heating run of the processed samples: (A)
Unprocessed, (B) ball milled for 15 minutes, (C) spray dried at optimal conditions and (D)
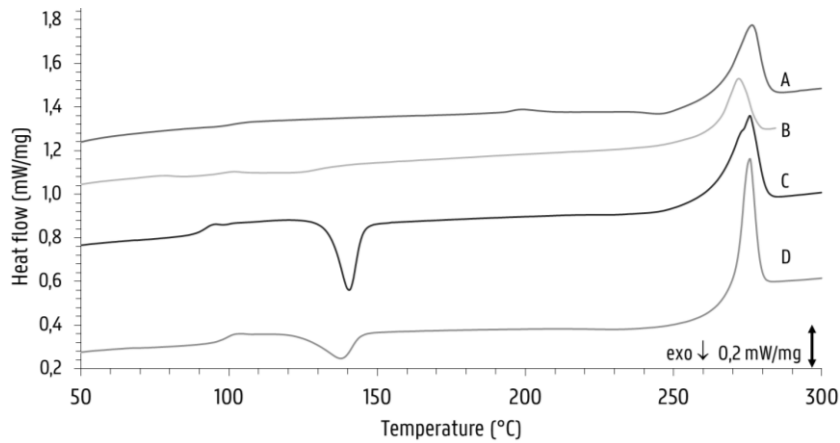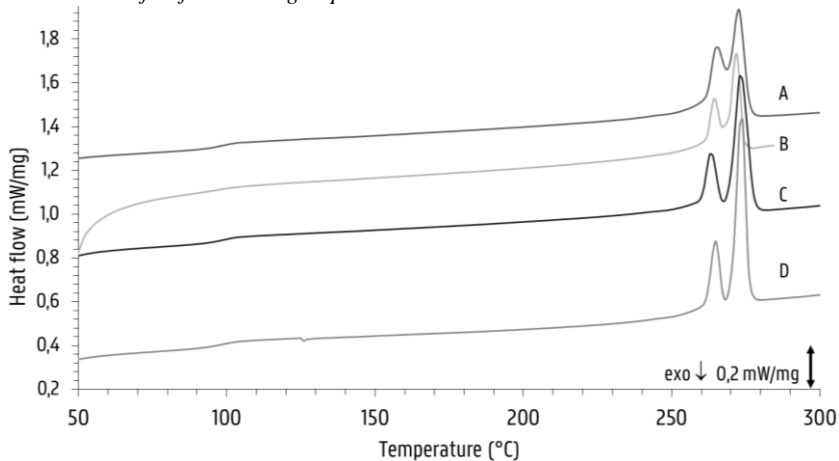*rotor milled after final sieving step*

Figure 5-9: Thermograms representing the second heating run of the processed samples: (A)
Unprocessed, (B) ball milled for 15 minutes, (C) spray dried at optimal conditions and (D)
rotor milled after final sieving step

5. 4. 4. Powder flow

A HR test was performed by gravimetrically measuring the densities of the powder at ambient conditions using a graduated cylinder and powder funnel. After measuring the bulk density the powder was subjected to a sequence of taps by placing the cylinder on the baseplate of a RETSCH Vibratory Sieve Shaker AS 200 digit for 60 seconds at 60 % of its maximal amplitude. Afterwards the volume was measured again to determine the tapped density. To increase its statistical outcome, each powder sample was measured over 10 times (using fresh powder every time) as the HR is highly dependent on the analyst due to the tapping of the powder samples and determination of the volume in the graduated cylinder. The HR of the rotor milled samples could only be calculated as the spray drying and ball milling experiments were conducted on lab scale and did not produce enough quantity to allow HR to be determined. Furthermore, the particle size of the samples was too small, enabling electrostatic buildup which interfered with accurate measurements of the powder flow.

Figure 5-10 depicts the Hausner ratio calculated from the tapped and bulk densities of each sample of the powders subjected to each processing step, these values are summarized again in Table 5-6. Throughout the milling steps the ratio decreases and ends at the limit of good powder flowability (1,25 for the final sieved fraction). As particle size is decreasing with every milling step one would expect the density to increase giving a better packing density. However with every successive milling step the density of the powders decreases. Ziegelmeier et. al. [14] noticed a similar behavior in when comparing the HR of different TPU powders and ascribed this to changes in dominating adhesive forces in the powder bulk. The principle reasoning behind this being that, if particle size increases, the weight forces would lower the influence of the Van der Waals interactions allowing the particles to slide more easily alongside each other. These results were enforced by extra powder rheometry measurements regarding avalanche angle measurement and specific energy measurement. As particle size decreases further with every milling step these Van der Waals forces tend to gain influence and could hinder a homogeneous distribution of the smaller particles over the bulk powder. These adhesive forces between the smaller particles can cause agglomeration of the smaller particles resulting in a decrease in the packing efficiency and a lowering in the density measured.
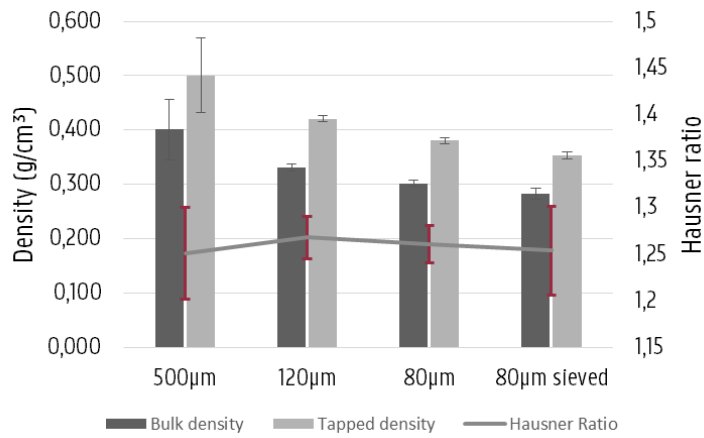
Figure 5-10: Hausner ratio of the rotor milled powder through each processing step. HR is calculated from the ratio of the tapped and bulk density depicted in graph

Table 5-6: Hausner Ratios calculated from the density measurements of each rotor milling processing step

Powder flow				
Fraction	500 µm	120 µm	80 µm	80 µm Sieved
Hausner Ratio	1.25 ± 0.05	1.27 ± 0.02	1.26 ± 0.02	1.25 ± 0.05

5. 4. 5. Single layer test

In an attempt to simulate sinter experiments a laser cutter was used with variable wattage and scan speed to perform single layer tests. An OFAT approach determined the optimal settings at a laser wattage of 20 W and scan speed of 200 mm/s. These settings gave a smooth surface without the visual appearance of laser scan tracks indicative of balling or necking due to full melting particles several layers deep [15], [16] (see Figure 5-12). Analysis of the laser spot during sintering with IR camera revealed temperatures reaching 301,7 °C (Figure 5-11), which is well above the melting point of sPS. As a result of the temperature gradient between laser spot and surrounding atmosphere (see Figure 5-11, left) parts experienced severe quenching giving amorphous parts which were transparent. Furthermore the thermal gradient also caused severe shrinkage and curling of the part. No fuming or discoloration occurred during sinter process and parts had a smooth surface at optimized parameter settings. Consequently, these preliminary tests were favorable towards further sinter experiments. Powder bed heating would be advised in order to prevent quenching and shrinkage due to crystallization and thermal gradient.
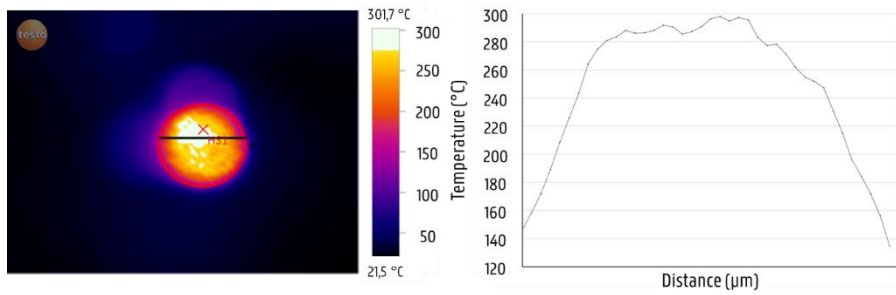
Figure 5-11: Temperature profile of the laser spot on 80 µm sieved rotor milled sPS powder. Temperature reaches values well above the melting temperature of sPS
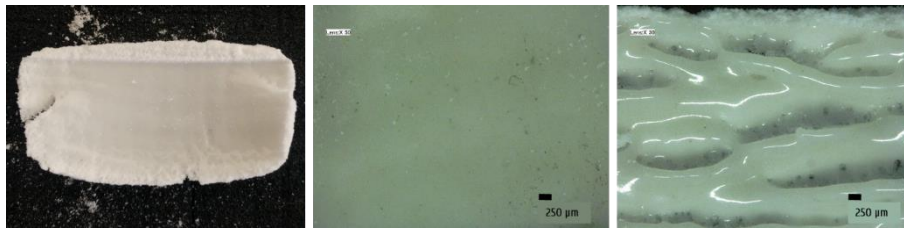
Figure 5-12: Left: Sintered rectangle on 80 micrometer final powder. Part caking is visible around the rectangle along with severe warpage. The parts produced at these best parameter setting displayed a smooth morphology (middle) whereas deviation from these parameters often results in non-consolidated layers or severe necking or balling (right) [15], [16]

5. 5. SINTER TESTS AT KU LEUVEN

The powder material was further investigated at the university of Leuven to evaluate the thermal properties of the material using dilatometry measurements by the Soft Matter Rheology and Technology (SMaRT) group and actual sinter tests by the Additive Manufacturing Research Group [17] [1,2].

As sPs is a semi-crystalline polymer a sharp viscosity drop is expected when heating above its melting temperature. Figure 5-13 depicts the zero-shear viscosity of sPS measured over temperature. The melt viscosity above melting temperature indicate low enough viscosity to allow proper coalescence in the melt when sintered. This viscosity drop upon melting also means that when cooling below crystallization temperature, crystallization will occur with the associated shrinkage. Dilatometry measurements performed by the SMaRT research group reveal a slightly smaller shrinkage in comparison to PA12 with a crystallization shrinkage of 3 % (see Figure 5-14). This decrease in specific volume should be delayed during sintering by heating the powder bed above its crystallization temperature yet below the melting temperature, i.e. in the so called processing window. DSC measurements of the sample show a sharp crystallization temperature to be at 244 °C with an onset temperature of 247 °C (see section 5. 4. 1.). Depending on the crystal structure of the sPS the onset melting peak can be seen at 260 °C leaving a rather narrow processing window. As commercial sinter stations can only achieve stable powder bed heating up to 200 °C, the powder bed temperature was set on the latter temperature. Note that this temperature is below the advised processing window enabling crystallization to take place and therefor expressing shrinkage and warpage. As a result, only single layers were printed.

Single layers were sintered on a DTM Sinterstation 2000 equipped with a CO_2-laser (Gaussian profile with diameter 450 µm). The process happens under N_2-atmosphere with up to 5.5 % O_2. An example of the single layer tests at different laser energy densities is depicted in Figure 5-15. While coalescence and powder deposition were not an issue, the thermal gradient together with the crystallization of the powder upon cooling to powder bed temperature caused warpage and curling of the edges. The latter hampering the building of multilayer structures. Single layers were found to be very brittle making recovery from the powder bed somewhat delicate. Syndiotactic

---

[1] Soft Matter Rheology and Technology (SMaRT), Department of Chemical Engineering (CIT), Celestijnenlaan 200f, Heverlee, KU Leuven, prof. dr. ir. Peter Van Puyvelde and prof. dr. ir. Paula Moldenaers

[2] Additive Manufacturing Research Group, Department of Mechanical Engineering, Celestijnenlaan 300B, Heverlee, KU Leuven, prof. dr. ir. Jean Pierre Kruth and prof. dr. ir. Brecht Van Hooreweder

polystyrene is commonly reinforced with glass fibres up to 40 wt.% to compensate for the more brittle character. Sinter tests on reinforced sPS could therefor diminish the brittle character provided that viscous flow is still low enough for acceptable coalescence. Included in Figure 5-13 is the zero-shear viscosity measured for 30 wt.% glass filled sPS which shows a higher viscosity for the filled grade due to the fibers [18]. Nevertheless, at melting temperature the viscosity remains sufficiently low in order to allow good coalescence.

Insufficient powder bed heating is a critical issue that counteracts the progress of the investigation of sPS as possible feed material for SLS. In this regard the problem seems to hold place more exactly in a shortcoming of the sintering apparatus. High-temperature laser sintering devices with stable powder bed heating in higher temperature ranges could prove a solution to this issue. However, these devices are pretty scarce and fairy expensive. Nowadays most LS machines are developed and fabricated by EOS GmbH and 3D systems Inc. Both companies have several machine types in their portfolio of which only the EOSINT P800 can achieve process temperatures up to 385 °C [19]. The Direct Manufacturing Research Center (DMRC) of the University of Paderborn is in progress of developing a test equipment for the processing of new materials. In their presentation at the Solid Freeform Fabrication symposium at Austin, Texas they alluded to maximum powder bed heating of 400 °C [20], [21]. More work has to be devoted to the development of high temperature laser sintering machines which will allow a significant expansion of possible materials for SLS.
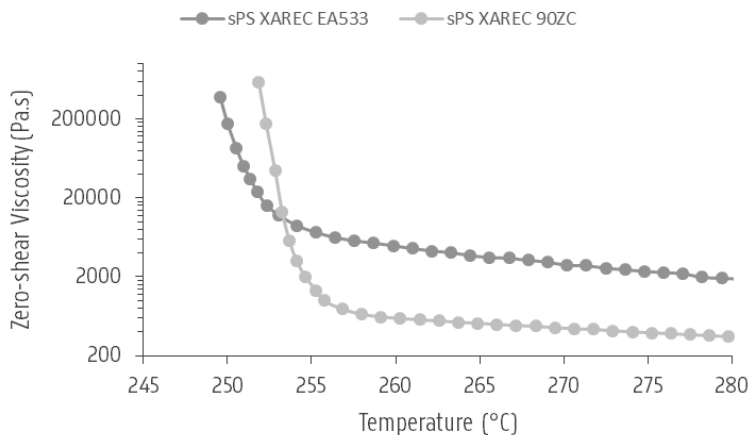

Figure 5-13: Zero-shear viscosity versus temperature of two sPS grades measured on a rotational rheometer at KU Leuven: unfilled sPS as XAREC 90ZC and 30 wt.% glass filled sPS as XAREC EA533
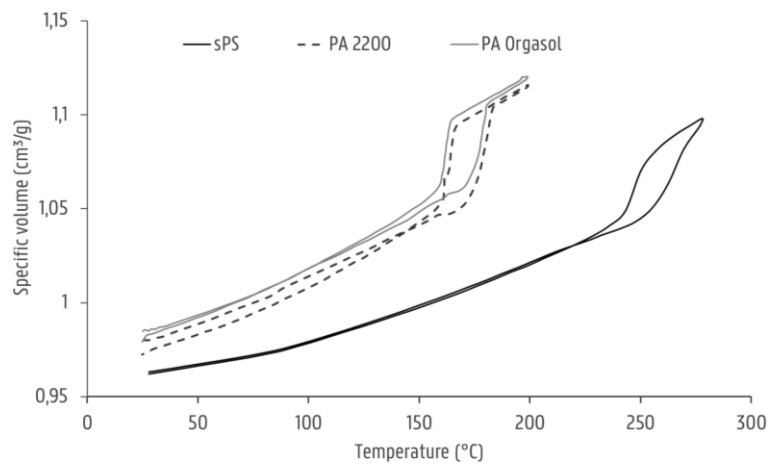
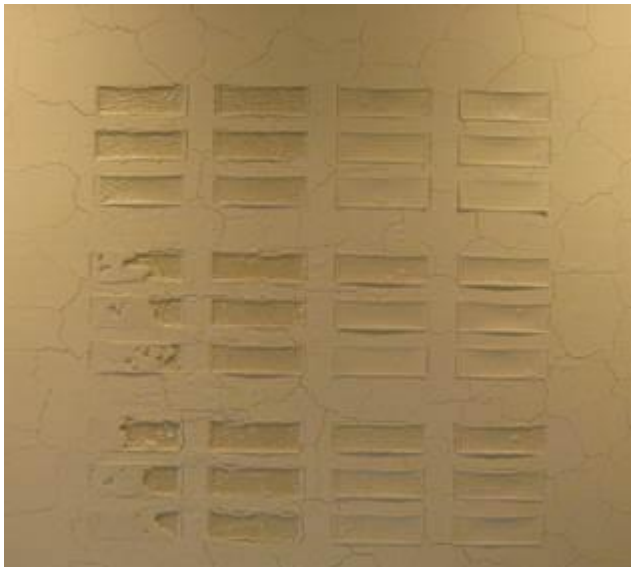*Figure 5-14: Dilatometry experiments performed at KU Leuven by SMaRT research group*

Figure 5-15: Single layer sinter testing on sPS at KU Leuven by the Additive Manufacturing Research group

5. 6. CONCLUSIONS

This chapter was dedicated to the processing and characterization of sPS pellets into powder form suitable for processing through SLS. By the use of spray drying sPS pellets could be transformed into spherical powders of which 56,7 % had favorable morphology. However particle size was loo low with a mean particle size of 6,6 μm and standard deviation of 6,9 μm. Because of its high crystallinity, sPS is not able to be dissolved in high concentrations. Furthermore, because of its ability to crystallize from gel a high clogging risk exists. These two factors make upscaling to a pilot scale spray dryer with larger nozzle size the only option to increase particle size.

Thermal investigation of the produced powders revealed that some quenching occurs when processing as a result of the temperature difference between the inlet of the drying chamber and the collection chamber where the particles are sieved off from the drying gas. As the cold crystallization peak around 140 °C and the powder bed temperature is set at 200 °C this should not be an issue. In the second heating run no significant decrease in crystallinity was observed leading to the assumption that no significant degradation has occurred.

Rotor milling the sPS particles and subjecting these to the three step refinement process lead to a favorable particle size of 49,22 μm with standard deviation of 15,61 μm. The amount of particles displaying a good morphology was 26,83 %. Though this percentage is considered on the lower side, Hausner Ratio measurements of the rotor milled fraction undergoing the complete rotor milling process were on the limit of good powder flow ability. This was confirmed by powder flow tests performed at the KU Leuven. Thermal investigation of the sample displayed amorphization due to the mechanical milling method, yet a good recovery of crystallization was reported after crystallization from melt. A decrease in crystallinity of 3.4 % was stated as a result of the processing method which was found insignificant compared to the unprocessed sPS. Again, powder bed temperature remains much higher than the cold crystallization peak sweeping away the thermal history imparted by the processing method.

Contrary to the above mentioned processes, the ball milling process came out as the worst processing technique exhibiting both bad morphology and particle size with a large deviation. The fractioned powders after 15 minutes displayed a mean particle size of 10,69 μm ± 9,24 μm. Furthermore, a discoloration was noticed during sampling which became more prominent with milling time, suggesting degradation. Thermal investigations revealed a strong decrease in crystallinity when recrystallizing from the melt (up to a decrease of 40.5 %). These findings strongly implicate occurrence of degradation during ball milling in a detrimental way, making this method undesirable as a processing method for SLS powders.

While further optimization is necessary for the spray dried particles in terms of particle size, the rotor milled particles are well within the desired form to be used as feed material for the sinter process. The rotor-milled powders were consequently used for single layer tests, both at the University of Ghent and more in depth at the KU Leuven. Due to the basic set-up at the university Ghent severe warpage of the layers was unavoidable due to the large temperature gradient between laser spot and surrounding atmosphere. Good coalescence could however be obtained without severe fuming or visible degradation. Smooth surfaces could be obtained using a scan speed of 200 mm/s and laser wattage of 20 W. Deviation from these parameters often resulted in rough structures not suitable for multilayer testing. At KU Leuven the powder bed was heated up to 200 °C, however, crystallization occurs around 244 °C which means that upon sintering of the individual layers crystallization still occurs leaving the material to shrink and cause curling or warpage. This prevented the building of multilayer parts. Until a feasible solution is found to delay crystallization by heating the powder ben stably just above its crystallization temperature this will hamper the sinter process. Sinter testing on high temperature laser sintering machines are highly advised as these machines are known to preheat the powder up to temperatures well in range of the processing window of the polymer.

5. 7. REFERENCES

[1]   C. M. Hansen, *Hansen Solubiliy Parameters: a user's handbook*, Second Edi. London: CRC Press, 2012.

[2]   Y. Liu, X. Yue, S. Zhang, J. Ren, L. Yang, Q. Wang, and G. Wang, "Synthesis of sulfonated polyphenylsulfone as candidates for antifouling ultrafiltration membrane," *Sep. Purif. Technol.*, vol. 98, pp. 298–307, 2012.

[3]   C. Arpagaus, N. Schafroth, and M. Meuri, "Laboratory Scale Spray Drying Of Inhalable Drugs: A Review," *Best@Buchi*, no. 59, 2010.

[4]   E. M. Woo, Y. S. Sun, and C. P. Yang, "Polymorphism, thermal behavior, and crystal stability in syndiotactic polystyrene vs. its miscible blends," *Prog. Polym. Sci.*, vol. 26, no. 6, pp. 945–983, 2001.

[5]   M. Malanga and T. H. Newman, "Syndiotactic Polystyrene," in *Encyclopedia of Polymer Science and Technology*, John Wiley & Sons, Inc., 2002.

[6]   R. Vehring, W. R. Foss, and D. Lechuga-Ballesteros, "Particle formation in spray drying," *J. Aerosol Sci.*, vol. 38, no. 7, pp. 728–746, 2007.

[7]   R. Vehring, "Pharmaceutical particle engineering via spray drying," *Pharm. Res.*, vol. 25, no. 5, pp. 999–1022, 2008.

[8]   I. C. Mcneill, M. Zulfiqar, and T. Kousar, "A Detailed Investigation of the Products of the Thermal Degradation of Polystyrene," *Polym. Degrad. Stab.*, vol. 28, pp. 131–151, 1990.

[9]   S. Stack, O. O'Donoghue, and C. Birkinshaw, "The thermal stability and thermal degradation of blends of syndiotactic polystyrene and polyphenylene ether," *Polym. Degrad. Stab.*, vol. 79, no. 1, pp. 29–36, 2003.

[10]   A. Guyot, "Recent Developments in the Thermal Degradation of Polystyrenc A Review," *Polym. Degrad. Stab.*, vol. 15, pp. 219–235, 1986.

[11]   M. Mukherjee, C. K. Das, A. P. Kharitonov, K. Banik, G. Mennig, and T. N. Chung, "Properties of syndiotactic polystyrene composites with surface modified short Kevlar fiber," *Mater. Sci. Eng. A*, vol. 441, no. 1–2, pp. 206–214, 2006.

[12]   D. Raabe, N. Chen, and L. Chen, "Crystallographic texture, amorphization, and recrystallization in rolled and heat treated polyethylene terephthalate (PET)," *Polymer (Guildf).*, vol. 45, no. 24, pp. 8265–8277, 2004.

[13]   C. Bai, R. J. Spontak, C. C. Koch, C. K. Saw, and C. M. Balik, "Structural changes in poly (ethylene terephthalate) induced by mechanical milling," vol. 41, pp. 7147–7157, 2000.

[14]   S. Ziegelmeier, F. Wöllecke, C. Tuck, R. Goodridge, and R. Hague, "Characterizing the Bulk & Flow Behaviour of LS Polymer Powders."

[15]   R. D. Goodridge, C. J. Tuck, and R. J. M. Hague, "Laser sintering of polyamides and other polymers," *Prog. Mater. Sci.*, vol. 57, no. 2, pp. 229–267, 2012.

[16]   R. Li, J. Liu, Y. Shi, L. Wang, and W. Jiang, "Balling behavior of stainless steel and nickel powder during selective laser melting process."

[17]   L. Verbelen, "Towards scientifically based screening criteria for polymer laser sintering," KU Leuven, 2016.

[18]   Idemitsu Kosan Co. ltd., "sPS XAREX EA533: Crystalline Polymers – 30% Glass Filled, Ignition Resistant, Impact Modified Polymer for Electronic and Electrical Applications," 2011. [Online]. Available: http://www.idemitsu-chemicals.de/files/datasheets/xarec/English/XAREC EA533 Data Sheet ISO -English R6 May 2011-.pdf. [Accessed: 18-Jul-2017].

[19]   EOS, "Plastic Laser Sintering System EOSINT P 800 - Processing High Performance Polymers Operating at up to 385° C," 2014. [Online]. Available: https://cdn1.scrvt.com/eos/public/446f91c814dfcdab/a552e77d1c5c6656a3c df3d4ba20c741/EOS_datasheet_EOSINT_P800.pdf.   [Accessed: 19-Jul-2017].

[20]   J. Lohn and H.-J. Schmid, "Aufbau einer Lasersinter-Versuchsanlage und Verarbeitung neuer Materialien am Beispiel von Polyamid 6 und Polyamid 613 Development of a test equipment and processing of new materials (PA 6 and PA 613)," in *Rapid. Tech–International Trade Show & Conference for Additive Manufacturing: Proceedings of the 14th Rapid. Tech Conference Erfurt, Germany, 20–22 June 2017*, 2017, p. 312.

[21]   J. Lohn and H.-J. Schmid, "Laser sintering of Nylon 6," in *27th Annual International Solid Freeform Fabrication Symposium*, 2016.

Chapter 6

SCALE-UP METHODOLOGY

This chapter describes possible scale-up methodologies in order to augment the lab-scale research to pilot-scale or more industrial proportions. As further optimization of the spray dried particles is necessary, a possible scale up methodology for the spray drying process is suggested albeit this section is mainly dedicated to the scale up of the mechanical milling method rotor milling.

6. 1. SPRAY DRYING

As mentioned in Chapter 2, a lab scale Buchi Mini Spray Dryer B-290, which can achieve a reported maximum particle size of 25 μm [62], was used for optimization of the processing parameters. After optimization of these processing parameters it was the goal of this research to scale up the process to a pilot system in order to achieve larger particles as optimization directly on a pilot system is not economically feasible.

The scale-up of spray drying processes has been mainly conducted based on experimental iterative procedures. Though some models do exist regarding scale-up from lab-scale set-up, due to the complexity of the drying process, often further fine-tuning of the process parameters is still necessary. Nevertheless, some fundamental models for upscaling the spray drying process do exist. Gil et al. [1] presented a pragmatic approach to process scale-up based on the drying kinetics and thermodynamic and fluid dynamics. In the thermodynamic step they propose a method based on energy and mass equations that aim to understand the correlations in temperature profile in the drying chamber (T_{in} and T_{out}), the drying gas and feed flow (GFR and FFR) between laboratory and a larger spray dryer. The atomization and particle formation step still today remains a much researched subject. Feed properties like solution viscosity and density as well as the atomization conditions like nozzle orifice, type and atomization energy are known to affect droplet size [2]–[4]. Assessment of mean droplet diameter is usually provided by instability theories as approximation for the actual droplet diameter from which the final particle size can be estimated. Particle formation is one of the most complex physical mechanisms of the whole technique and is specific to the material properties (viscosity, density, concentration, molecular weight) [4], [5]. Often the apparent density of the formed particles is necessary for a good estimation of particle size.

Arpagaus and Schwartzbach [2] have set up crude guidelines in expanding the spray drying methodology on the Buchi mini spray dryer to a larger pilot scale, the MOBILE MINOR™. As the drying chamber volume affects the complex drying process of the droplets greatly, using a larger chamber will have a strong effect on the process

requiring some changes in parameters. Starting from the optimal processing conditions of the Buchi laboratory spray dryer, a similar set of parameters is derived for the MOBILE MINOR™. Further adjustments subsequently allow for an increase in particle size. Figure 6-1 illustrates the difference in capacity between MOBILE MINOR™ and the Buchi B-290 Spray Dryer. The model is largely based on the use of aqueous solvents and although conversion factors do exist for extrapolation to more organic solvents, it does not seem to be directly applicable to the current solvent system used for PSU (DMF, 210 °C inlet temperature, 114 °C outlet temperature, 12 wt.%, 7,41 mL/min Feed Flow Rate, 821 L/h Gas Flow Rate). Table 6-1 compares the technical features of the MOBILE MINOR™ against the current Buchi B-290 Mini spray dryer as possible solution for spraying larger batches of polymeric powders. Notice the significant increase of particle size from the mini spray dryer B-290 to the MOBILE MINOR™.

The MOBILE MINOR™ is a product of GEA which produce a variety of lab scale as well as pilot scale spray dryers. GEA also has a Spray Dryer pilot test plant in Denmark which lends itself for initial upscale R&D testing. Other industrial companies also skilled in the art of spray drying which are susceptible for R&D testing include VITO [6] and ProCepT [7], the latter producing its own spray drying equipment achieving throughputs of 24 L per 8 h. The Advanced Powder Technologies and Innovative Solutions platform, APTIS [8], of the University Liege has one mobile minor for aqueous solutions and an ATEX rated spray dryer working on nitrogen or argon which lends itself more to organic solutions. Most of these pilot scale spray dryers work in closed loop meaning the recuperation of organic solvents is possible, decreasing the economic and ecologic factor bound to upscaling.
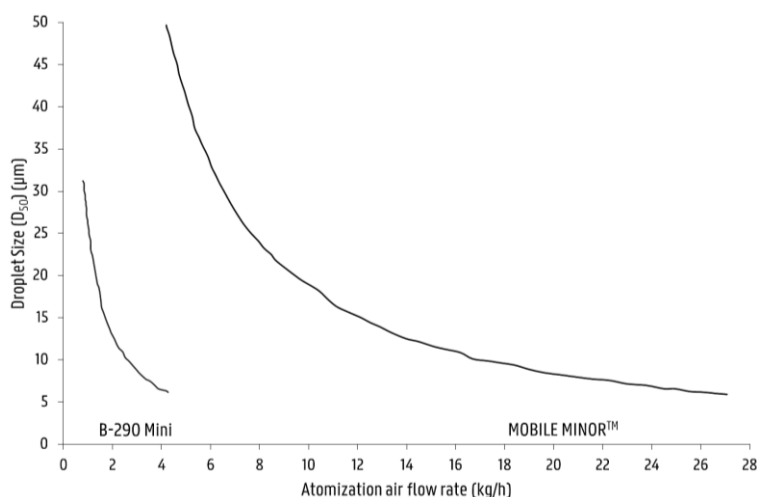

Figure 6-1: Water droplet size (D₅₀) as a function of atomization air flow rate for the MOBILE MINOR™ and the Mini Spray Dryer B-290 two-fluid nozzle [2]

Table 6-1: Technical features of the Buchi B-290 Mini Spray Dryer compared to the MOBILE MINOR™ [2]

Technical features	Mini Spray Dryer B-290	MOBILE MINOR™
Water evaporation capacity (higher for organic solvents)	1,0	0,5-6,0
Sample volume	30 mL – 1L	100 mL – 10L
Maximum drying flow rate (kg/h)	40	80
Atomization flow rate (two-fluid) (kg/h)	0,1 – 1 at 5 - 8 bar	4 – 25 at 0,5 – 6 bar
Heating power (kW)	2,3	9
Maximum inlet temperature (°C)	220	350
Volume drying chamber (m³)	0,0128	0,312
Nozzle configurations	Two-fluid (co-current), VOG[1]	Rotary atomizer, two-fluid (co-current and fountain mode)
General particle size (µm)	2 - 25	2 - 80

[1] VOG = Vibrating Orifice Generator, i.e. ultrasonic nozzle

6. 2. ROTOR MILLING

In this section the planning of a scale-up from laboratory scale to a production unit for a desired throughput is carefully considered. There is little research being done on the scale up of mechanical milling in terms of rotor milling. Often, empirical factors are provided by the manufacturer itself. Muller et al. [9] made a general review on the expansion of communition methods like ball milling and rotor milling to a facility size installation. They affirm that a crucial factor for scale-up of the laboratory rotor mill set-up is the grinding area A available in the mill. In the case of rotor milling this encompasses the surface area of the beater mills and the sieve area of the inset sieve. In this regard the grinding area of the rotor mill will increase with the square of the mill diameter. This is because both the height of the milling rods and the breath are proportional to the milling diameter.

$$height \sim Diameter; breath \sim Diameter: A \sim D^2$$

Muller et al. [9] further compared their theoretical correlation against the empirical data received from the manufacturers and found a good correspondence between the data. Furthermore they stress that, while expanding the milling set up, the stress intensity must be kept constant. Thus, the tip speed of the rotor, the stress tools, stress probability and classifying conditions must be kept constant.

In view of these postulations one can chose to increase production in two different ways. As the rotor milling procedure consists of three milling steps each by milling at different revolution speeds and different mesh size of the inset sieve, a set-up in which

different rotor millers are put in cascade ensures no change in stress intensity as the geometry of the millers are identical. In this way, the throughput of the process changes dramatically as the processing time is no longer the sum of all processing steps but only dependent on the limiting process step's time. A disadvantage of this option is that in case of a defect or overheating the whole line must be shut down to correct the problem.

Another option is to simply increase the throughput of each machine by simply expanding the milling technique to a pilot scale impact miller. There are several manufacturers that sell potential production scale pulverizers. Listed below in Table 6-3 is a short list of the most promising plants. All mentioned installations consist of an impact mill with classifier and are specialized in processing of softer more visco-elastic materials. Depending on manufacturer the mill is setup horizontally or vertically.

Due to short supply of research funds the latter options were not pursued and a scale up by cascade configuration was elected. More specifically, two Pulverisette 14 millers were set in cascade in combination with a large scale classifier (Analysette 18 (A18)) in order to speed up the final sieving step as well. The laboratory and more industrial sieve are also depicted in Table 6-4. Throughput and yield of the laboratory and cascade setup were compared to each other to see if the finished product can be obtained faster. In both cases sieving was performed with the use of sieving aids (glass balls) in order to punch out and prevent excessive blockage of the sieve during the classifying process.

6. 3. LABORATORY SET-UP

As described above the throughput and yield of the rotor milled process was calculated of the finished PSU product going through the three rotor milling steps and the finishing sieving step. Given below in Table 6-2 are the respective values of throughput and yield for each processing step while comparing the yield over time of the sieving step using the AS 200 vibratory sieve shaker and the A18 heavy duty sieve shaker. From Table 6-2 one can see that from the three-step communition method the rate defining step is the last milling step. From these values a scale-up is strongly recommended in order to increase production. From a laboratory standpoint a cascade setup with the P14 units is more feasible which will eliminate the time of the two proceeding milling steps. Additionally and more importantly, a splitting of the 80 µm milling step to two or more P14 units should also be considered. As the yields of the milling processes are very high thanks to the cyclone system, no considerable losses are expected. However, when high volumes of SLS powders are required pilot scale millers should be considered. Using the extra P14 units the milling work could be divided cutting the production time in half.

Another time limiting process is the final sieving step in order to achieve a better PSD. Here a RETSCH vibratory sieve was used. Due to the small diameter of the sieves, blockage occurs more rapidly, hampering the sieving process. When increasing the sieve diameter from 20 cm to 40 cm using the A18 this step is accelerated considerably (see Figure 6-2). Yields of 80 % are already achieved within the first half hour while for the AS 200 this is only around 20 %. As sieving time continues both yields continue to increase achieving 88 % after one hour for the A18 while the AS 200 reaches roughly 48%. Only after considerable time the AS 200 reaches comparable yields as the A18 is achieving yields of 90 % after 15 h (data not shown).

Table 6-2: Throughput and yield of the Pulverisette P14 going through its three-step communition process

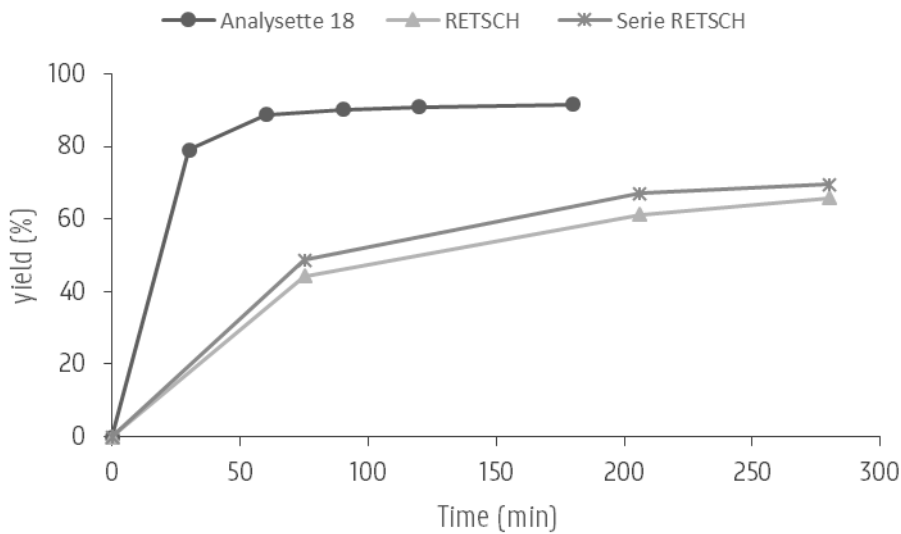| Rotor Milling		
Sample	Throughput (kg/h)	Yield (%)
Milling to 500 µm	0,265	99,42
Milling to 120 µm	0,022	99,72
Milling to 80 µm	0,009	99,02

Figure 6-2: Yield of the different sieve setups over time

Table 6-3: Upscale possibilities for the FRITSCH pulverisette 14 laboratory pulverizer (listed first in table). External (outside milling unit) or internal (inset sieves around milling unit) classifiers are present in all cases

Figure	Product series	Manufacturer	Communition principle	Classifier	Capacity (kg/h)	Fineness (µm)	Cooling
A	Pulverisette 14	FRITSCH Gmbh	Impact pulverizing from high speed rotor with rods	internal	1-5	Down to 40 µm	Air cooled
B	Impact Classified Mill	Mill Powder Tech Solutions	Impact pulverizing from high speed rotor with rods	internal	50– 300	400 – 5	Water cooling and/or cool air feeding
C	TM Series	Mill Powder Tech Solutions	High speed rotating wings, impact related communition	internal	50 - 2000	2000 - 44	Air cooling
D	PM series	Mill Powder Tech Solutions	Impact pulverizing from high speed rotor with multiple sets of rods	internal	30 - 2000	841 - 100	Air cooling
E	Condux	NETZSCH	Impact pulverizing from high speed rotor with rods	internal	DNF	30 - 800	Air cooling
Figures:							
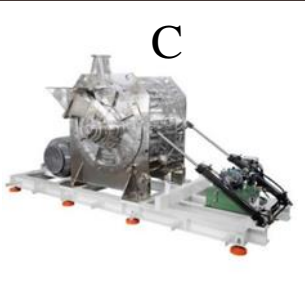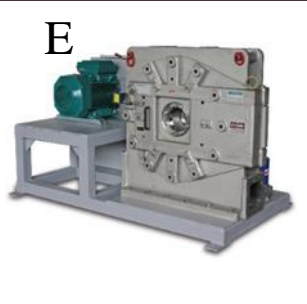
Table 6-4: Upscale possibility for the RETSCH Vibratory Sieve Shaker AS 200 digit (listed first in table) with the Analysette 18 of FRITSCH.

Figure	Product series	Manufacturer	Classifying principle	Classifier diameter (mm)	Fineness (µm)	Set used	Maximal sample quantity (kg)
A	Vibratory Sieve Shaker AS 200 digit	RETSCH Gmbh	Analytical Sieve Shaker	200	125 & 90	Up to 3 sets of collection pan, 90µm and 125 µm sieve	3
B	Analysette 18	FRITSCH Gmbh	Analytical Sieve Shaker	400	125 & 90	1 set of collection pan, 90µm and 125 µm sieve	15
Figures:	A			B			

6. 4. CONCLUSIONS

Both the spray drying process and the rotor milling process have been proven in the previous chapters to achieve spherical particles when processing polymer pellets. As both methods were optimized on laboratory scale equipment increasing throughputs through scale-up seems logical. Though several methods and pilot plants exist for the scale up of spray dryers, further optimization of the laboratory technique is necessary regarding particle density before examining these steps in depth.

As for the rotor milling technique, increasing throughput is usually done by increasing the grinding area. This can be done in several ways. One of them is putting several P14 units in cascade formation, limiting the process time to the rate defining step, being the 80 µm milling step. Splitting this milling step over several P14 units further decreases milling time in this regard. A less cumbersome approach however would be upgrading the P14 to a more industrial size miller. These however are often quite costly but operate on the same principle. In the current work, an additional P14 unit was obtained and a larger size vibratory sieve. Especially in the case of the vibratory sieve high yields (88% in 1 h) were achieved much earlier into the sieving process speeding up this step significantly.

6. 5. REFERENCES

[1]   M. Gil, J. Vicente, and F. Gaspar, "Scale-up methodology for pharmaceutical spray drying," *Chim. oggi/Chem Today*, vol. 28, no. 4, pp. 18–22, 2010.

[2]   Buchi and GEA Niro, "Scale-up from the Buchi Mini Spray Dryer B-290 to the Niro Mobil Minor," *Information Bulletin*, 2008. [Online]. Available: http://static1.buchi.com/sites/default/files/downloads/B-290_Scale-up_B-290_Niro_MOBILE_MINOR_en_01.pdf.

[3]   J. Vicente, J. Pinto, J. Menezes, and F. Gaspar, "Fundamental analysis of particle formation in spray drying," *Powder Technol.*, vol. 247, pp. 1–7, 2013.

[4]   R. Vehring, "Pharmaceutical particle engineering via spray drying," *Pharm. Res.*, vol. 25, no. 5, pp. 999–1022, 2008.

[5]   A. B. D. Nandiyanto and K. Okuyama, "Progress in developing spray-drying methods for the production of controlled morphology particles: From the nanometer to submicrometer size ranges," *Adv. Powder Technol.*, vol. 22, no. 1, pp. 1–19, Jan. 2011.

[6]   "VITO," 2017. [Online]. Available: https://vito.be/en/materials/optimising-products-and-processes/customised-and-versatile-granules.

[7]   "ProCepT: Particle Processing Equipment." [Online]. Available: http://www.pro-c-ept.com/.

[8]   U. Liege, "Advanced Powder Technologies and Innovative Solutions," 2017. [Online]. Available: http://www.aptis.be/.

[9]   F. Muller and R. F. Polke, "From the product and process requirements to the milling facility," *Powder Technol.*, no. 105, pp. 2–13, 1999.

Chapter 7

PROCESSING OF POLYSULFONE/LAYERED SILICATE NANOCOMPOSITES

This chapter is devoted to an alternative way of expanding the gamma of materials: by making composites with enhanced properties. It encompasses a state of the art of polymer/clay nanocomposites and extrapolates this knowledge to the polysulfone-montmorillonite system. The functionalization of the nanoclays is discussed in a first part after which the blending via twin-screw extrusion with the associated characterization follows.

7. 1. STATE-OF-THE-ART

7. 1. 1. Introduction

As mentioned earlier, one of the main stumbling blocks in the progression of the laser sintering technology is the limited range of materials that can be processed using SLS. Next to adding new materials with significantly different properties than the currently available polymers, another way of expanding the material palette is by modifying the existing polymers. This is usually done by making blends [1], [2], adding fillers [3], [4] or grafting new functional groups on the polymer backbone [5]–[7] to enhance certain properties of the material or add a new property entirely. Most of the published work however focusses on adaptations of polyamide materials while not much has been carried out on distinctly new polymers. For this reason, this work builds further on the modification of novel polymers which have been proven to be able to be processed successfully to spherical powders in this thesis. Chapter 4 pointed out that polysulfone could be processed mechanically through rotor milling and physicochemically by spray drying into spherical powders and was therefore chosen as test material. The sulfone polymers combine thermal stability, high strength and toughness, hydrolytic stability and resistance to various chemical solutions, making them ideal suitors for membrane applications such as for solvent (nano-)filtration [8]–[10], microfiltration, reverse osmosis and gas separation [9]. The sulfone moiety in the polymer backbone makes the polymer relatively more polar yet renders it a bit more prone to hydrolysis. The addition of nanofillers could improve this resistance to hydrolysis. There has been growing interest in clay-containing polysulfone nanocomposites [9], [11], [12]. Most used minerals in these polymer composites are smectic clays of which montmorillonite (MMT) is the most popular in scientific work. The layered silicates of the MMT can improve hydrolytic stability by increasing the tortuosity of the diffusive path of the penetrating solvent molecule [13]. The incorporation of more polar MMT fillers results moreover in the improved wettability of the membranes which in turn could cause improved anti-fouling properties [9].

Furthermore, nanofillers only require a small amount to be added to the neat polymer in order to experience these benefits, usually between 0,5 to 5wt.% [9], [12], [14].

Conventionally, nanocomposite polymers are produced by phase-inversion (i.e. solution-dispersion) [12], in situ polymerization [9] or melt-intercalation [15]. In this work, the latter method will be used as a way of homogeneously distributing the MMT clay through the polymer matrix while attempting to achieve intercalation of the polymer through the MMT clay platelets. This method eliminates the excessive amounts of solvent often needed for phase inversion and can be easily scaled up to industrial levels. As the polymer and silicates differ in polarity, a chemical modification of the MMT is performed in order to achieve better compatibility with the polymer matrix. After melt processing, the extruded films are characterized on their intrinsic and extrinsic properties in order to determine any changes in thermal, mechanical or chemical behavior. Upon successful creation of the polymer composites, the strategy for creating the feed material for SLS would be to shred the extruded nanocomposite films and process this material via the three step rotor milling procedure.

7. 1. 2. Montmorillonite nanoclays

Montmorillonite is a natural silicate consisting of a layered structure of platelets of only a few nanometers thick. Its general formula is $(Na, Ca)_{0,33}(Al, Mg)_2(Si_4O_{10})$. The basic structure of the clay layers can be seen as a stacking of two types of structural sheets in a certain ratio. MMT is the most common member of the smectite group and has a 2:1 confirmation (T-O-T) in which the octahedral alumina sheet (O) is sandwiched between two tetrahedral silicate layers (T) (Figure 7-1). These platelets are weakly bound by Van der Waals forces. Partial isomorphous substitution of Si^{4+} by the trivalent metal cation Al^{3+} in the tetrahedral sheet and substitution of Al^{3+} by the divalent metal cation Mg^{2+} in the octahedral sheet causes a charge deficit. This overall negative charge is balanced out by a number of exchangeable cations electrostatically fixed in between the layers of the clay platelets keeping the platelets together. This phyllosilicate has a large cation exchange capacity (CEC, 145 meq/100g [16]) and can easily swell in aqueous solutions making it an ideal candidate for functionalization to improve compatibility with the polysulfone matrix.
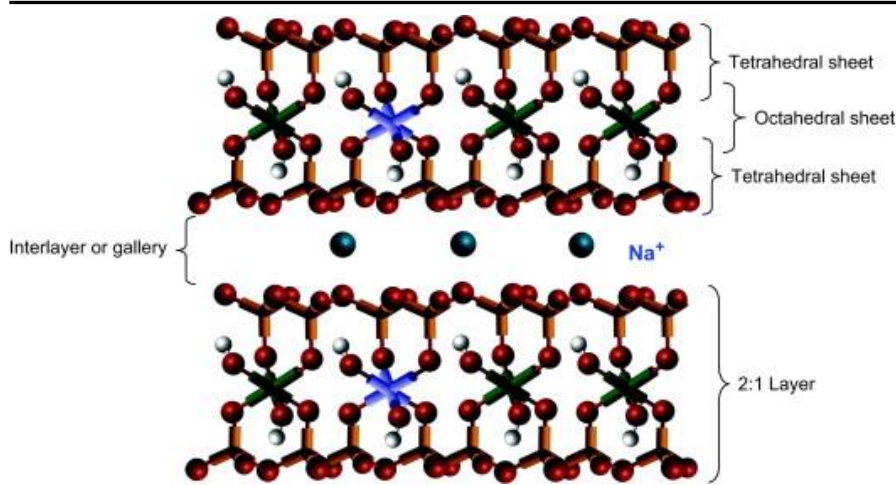
Figure 7-1: The 2:1 smectite structure showing an octahedral sheet sandwiched between two tetrahedral sheets [17]
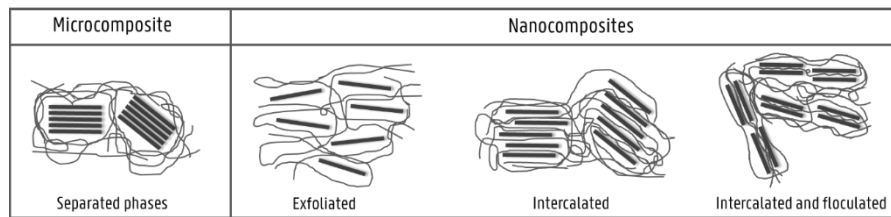
Figure 7-2: The different polymer-nanoclay morphologies possible

7. 1. 3. Polymer-clay nanocomposite morphology

MMT is a densely packed phyllosilicate with a basal spacing in the order of 1 nm [18]. This spacing is too dense for the polymer to properly penetrate the layers and achieve a good dispersion. This aspect of penetration of the polymer chains between the clay platelets is of upmost importance in order to benefit from the exquisite properties that come about MMT-composites. Figure 7-2 depicts the different composites that can be formed when distributing clay particles in a polymer matrix. In the case of a microcomposite no penetration of the polymer chains into the phyllosilicate interlayers has occurred. Two phases are present: the clay particles clustered together and the polymer phase. In an intercalated composite the polymer chains have achieved a certain amount of penetration between the clay platelets, increasing the interlayer distance. The repetitive multilayered structure is preserved however, causing the polymer chains to orient themselves in a parallel manner with the phyllosilicate sheets. This expansion in the interlayer distance can be measured using XRD analysis and manifests itself as a shift in the diffraction peak towards lower angles in the diffractogram [7], [15], [18]. In the flocculated nanocomposites there is no real intercalation of the polymer molecules into the clay galleries. The layers exhibit a partly exfoliated structure with either individual or nanometer thick multilayer aggregates. A smaller diffraction peak can be observed in the XRD diffractograms

131

indicating the existence of the smaller nanometer-thick layer aggregates. The diffraction peak usually exhibits angles smaller than that of pristine nanoclays as some degree of intercalation usually occurs [19]. Finally, exfoliated clays can occur in which the clay galleries are completely separated from each other in the polymer matrix and randomly oriented. This type of composite gives the best material properties and is accompanied by a loss of diffraction peaks in the XRD diffractogram [19], [20].

7. 1. 4. Polymer-clay nanocomposite production method

Conventionally, nanocomposite polymers are produced by phase-inversion (i.e. solution-dispersion) [12], in situ polymerization [9] or melt-intercalation [15]. The first method developed was in situ polymerization. In this technique the monomer was used for the dispersion of the clay and polymerization was carried out in between the clay platelets by choice of favorable production conditions of fixed catalyst inside the clay gallery [9], the driving force for complete exfoliation being the polymerization reaction. A second method is solution dispersion in which the clay minerals are first exfoliated in a suitable solvent that also serves as a solvent for the polymer. The solvent is subsequently evaporated reuniting the layers which are now intercalated with the polymer chains [12]. Melt intercalation is a technique based on the distributive and dispersive mixing of the clay minerals in the polymer melt state. It is generally considered more economical as it does not involve the use of solvents and it is more flexible for upscaling to industrial size production. In this process the polymer chains are dragged through the clay galleries causing intercalation or even exfoliation. As the overall entropy of the polymer chains decreases upon intercalation the driving force of the melt intercalation process is the enthalpic contribution of the polymer-clay interaction. If the layer surface isn't sufficiently compatible with the matrix, several methods can be addressed to increase compatibility [15]. These are addressed in the next section.

7. 1. 5. Polymer-clay nanocomposite interaction

As mentioned before, a difference in polarity exists between the smectite and polysulfone. In case of a large difference between the filler and matrix, the former will not be dispersed homogeneously in the latter causing agglomeration which will result in a phase separated composite. In order to prevent this, surface modification of the nanoclays is usually performed to reduce the surface energy of the clay layers and match their polarity with that of the polymer. This tailoring of the clays is generally done in three ways: in the first method, the cations of the montmorillonite are exchanged with cationic surfactants (alkylammonium or alkylphosphonium ions) fitted with a hydrocarbon tail which ideally mimics the molecular structure of the polymer matrix. This method is commonly called organophillization [21], [22]. A second approach is through the use of compatibilizers. Often these consist of a polymeric backbone with a reactive group as side chain. The low molecular weight

polymer can penetrate the layers of the montmorillonite more easily and binds with the functional group of the counter ion of the organoclay [14], [23]. In this way, it can reduce the aggregation of MMT in the non-polar matrix. Maleic anhydride is an often used reactive group of the compatibilizers. A third approach is the chemical functionalization of the clay platelets themselves. In this case a covalent attachment of the functional groups on the phyllosilicate sheets is performed. The compounds would benefit from a higher chemical stability as they are irreversibly bound to the sheets [24]. Grafting of these functional groups is most commonly done by silylation on the surface hydroxyl groups. In this regard (3-aminopropyl)triethoxysilane (APTES) is a compound used by many researchers [7], [21], [24], [25].

7. 1. 6. Polymer-clay properties

7. 1. 6. a. Mechanical properties

With the addition of nanoclays the polymer properties can be improved in areas where it is lacking creating a nanocomposite with demand characteristics for a desired application. Nanoclays have been known to increase modulus and stiffness of the polymer matrix because of their rigid structure. The mechanism of this reinforcement lies in the higher resistance against straining of the filler materials. When the composite is subjected to a stress condition, part of the load will be carried by the clay platelets. The better the dispersion, interaction and exfoliation/intercalation of the clay particles, the better the load can be transferred to the more rigid clay plates. Enhancing the polymer-clay interfacial contact is of prime importance in order to increase more sufficiently the mechanical properties of the nanocomposite.

The use of nanoclays in the polymer matrix has a significant effect on the polymers' mechanical properties. MMTs have been widely incorporated in a large variety of materials like polypropylene and polyamide materials like PA6 [13], [15], [18]. Suprakas et al. [18] and Ali Olad [13] reported some of the research done on polymer-clay nanocomposites and summarized that polyamide-clay nanocomposites have shown a highly improved stress at break because of the higher degree of exfoliation due to the better compatibility of the more polar polymer chains and the surface of the clay. Non-polar polymers such as polyolefines exhibit less favorable interactions resulting in lower degree of exfoliation. These generally exhibit less improved or even decreased values of stress at break and require the use of compatibilizers in order to improve. Elongation at break is found to be similarly dependent on the interfacial interactions with both increasing and decreasing values reported in literature.

Polysulfone-clay polymers have also been subject to investigation. Sur et al. [11] investigated the use of organically modified MMT in PSU composites in 1, 3 and 5wt.% by mixing through the solution-precipitation technique and reported modest improvements in mechanical properties. They postulated that, since PSU already has outstanding mechanical properties [26], the extent of improvement will never be as

significant as with relatively weaker polymers. They continue to encourage the investigation of other properties like permeability, flame resistance, resistance to solvents and hostile environments in general. They conclude with the remark that only a low amount of weight percentage nanoclays is needed for good exfoliation, reporting a decrease in tensile strength when exceeding 3wt.% (Figure 7-3).

As polysulfone already exhibits good mechanical properties, these are only subject to slight improvement. Nevertheless, the effect of clay content and modified clay content on the mechanical properties of the PSU matrix is investigated in this work. The purpose is to determine the influence of melt intercalation on the mechanical properties and determine if any detrimental effect of the MMT on the PSU properties exists.
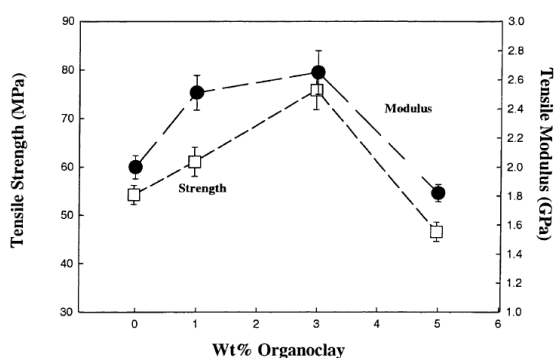
Figure 7-3: Effects of modified clay content on the tensile strengths and moduli of the PSU nanocomposites in elongation reported by Sur et al. [11]

7. 1. 6. b. Barrier properties

One of the most prominent features that occur in clay nanocomposites is the significant improvement of the barrier properties. The clay platelets of the montmorillonite are naturally impermeable for liquids and gasses. When added to a polymer matrix they hamper the diffusion of solvent or gas molecules by increasing their diffusive path through the composite. This increased pathway is also known as the *tortuous path*. This enhanced tortuous path (Figure 7-4) increases the stability towards oxidation and decreases solvent adsorption [13]. Yeh et al. [27] investigated the corrosion prevention by incorporation of MMT into the PSU matrix. They reported that low amounts of clays (e.g. 1 wt.%) were found to be superior in anticorrosion properties compared to the bulk and related the increase of tortuosity of the diffusion pathway to this phenomenon.

Figure 7-4: Tortuous path model for molecules in nanocomposites (left) versus conventional composites (right)

7. 1. 6. c. Anti-fouling properties

Membrane technology is an efficient and powerful technique which is growing at considerable pace because of a number of attractive features in the separation process for the removal of contaminants from aqueous and organic systems. It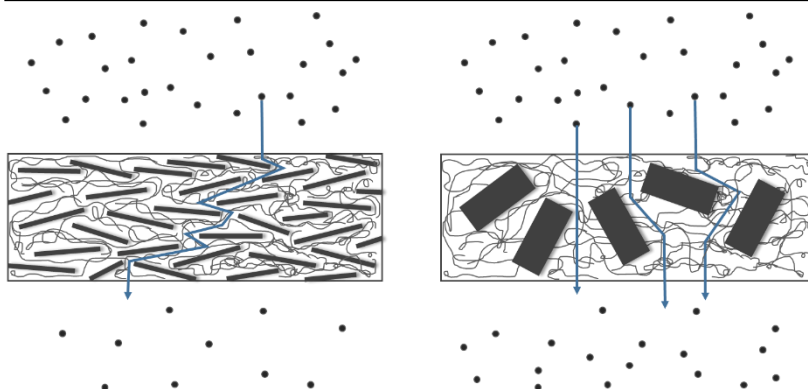 is an environmentally friendly technique operating under mild conditions, low energy consumption and requires no additives or phase changes. However, one of the main problems in the separation process is the adsorbance of hydrophobic substances like proteins on the surface or adherence of substances inside the pores of the membrane [6]. This fouling of the polymer membrane results in a deterioration of the filtering performance and increases energy consumption to repair or replace the membrane. It is therefore critical in the field of membrane technology to develop a polymer membrane with good anti-fouling properties and high chemical and biological stability. Polysulfone, as mentioned before, is an amorphous high performance engineering polymer that offers good toughness and rigidity, strength and chemical stability towards a wide variety of solvents as well as heated aqueous systems making it possible to operate at elevated temperatures [26]. Because of its more hydrophobic nature, the application for filtration in aqueous systems remains rather limited due to the risk of fouling. Studies have demonstrated that an increment in the hydrophilicity of the membrane material could reduce the fouling by diminishing the adsorption of substances [6]. This can be done by adding the more hydrophilic MMT nanoclays to the polymer matrix. Wang et al. [28] investigated the surface wettability of the nanocomposite consisting of poly(vinylidene fluoride) (PVDF) with polyvinylidone (PVP)-grafted MMT through contact angle measurements and stated that surface hydrophilicity increased with addition of the nanoclays. They modified the MMT by grafting with N-vinylpyrrolidone, stressing the importance of a chemical compatibilizer in order to achieve good dispersion.

In this study MMT will be modified in a two-step process: the clay platelets will be grafted by silylation following amide bond formation with 4-sulfophtalic acid in order to achieve good compatibility with the polysulfone matrix.

7. 1. 7. Functionalization of pristine montmorillonite

In this research MMT is functionalized chemically by grafting an organic compound with a sulfon moiety onto the nanoclays to ensure wetting of the clay particles by the polysulfone matrix. This is done in a two-step chemical reaction in which the clay particles are first coupled to a silane compound (APTES) followed by coupling with 4-sulfophtanic acid (Figure 7-5).

The method of grafting (3-aminopropyl)triethoxysilane on pristine Na⁺-montmorillonite was adopted from Liao et al. [21] who investigated both the effect of organophillization using cetyl trimethyl ammonium chloride (CTAC) and chemical functionalization of the clay particles using APTES in polysulfone for anion-exchange membranes. Liao used the solution precipitation technique to form the membrane and characterized them using XRD and Fourier transform infrared (FTIR) to determine the functionalization to be successful. Prasad et al. [25] further builds on this research and links 4-sulfophthalic acid (SPA) via formation of an amide bond on the amine moiety of the APTES molecule. The coupling of the SPA is an interesting addition as it binds both an aromatic structure and a sulfonic acid to the clay platelets ensuring better interaction with the polysulfone matrix. Again, the composite is formed by using solution precipitation and characterized using XRD and FTIR. The functionalization procedure described is adopted in order to ensure good distribution of the clay platelets in the PSU matrix and is discussed in the following sections.
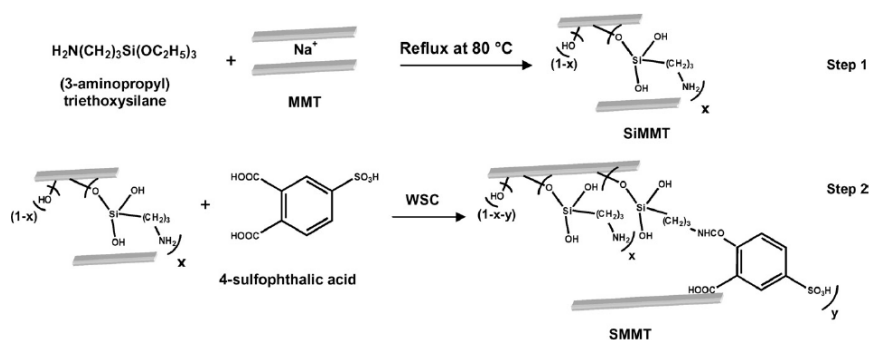

Figure 7-5: Chemical functionalization of pristine NaMMT to sulfonated MMT (SMMT) via silylation of the NaMMT using (3-aminopropyl)triethoxyamine (APTES) and a carbodiimide (WSC). Method described by [7]

7. 1. 8. Silylation of pristine NaMMT

Grafting by silylation on the clay particles is one of the most effective ways to chemically immobilize functional groups on the surface and in the interlayer space of the MMT clays. In the first functionalization step (Figure 7-5, Step 1) the surface hydroxyl groups act as anchoring points for a condensation reaction with the APTES molecules. In order to ensure intercalation of the polysulfone, functionalization of the MMT clay predominantly has to occur inside the clay galleries. In the case of montmorillonite, the broken edges are known to be the most reactive sites for grafting [24]. Next to this, a number of hydroxyl groups is conjectured to be present in the interlaminar space as a result of structural defects and irregularities. The abundance of occurrence of the hydroxyl groups can furthermore greatly be affected by acid activation in which the interlayer cations are exchanged with H^+ ions. The successful grafting in the clay galleries is often corresponding with a shift in the basal spacing of the MMT.

Figure 7-6 depicts the silylation step of the reactive silanol groups of the clay galleries using APTES. In a first step hydrolysis of the reactive siloxanes occurs with the expulsion of EtOH. Afterwards condensation occurs between the hydroxyl groups of the silanol and MMT sheets [7], [24], [25].
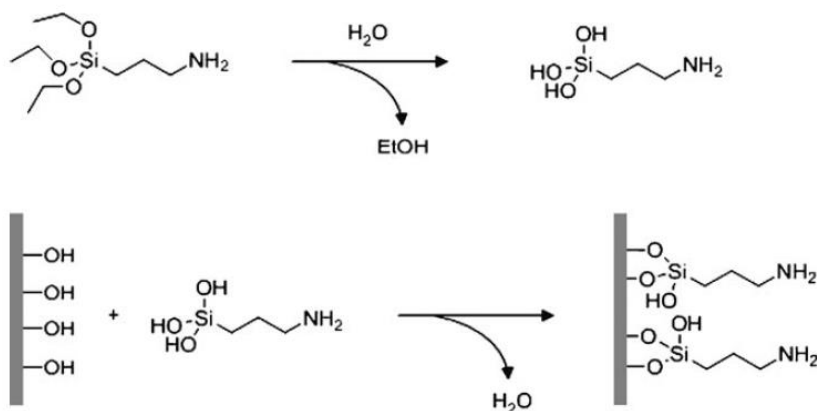
Figure 7-6: Mechanism for the silanization with (3-aminopropyl)triethoxyamine (APTES). Hydrolysis of the reactive siloxanes occurs in a first step followed by condensation with the surface silanol groups of the MMT platelets [29]

The polarity of the solvent plays an important role during silylation as it influences the amount of silane loading. During grafting silanes simultaneously condensate with themselves and form oligomers. These silanes can then condensate with the two adjacent layers of the MMT locking the two sheets covalently together. Su et al. [30], [31] did extensive research on this 'locking effect' and made a clear distinction on the influence of polar protic solvents and apolar solvents used in the silylation process.

Their claim is dual; they state that, as polar protic solvents contain dipoles they solvate the silanol groups on the MMT sheets and form a solvent cage around the latter making the silanol less available to react with the silane. Meanwhile apolar solvents do not solvate the silanol moieties which leads to a higher degree of silane loading on the MMT. This greater ease of silylation however leads to polysiloxane oligomers to be formed and grafting of neighboring MMT sheets locking the interlaminar space. Silylated clays using polar protic solvents remain expandable. Figure 7-7 recapitulates their findings for the different solvents used.
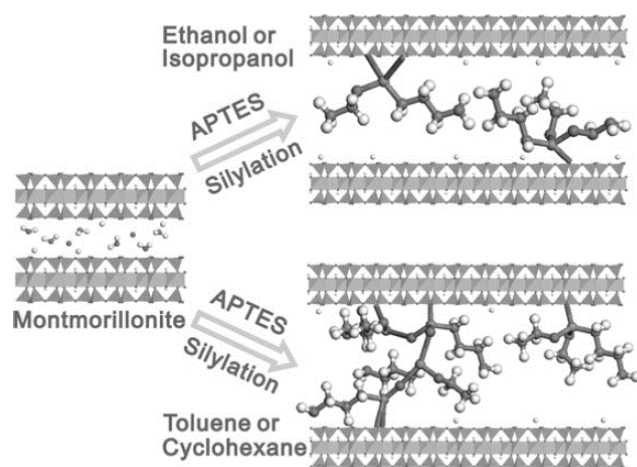
Figure 7-7: Schematic illustration of MMT silylation with APTES in various solvents according to Su et al. [31]

7. 1. 9. Sulfonation of the silylated MMT

The second step in the functionalization of the nanoclays encompasses a sulfonation of the silylated clays through formation of an amide bond between the amine moiety of the grafted APTES molecules and the carboxylic acid moiety of the 4-sulfophthalic acid (Figure 7-5, step 2).

When mixing an amine with a carboxylic acid, an acid-base reaction occurs first to form a stable salt. As depicted by Figure 7-8 adverse thermodynamics have to be overcome in order to obtain the amide bond and prevent hydrolysis [32].
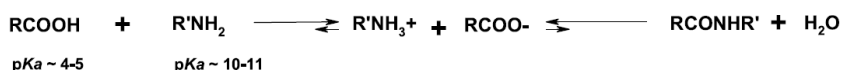
Figure 7-8: Reaction scheme of amide bond formation [32]

In order to lower the activation energy of the amidation a carboxyl activating agent is used to form a reactive intermediary. 1-Ethyl-3-(3-dimethylaminopropyl)

carbodiimide (EDC) is a compound often used in literature [7], [25], [32], [33]. The reaction scheme is depicted in Figure 7-9. It shows the formation of an active ester which can easily be detached by a nucleophilic attack of the amine group of APTES forming an ureum derivate as side product. The reaction mechanisms are elaborately described in literature [32], [34].

Figure 7-9: Reaction scheme of amide bond formation with the amine from APTES using a carbodiimide for the formation of a reactive intermediary with the carboxylic acid of 4-sulfophthalic acid (SPA) [35]

The formation of the active ester called O-acylisourea is depicted in Figure 7-11. The intermediary is generated by the protonation 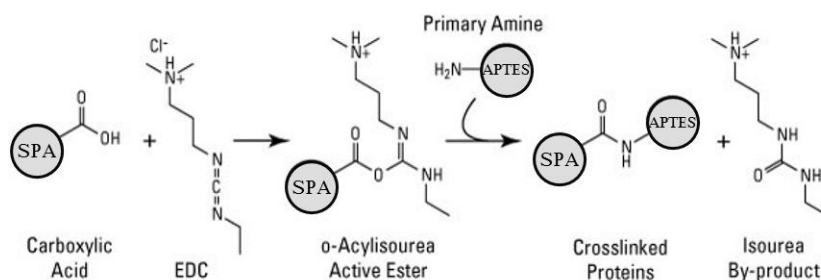of the EDC to a carbocation (1, Figure 7-10). The active carbocation can either react with a dissociated carboxylic acid to form the active ester (3, Figure 7-11) or hydrolyze into a urea derivate (2, Figure 7-10). In the former case, the dissociated carboxylic acid attacks the carbocation.

With the formation of the active ester, amide bond formation is possible in two ways. In the first, a non-dissociated nucleophile, such as the primary amine from the grafted APTES (5, Figure 7-12), attacks on the carbonyl of the O-acylisourea (3) resulting in the desired amide (6) with the urea formation (2) as a side product. In the second case, a carboxylate, which is a strong nucleophile, can also attack on the carbonyl moiety of the O-acylisourea giving an acid anhydride (7, Figure 7-13) and urea derivate. Here, a non-dissociated primary amine can also attack on the carbonyl moiety resulting in the amide bond (6) and a carboxylate.

In the absence of other nucleophiles the activated ester is prone to hydrolysis which regenerates the carboxylic group of SPA. Since there is an excess of H_2O compared to amines hydrolysis is assumed to be the most pronounced reaction mechanism. Furthermore, often racemization and acetyl transfer can occur creating the unreactive N-acylurea (4, Figure 7-14) which is unreactive towards primary amines. According to Hotan Mojarradi [34] often the unreactive N-acylurea is formed. Montalbetti et al. [32] states that this side reaction however can be greatly diminished by reacting the EDC and SPA at 0 °C before adding the amine. Gosalawit et al. [7] and Prasad et al. [25] both confirmed the successful amidation on MMT by the use of APTES, SPA and the EDC through and increase in interlayer space visible in XRD and the existence of characteristic peaks in FTIR.

The activation of the carbodiimide requires slightly acidic pH for protonation to a carbocation (pH 3.5 – 4.5 [35], [36]). However, at a pH of 4.75 the hydrolysis rate of O-acylisourea has been estimated to be 2-3 s^{-1} [34] meaning that the active ester is deactivated fast resulting in a low amount of amide to be formed. The formation of a more stable active ester with lower hydrolysis rate could greatly increase the amount of amide formed. N-hydroxysuccinimide (NHS, 8, Figure 7-15) has been reported in several papers to be successful in this regard [32], [34], [36]. NHS binds with the O-acylisourea to form a succinimidyl ester, which is more hydrolytically stable. ThermoScientific reports half-life values of 4-5 hours at pH 7, 1 hour at pH 8 and 10 minutes at pH 8,6 [36]. The substitution reaction with the formation of the more stable succinimidyl ester is shown in Figure 7-15. The hydroxyl group of the NHS (8) makes a nucleophilic attack on the carbonyl of the O-acylisourea (3) resulting in the succinimidyl ester and an urea derivate. The hydrolysis stable NHS-ester can be attacked by a non-dissociated primary amine resulting in the amide bond (6) and regenerating NHS. Furthermore, the formation of the unreactive N-acylurea is hindered as the NHS-ester cannot undergo the N $\rightarrow$ O displacement.

In order to buffer the pH increase due to the consumption of a proton by the activation of the carbocation a buffer is advised [34]–[36]. 2-(N-morpholino)ethanesulfonic acid (MES) is often used, it is a buffer which will not take part in the amidation in any way and has a pKa value of 6,15.
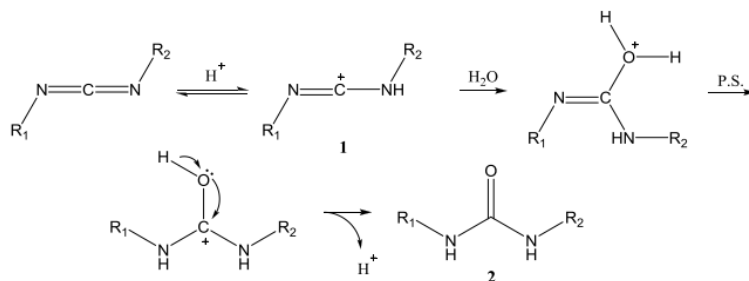
Figure 7-10: activation of the carbodiimide and possible hydrolysis of the activated carbocation to an urea derivate [34]
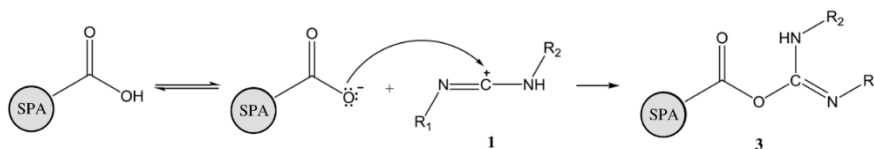
Figure 7-11: Formation of O-acylisourea [34]
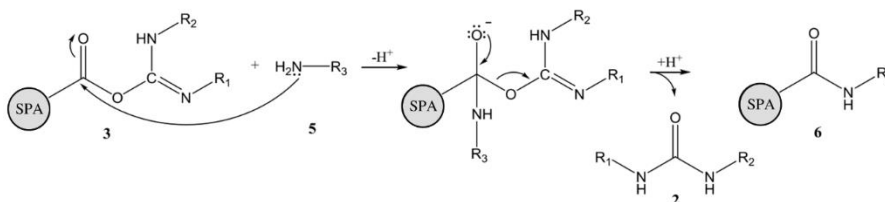
Figure 7-12: Formation of the amide via the O-acylisourea intermediary [34]
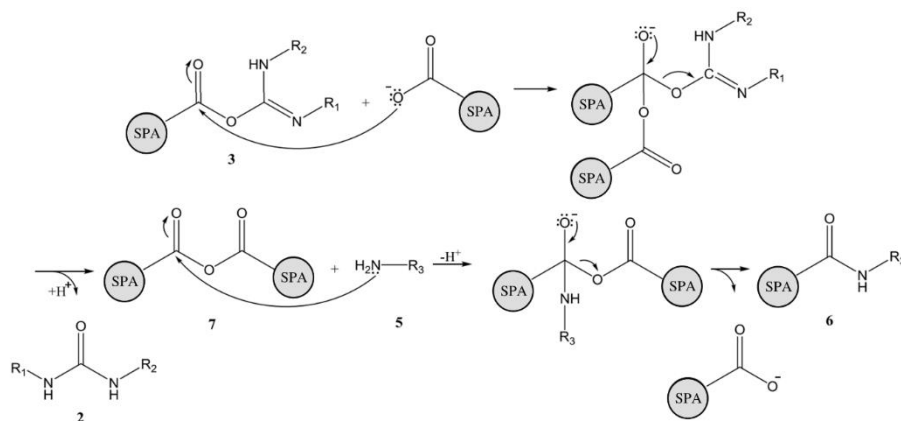
Figure 7-13: formation of the amide bond via acid anhydride formation [34]
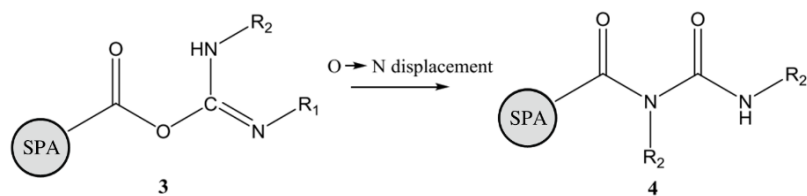
Figure 7-14: Formation of the more energetically stable N-acylurea which is unreactive towards amines [34]
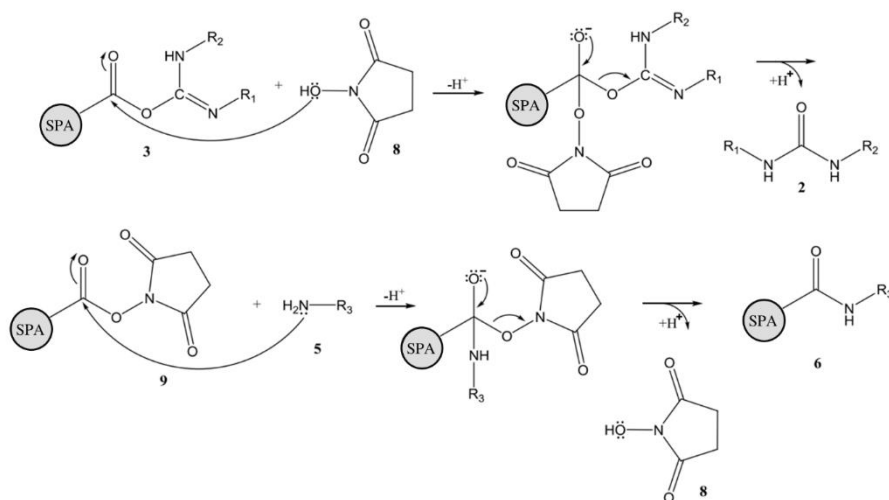
Figure 7-15: Formation of amide via the more stable succinimidyl ester [34]

7. 1. 10. Twin-screw extrusion

As mentioned above, melt intercalation is generally considered more economical as it does not involve the use of solvents and is more flexible for upscaling to industrial size production. The high shear and elongational flow in twin-screw extruders is said to be much more effective in dispersing tactoid clay particles than single screw extruders [37]. For this reason along with the buildup expertise of the CPMT research group on the subject [37], this technique was chosen for the processing of the polysulfone-montmorillonite composite. As the optimization of the twin-screw process lies beyond the scope of this research a brief introduction into the principles of twin-screw extrusion as a method for melt intercalation of montmorillonite nanoclays in the polysulfone matrix will be given.

7. 1. 10. a. Twin-screw extrusion principle

Figure 7-16 depicts a schematic description of the twin-screw extruder. It illustrates two auger screws which rotate in a heated cylindrical barrel causing the material that is fed through a hopper to be pushed forward. In the melting zone the material starts to melt because of the applied heat of the heated barrel, viscous dissipation and friction. Other materials may be fed from different side feeders along the heated barrel depending on the residence time needed. The molten polymer passes a series kneading blocks and conveying elements that improve the level of mixing. Eventually, the polymer is pumped out through a die at high pressure.

The twin-screw extruder can be further classified according to the interpenetration and the direction of rotation of the screws. Based on the degree of interpenetration the twin-screw extruder can be seen as intermeshing or non-intermeshing. The former implying that C-shaped chambers are formed which positively convey the polymer material towards the end of the extruder. In the latter this is not the case. Additionally, when the two screws rotate in the same direction the extruder operates in a co-rotating regime which is most common for compounding. In the counter-rotating regime the screws rotate in opposite directions. These are known to impart significantly higher stresses over a longer residence time due to partial reverse conveying of the material. This however comes at much greater risk of thermomechanical degradation [38] and is therefore not selected.

In this research the co-rotating twin-screw extruder Coperion ZSK 18 MEGAlab is used with closely intermeshing screws.
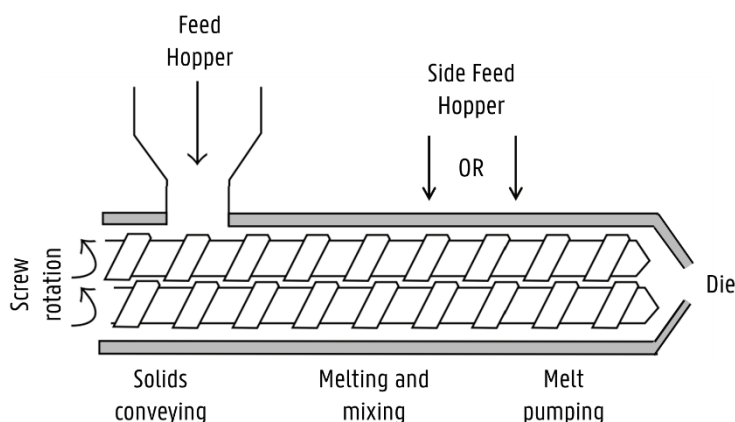
Figure 7-16: Schematics of the twin-screw extruder, adapted from [39]

7. 1. 10. b. Factors influencing nanoclays dispersion

The dispersion of the polymer/layered silicate nanocomposites is affected by both the type of twin-screw extruder and its settings. Research has shown that the dispersion of the nanocomposites is dependent on temperature, residence time, screw speed and feed rate [38], [40], [41]. In general, increasing the shear intensity and mean residence time tend to lead to better dispersion and intercalation and/or exfoliation. In this regard lower feed rates are often preferred because of their better dispersion due to a longer mean residence time. Lertwimolnun et al. [40] found the ratio of screw speed to feed rate to be a determining factor for the exfoliation level. Additionally, the location of the feeding of the clay plays an important role in this part as it determines for a great deal the residence time of the clay in the barrel. An optimal shear stress needs to be found for each process, exceeding a critical level of shear stress could lead to thermomechanical degradation resulting in bad final properties of the nanocomposite. In order to further prevent thermomechanical degradation, lower temperatures are also favored. They lead to higher melt viscosity, also increasing the shear stress and promoting exfoliation.

The screw configuration of the twin-screw extruder is another parameter that has an influence on the dispersion of the clay platelets in the polysulfone matrix. L. Delva [37] did extensive research on the influence of the screw configurations affecting the state of intercalation and exfoliation of MMT nanoclays in a polypropylene matrix. In his research he combined different kneading blocks (Figure 7-17) with positive transport elements. Kneading blocks consist of alternating kneading disks which are staggered in different angles. Positive kneading blocks transport the material forward and induce a small amount of distributive mixing. Negative kneading blocks only make up for a large amount of distributive mixing [37]. By introducing different configurations of negative kneading blocks an augmentation of the elongational flow of the particles is expected due to obstacles that reorient and interrupt the interfacial

144

area [42]. Elongational flow is considered more influential in mixing than applying shear. In the latter particles are also rotated next to shear decreasing the stress on the particle whereas in the former particles undergo a stretching type of rotation which generates significantly higher stresses to disperse the agglomerates [42]. The research of Delva et al. [37] showed that the different configurations of kneading blocks and transport elements did not affect the degree of exfoliation or intercalation in a significant manner. Their principle reasoning being that the maximal state of exfoliation is already achieved in the melting zone of the extruder and the different configurations did not impart significant changes in the matter. In this research the same twin-screw configuration as used in their research will be used. This is described in the experimental part.
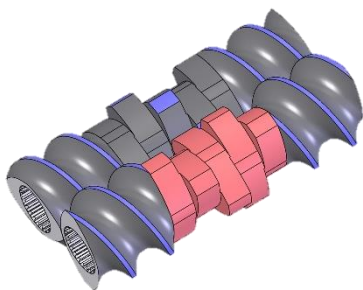
Figure 7-17:Kneading blocks (middle) and transport elements (outside) that make up the screw configuration of the twin-screw extruder [43]

7. 1. 11. Rotor Milling

After the successful functionalization of the Montmorillonite nanoclays and following dispersion into the polysulfone matrix by melt-intercalation, the extruded films are transformed into spherical powders for SLS. In this regard, the extruded films are shredded and fed to the rotor miller in the predefined three-step communion process to achieve feed material of the desired size and morphology.

As the Montmorillonite clays have a rigid structure with high aspect ratio they will carry the major portion of the applied load under stress conditions, providing the interfacial interactions between filler and matrix are sufficient. Nanoclays have the tendency to increase modulus and tensile strength in well dispersed conditions while decreasing elongation at break [13], [23], [44]. This effect should ease the communion process by the rotor milling technique to a small extent by the decrease in the energy of break that accompanies these effects. The aforementioned effects are expected to be more pronounced with higher filler volume content leveling off at a threshold limit [13]. It should be noted that in the case of bad compatibility between the polysulfone matrix and the MMT nanoclays, the latter can be seen as stress concentrators which are potential sites for the formation of cavities that can be transformed under certain conditions into cracks [50].

7. 2. EXPERIMENTAL

7. 2. 1. Materials

In this section pristine montmorillonite (NaMMT, Nanomer® PGV, Sigma-Aldrich) is functionalized following the protocol Gosalawit et al. [7] and Prasad et al. [25] by dispersion of the nanoclay in 75% EtOH ($\geq$ 99,8%, Carl Roth). The solution was stirred vigorously for 3 hours after which (3-aminopropyl)triethoxysilane (APTES, $\geq$ 98%, Sigma-Aldrich) was added dropwise. The mixture is subsequently refluxed at 80 °C for 24h. Thereafter it is filtered and washed using cold H_2O to obtain the SiMMT. In the next step, the SiMMT is dispersed again by stirring vigorously in a buffered solution of (N-morpholino)ethanesulfonic acid (MES, $\geq$ 99%, Sigma-Aldrich), 1-ethyl-3-(-3-dimethylaminopropyl) (EDC, Sigma-Aldrich), N-hydroxysuccinimide (NHS, 98%, Sigma-Aldrich) and 4-sulfophthalic acid (SPA , 50wt.%, Sigma-Aldrich) for 24h. The pH of the solution was controlled by titration of either a 0,1 M NaOH solution (Merck) or 0,1 M solution of HCl (37%, Merck). The product was filtered off afterwards and washed using cold H_2O then dried for 24h at 60°C before any analysis or processing. In order to increase loading, pretreatment of the NaMMT by acid treatment was tested and carried out using H_2SO_4 (98%, Merck). The functionalized product was compared in interlayer space with a commercial grade MMT and a surface modified with methyl dihydroxyethyl hydrogenated tallow ammonium, called Nanomer® I34NM (25-30 wt.%, Sigma-Aldrich) commercially used for compounding with polyamides.

7. 2. 2. Methods

Characterization of the functionalized MMT was performed using XRD measurements to investigate a change in interlaminar spacing of the clay sheets, FTIR and CHNS measurements to validate the functionalization and DSC and TGA to determine any change in thermal properties of the MMT clays. The clay particles were thereafter dispersed in the polysulfone matrix using twin-screw extrusion. The extruded films were characterized on morphology using SEM micrographs and XRD measurements to determine the amount of intercalation. Contact angle measurements and flame retardancy measurements were performed to determine any improvement in barrier properties and TGA and DSC analysis was performed to investigate any change in thermal properties. Lastly, tensile bars were punched out from the extruded films which were used for tensile measurements to determine any change in mechanical properties

7. 2. 3. Functionalization of montmorillonite

7. 2. 3. a. Silylation using (3-aminopropyl)triethoxysilane (APTES)

Silylation was performed according to the research of Prasad et al. [25] and Gosalawit et al. [7]. In this study, pristine NaMMT (2,01 g) was added to a 75% EtOH-solution (800 mL) and stirred vigorously during 3 h at ambient temperature. Next, APTES (2.4 mL; $1{,}03 \times 10^{-2}$ mol) was added to the solution dropwise. The solution is thereafter refluxed at 80 °C during 24 h and filtered off. The residue is washed with cold water and dried for 24 h at 60 °C.

In order to increase the loading of APTES in the clay galleries the NaMMT was also subjected to an acid treatment. In this regard the protocol of Shen et al. [45] was adopted in which the NaMMT (2,01 g) was added to 10 % H_2SO_4 solution (100 mL) and stirred at 90 °C for 2,5 h. After that the solution was filtered and washed using H_2O until the filtrate was neutral in pH. The residue was finally dried for 24 h at 60 °C before grafting with APTES. The silylated material is denoted SiMMT.

7. 2. 3. b. Sulfonation using 4-sulfophthalic acid (SPA)

Due to the difficult amide bond formation different reaction conditions were tested. The first reaction was performed according to the recommendations of Thermo-Scientific [36]. In this case the pH was kept at 4,5 for protonation of the EDC prior to adding the SiMMT. After addition of the latter the pH is increased to 7,2 to activate the amine of the grafted APTES. In the second reaction, the pH was kept at 4,5 to promote formation of the active NHS-ester. In reaction 3 these conditions are repeated yet the temperature of the solution is kept at 4 °C to hamper the formation of unreactive N-acylurea. In reaction 4 the same conditions are repeated again yet after the addition of EDC the solution is left to react longer in order to stimulate the protonation of EDC and formation of the active ester even more. Reaction 5 operates under the same conditions as reaction 1 yet here the solution temperature is also lowered to 4 °C. Reaction 5 and 6 are executed in aprotic apolar solvents (DMF) to prevent hydrolysis. In this regard, reaction 6 is executed at room temperature while reaction 7 is performed at elevated temperature to fight the adverse thermodynamics of amidation. For the same reason reaction 8 is performed in aqueous solvent (cfr. Reaction 1) yet refluxed at 100 °C. The materials that underwent the sulfonation procedure are denoted SMMTx, with x the number of the reaction.

Reaction 1 (SMMT1)

In this case a 0,1 M MES-buffer with 0,5 M NaCl was made (800 mL) containing SPA (3.8 mL; $2{,}0 \times 10^{-2}$ mol). The pH was set at 4,5 by titration with 10 M NaOH. The solution was vigorously stirred and NHS (1,17 g; $1{,}02 \times 10^{-2}$ mol) was added and shortly thereafter EDC (1,95 g; $1{,}02 \times 10^{-2}$ mol). The solution was stirred for 30 minutes at ambient temperature to allow protonation of the EDC and the subsequent

formation of the active NHS-ester. The pH was controlled by titration with NaOH-solution. After 30 minutes, the solution pH was increased to pH 7,2 by titration of NaOH and buffered at this pH by adding $NaH_2PO_4.2H_2O$ to the solution. To this 2,01 g of the silylated MMT was added and left to stir at room temperature for 24h prior to filtration, washing and drying the residue at 60 °C for 24 h.

Reaction 2 (SMMT2)

The reaction formula of SMMT1 was repeated. After adding NHS and EDC the solution was stirred for 30 minutes at ambient temperature to allow protonation of the EDC and the subsequent formation of the active NHS-ester. The pH was controlled by titration with NaOH-solution and kept at 4,5 during the whole reaction to promote the active ester formation. To this 2,01 g of the silylated MMT was added and left to stir at room temperature for 24 h prior to filtration, washing until the filtrate was at neutral pH and drying the residue at 60 °C for 24 h.

Reaction 3 (SMMT3)

The reaction conditions of SMMT2 were repeated yet the solution temperature before adding the amine was cooled to 4 °C according to the recommendations of Montalbetti et al. [32].

Reaction 4 (SMMT4)

The reaction conditions of SMMT1 were repeated. After the addition of EDC the solution was stirred for 1 hour in order to maximize the formation of the active NHS-ester. Afterwards the SiMMT is added and the SMMT1 protocol is followed.

Reaction 5 (SMMT5)

SMMT1 protocol is followed using a solution temperature of 4 °C when adding the SiMMT.

Reaction 6 (SMMT6)

In order to hamper hydrolysis of the EDC or active ester the reaction is executed in the apolar aprotic solvent N,N-dimethylformamide (DMF). To this end SPA (1,9 mL; $1,00\times10^{-2}$ mol) is mixed in DMF (400 mL) after which NHS (0,585; $0,51\times10^{-2}$ mol) is added and a 3-fold excess of EDC ($1,53\times10^{-2}$ mol). The solution is stirred for 1 hour and SiMMT (1,005 g) is added after that. Vigorous stirring ensues for 24 h after which the solution is filtered and the residue washed and dried at 60 °C for 24 h.

Reaction 7 (SMMT7)

Reaction 6 is repeated with an equimolar amount of EDC to NHS in the solution ($0,51\times10^{-2}$ mol). The solution is stirred vigorously for 1 hour after which SiMMT is

added (1,005 g). The solution is then refluxed at 130 °C for 24 h. Next, the residue is filtered, washed and dried at 60 °C for 24 h.

Reaction 8 (SMMT8)

Reaction 1 is repeated with the addition that the solution is refluxed at 100°C after addition of SiMMT for 24 h.

7. 2. 4. Structural characterization

7. 2. 4. a. CHNS measurements

A quantitative indication of the presence of functional groups attached to the NaMMT was determined using a 2400 CHNS/O Series II System of PerkinElmer. Samples were dried 24 h prior to analysis to remove any residual solvent or moisture. In the elemental analysis the nitrogen sorption denotes the successful loading of APTES on the MMT sheets while the presence of a sulfur peak in the chromatogram represents the successful amidation on the nanoclay sheets. The amount of nitrogen, carbon, hydrogen and sulfur are represented in weight percentage in Table 7-1.

Whereas a definite increase in nitrogen is visible from the CHNS measurements denoting a successful silylation, no sulfur is present in any of the experiments. This would entail that the amidation reaction between the carboxylic acid moiety of the SPA and the amine moiety of the APTES did not occur. Conceivably the cause of this strenuous bond formation lies in the intricate reaction conditions. During the addition of the EDC to the solution an increase in pH was observed indicating a definite protonation of the latter to its active carbocation form (Figure 7-10). The formation of the O-acylisourea cannot be confirmed in the same manner however. Due to the short lifespan of the O-acylurea, O $\rightarrow$ N displacement to the energetically more stable yet unreactive N-acylurea is more likely to have occurred. Hydrolysis of the carbocation seems less likely as formation of the urea derivate is associated with the release of a proton causing a decrease in pH which was not observed. The low yield of coupling also has its origin in the low amount of non-protonated amine functions of the grafted APTES at the solutions' pH during reaction. Primary alkyl amines typically have a pKa value of ~10,6 meaning that, according to the Henderson-Hasselbalch equation, at a pH equal to this pKa 50% of the total amount of amine moieties is in its active non-protonated form. As reaction conditions are below this pH (4,5 or 7,2) the amount of active amine is less than 1 %. As mentioned before however, at higher levels of pH, the succinimidyl ester is not stable enough displaying a half-life of 10 minutes at a pH of 8,6 [36].

Sehgal and Vijay [33] performed the coupling reaction of butyric acid on Affi-Gel 102 under similar reaction conditions as described above yet reported a maximum coupling of 80%. In order to achieve this they varied the NHS:EDC ratio to an

optimum of 1:15. Given the volumes sulfonated MMT needed for melt intercalation later on however, this 15-fold excess of EDC was not practically feasible.

Table 7-1: CHNS measurements results

	N (wt.%)	C (wt.%)	H (wt.%)	S (wt.%)
NaMMT	0,334	0,593	1,358	0
SiMMT	3,026	8,801	2,512	0
Acid treated SiMMT	3,563	9,823	2,854	0
SMMT1	3,020	9,288	2,394	0
SMMT2	2,946	9,778	2,331	0
SMMT3	3,416	10,456	2,990	0
SMMT4	3,042	8,408	2,856	0
SMMT5	3,206	8,858	2,701	0
SMMT6	3,624	10,525	3,031	0
SMMT7	3,553	11,258	2,678	0
SMMT8	1,930	4,737	1,950	0

7. 2. 4. b. Fourier transform infrared spectroscopy (FTIR)

FTIR spectra of NaMMT, SiMMT and SMMT were used to characterize the progress of the reaction of silylation and sulfonation and are shown in Figure 7-18. A Bruker Tensor 27 was used measuring the absorption between 4000 and 600 cm^{-1} of the dried powder at room temperature with a resolution of 2 cm^{-1} over 40 scans.

In the NaMMT spectrum, typical bands are found as reported in literature [45]–[48]. The sharp peak around 3613 cm^{-1} corresponds to the stretching vibration of the OH units bound to the aluminum and/or magnesium in the octahedral sheets while the broad peak at 3392 cm^{-1} corresponds to the –OH stretching of absorbed water. The OH bend is visible at 1635 cm^{-1} and a large peak at 1009 cm^{-1} denotes the Si-O-Si stretching vibration (not in figure). Upon silylation extra peaks become visible in the spectrum: the symmetric and asymmetric stretching vibrations of -CH$_2$ around 2935 and 2862 cm^{-1} reflecting the alkyl chains of the APTES molecule. The strong absorption band at 1448 cm^{-1} corresponds to the N-H bending vibration of the amine moiety. The N-H stretching vibration in the 3500-3200 cm^{-1} region is less visible due to the broad OH-peak already present. The peak occurrence is dependent on the degree of hydrogen bonding between the atoms and is possibly situated at 3274 cm^{-1}. The C-N stretching vibration is situated around 1330 cm^{-1}. The appearance of these characteristic absorptions denote a successful grafting of the APTES on the nanoclay sheets. Upon analyzing the sulfonated sample a large mixing of different functional groups between 1600 – 1000 cm^{-1} makes the determination of a successful amidation difficult to determine. Most of the absorption peaks of the sulfone functional group are contained in the wide silicon-oxygen stretching peaks around 1100 cm^{-1}. For aromatic six membered rings like the benzene moiety of the SPA molecule the two most prominent C=C stretch vibrations are said to occur around 1600 and 1515 cm^{-1} with the =C-H stretch visible in the 3125 – 3030 cm^{-1} region yet these are not considered present. Furthermore, the C-O and C=O stretch vibrations in 1250 cm^{-1}
150

and 1695 – 1665 cm^{-1} respectively are not visible as well suggesting no sulfonation to have occurred.
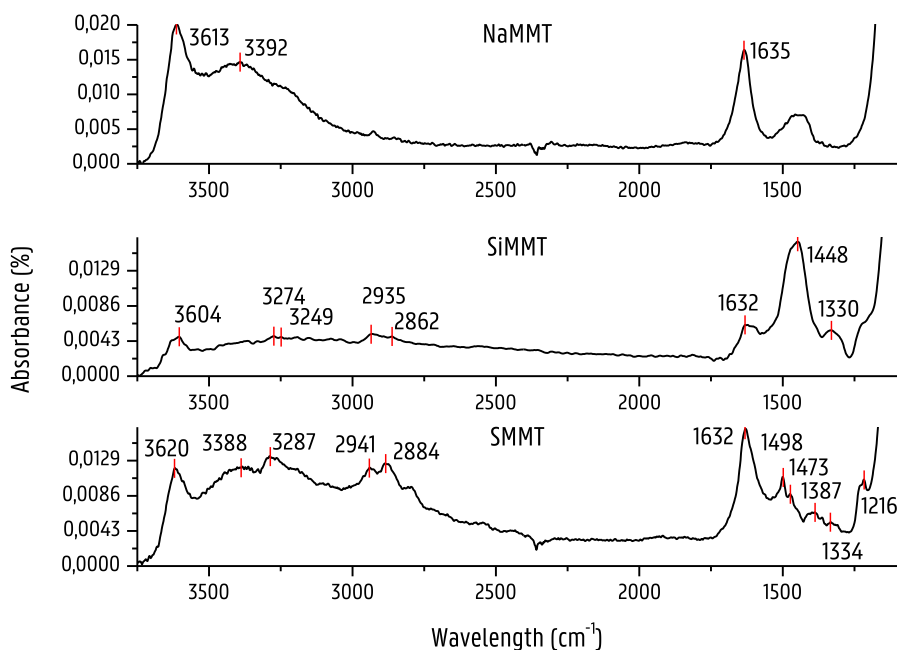

Figure 7-18: FTIR spectra of the NaMMT, SiMMT and SMMT

7. 2. 4. c. Interlayer distance of the modified MMT

The interlayer distance of NaMMT, SiMMT and SMMT was determined using X-Ray Diffraction. The grafting of the silane with the clay minerals can either occur on the surface or edges of the clay or inside of the clay galleries if sufficiently swollen and dispersed during functionalization. In the latter case an expansion of the basal spacing is expected [24]. This expansion of the interlayer space infers a shift of the diffraction peak towards lower angle values. The angle and layer spacing values are correlated by Bragg's law:

$$n\lambda = 2d sin\theta$$
<div align="right">*Equation 7-1*</div>

with n the order of the diffraction spectrum, λ the wavelength of the incident X-ray beams (nm), d the interlayer spacing (nm) and θ the angle of the incident beam and the scattering plane (°). The XRD analysis was performed using a powder XRD Thermoscientific ARL X'TRA with Cu Kα radiation (λ = 0,1540562 nm) and a 2θ range from 1,5 to 20 °. The diffractograms of NaMMT, SiMMT and SMMT are depicted in Figure 7-19 and their corresponding interlayer spacing is calculated and summarized in Table 7-2.

Figure 7-19 shows the diffraction of NaMMT with weak intensity around 6,6 - 6,9 ° giving a basal spacing of 1,34 nm which is consistent with literature findings [11], [25]. No organic molecules are present inside the clay galleries leading to a tight

packing of the sheets. Upon silylation a clear shift in diffraction peak occurs towards lower angles. SiMMT diffracts around 4 -4,3 ° giving a mean interlayer distance of 2,13 nm. The shift in basal spacing indicates successful functionalization inside the clay galleries signifying a successful swelling to have occurred in solution during functionalization that allows for the APTES to penetrate the clay sheets. As base of comparison, a commercial grade montmorillonite, Nanomer® I34MN, used for compounding with polyamides, is subjected to XRD analysis. Its diffraction peak lies around 5,2 ° corresponding with a d-spacing of 1,7 nm. The silylated product hence shows a larger d-spacing implying a better ease of intercalation in the melt intercalation stage later on.
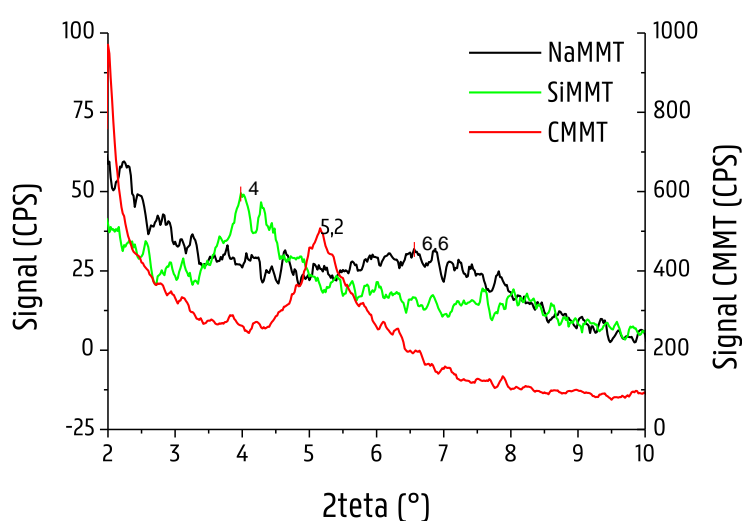
Figure 7-19: XRD diffractograms of virgin MMT (NaMMT), silylated MMT (SiMMT) and commercial grade MMT (CMMT, Nanomer® I34MN, scaled on secondary y-axis)

Table 7-2: The calculated interlayer spacing using Bragg's law from the spectra in Figure 7-19

	2θ (°)	d_{001} (nm)
NaMMT	6,6	1,34
SiMMT	4,15	2,13
CMMT	5,2	1,70

7. 2. 4. d. Thermogravimetric analysis

The thermal stability of the functionalized MMT using APTES was studied by thermogravimetric analysis in two ways. First the loading of the functionalized nanoclays was measured as the weight loss occurring in a defined temperature. To this end the latter was subjected to a linear temperature increase of 10°C/min under nitrogen atmosphere using a Netzsch STA449 JUPITER F3 from room temperature to 600 °C. The amount of APTES loaded on the clay was then determined from the difference between the residual weights of the pristine NaMMT and the silylated MMT at 600 °C as described by Greesh et al. [49] and Kim et al. [50].

Second, the thermal stability of the nanoclays was determined by subjecting the clays to a isothermal program at 330° for 10 minutes to simulate the thermal conditions the nanoclays would have to endure while melt producing the PSU-MMT composite in the twin-extruder (see section 7. 2. 5. a.).

APTES loading on nanoclays

The nanoclays were subjected to a linear temperature increase from ambient temperature to 600 °C, the thermograms of the pristine and functionalized MMT are depicted in Figure 7-20. Pristine montmorillonite remains thermally stable in the temperature range of 100 – 600 °C. Up to 100°C the weight loss of the clays can be ascribed to a loss of free or adsorbed water in the interlayers while the weight loss in the temperature range of 100 – 600 °C is attributed to loss of hydrogen-bonded water molecules inside the gallery and loss of some of the hydroxyl groups from the octahedral sheets of the clay [49]. Beyond 600 °C clays begin to lose their structural hydroxyl groups and start to decompose. In the silylated species two major decomposition steps can be observed: one around 300 °C and one around 430 °C, both attributed to the degradation of the APTES molecules and the grafted silane moieties [45]. Table 7-3 summarizes the change in residual mass and the correlated percentage of APTES grafted on the clays. It shows an APTES loading of 9,24 wt.% relative to the weight loss of NaMMT meaning that 8,14 wt.% of the added APTES during functionalization has been successfully grafted on the nanoclays. The APTES loading for the acid treated sample was assessed in the same manner at 8,48 wt.%, statistical comparison of the loading of the acid treated MMT and pristine MMT did not show a significant difference in APTES loading.
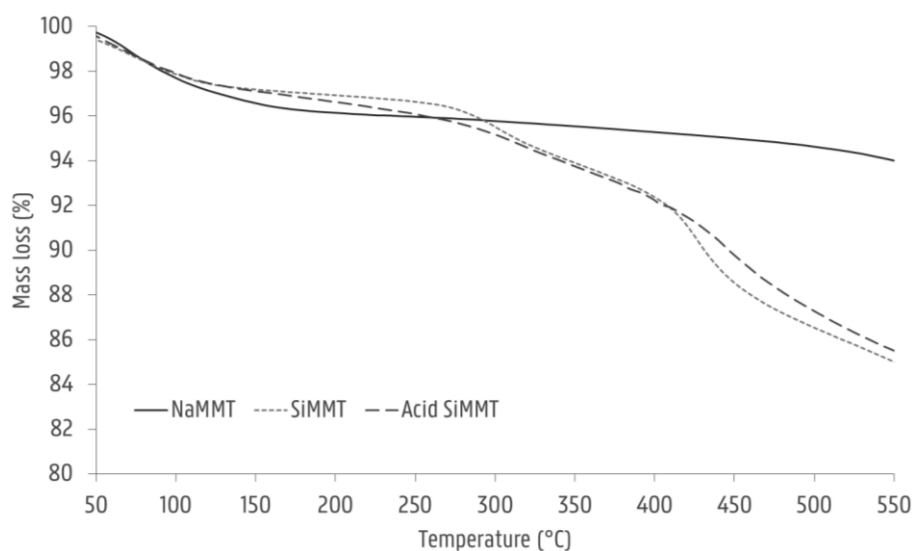

Figure 7-20:TGA curves from pristine MMT (NaMMT); silylated MMT (SiMMT) and silylated MMT that has been subjected to acid treatment before silylation (acid SiMMT)

Table 7-3: The calculated loading on the MMT via TGA measurements based on the weight loss of the pristine NaMMT

	NaMMT	SiMMT	Acid -SiMMT
Weight loss at 600 °C (%)	$5,06 \pm 0,25$	$14,30 \pm 0,92$	$13,54 \pm 0,51$
APTES loading (%)	/	9,24	8,48

Thermal stability of nanoclays

As PSU is conventionally processed at higher temperatures than normal polyolefines a thermogravimetric analysis is performed at the highest processing temperature of PSU in order to determine the possible extent of degradation that could occur during processing. In this regard, the silylated clays were subjected to an isotherm at 330 °C for 10 minutes. The critical weight loss of the nanoclays can in this way be correlated to a maximum residence time for the MMT in the twin-screw extruder. Figure 7-21 depicts the thermograms of pristine and silylated montmorillonite. NaMMT exhibits good thermal stability during the linear and isothermal temperature program. The large decay of mass between 40 and 170 °C is due to the loss of water. SiMMT displays a mass loss starting from 278 °C. Degradation of the APTES molecules can infer bad compatibility of the polysulfone matrix and the nanoclays. However, the weight loss stagnates after 10 minutes which point to the complete disappearance of the APTES. During twin-screw extrusion the residence time of the nanoclays is limited to 57 seconds by the use of a side feeder (see further on). This residence time corresponds to a mass loss of 57,5 %. It is therefore possible that a part of the bound APTES molecules would remain on the nanoclays and thus allow good dispersion and distribution in the matrix. Increasing screw speed during processing in this case could be beneficial as this shortens the residence time of the functionalized clays. When increasing screw speed from 290 RPM to 580 RPM for example, the residence time would decrease to 40 seconds.
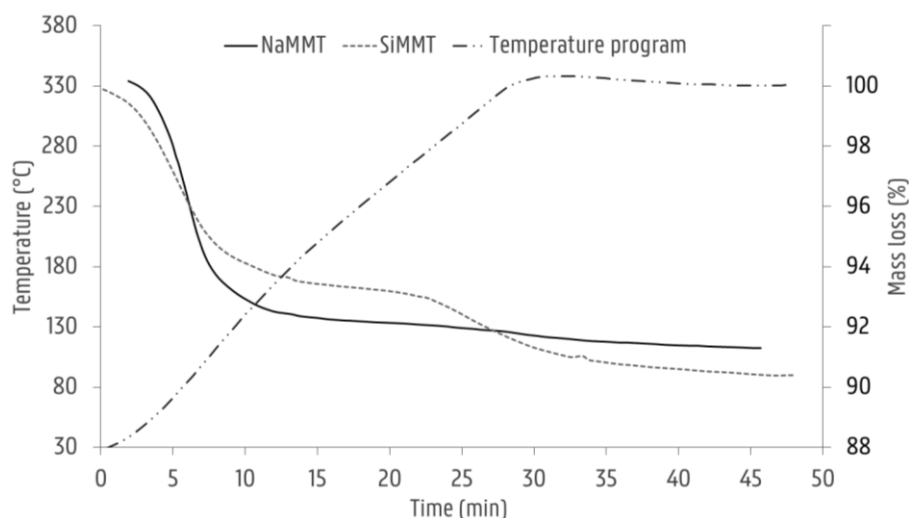
Figure 7-21: TGA measurement of the NaMMT and SiMMT subjected to an isotherm of
330 °C; the highest processing temperature in the melt intercalation process of polysulfone

7. 2. 5. Influence of the MMT on the properties of polysulfone

7. 2. 5. a. Preparation of PSU-MMT composite

The influence of the nanoclays on the properties of polysulfone were investigated by
melt intercalation using a tightly intermeshing co-rotating twin-screw extruder
Coperion ZSK 18 MEGAlab. The extruder consists of two screws of diameter 18 mm
and L/D ratio of 40. The screw configuration consists of 10 different zones conform
the setup used by the work of L. Delva et al. [37]. Figure 7-22 depicts the screw
configuration and the thermal profile of the barrel used for melt processing the
polysulfone-montmorillonite composite. The degassing zones are present in the
fourth, sixth and ninth zone with the side feeder installed directly after the degasser in
the fourth zone. The screws consist of different kneading blocks and mixing elements.
Zone 1-3 is used to plasticize the polysulfone pellets. The fourth zone consists of
forward conveying elements as the MMT is introduced here via the side feeder. The
fifth zone consists of kneading blocks which are staggered 45 ° and serve the purpose
of pulling apart the MMT agglomerates. Zone six and seven serve the same purpose
of 4 and 5. Zone 8 and 9 consist of smaller kneading blocks designed to improve the
distribution of the MMT in the polysulfone matrix. The extruder was fitted with a slit
die of 19 mm × 2 mm to retain sufficient extrusion pressure at the extrusion point. All
composites and virgin polymer were processed using a screw speed of 290 RPM. Thin
sheets were extruded and cooled between calender rolls at RT for characterization.
The calender speed was adjusted to the screw speed. The sheets were afterwards used
to die cut tensile bars for tensile tests.

PSU and nanoclays were dried 24h prior to processing, the PSU at 120 °C while the MMT at 60 °C. Polysulfone P 1700 pellets and the nanoclays (Nanomer® PGV, Nanomer® I34NM and chemically modified Nanomer® PGV) were fed gravimetrically using the main feeder for the pellets (zone 1 in Figure 7-22) and the side feeder for the clays (zone 4 in Figure 7-22). Table 7-4 represents the nanocomposites prepared with their respective weight percentages nanoclays added to the polymer matrix. 1 and 3 wt.% nanoclays were added in this regard to the polysulfone matrix and compared to the research of Sur et al. [11] and Monticelli et al. [12]. The produced composite sheets were left to condition in an acclimatized room at 23 °C and a relative humidity of 50 % for a period of two weeks before characterization in accordance with ISO 527 standard. Figure 7-23 shows the different PSU nanocomposites produces via twin-screw extrusion in the method described above. Upon adding NaMMT the samples obtained a grey opaque look (Figure 7-23, B-C) in comparison to the virgin PSU (Figure 7-23, A). When adding SiMMT this changed into a brown sand-like color and the sample lost most of its transparency (Figure 7-23, D-E). This change of color could indicate degradation upon processing. The same changes were noticed upon processing the commercial organophillisized MMT (Figure 7-23, F-G).
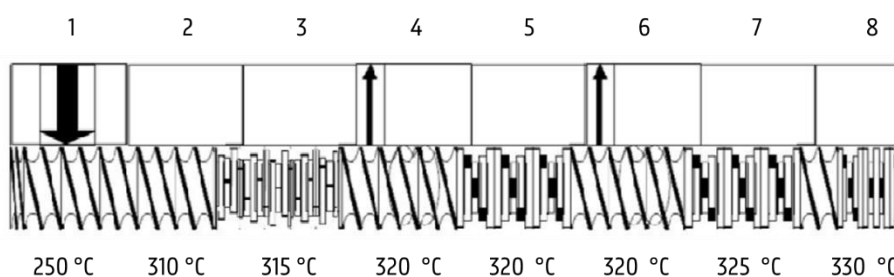
Figure 7-22: Twin-screw configuration and thermal profile of the barrel for the processing of the PSU-MMT composite. Figure adapted from [37]

Table 7-4: Extruded samples with respective weight percentages MMT added to the PSU matrix with added amounts denoted in subscript for the various MMT materials

	wt.% NaMMT	wt.% SiMMT	wt.% CMMT
Virgin	0	0	0
NaMMT₁	1	0	0
NaMMT₃	3	0	0
SiMMT₁	0	1	0
SiMMT₃	0	3	0
CMMT₁	0	0	1
CMMT₃	0	0	3
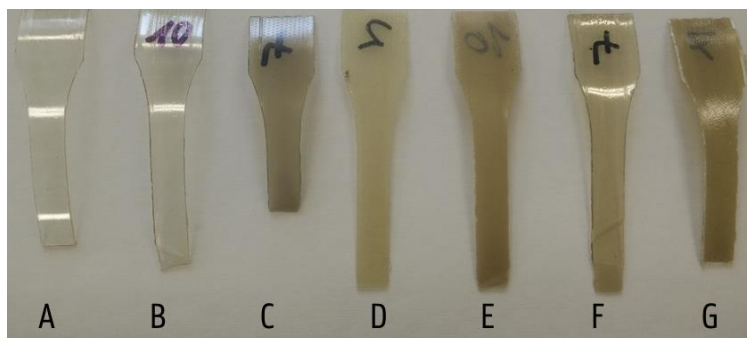
Figure 7-23: the prepared PSU nanocomposites via twin-screw extrusion: (A) virgin PSU, (B) 1wt.% NaMMT, (C) 3wt.% NaMMT, (D) 1wt.% SiMMT, (E) 3wt.% SiMMT, (F) 1wt.% CMMT and (G) 3wt.% CMMT

7. 2. 5. b. Thermogravimetric analysis

In this section the thermal stability of the polysulfone composites are determined by thermogravimetric analysis. For this purpose the samples were subjected to a linear temperature program of 10 °C/min going from ambient temperature to 800 °C under nitrogen atmosphere. The onset temperature of degradation was determined by the 1 % weight loss threshold and compared to that of the virgin polysulfone. The addition of nanoclays is expected to increase the thermal stability of the polysulfone matrix because of the high thermal stability of the clays themselves and the increase in barrier properties which limit diffusion of volatile degradation products. However, as PSU already has a high degradation temperature ($T_{deg,1\%} = 500,8$ °C, Figure 7-24) this effect is difficult to observe. The degradation temperatures of the samples in question are represented in Table 7-5. In fact, a general decrease in degradation temperature is observed for all samples. When looking at the composite mixed with 1 and 3 weight percent pristine MMT this decrease can be explained by looking at the TGA analysis of the pure NaMMT nanoclays (Figure 7-20); after an initial decrease due to loss of water molecules the sample begins slowly to decrease in mass due to dehydroxylation of the free silanol moieties. This slow decline becomes more outspoken when exceeding 500 °C, i.e. the nanoclays begin to slowly degrade before the degradation onset of polysulfone. The free O^{2-} from the dihydroxylation works against the high degradation temperature as it can initiate early degradation of the polymer chains [51]. The PSU-SiMMT composite shows an earlier onset in degradation temperature which increases with the weight percentage SiMMT added. Again, when comparing to the thermogram of pure SiMMT depicted in Figure 7-20 one can see that the APTES starts to degrade at 275 C°, because of the high processing temperatures (Figure 7-22) the APTES molecules are partially degraded. Upon extrusion and cooling on the calendar the degradation products are captured in the matrix structure. The degradation simply continues when heating the material to these temperatures again. Moreover, because of the partial degradation, the tortuous structure normally formed is completely

disturbed, aiding in the diffusion of the degradation products. The effect described for the organically modified nanoclays can also be seen in the 1 and 3 wt.% CMMT nanocomposites. Here, the organic spacer degrades around 400 °C after which at 503 °C the PSU begins to degrade. The effect is more pronounced at higher weight percentage of CMMT in PSU as higher amounts of organic spacers are present leading to more volatiles being released due to degradation.
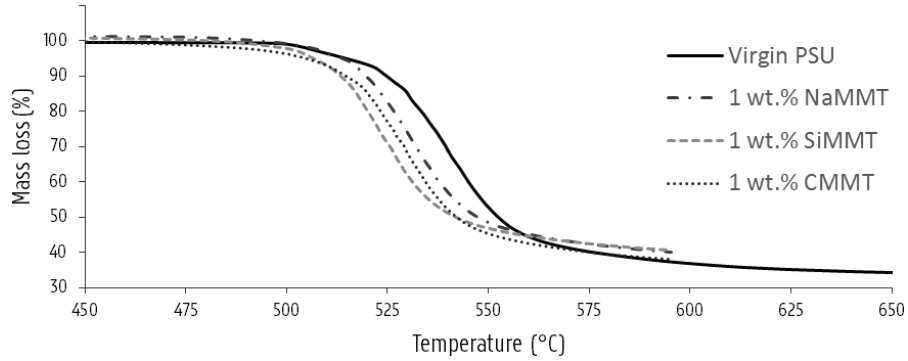
Figure 7-24: TGA curves of the PSU composites with 1wt.% added nanoclays compared to that of the virgin polysulfone
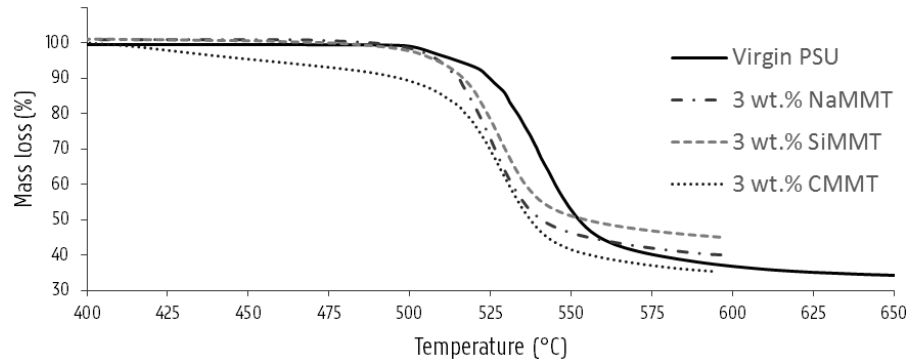
Figure 7-25: TGA curves of the PSU composites with 3wt.% added nanoclays compared to that of the virgin polysulfone

Table 7-5: Degradation temperatures of the polysulfone composites determined by TGA measurements at 1% mass loss

	$T_{degradation, 1wt.\%}$ (°C)
Virgin	500,8
NaMMT$_1$	494,2
NaMMT$_3$	490,8
SiMMT$_1$	483,2
SiMMT$_3$	467,8
CMMT$_1$	434,3
CMMT$_3$	401,3

7. 2. 5. c. X-ray diffraction measurements

The structure of the layered silicates is determined using XRD analysis to determine if the polymer matrix has achieved intercalation due to the functionalization of the nanoclays. Figure 7-26 portrays the diffractograms of each of the classes of composites made in comparison with its pure clay form. As PSU is fully amorphous no diffraction peaks of PSU are expected to interfere with those of the nanoclays. The upper panel depicts the diffractograms of composites using pristine MMT with the inset minute diffractions of the composite. The middle panel shows the diffraction of the silylated MMT composites while the lower panel depicts the XRD measurements of the commercial MMT with an organic spacer (Nanomer I34NM). For the composites using pristine MMT as filler almost no diffractions occur. A weak signal is visible at 5,3° and 5,6° for the 1 and 3 wt.% NaMMT filler content in the composite. This corresponds to a slight increase in d-spacing (to 1,67 and 1,58 nm respectively) in comparison to the values measured for the pristine unprocessed NaMMT (see Table 7-2). With addition of the silylated nanoclays the diffractions disappear almost completely and make it difficult to draw any conclusions about this type of nanoclay. Only by heavily processing the signal barely discernable peaks diffracting at 5,1°; 5,5° and 6,5° for the $SiMMT_1$ and 4,4°; 5,1° and 6,6° for the $SiMMT_3$ respectively become visible. Explaining these peaks must be taken with caution in view of the very low intensity in which they occur. One could argue that due to the partial degradation of the APTES on the MMT a wide range of diffractions occur which scatters the diffraction profile. Due to the high thermal profile used in the twin-screw extruder for processing PSU, the APTES molecules are partially or completely degraded leaving either small organic degradation products behind in the interlayers or none at all. This implies that a wide range of basal spacings exists, all smaller than the pure SiMMT peak (4.15 °, Table 7-2). Due to the already low intensity of the signal these diffractions scatter out and are lost in the noise. The decrease in intensity of the basal diffraction peak is further explained by the fact that intercalation takes place in a disordered manner and not by a parallel displacement of the silicate layers. With the loss of the ordered structure due to this disordered intercalation peak intensities will decrease as well [37], [52]. The commercial grade MMT does display good diffraction peaks however a shift of the peaks to higher angles is observed. This suggests a shrinkage of the basal spacing and causes us to suspect that during extrusion the organic spacer has completely been degraded causing the MMT clay platelets to relax and rearrange into their ordered structure.
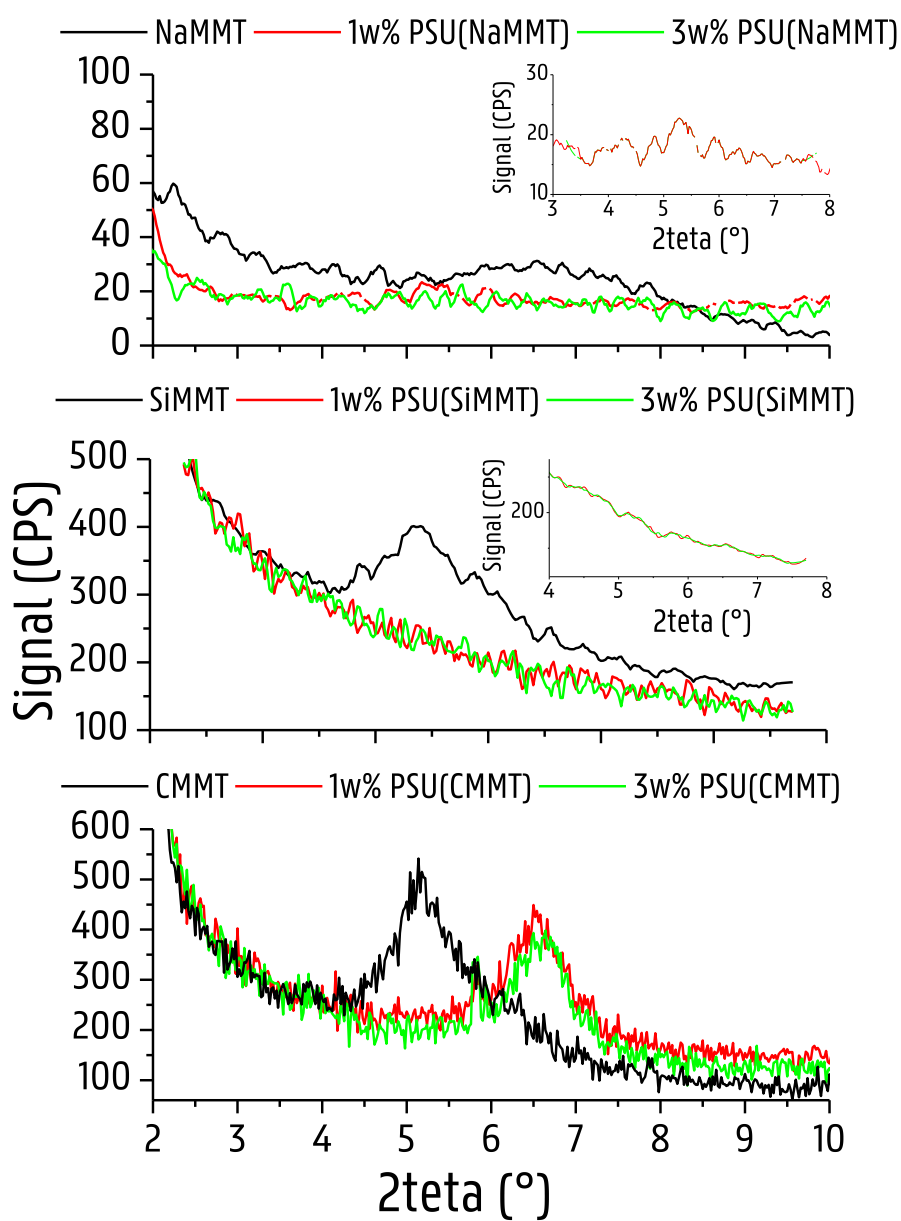
Figure 7-26: XRD measurements of the PSU composites using pristine NaMMT (upper panel), silylated MMT (middle panel) and organophillisized MMT (lower panel).

Table 7-6: XRD measurements of the PSU composites using different nanoclay fillers

Composite filler	2θ (°)			d_{001} (nm)		
NaMMT₁	5,3			1,67		
NaMMT₃	5,6			1,58		
SiMMT₁	(5,1)	(5.5)	(6.5)	(1,73)	(1,6)	(1,36)
SiMMT₃	(4.4)	(5,1)	(6.6)	(2,00)	(1,73)	(1,34)
CMMT₁	6,5			1,36		
CMMT₃	6,6			1,34		

7. 2. 5. d. Scanning Electron Microscopy

A detailed characterization of the layered silicates' dispersion and nanocomposite morphology was obtained by investigating the fracture surfaces of the PSU composites using SEM. In order to obtain these fracture surfaces the extruded films were immersed in a bath of liquid nitrogen. After this the films were cryogenically broken. The surfaces were sputter coated with gold using an Emitech SC7620 Sputter Coater at 25 mA for 50 s, afterwards micrographs were obtained using a FEI Quanta 200FEG operating at an accelerating voltage of 20 kV. As a matter of comparison micrographs were also taken of the virgin PSU.

PSU is itself a very tough polymer and does not easily fracture. As the extruded films are only 2 mm thick the films lose their cryogenic temperature fairly quickly after removal from the liquid nitrogen. This can be seen by the plastic deformation at the edges of the fraction surface in Figure 7-27,A. The surface itself has a relatively large, smooth surface with the mean distance between the fracture lines being $10,77 \pm 4,72$ µm.
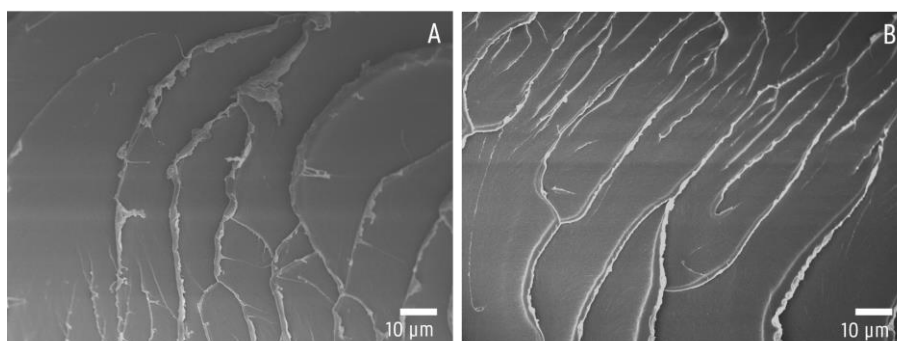
Figure 7-27: Micrographs of the fraction surface of cryogenically fractured virgin polysulfone

The micrographs of the 1wt.% NaMMT composite depicts large agglomerates with minimal dispersion. The nanoclays appear in stacks of different sizes averaging to a mean size of 8,36 µm and a standard deviation of 4,87 µm. Most of the agglomerates reside in pockets (Figure 7-28, A-B) indicating a bad compatibilization between the clay particles and the polysulfone matrix. These clusters have almost detached

themselves from the matrix due to the difference in polarity. The average distance of the fracture lines is slightly lower than that of the virgin PSU due to the bad interfacial interactions which do not allow efficient transfer of stress to the more rigid filler. The mean distance of the fracture lines was assessed at $6,21 \pm 1,70$ µm. When increasing the weight percentage NaMMT to 3wt.% the clusters become more apparent (Figure 7-28,C). The mean size of the masses is measured at $11,26 \pm 5,46$ µm. The micrograph in Figure 7-28,D noticeably shows the fracture lines running through the clusters' pockets indicating that these pockets play an active role in the propagation of the fracture. The mean distance of the fracture lines is measured at $5,96 \pm 1,66$ µm in this case which is again smaller than that of the virgin PSU.

Figure 7-28: Micrographs of the fraction surface of cryogenically fractured polysulfone composite with 1wt.% NaMMT (A-B) and 3wt.% NaMMT (C-D)

With the addition of 1 wt.% SiMMT to the polysulfone matrix the agglomerates decrease in size (see Figure 7-29, A & B). The mean diameter of the clusters was measured at $2,65 \pm 3,75$ µm. Not only an improvement in the dispersion of the clay can be observed, the pocket structure is also less prominently manifested. The masses are more embedded in the matrix which is visible by the fracture lines who only cross the bigger clusters (Figure 7-29, B). The mean distance between fracture lines was estimated at $6,57 \pm 2,84$ µm, a value comparable to that of 1wt.% NaMMT. A striking difference in the micrographs of SiMMT compared to the pristine nanocomposite is the presence of air bubbles at the outer surface of the films (Figure 7-29, A). These bubbles are ascribed to the gaseous degradation products of the APTES which are

formed when processing at temperatures above 275 °C. The composite composed of 3 wt.% SiMMT has a similar morphology as the 1 wt.% composite. Here, the bubbles on the outside of the film are more abundant. The mean diameter of the more distributed clusters was measured at $3,67 \pm 4,35$ µm, the larger deviation caused by the presence of larger clusters. Likewise, the clusters are better immersed with the polysulfone matrix than was the case with the pristine nanoclays composites. Measuring the distance of the fracture lines yielded comparable results as its lower weight percentage composite and was noted at $5,02 \pm 1,70$ µm.
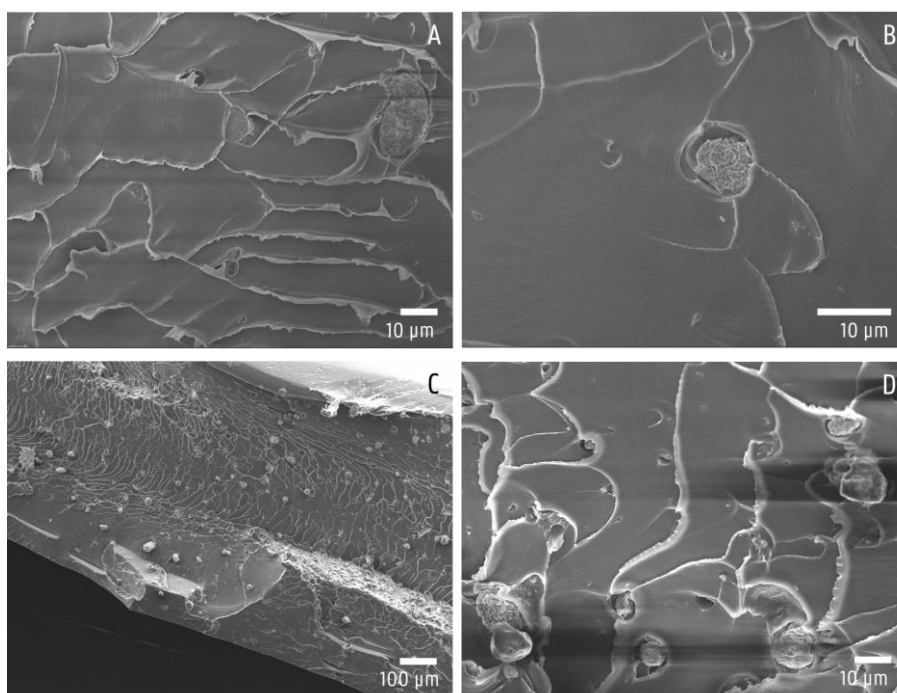

Figure 7-29: Micrographs of the fraction surface of cryogenically fractured polysulfone composite with 1wt.% SiMMT (A-B) and 3wt.% SiMMT (C-D)

When comparing the commercial organoclay composites (Figure 7-30) one can see that for the 1 wt.% composite no large bubbles exist in the extruded sheet. Instead, many small bubbles are distributed throughout the polymer matrix. The presence of these bubbles indicates that the nanoclays have been distributed very well through the matrix and the organic spacers have degraded. Nearly no agglomerations are visible on the micrographs also denoting a good dispersion. The agglomerates have a mean diameter of $5,35 \pm 6,66$ µm and the mean distance of the fracture lines was assessed at $11,47 \pm 2,72$ µm. Increasing the filler content increases the abundance of the above mentioned bubbles. Larger agglomerations are now visible yet due to the presence of the larger part of small clusters the mean size was measured at $4,23 \pm 4,04$ µm. The larger agglomerates are found in pockets and empty pockets can be seen as well corresponding to the location of MMT particles that have detached from the

polysulfone matrix. This decreased compatibility is off course a result of the degradation of the organic spacer leaving the clay platelets to relax into their ordered structure and resulting in this lower adhesive energy between the PSU and MMT. The mean size of the fracture lines here was measured at $3,42 \pm 1,47$ µm which is a large decrease in comparison to the 1 wt.% fillers. The rugged morphology is due to the large amount of small bubbles in the matrix, serving as a pathway for the fracture lines.
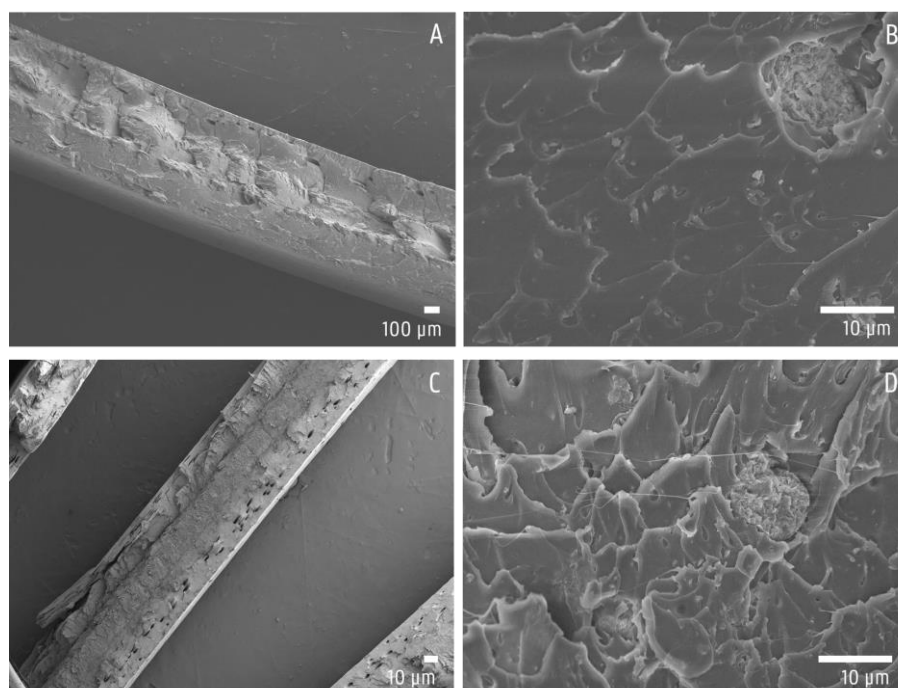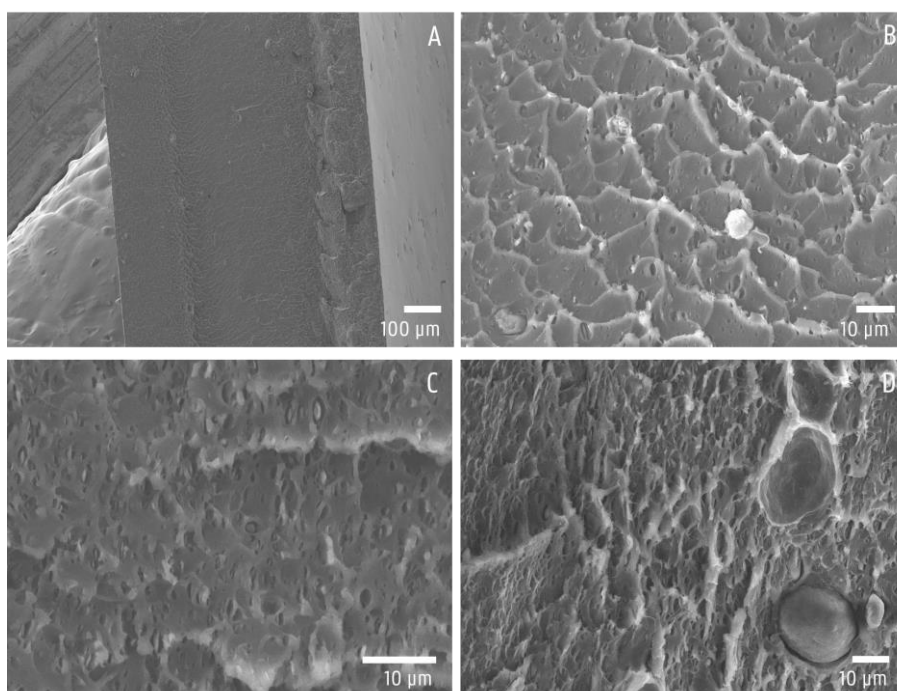

Figure 7-30: Micrographs of the fraction surface of cryogenically fractured polysulfone composite with 1wt.% CMMT (A-B) and 3wt.% CMMT (C-D)

7. 2. 5. e. Tensile testing

The extruded films were used to punch out tensile bars using a hydraulic press and an ISO 527 die cut. The dimensions of the tensile bars are given in Figure 7-31. Thereafter these were used for mechanical characterization using an Instron 5565 dynamometer with a load cell of 5 kN according to ISO 527 standard at 23 °C and a relative humidity of 50%. A crosshead speed of 2 mm/min was uphold while using the clip-on extensometer (gauge length 25 mm) after removal of the extensometer the speed was increased to 10 mm/min. The properties were determined one week after conditioning in an acclimatized room at 23 °C and 50 % humidity. Data evaluation was performed using the Bluehill 2 software and all tests were performed 15 times and evaluated statistically using 1-way analysis of variance (ANOVA) and Turkey's multiple comparisons post hoc analysis with a significance level of 0,05.

Figure 7-31: Tensile bar dimensions punched out from extruded sheets using an ISO 527 die cutter

Figure 7-32 gives a general overview of the tensile tests performed on the different nanocomposites compared to the virgin polymer while Figure 7-33 to Figure 7-35 display bar graphs showing the Modulus, Ultimate Tensile strength (UTS) and Elongation at break (EAB) of the measured test specimens after statistical evaluation and removal of outliers.

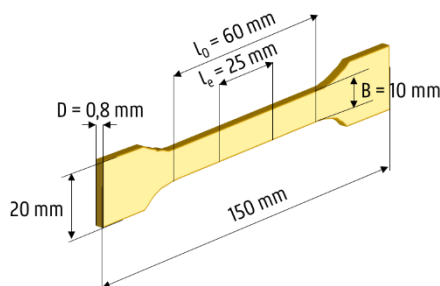Adding pristine MMT or silylated MMT to the PSU matrix does not lead to significant changes in elasticity (Figure 7-33). The stiffness increases only noticeably when adding CMMT with a significant difference in modulus for the 3 wt.% composite (see significance in Table 7-7). An increase in stiffness is usually found in polymer/layered silicate nanocomposites [12], [13] which would imply a good distribution of the nanoclays throughout the matrix. This can also be seen in the micrographs of the respective composites of CMMT by the abundance of the small bubbles which represent the nanoclays.

The ultimate tensile strength of all composites (Figure 7-34) lies below the value of the virgin PSU indicating a reduction in strength for all composites. A significant decrease was found for 1wt.% SiMMT, 3 wt.% SiMMT and 3 wt.% CMMT. The tensile strength is influenced by the final morphology of the nanocomposites. When looking at the micrographs in Figure 7-29 & Figure 7-30 one can see that the appearance of the bubbles has a major effect on the UTS. The empty pockets visible on the micrographs indicate the location of MMT particles that have detached from the PSU matrix during fracture and point to a bad adhesive energy of the nanoclay and polymer, generally weakening the composite. This is also reflected by the large standard deviations on the elongation at break (Figure 7-35). Here no significant differences can be noticed between all of the composites. The large deviations in elongation at break are ascribed to the bad compatibility of the nanoclays in the polysulfone matrix. Especially in the case of the organoclays bubbles are formed which act as defects in the matrix structure causing easier breakage by these local weaknesses. This phenomenon is more pronounced in the silylated nanoclays, hence their lower values of UTS and EAB.

Overall, the deterioration of the mechanical properties of the nanoclays can be ascribed to the degradation of the organic molecules, either present as spacer or grafted on the clay platelets. Preventing this degradation should be of primal concern in further investigations. This can either be done by decreasing residence time by changing the side feeder to a position further down the extrusion line (e.g. position 6 after the degassing unit in Figure 7-22) or increasing screw speed. However, the organoclays would still be exposed to the high processing temperature needed for PSU. A better solution would be to decrease the processing temperature. In this case, a low viscous grade of PSU could prove a solution to this matter. Furthermore, it is believed that the aromatic structure which is added in the second functionalization step of the MMTs should stabilize the organic linkers, resulting in better mechanical properties in the end.
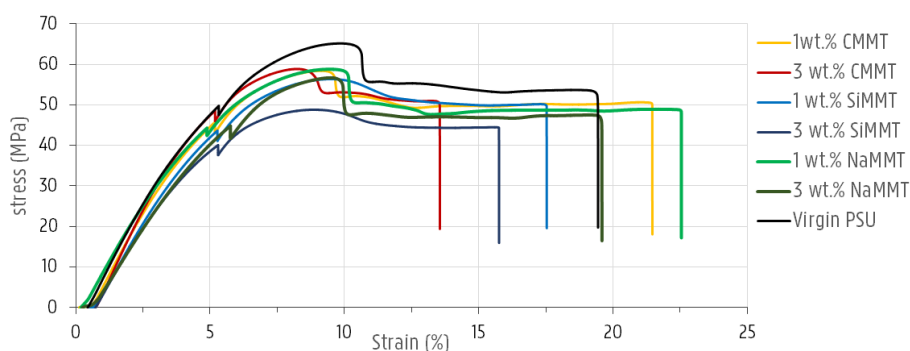
Figure 7-32: Stress-strain diagram giving a general overview of the properties of the 1 wt.% NaMMT, 3 wt.% NaMMT, 1 wt.% SiMMT, 3 wt.% SiMMT, 1 wt.% CMMT and 3 wt.% CMMT properties

Table 7-7: One-way-ANOVA-test results of the Young modulus, maximal tensile strength and elongation at break in comparisson with values for the virgin PSU

	Significance p ($\alpha = 0{,}05$)		
Composite	Modulus	UTS	EAB
NaMMT$_1$	0,618	0,370	0,979
NaMMT$_3$	1,000	0,494	0,996
SiMMT$_1$	1,000	0,000	0,957
SiMMT$_3$	0,912	0,000	1,000
CMMT$_1$	0,154	0,156	1,000
CMMT$_3$	0,000	0,001	0,256
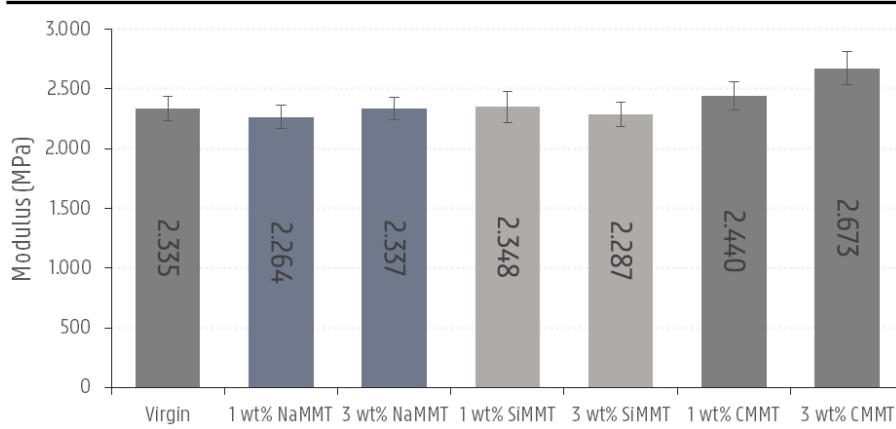
Figure 7-33: Bar graphs displaying the modulus measured for each of the types of composites
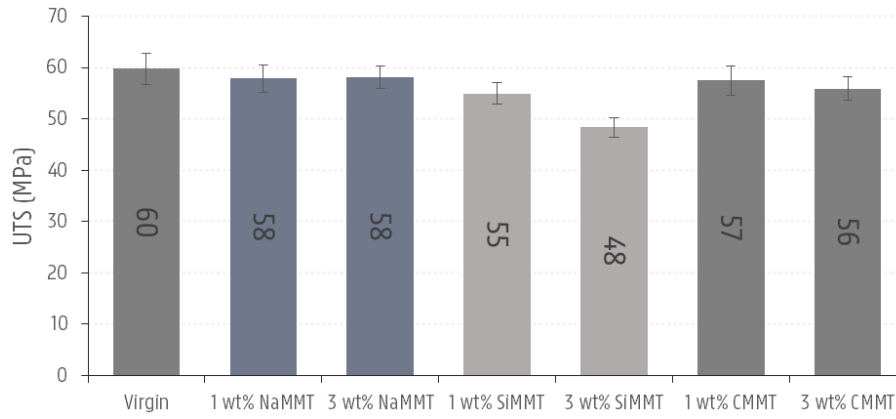
Figure 7-34: Bar graphs displaying the ultimate tensile strength measured for each of the types of composites
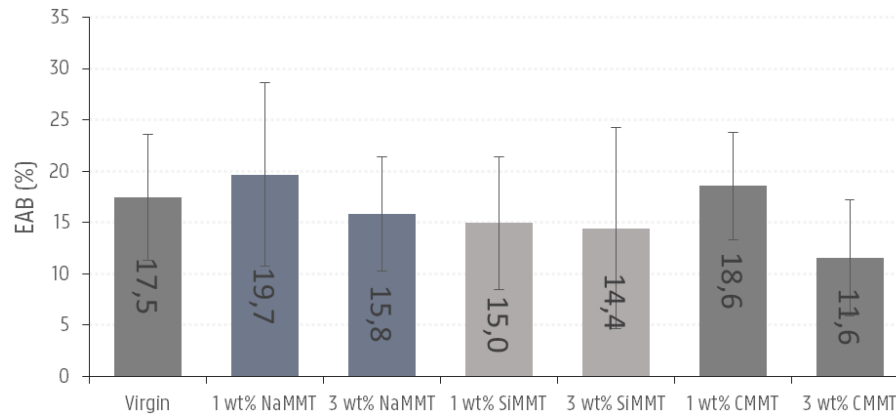
Figure 7-35: Bar graphs displaying the elongation at break measured for each of the types of composites

7. 3. CONCLUSIONS

In this chapter an attempt to create a polysulfone nanocomposite with increased properties using montmorillonite as filler has been made. In order to increase compatibility of the MMT with the PSU matrix a chemical functionalization of the nanoclays was set up using (3-aminopropyl)triethoxysilane as chemical linker to 4-sulfophthalic acid. The purpose of this functionalization was to graft the APTES between the clay galleries and achieve a successful coupling with SPA through an amidation reaction using a carbodiimide (EDC) and NHS to create an active ester intermediary. In doing so the compatibility of the hydrophilic MMT with the more hydrophobic PSU would increase through affinity of the benzene and sulfone groups attached on the MMT. These modified clays would then be processed using melt intercalation in the polysulfone matrix to achieve the desired increased properties. To this end the properties of the newly developed composite would be compared to that of a composite made with a commercially available nanoclay with an organic spacer and a composite with pristine MMT.

Functionalization of the APTES was deemed successful by CHNS analysis revealing an increased amount of carbon and nitrogen on the MMT clay platelets. The loading of APTES on the clay platelets was measured at 9,24 wt.% using TGA measurements. XRD measurements concluded that functionalization was also performed at the interlayer space by an increase in d-spacing compared to that of pristine NaMMT. The amidation reaction however was not successful as no sulfur was measured in the CHNS chromatogram. As an increase in pH was measured during addition of EDC to the solution, the protonation of the EDC to its active form did occur yet it is unclear if either hydrolysis of the carbocation ensued or the O $\rightarrow$ N displacement to its unreactive intermediary has occurred which prevents the amidation from happening. In order to create a more active ester with a longer lifespan NHS was added. This NHS-ester impedes the O $\rightarrow$ N displacement and performs the amidation reasonably well. However, as no sulfur was present on the CHNS chromatogram either, one can only conclude that the hydrolysis of the EDC prevents the reaction from occurring. A large excess of EDC (13 to 15-fold) to NHS has been reported to be successful in literature yet this was not feasible for the current reaction conditions considering the amount of MMT needed for twin-screw extrusion. Finally, in the conditions used to form the amidation, the pH has a restriction as the NHS ester does not have a high lifespan above a pH of 8. This limits the amount of active amine which can act as nucleophile for reaction as its pKa value is around 10,6.

Melt intercalation of the silylated clays, pristine MMT and a commercial grade CMMT (NANOMER I34NM) was performed and the resulting composites were investigated for improvement in their properties. SEM imaging of the extruded sheets revealed better distributions for the silylated and organophillisized nanoclay. However, due to the high processing temperatures of the polysulfone the organic

components start to degrade which manifests itself in the formation of air bubbles. The latter being the most pronounced in the silylated nanoclays. This has significant effects on the mechanical properties with a significant reduction in strength for both silylated and organophillisized nanoclay composites. These effects were more pronounced with the filler content. Furthermore, the presence of the air bubbles act as weaknesses in the polymer matrix which can initiate or propagate breakage resulting in large variations in elongation at break. XRD measurements of the extruded sheets revealed a small amount of intercalation occurring for the pristine NaMMT with an increase of basal spacing. The bad compatibilization of the pristine clays and the polysulfone matrix nonetheless does not result in any improvement nor decrease in mechanical properties. This leads to the conclusion that a phase separated composite is formed which can be seen in SEM by the pockets in which the nanoclays are comprised. Diffraction peaks for the silylated nanoclays disappear almost completely when mixing in the polymer matrix which can be caused by disordered intercalation and a large spread in interlaminar spacing due to the degradation of the organic grafted moieties. In the case of the CMMT a better spread is achieved yet a peak shift in XRD is noticed towards smaller basal spacing of the nanoclays suggesting relaxation of the clays into their original form.

7. 3. 1. Future research

In general, the high processing temperature for the polysulfone matrix hampers good compatibility with the MMT's due to the caused degradation of the organic spacers or grafted molecules. Reducing the residence time in the Coperion could improve intercalation by shortening the time at which the organic compounds are exposed to the elevated temperatures. This can be done by either increasing screw speed or changing the position of the side feeder further down the extrusion route. Another possible way is to make a composite using a low viscous PSU grade requiring less elevated temperatures for processing. Successful functionalization is also believed to render some more thermal stability to the grafted molecule by the conjugated benzene-sulfone system.

Due to the multi-step functionalization reaction of MMT the process encounters a lot of difficulties. Focusing on a different spacer with aromatic structures and a sulfone moiety might solve the thermal degradation problem. This spacer can then either be grafted or just incorporated in the clay galleries using the solution-precipitation technique.

One possibility of still continuing the amidation reaction is by increasing the amount of EDC to the system. Literature has reported promising results in this regards. As hydrolysis is considered the foremost reason of halting the reaction one can opt a different direction to continue amidation by activating the carboxylic acid moieties of the SPA in inert dry solvents using acyl chlorides. The use of an additional base is advised in this case in order to trap the HCl released during the reaction.

Alternatively, as most literature regarding polysulfone-nanofiller composites encompasses the use of the solution precipitation technique, it could be favorable to implement the spray drying technique already researched on virgin polysulfone for the preparation of polysulfone-nanoclay composites in usable powder form. This would entail the incorporation of the functionalized MMT in polymer solution and processing it via the spray drying technique requiring less severe thermal steps. Furthermore, the use of a polymer solution would conceivably stimulate exfoliation with the right choice of solvent. Upon drying of the particles this exfoliated structure would be eventually 'frozen' in the polymer matrix.

Upon successful functionalization and dispersion of the MMT nanoclays into a polysulfone matrix the obtained extrudates should be subjected to contact angle measurements in order to determine the effect of the MMT nanoclays on the polysulfone matrix regarding the anti-fouling properties. Swell tests to determine any improvement in chemical resistance would add valuable information to these test as well. Finally, the extrudates should be subjected to the three step refinement process on the rotor miller in order to produce nanocomposite feed material for laser sinter testing. These test could provide valuable information on the suitability of both the rotor milling technique as a production method for nanocomposite powders and the melt-intercalation process as production method for the nanocomposite materials.

7. 4. REFERENCES

[1]   G. V. Salmoria, J. L. Leite, and R. A. Paggi, "The microstructural characterization of PA6/PA12 blend specimens fabricated by selective laser sintering," *Polym. Test.*, vol. 28, no. 7, pp. 746–751, 2009.

[2]   G. V. Salmoria, J. L. Leite, R. A. Paggi, A. Lago, and A. T. N. Pires, "Selective laser sintering of PA12/HDPE blends: Effect of components on elastic/plastic behavior," *Polym. Test.*, vol. 27, no. 6, pp. 654–659, 2008.

[3]   S. C. Lao, W. Yong, K. Nguyen, T. J. Moon, J. H. Koo, L. Pilato, and G. Wissler, "Flame-retardant Polyamide 11 and 12 Nanocomposites: Processing, Morphology, and Mechanical Properties," *J. Compos. Mater.*, vol. 44, no. 25, pp. 2933–2951, 2010.

[4]   S. R. Athreya, K. Kalaitzidou, and S. Das, "Processing and characterization of a carbon black-filled electrically conductive Nylon-12 nanocomposite produced by selective laser sintering," *Mater. Sci. Eng. A*, vol. 527, no. 10, pp. 2637–2642, 2010.

[5]   R. Naim, a. F. Ismail, H. Saidi, and E. Saion, "Development of sulfonated polysulfone membranes as a material for Proton Exchange Membrane (PEM)," *Proc. Reg. Symp. Membr. Sci. Technol. 2004*, 2004.

[6]   Y. Liu, X. Yue, S. Zhang, J. Ren, L. Yang, Q. Wang, and G. Wang, "Synthesis of sulfonated polyphenylsulfone as candidates for antifouling ultrafiltration membrane," *Sep. Purif. Technol.*, vol. 98, pp. 298–307, 2012.

[7]   R. Gosalawit, S. Chirachanchai, S. Shishatskiy, and S. P. Nunes, "Sulfonated montmorillonite/sulfonated poly (ether ether ketone)(SMMT/SPEEK) nanocomposite membrane for direct methanol fuel cells (DMFCs)," *J. Memb. Sci.*, vol. 323, no. 2, pp. 337–346, 2008.

[8]   S. Darvishmanesh, J. C. Jansen, F. Tasselli, E. Tocci, P. Luis, J. Degrève, E. Drioli, and B. Van der Bruggen, "Novel polyphenylsulfone membrane for potential use in solvent nanofiltration," *J. Memb. Sci.*, vol. 379, no. 1–2, pp. 60–68, Sep. 2011.

[9]   P. Anadão, "Clay-Containing Polysulfone Nanocomposites," in *Advances in Nanocomposite Technology*, InTech, 2011.

[10]   I. Strużyńska-Piron, J. Loccufier, L. Vanmaele, and I. F. J. Vankelecom, "Synthesis of solvent stable polymeric membranes via UV depth-curing," *Chem. Commun.*, vol. 49, no. 98, p. 11494, Nov. 2013.

[11]   G. S. Sur, H. L. Sun, S. G. Lyu, and J. E. Mark, "Synthesis , structure , mechanical properties , and thermal stability of some polysulfone / organoclay nanocomposites," *Polymer (Guildf).*, vol. 42, pp. 9783–9789, 2001.

[12]   O. Monticelli, A. Bottino, I. Scandale, G. Capannelli, and S. Russo, "Preparation and properties of polysulfone–clay composite membranes," *J. Appl. Polym. Sci.*, vol. 103, no. 6, pp. 3637–3644, 2007.

[13]   A. Olad, "Polymer/clay nanocomposites," in *Advances in diverse industrial applications of nanocomposites*, InTech, 2011.

[14]   J. Pascual, E. Fages, O. Fenollar, D. García, and R. Balart, "Influence of the compatibilizer/nanoclay ratio on final properties of polypropylene matrix modified with montmorillonite-based organoclay," *Polym. Bull.*, vol. 62, no. 3, pp. 367–380, 2009.

[15]   L. Delva, T. Van De Keere, R. Alves, K. Ragaert, A. Gaspar-Cunha, L. Cardon, and J. Degrieck, "Extrusion and characterization of nanoclay filled polypropylene," *Adv. Prod. Eng. Manag.*, vol. 8, no. 2, p. 88, 2013.

[16]   Sigma Aldrich, "Nanomer Technical Datasheet," 2006.

[17]   D. R. Paul and L. M. Robeson, "Polymer nanotechnology: Nanocomposites," *Polymer (Guildf).*, vol. 49, no. 15, pp. 3187–3204, Jul. 2008.

[18]   S. S. Ray and M. Okamoto, "Polymer/layered silicate nanocomposites: a review from preparation to processing," *Prog. Polym. Sci.*, vol. 28, no. 11, pp. 1539–1641, 2003.

[19]   Y. Lvov, B. Guo, and R. F. Fakhrullin, *Functional polymer composites with nanoclays*. Royal Society of Chemistry, 2017.

[20]   M. Galimberti, "Rubber-clay nanocomposites: science, technology, and applications." John Wiley & Sons, 2011.

[21]   X. Liao, L. Ren, D. Chen, X. Liu, and H. Zhang, "Nanocomposite membranes based on quaternized polysulfone and functionalized montmorillonite for anion-exchange membranes," *J. Power Sources*, vol. 286, pp. 258–263, 2015.

[22]   M. S. Nazir, M. H. M. Kassim, L. Mohapatra, M. A. Gilani, M. R. Raza, and K. Majeed, "Characteristic Properties of Nanoclays and Characterization of Nanoparticulates and Nanocomposites," in *Nanoclay Reinforced Polymer Composites*, Springer, 2016, pp. 35–55.

[23]   Y.-C. Chung, T. K. Cho, and B. C. Chun, "Dependence of montmorillonite dispersion in nanocomposites on polymer matrix and compatibilizer content, and the impact on mechanical properties," *Fibers Polym.*, vol. 9, no. 1, pp. 7–14, 2008.

[24]   G. B. B. Varadwaj, K. Parida, and V. O. Nyamori, "Transforming inorganic layered montmorillonite into inorganic–organic hybrid materials for various applications: a brief overview," *Inorg. Chem. Front.*, vol. 3, no. 9, pp. 1100–1111, 2016.

[25]   M. Prasad, S. Mohanty, and S. K. Nayak, "Polymer electrolyte membranes based on sulfonated polysulfone and functionalized layered silicate for direct methanol fuel cell applications," *High Perform. Polym.*, vol. 27, no. 6, pp. 714–723, 2015.

[26]   Solvay, *Udel Polysulfone Design Guide*. Solvay.

[27]   J. Yeh, C. Chen, Y. Chen, C. Ma, H. Huang, and Y. Yu, "Enhanced corrosion prevention effect of polysulfone–clay nanocomposite materials prepared by solution dispersion," *J. Appl. Polym. Sci.*, vol. 92, no. 1, pp. 631–637, 2004.

[28]   P. Wang, J. Ma, Z. Wang, F. Shi, and Q. Liu, "Enhanced separation performance of PVDF/PVP-g-MMT nanocomposite ultrafiltration membrane based on the NVP-grafted polymerization modification of montmorillonite (MMT)," *Langmuir*, vol. 28, no. 10, pp. 4776–4786, 2012.

[29]   P. Jonkheijm, D. Weinrich, H. Schröder, C. M. Niemeyer, and H. Waldmann, "Chemical strategies for generating protein biochips," *Angew. Chemie Int. Ed.*, vol. 47, no. 50, pp. 9618–9647, 2008.

[30]   L. Su, Q. Tao, H. He, J. Zhu, and P. Yuan, "Locking effect: A novel insight in the silylation of montmorillonite surfaces," *Mater. Chem. Phys.*, vol. 136, no. 2–3, pp. 292–295, Oct. 2012.

[31]   L. Su, Q. Tao, H. He, J. Zhu, P. Yuan, and R. Zhu, "Silylation of montmorillonite surfaces: Dependence on solvent nature," *J. Colloid Interface Sci.*, vol. 391, pp. 16–20, Feb. 2013.

[32]   C. A. G. N. Montalbetti and V. Falque, "Amide bond formation and peptide coupling," *Tetrahedron*, vol. 61, no. 46, pp. 10827–10852, 2005.

[33]   D. Sehgal and I. K. Vijay, "A method for the high efficiency of water-soluble carbodiimide-mediated amidation," *Anal. Biochem.*, vol. 218, no. 1, pp. 87–

172

91, 1994.

[34]   H. Mojarradi, "Coupling of substances containing a primary amine to hyaluronan via carbodiimide-mediated amidation." 2010.

[35]   ThermoFisher Scientific, "Carbodiimide Crosslinker Chemistry," 2013. [Online]. Available: https://www.thermofisher.com/us/en/home/life-science/protein-biology/protein-biology-learning-center/protein-biology-resource-library/pierce-protein-methods/carbodiimide-crosslinker-chemistry.html.

[36]   Thermo Scientific, "Procedure for EDC/NHS Crosslinking of Carboxylates with Primary Amines," 2009.

[37]   L. Delva, K. Ragaert, and L. Cardon, *Twin-screw extrusion of montmorillonite filled polypropylene: (re)processing and characterization*. Ghent: Ghent, Belgium Ghent University. Faculty of Engineering and Architecture 2015, 2015.

[38]   M. A. Treece, W. Zhang, R. D. Moffitt, and J. P. Oberhauser, "Twin-screw extrusion of polypropylene-clay nanocomposites: Influence of masterbatch processing, screw rotation mode, and sequence," *Polym. Eng. Sci.*, vol. 47, no. 6, pp. 898–911, 2007.

[39]   M. Maniruzzaman, J. S. Boateng, M. J. Snowden, and D. Douroumis, "A review of hot-melt extrusion: process technology to pharmaceutical products," *ISRN Pharm.*, vol. 2012, 2012.

[40]   W. Lertwimolnun and B. Vergnes, "Influence of screw profile and extrusion conditions on the microstructure of polypropylene/organoclay nanocomposites," *Polym. Eng. Sci.*, vol. 47, no. 12, pp. 2100–2109, 2007.

[41]   W. Lertwimolnun and B. Vergnes, "Influence of compatibilizer and processing conditions on the dispersion of nanoclay in a polypropylene matrix," *Polymer (Guildf).*, vol. 46, no. 10, pp. 3462–3471, 2005.

[42]   L. Delva, K. Ragaert, K. Allaer, A. Gaspar-Cunha, J. Degrieck, and L. Cardon, "Influence of twin-screw configuration on the mechanical and morphological properties of polypropylene-clay composites," *Int. J. Mater. Prod. Technol.*, vol. 52, no. 1–2, pp. 176–192, 2016.

[43]   Coperion GmbH, "Patent for 5A Kneading Blocks," EP 1 508 424 B2, 2016.

[44]   F. Chavarria, R. K. Shah, D. L. Hunter, and D. R. Paul, "Effect of melt processing conditions on the morphology and properties of nylon 6 nanocomposites," *Polym. Eng. Sci.*, vol. 47, no. 11, pp. 1847–1864, 2007.

[45]   W. Shen, H. He, J. Zhu, P. Yuan, Y. Ma, and X. Liang, "Preparation and characterization of 3-aminopropyltriethoxysilane grafted montmorillonite and acid-activated montmorillonite," *Chinese Sci. Bull.*, vol. 54, no. 2, pp. 265–271, 2009.

[46]   A. M. Slavutsky, M. A. Bertuzzi, and M. Armada, "Water barrier properties of starch-clay nanocomposite films," *Brazilian J. Food Technol.*, vol. 15, no. 3, pp. 208–218, 2012.

[47]   K. C. Cole, "Use of infrared spectroscopy to characterize clay intercalation and exfoliation in polymer nanocomposites," *Macromolecules*, vol. 41, no. 3, pp. 834–843, 2008.

[48]   C. J. Pouchert, "The Aldrich library of infrared spectra," 1975.

[49]   N. Greesh, P. C. Hartmann, V. Cloete, and R. D. Sanderson, "Adsorption of 2-acrylamido-2-methyl-1-propanesulfonic acid (AMPS) and related compounds onto montmorillonite clay," *J. Colloid Interface Sci.*, vol. 319, no. 1, pp. 2–11, Mar. 2008.

[50]   Y. Kim, Y. Choi, H. K. Kim, and J. S. Lee, "New sulfonic acid moiety grafted on montmorillonite as filler of organic–inorganic composite membrane for non-humidified proton-exchange membrane fuel cells," *J. Power Sources*, vol. 195, no. 15, pp. 4653–4659, 2010.

[51]   I. Horvath and L. Galikova, "Mechanism of the H 2 O (g) release during a dehydroxylation of montmorillonite," *Chem Zvest*, vol. 33, pp. 604–611, 1979.

[52]   Z. Martín, I. Jiménez, M. Á. Gómez, H. W. Ade, D. A. Kilcoyne, and D. Hernádez-Cruz, "Spectromicroscopy study of intercalation and exfoliation in polypropylene/montmorillonite nanocomposites," *J. Phys. Chem. B*, vol. 113, no. 32, pp. 11160–11165, 2009.

Chapter 8

CONCLUSIONS AND OUTLOOK

This chapter summarizes the key findings and objectives of this doctoral research. Based upon these conclusions, suggestions are formulated for future research on the topic.

8. 1. CONCLUSIONS

This doctoral research has contributed to the search for new polymers for laser sintering. Only a limited variety of polymer materials exist for SLS, in stark contrast with the variety of polymers available for traditional processing techniques such as injection molding and extrusion. In order to balance out this equation commercially available polymers should be investigated for the use in selective laser sintering. Polymer powders usable for SLS have to fulfill specific requirements in order to be easily processable using said technique. Ideally, the powders should exhibit spherical morphology with a smooth surface and a particle size in the range of 45-95 µm. So as to achieve powders with these specific properties new processing techniques have to be investigated. To that end this research has focused on both the mechanical as physicochemical techniques to process commercial polymer pellets into these spherical powders. From the mechanical part, rotor milling was investigated and compared briefly to its (cryogenic) ball milling equivalent -which is most commonly used in industry. From a physicochemical view, spray drying was explored as this technique is said to create spherical particles with smooth surface morphology. Using these processing methods, three interesting engineering polymers were investigated as case studies: PPSU, PSU and sPS. In each case study the polymers in question were processed and investigated on their size and morphology as well as any change occurring in their intrinsic properties due to the processing technique. Afterwards they were tested for actual sinter experiments at the University of Leuven.

In all three case studies the polymers could be processed in spherical powders using the rotor milling technique. Powders were found to have a spherical nature with good powder flowability assessed by the Hausner ratio. Particle size distributions all lie within the desired range and were easily obtained using a three step refinement process in which the pellets were milled sequentially from pellets to powders of decreasing size with each step. PSD of all three case studies presented a mean diameter around 50 µm with a standard deviation of 15 µm. A final sieving step ensured the removal of inconsistencies and ensured good powder flow behavior.

Though the spray drying process shows great promise, further research still has to be done on this subject. From the three case studies polysulfone presented the most

175

promise displaying smooth morphology and particle size of 26,1 µm with a standard deviation of 12,8 µm. In the other cases, sPS did show spherical morphology albeit at a particle size of 6,6 and standard deviation of 6,9 µm. The low concentration at which sPS could be dissolved in m-xylene was mostly responsible for this. In the case of PPSU a maximum particle size of 14,5 ± 11,5 µm was obtained with only a limited amount of spherical particles (22,3 %). A response surface model was elaborated in order to discern the most critical factors influencing particle size and particle morphology in the spray drying process in this regard. Gas flow rate was found to be the post prominent factor affecting particle size and in lesser extent the positive interaction of material grade and inlet temperature. However, this lead to mostly deflated, shriveled particles which puts forward the notion of the particles being not fully dense. The sphericity of the particles is promoted by high inlet temperatures, low gas flow rates high concentrations and high feed flow rates. These settings were found to promote the formation of a thick rigid shell which is mechanically stable enough to sustain itself throughout the drying process. At these settings particle size decreases slightly to 11,39 µm. FIB-SEM measurements provided clarity about the density of the particles confirming the above-mentioned hypothesis. The low diffusion rate of the polymers prevents homogeneous drying out of the particles by creating hollow spheres.

As a way of comparison cryogenically milled and ball milled samples were studied. These were found severely lacking in morphology. Except for the cryogenically milled sample, all ball milled samples showed large deviations on particle size with incomplete fractionation and very fine particles.

Investigation of the thermal properties of the case studies displayed a reversible influence of the processing methods on the thermal properties of the polymers. In the case of rotor milling small endothermic peaks are seen which disappear in the second heating run. For the semi-crystalline sPS however, amorphization due to the processing method occurs leading to cold crystallization in the first heating curve. This is explained when looking at the process of spray drying the sPS: due to the thermal gradient the particles undergo from going to the heated drying chamber to the collection vessel at ambient temperature. All changes were reversible in these cases. For the cryogenically milled sample a strange endothermic peak and crystallization peak become apparent. These are possibly ascribed to the addition of free flowing additives of the powder by the producer. Finally, the ball milling samples showed some amorphization in the case of sPS and a strange orientation in the form of an endothermic peak in the high temperature regions of PSU, both reversible.

GPC measurements were performed to see if the processing methods caused degradation of the polymers in a significant amount. In the case of PSU and PPSU no significant degradation for the rotor milling and spray drying method was observed. sPS was unable to be dissolved in the eluens used for GPC measurements, instead the

decrease in crystallinity using the DSC curves was used as an indirect indication of degradation. In this regard the ball milled sample displayed a decrease in crystallinity of 40,5 % indicating severe degradation. Rotor milling and spray drying displayed a reduction of 3,4 % and 1,9 % respectively, indicating no severe degradation.

The rotor milled samples of PSU and sPS were sent to the University of Leuven for sinter testing. Single layers were sintered of the sPS powder samples displaying warpage and curling of the edges. While coalescence and powder deposition were not a problem, due to the bed temperature of the DTM Sinterstation 2000 that can only be heated stably up to 200 °C crystallization of the layers occurred. This hampers the building of multilayer structures and requires a higher temperature of the sinterstation in order to continue investigating the sinter properties of the sPS. As the PSU is an amorphous polymer the processing temperature for laser sintering is just above the glass transition temperature. This means that the powder bed temperature is high enough to minimize the thermal gradients and multilayer structures can be printed. Though further optimization in laser sintering of the PSU is still necessary, tensile bars could be sintered for mechanical characterization. With the sintering of multilayers possible, applications in different fields like in membrane technology are already conceivable.

As the production of powders is at lab-scale with throughputs of 8,6 g/h for the rotor milling process and approximately 20 g/h for the spray drying process an increase to pilot scale levels would be beneficial for more efficient laser sintering experiments and later on for production. In this regard, upscaling has been investigated in which the Pulverisette 14 unit is exchanged for a pilot scale rotor miller. Throughputs should significantly increase as the grinding area of the machines shows a larger surface. Another way is to invest in a battery op P14 units which limit the throughput to the rate determining step of the three-step milling process elaborated on the P14. As for the spray drying units, upscaling to pilot scale designs such as the Mobile Minor spray dryers is also feasible. This spray dryer is said to have higher throughputs and can achieve larger particle sizes which is one of the workpoints of the technique. However, the production of hollow spheres remains an obstacle in this technique for the production of laser sintering feed materials as the hollow interior in turn imparts a low bulk density of the powder. Further optimization regarding the thickness of the shell needs to be done in this regard. These unique properties however might be applicable in other fields requiring lightweight materials.

In a second experimental hatch the production of polymer composites was explored as an alternative way of adding to the material palette of SLS. Here, polysulfone was blended with functionalized nanoclays in order to improve other features of PSU. Functionalization of the nanoclays was performed in two steps of which the first consisted in a silylation on the surface and inside the clay galleries. The second step involved an amidation reaction in which 4-sulfophthalic acid was covalently bound.

This step was expected to increase the compatibility of the nanoclays with the polysulfone matrix considerably. However, due to the low lifespan of the O-acylisourea and the possible hydrolysis of the EDC-carbocation the reaction did not take place. Literature advises a large excess of EDC to be used in order to allow the reaction to continue yet this is not feasible in practice. The blending of the composites occurred using twin screw extrusion with polysulfone as a matrix and the organically modified nanoclays by silylation. The high processing temperatures of polysulfone proved to be an impediment in the blending process as they provided the onset of degradation for the organic linkers. This caused the formation of air bubbles made by volatile degradation products which caused bad compatibilization of the nanoclays with the matrix and did not result in a significant increase in properties. Before subjecting the nanocomposite extrudates to the three step refinement process of the rotor miller to produce feed material for laser sintering, the optimization of the functionalization process needs to be further investigated.

8. 2. OUTLOOK

This doctoral research consisted of two parts. On the one hand it has focused on the processing of three polymer candidates for selective laser sintering while on the other hand, it focused on the functionalization of a polymer filler and subsequent processing of said filler in a polysulfone matrix using twin screw extrusion. Several research topics have been identified which could merit further research.

The field of physicochemical processing of polymers through the medium of spray drying has shown great promise in regards to creating spherical particles albeit with decreased density or as hollow spheres. A Response Surface Model was already elaborated on this part in order to optimize particle size and morphology. Further fine-tuning could entail an augmented design in which validation experiments and reproducibility is checked. Another design of experiments could be set up in which the density of the particles is checked in regard to these processing parameters for morphology and particle size with shell thickness as additional response value to maximize. The hollow spheres created however can find their applications in other fields requiring lightweight materials for thermal insulation or in the research field of microencapsulation, pigmentation, opacifyers, damping materials,… and should be investigated for these purposes.

In the case of the amidation reaction; because hydrolysis is considered the foremost reason of halting the reaction, one can opt a different direction to continue amidation by activating the carboxylic acid moieties of the SPA in inert dry solvents using acyl chlorides. Also, due to the many reaction steps the functionalization becomes quite complex. Simplifying the reaction by direct silylation with an organic linker already consisting of the aryl sulfone moiety could also improve success of functionalization significantly.

178

It is noteworthy to mention that, as most literature regarding polysulfone-nanofiller composites encompasses the use of the solution precipitation technique, it could be favorable to implement the spray drying technique for the preparation of polysulfone-nanoclay composites in usable powder form. The solution precipitation method has been known to achieve complete exfoliation in polymer solution and does not use as high processing temperatures as used in twin-screw extrusion. In this aspect one can use the powders produced for laser sintering as such or blend with virgin material to reduce porosity.

Shortening the residence time of the nanoclays in the blending process could decrease the thermal degradation. This can be done either by increasing screw speed or changing the position of the side feeder further along the extrusion line. As the intercalation of the polymer into the interlaminar space has been proven to occur early on in the blending process this should not affect the distribution significantly. Also, using a lower viscous grade of polysulfone which can be processed at lower temperatures could help considerably.

This dissertation has contributed to the material palette for SLS by identifying two processing routes to transform polymer pellets into spherical powders and adding three virgin engineering polymers to the gamma. The additive manufacturing branch is still relatively young and expected to grow even more in the forthcoming years. Along with technological advances, a significant increase in research efforts is required. The expansion of the SLS material palette must be in line with a need for technological advances in the construction of cheaper high temperature sintering machines. These would allow to control better quality of print by carefully controlling the sintering process.

ABOUT THE AUTHOR

Nicolas Mys was born on October 24th, 1988 in Ghent, Belgium. He followed his high school education at Sint-Pietersinstituut in Ghent, obtaining his degree in Science and Mathematics in 2006. After this he started studying Chemistry at the Faculty of Sciences at the University of Ghent and combined his passion for Science with his passion for mountaineering under top-level sport statue with University Ghent. For his master's degree he wrote a dissertation on the deposition of Al-doped ZnO layers via inkjet printing under supervision of prof. Klaartje De Buysser. He then joined the Center for Polymer and Material Technologies (CPMT) to work on a research project as a doctoral student (University Ghent, Faculty of Engineering and Architecture). His work encompassed the processing and characterization of novel polymeric materials to spherical powders for fusion based additive manufacturing under supervision of prof. Ludwig Cardon and co-supervisor prof. An Verberckmoes. Throughout his time as a PhD student, the author has followed several specialist courses at Ghent University as part of the doctoral training program and gave the practicals in the courses of polymer and composite materials. He furthermore attended an immersion program at the Chemical Engineering department in Sichuan University, China. In the CPMT lab, the author also assisted in other research projects concerning the characterization of polymers.

Nicolas Mys is author of several scientific publications in international journals and participated actively in national and international conferences by means of posters and oral presentations.

PUBLICATIONS

N. Mys, R. Van De Sande, A. Verberckmoes, and L. Cardon, "Processing of Polysulfone to Free Flowing Powder by Mechanical Milling and Spray Drying Techniques for Use in Selective Laser Sintering" *Polymers*, vol. 8, no. 4. 2016.

N. Mys, A. Verberckmoes, and L. Cardon, "Processing of Syndiotactic Polystyrene to Microspheres for Part Manufacturing through Selective Laser Sintering" *Polymers*, vol. 8, no. 11, p. 383, 2016.

N. Mys, A. Verberckmoes, and L. Cardon, "Spray Drying as a Processing Technique for Syndiotactic Polystyrene to Powder Form for Part Manufacturing Through Selective Laser Sintering" *JOM*, pp. 1–6, 2016.

N. Mys, R. Van de Sande, A. Verberckmoes, and L. Cardon, "Processing of Polysulfone to Free Flowing Powder for Part Manufacturing Through Selective Laser Sintering," *Regional Conference Polymer Processing Society Graz*, 2015. .

SUBMITTED FOR REVIEW

N. Mys, A. Verberckmoes, and L. Cardon, "Physico-Chemical Processing Of Polyphenylsulfone: Optimization Of Processing Parameters For Microsphere Production Via Spray Drying Using A Response Surface Model", *Journal Advanced Powder Technology*

L. Delva, M. Kuzmanovic, T. Wieme, N. Mys and K. Ragaert, "Functional evaluation of compatibilization systems for recycles PP-PET blends", *International Conference Polymer Processing Society Cancun*, 2017

CONFERENCE CONTRIBUTIONS

N. Mys, A. Verberckmoes and L. Cardon
Oral: "Processing and characterization of Polysulfone to spherical powders for SLS purposes", 7th bi-annual International Conference on Polymers and Moulds Innovations, Ghent, Belgium, September 21-23rd, 2016

N. Mys, A. Verberckmoes and L. Cardon
Oral: "Spray drying as a processing technique for syndiotactic polystyrene to powder form for part manufacturing through selective laser sintering", Solid Freeform Fabrication Symposium, Austin, USA, August 8-10th, 2016

N. Mys, R. Van de Sande, A. Verberckmoes, and L. Cardon
Oral: "Processing of polysulfone to free flowing powder for part manufacturing through selective laser sintering", Regional Conference Polymer Processing Society, Graz, Austria, September 21-25th, 2015

N. Mys, T. Haverans, A. Verberckmoes and L. Cardon
Oral: "Processing and characterization of Polysulfone to spherical powders for SLS purposes", 6th bi-annual International Conference on Polymers and Moulds Innovations, Guimarães, Portugal, September 10-12th, 2014

POSTER PRESENTATIONS

N. Mys, A. Verberckmoes and L. Cardon
"Powder based 3D printing: overcoming the stumbling block of material shortage by novel processing routes of polymer pellets" 17th annual FEA Research Symposium, Ghent, Belgium, February 15th, 2017

N. Mys, A. Verberckmoes and L. Cardon
"POLYFORCE-Polymers with and without reinforcements for part manufacturing by Selective Laser sintering", 16th annual FEA Research Symposium, Ghent, Belgium, December 9th, 2015

N. Mys, A. Verberckmoes and L. Cardon

"Processing and characterization of syndiotactic Polystyrene into a free flowing powder", 4th SIM user forum, Ghent, Belgium, October 27th, 2015

N. Mys, A. Verberckmoes and L. Cardon

"POLYFORCE-Polymers with and without reinforcements for part manufacturing by Selective Laser sintering", 3rd SIM user forum, Ghent, Belgium, December 19th, 2014